Coupled Simulations of Wind Turbines and Offshore Support Structures

Strategies based on the Dynamic Substructuring Paradigm

PROEFSCHRIFT

ter verkrijging van de graad van doctor
aan de Technische Universiteit Delft,
op gezag van de Rector Magnificus Prof. ir. K.C.A.M. Luyben,
voorzitter van het College voor Promoties,
in het openbaar te verdedigen
op vrijdag 31 oktober 2014 om 10:00 uur
door

Paulus Leonardus Carolus VAN DER VALK

werktuigkundig ingenieur
geboren te Naaldwijk.

Dit proefschrift is goedgekeurd door de promotor:

Prof. dr. ir. D.J. Rixen

Samenstelling promotiecommissie:

Rector Magnificus,	voorzitter
Prof. dr. ir. D.J. Rixen,	Technische Universiteit Delft / TU München, promotor
Prof. dr. A.V. Metrikine,	Technische Universiteit Delft
Prof. dr. ir. A. de Boer,	Universiteit Twente
Prof. dr. ir. W. Desmet,	Katholieke Universiteit Leuven
Prof. dr. C.L. Bottasso,	Technische Universität München
Dr. ir. A. Simone,	Technische Universiteit Delft
Dr. ir. D-P. Molenaar,	Siemens Wind Power
Prof. dr. ir. A. van Keulen,	Technische Universiteit Delft, reservelid

ISBN 978-94-6203-681-9

Printed by: Wöhrmann Print Service, Zutphen
Cover design: Frank van der Knaap

Author email: plcvandervalk@gmail.com

Abstract

Coupled Simulations of Wind Turbines and Offshore Support Structures
- Strategies based on the Dynamic Substructuring Paradigm -

The concept of using wind energy to power all different types of machines has been known to mankind for centuries, with the first recorded instances dating back almost two millennia. Within the Netherlands it was in fact one of the main sources of energy in the 16^{th} and 17^{th} century. Nowadays, after two centuries of relying mainly on fossil fuels for our power needs, wind energy is again considered as an attractive, and clean, alternative. This energy transition is driven partly by the realization that, in order to prevent disruptive climate changes, we need to reduce our greenhouse gas emissions and partly to reduce our dependence on foreign governments for the supply of fossil fuels.

This transition has led to an exponential increase in the size of wind turbines, as well as the number of installed onshore and offshore units worldwide. Whereas onshore wind energy is increasingly often beating conventional sources of electricity for cost effectiveness, offshore wind is currently still too expensive. Cost reductions are to be achieved, for instance, by installing larger turbines in larger offshore wind farms in order to benefit from economies of scale. Many of these wind farms have to be built further offshore in deeper waters, where the waves are also higher. As a result traditional monopile foundations are not always feasible and multi-membered foundations, such as jackets and tripods, are required.

The design of these foundations is generally done by a specialized company. In order to be able to design the foundation, the loads resulting from the wind turbine need to be taken into account. In order to quantify this loading over the design lifetime, typically thousands of aero-elastic simulations are required. These aero-elastic models account for all the physical phenomena that are relevant for an offshore wind turbine, such as the structural-, aero-, hydro-, and controller dynamics. However, as models of multi-membered foundations are significantly larger than their monopile counterparts, more compact models are required to limit the computational costs of these simulations. Hence, advanced methods are required to enable the use of reduced models in wind turbine simulations. In addition, these techniques should also be used in an efficient and accurate design process involving multiple parties. The dynamic substructuring paradigm is an analysis strategy that is able to fulfill these needs.

In the dynamic substructuring methodology one uses a component-wise approach for solving the dynamics of large and complex structures. In part I of this thesis three different substructuring approaches are identified that can be used for efficiently and accurately including complex foundation models in wind turbine simulations. Firstly, foundation models can be reduced and assembled using the classical Component Mode Synthesis methods. Secondly, a framework for the Impulse Based Substructuring method is introduced, that enables one to couple multiple impulse response functions and finite element models in a time-stepping scheme. This approach allows to include linear foundation models as impulse response functions in the integrated

wind turbine analysis. Finally, a family of strategies is introduced to couple the individual time integration schemes of multiple modeling environments. These methods enable to obtain coupled time responses of structures where the individual components are modeled and simulated in different programs. Therefore, they can be used to take into account nonlinear foundation models, as would for instance be the case for floating foundations.

In addition it is shown that the amount of data transfer between the design parties can be reduced by transforming the distributed forces, acting on linear substructures, to the interface degrees of freedom. This enables to only exchange interface data in a design process involving multiple project groups.

In part II of this thesis, the outlined substructuring approaches are applied in a realistic test case. Here, the response of a wind turbine, installed on a jacket foundation, is simulated for a normal production load case using an aero-elastic simulation tool. In order to close the computational loop, the foundation designer's job of computing the fatigue damages in the elements of the jacket is also performed. As the simulations have been performed using either a reduced model of the foundation or its impulse response functions, one first has to reconstruct the full nodal response of the jacket. This is done by either expanding the reduced results, or by performing an extra set of (static or dynamic) simulations using the full jacket model.

Firstly, it is found that by coupling the simulations of the wind turbine, performed in the aero-elastic code, with the jacket simulations, performed in an external program, the solution of the unreduced problem can efficiently be obtained. This solution was used as the reference solution and allows to evaluate the performance of the different substructuring and reconstruction approaches. From this exercise it was found that, except for the static condensation, all substructuring methods evaluated will result in accurate estimates for fatigue damages. In addition, it was found that the static reconstruction methods will result in a significant underestimation of the fatigue loads. This confirms that the internal dynamics of the jacket cannot be neglected in the coupled aero-elastic simulations and that its damping and inertia contributions should be included in the analysis.

Finally note that the biggest contribution of this thesis is in defining, implementing and evaluating multiple analysis methods (and combinations of methods) that enable one to accurately determine the loading in both the wind turbine component and its foundation. As one is not limited to a single approach, the methods that best fit ones existing modeling and simulation capabilities can be applied.

Samenvatting

Gekoppelde Simulaties van Windturbines en Offshore Ondersteuningsstructuren
- Strategieën gebaseerd op het Dynamische Substructureringsparadigma -

De mensheid gebuikt al vele eeuwen windenergie om allerlei soorten machines aan te drijven. In de 16e en 17e eeuw was het zelfs één van de belangrijkste bronnen van energie in Nederland. Nu, na twee eeuwen op vooral fossiele bronnen van energie te hebben vertrouwd, wordt windenergie weer beschouwd als een aantrekkelijk en schoon alternatief. Deze energietransitie is vooral het resultaat van de realisatie dat we de uitstoot van de hoeveelheid broeikasgassen moeten reduceren om ernstige klimaatveranderingen te voorkomen. Daarnaast kan tegelijkertijd de afhankelijkheid van buitenlandse regeringen voor de toevoer van fossiele brandstoffen worden teruggebracht.

Deze transitie heeft mede geleid tot een exponentiële groei in zowel de grootte van windturbines als het wereldwijde aantal geïnstalleerde eenheden op land en op zee. Terwijl op land gegenereerde windenergie steeds vaker de directe concurrentie met conventionele methodes van elektriciteitsopwekking aan kan, is windenergie op zee momenteel nog steeds te duur. Kostenreducties kunnen worden gerealiseerd door middel van schaalvergroting, door bijvoorbeeld steeds grotere turbines in steeds grotere parken op zee te plaatsen. Veel van deze parken moeten worden gerealiseerd op steeds diepere locaties, welke zich verder van de kust bevinden en waar de golven hoger zijn. Hierdoor zijn de traditionele "monopaal" funderingen niet altijd meer toepasbaar en zijn complexere funderingstypes benodigd, zoals "jackets" of driepoten.

Het ontwerp van deze funderingen wordt over het algemeen gemaakt door gespecialiseerde bedrijven. Om dit ontwerp te kunnen maken, moeten de krachten berekend worden die afkomstig zijn van de windturbine. Hiervoor worden over het algemeen vele duizenden dynamische simulaties gedaan met aero-elastische simulatiemodellen. Deze modellen houden rekening met alle fysische fenomenen die relevant zijn voor een windturbine, zoals de structuur-, aero-, hydro- en regelaardynamica. De modellen van de complexere funderingen zijn vele malen groter dan die van de traditionele monopaal. Om de berekeningskosten te beperken, moeten deze modellen zo compact mogelijk worden gemaakt. Hiervoor zijn geavanceerde methodes benodigd die deze gereduceerde modellen kunnen creëren, zodat deze kunnen worden toegepast in windturbinesimulaties. Daarnaast moeten deze technieken ook in een efficiënt en nauwkeurig ontwerpproces met meerdere partijen kunnen worden gebruikt. Het dynamische substructureringsparadigma is een analysestrategie die deze behoeften kan vervullen.

De dynamische substructureringsmethodologie houdt in dat het dynamische gedrag van een groot en complex systeem kan worden bepaald aan de hand van de componentdynamica. In deel I van het proefschrift worden drie verschillende substructureringsmethoden geïdentificeerd welke gebruikt kunnen worden om complexe funderingsmodellen te integreren in windturbinesimulaties. Ten eerste kunnen de modellen worden gereduceerd en geassembleerd met de klassieke Component Mode Synthesis methodes. Daarnaast is er een raamwerk voor de Im-

pulse Based Substructuring methode geïntroduceerd, welke het mogelijk maakt verscheidene impulsresponsies te koppelen met eindige elementenmodellen in een tijdsintegratieschema. Deze techniek maakt het mogelijk om lineaire funderingsmodellen als impulsresponsies te integreren in de windturbinesimulaties. Ten slotte is er een familie van strategieën geïntroduceerd waarmee men de individuele tijdssimulaties van meerdere modelleringsomgevingen kan koppelen. Hierdoor kan de gekoppelde responsie worden bepaald in het geval dat de verschillende componenten in verschillende simulatieprogramma's zijn gemodelleerd. Dit maakt het mogelijk om ook niet-lineaire funderingsmodellen, zoals bijvoorbeeld drijvende funderingen, te koppelen aan de bestaande windturbinesimulatiemodellen.

Ook is het aangetoond dat de verdeelde krachten, die op een lineair componentmodel werken, getransformeerd kunnen worden naar een set equivalente belastingen op de interface. Hierdoor hoeft slechts data op de interface tussen de verschillende projectgroepen te worden uitgewisseld.

In deel II van het proefschrift zijn de eerder besproken substructureringsmethoden gedemonstreerd met een realistisch voorbeeld. In het voorbeeld is de responsie van een windturbine, geïnstalleerd op een jacketfundering, gesimuleerd tijdens normale productie met een aero-elastisch simulatiepakket. Een deel van het werk van de funderingsontwerper, het berekenen van de materiaalvermoeiing in de fundering, is daarbij ook uitgevoerd, zodat de complete analysecyclus is doorlopen. Omdat de simulaties zijn gedaan met óf een gereduceerd model van de fundering óf een set van impulsresponsies hiervan, moeten na de simulaties de volledige responsies van de jacket worden gereconstrueerd. Dit is gedaan door de gereduceerde resultaten zowel te expanderen als een extra set van (statische of dynamische) simulaties met alleen het jacketmodel uit te voeren.

De referentieoplossing is efficiënt berekend door de aero-elastische simulaties van de windturbine te koppelen met een extern model van de volledige jacketfundering. Vervolgens zijn deze resultaten met die van de verschillende gereduceerde modellen vergeleken. Nauwkeurige schattingen voor de vermoeiingsschade konden worden verkregen met alle methodes, op de statische condensatie na. Daarnaast is gebleken dat de statische reconstructiemethodes resulteren in significante onderschattingen van de materiaalvermoeiing t.o.v. de referentieoplossing. Dit bevestigt dat de interne dynamica van de jacket niet kan worden verwaarloosd in de gekoppelde aero-elastische simulaties.

Uiteindelijk kan worden geconcludeerd dat de grootste bijdrage van dit werk het definiëren, implementeren en evalueren van verscheidene analysemethodes (en combinaties van methodes) is, welke men in staat stelt om nauwkeurig de belastingen in zowel de windturbine als de fundering te bepalen. Daardoor is men niet gelimiteerd tot één enkele methode en kunnen de methodes gekozen worden die het beste bij de huidige modellerings- en simuleringscapaciteiten passen.

Acknowledgements

Four and a halve years ago the possibility of performing a PhD. research project in cooperation with Siemens Wind Power arose. After having graduated for the MSc. of Mechanical Engineering at Siemens Wind Power a couple of months earlier, I was given the opportunity to continue researching the topic of dynamic substructuring, but now with a focuss on the support structures of offshore wind turbines.

Like I already mentioned in my MSc. thesis, one can compare working on such a project to a journey with an undetermined routing. During this journey you have to navigate trough unmapped territory and you will come across a lot of intersections and dead-end side streets. It is therefore essential to have a number of people which will guide and support you during this journey. Hence, having arrived at the end of this journey, the time has come to thank those who provided this support over the years.

Firstly, I would like to thank prof. Daniel Rixen who has supervised, inspired and motivated me during the entire project. I especially appreciate the numerous technical discussions we had over the years and the fact that you were always available for exchanging some quick thoughts. Even though the move to Munich put us on some physical distance, you've always remained closely involved with me and the project.

Secondly, I'd like to thank David-Pieter Molenaar and Sven Voormeeren from Siemens Wind Power. Without their support this project never would have been initiated. David, you were instrumental in making me look beyond the technical details and keeping an eye on the bigger picture and goals of the project. Sven, your contribution was not only in writing and presenting the project proposal for Siemens, but we've also spend numerous hours working together on different topics and you were always available to brainstorm on some of the ideas. Note that this project was enabled by the financial support of Siemens Wind Power, for which I'm very grateful.

In addition, I want to thank all my colleagues, both at Siemens in The Hague and at the university in Delft, for the pleasant working environment. Even though I won't name everybody here, as that would probably extend the acknowledgements with an extra page, the help at the technical level and the fun at the personal level you have offered has been essential. Finally, I'd also like to thank the Danish colleagues from Siemens and especially Jesper Winther Stærdahl, Jørgen Thirstrup Petersen and Peter Fisker Skjoldan for their involvement.

Furthermore, my special thanks goes to the MSc. students I had the honor to supervise: Rad, Wei, Marco, Roel, Pauline, Tim and Dick. I enjoyed the cooperation and also learned a lot from the experience.

I'd also like to thank all the friends and relatives, who were not involved directly in the work, but still provided the needed social support. Mom and dad, thanks for your support and

encouragement, not only in this project, but also in all the years prior. Without this, I would never have gotten to this point.

Last, but absolutely not least, I would like to thank Lidka for her love, care and support over all these years, but also for improving much of the figures in this thesis. Living with somebody finishing a PhD. is not always easy and especially over the last year we've had too little time to spend together. Therefore, I really appreciate that you've been so patient and also motivated and stimulated me at the times that it was needed!

Paul van der Valk
October 2014

Contents

Nomenclature

List of symbols

Meaning of often used symbols, unless stated otherwise:

$\boldsymbol{A}$	Newmark block matrix	$\boldsymbol{P}$	Orthogonal projector
$\boldsymbol{B}$	(signed) Boolean matrix	$\boldsymbol{p}$	array of nonlinear forces
$\boldsymbol{C}$	damping matrix	$\boldsymbol{Q}$	Newmark block matrix
$\boldsymbol{F}$	matrix of external forces	$\boldsymbol{q}$	array of generalized DoFs
$\boldsymbol{f}$	array of external forces	$\boldsymbol{R}$	reduction matrix
$\boldsymbol{G}$	flexibility matrix	$\boldsymbol{r}$	array of residual forces
$\boldsymbol{g}$	array of connection forces	$\boldsymbol{S}$	Jacobian matrix
h	time step size	$\boldsymbol{T}$	orthogonal projector
$\boldsymbol{I}$	identity matrix	t	time
$\boldsymbol{K}$	stiffness matrix	$\boldsymbol{u}$	array of nodal DoFs
$\boldsymbol{L}$	Boolean matrix	$\boldsymbol{Y}$	impulse response function
$\boldsymbol{M}$	mass matrix	$\boldsymbol{Z}$	dynamic stiffness matrix
$\boldsymbol{N}$	Newmark block matrix		

Greek symbols:

$\boldsymbol{\alpha}$	rigid body modal amplitudes	$\boldsymbol{\lambda}$	array of Lagrange multipliers
α_f	generalized-α parameter	$\boldsymbol{\Phi}$	set of vibration mode shapes
α_m	generalized-α parameter	$\boldsymbol{\phi}$	vibration mode shape
β	Newmark parameter	$\boldsymbol{\Psi}$	set of static deformation shapes
γ	Newmark parameter	$\boldsymbol{\psi}$	static deformation shape
$\boldsymbol{\zeta}$	MTA modal amplitudes	ω	eigenfrequency, circular frequency
$\boldsymbol{\eta}$	modal amplitudes	$\boldsymbol{\Omega}$	diagonal eigenfrequency matrix

Sub- and superscripts:

$\star_{[i]}$	pertaining to internal DoFs	$\star^{(s)}$	pertaining to substructure s
$\star_{[b]}$	pertaining to boundary DoFs	$\star^{(S)}$	pertaining to a “source” substructure
$\star_n$	pertaining to $t(n)$	$\star^{(R)}$	pertaining to a “receiver” substructure

Notation convention

Throughout this thesis the following notation convention is used:

- Scalars are denoted by normal upper and lower case symbols (x or X).
- Arrays and vectors are denoted by bold lower case symbols ($\boldsymbol{x}$).
- Matrices are denoted by bold upper case symbols ($\boldsymbol{X}$).
- Block diagonal matrices are denoted by:

$$diag(\boldsymbol{X}^{(1)}, \boldsymbol{X}^{(2)}) = \begin{bmatrix} \boldsymbol{X}^{(1)} & \boldsymbol{0} \\ \boldsymbol{0} & \boldsymbol{X}^{(2)} \end{bmatrix}.$$

- Stacked column vectors and arrays are denoted by:

$$col(\boldsymbol{x}^{(1)}, \boldsymbol{x}^{(2)}) = \begin{bmatrix} \boldsymbol{x}^{(1)} \\ \boldsymbol{x}^{(2)} \end{bmatrix}.$$

- Concatenated row vectors and arrays are denoted by:

$$row(\boldsymbol{y}^{(1)}, \boldsymbol{y}^{(2)}) = \begin{bmatrix} \boldsymbol{y}^{(1)} & \boldsymbol{y}^{(2)} \end{bmatrix}.$$

List of abbreviations and definitions

The following abbreviations are regularly used throughout this thesis:

BHawC	*Bonus Horizontal axis wind turbine Code*		
CAPEX	*Capital Expenditure*	FRF	*Frequency Response Function*
CB	*Craig-Bampton*	GR	*Guyan's Reduction*
CMS	*Component Mode Synthesis*	IBS	*Impulse Based Substructuring*
DC	*Displacement Control*	IRF	*Impulse Response Function*
DEL	*Damage Equivalent Load*	LCOE	*Levelized Cost of Electricity*
CB	*Craig-Bampton*	MTA	*Modal Truncation Augmentation*
DLC	*Design Load Case*	OMA	*Operational Modal Analysis*
DoF	*Degree of Freedom*	OWT	*Offshore Wind Turbine*
DS	*Dynamic Substructuring*	POD	*Proper Orthogonal Decomposition*
FBS	*Frequency Based Substructuring*	POM	*Proper Orthogonal Mode*
FC	*Force Control*	RNA	*Rotor Nacelle Assembly*
FD	*Foundation Designer*	WT	*Wind Turbine*
FE(M)	*Finite Element (Method)*	WTM	*Wind Turbine Manufacturer*
FETI	*Finite Element Tearing and Interconnecting*		

The following definitions are used throughout this thesis:

Wind Turbine	Assembly of the RNA and Tower
(Offshore) Support Structure	Assembly of the (Offshore) Foundation and Tower
Offshore Wind Turbine	Assembly of the RNA and (Offshore) Support Structure

1

Introduction

"Architects and engineers are among the most fortunate of men since they build their own monuments with public consent, public approval and often public money."

– John Prebble

1.1 Wind energy; from wind mills to offshore wind turbines

Long before the Dutch started using windmills on a large scale in order to reclaim parts of land from the sea in the 17th century, other civilizations had already successfully used the same principle to power all types of machines. The first recorded instance of using a windmill dates from the first century AD, when the Greek engineer Heron of Alexandria used a wind-driven wheel to power a machine. The working principle of a wind mill is that the kinetic energy of the wind, which is contained in the mass of the flowing air, is converted into mechanical energy used to, for instance, drive pumps or to power mill stones. The first wind turbines, i.e. the type of wind mill that converts the kinetic energy of the wind into electric energy, were not built until the late 19th century by wind energy pioneers such as prof. James Blyth in Scotland [126], Charles F. Brush in the United States [131] and Poul la Cour in Denmark [100]. At the same time the *electrification* of cities throughout Europe and the United States started by means of fossil fuel power plants.[1] All these developments started locally without a centralized grid to interconnect different cities or connect the rural areas. Hence, already in the first quarter of the 20th century, wind turbines based on the design of Poul la Cour were applied as means to provide electricity in rural settlements and farms [71].

Nonetheless, it took over seventy years for wind energy to be reconsidered as a serious (alternative) energy source. This was a direct result of the oil crises in the 1970's, when the supply of oil was disrupted, prices soared and people started to get concerned with the high level of dependence on foreign fossil energy sources. During the *Great California Wind Rush* in the 1980's strong government incentives led to the first large scale commercial development of wind

[1] Note that some of the first developments for dynamos, that were used to generate electricity, can even be traced back to Werner von Siemens [153], the founding father of the Siemens conglomerate.

farms in California and thereby started a true wind energy industry. In the 1990's and 2000's wind energy was becoming a serious alternative source of energy, resulting in ever increasing amounts of installed wind power. At the same time, growing protests against the noise and visual pollution caused by wind turbines, led to the commercial development of the first offshore wind farms. Nowadays, with the "20-20-20" targets as set by the European Union, aiming at a 20% reduction in greenhouse gases and 20% share of renewable energy in 2020, wind power can no longer be considered as an alternative source of energy, but has become a mainstream source of energy.

1.2 The economics of wind power

Questions that often arise are: "If the wind is for free, why is wind energy still too expensive?" and "Is wind energy more expensive or too expensive?". In order to allow the readers to form their own answers to these fundamental questions, some of the aspects and terms related to these questions will be explained in this section.

In addition to the purely monetary issues, there is also the issue of energy-effectiveness of wind generated power. A common false argument employed by those who oppose wind energy is that more energy is required to produce and install a wind turbine, than it produces over its lifetime. However, a recent study found the energy yield ratio (EYR), which defines the ratio between energy produced versus energy consumed, for modern wind turbines to be higher than 20 in case of a 20 year lifetime [26]. Hence, this means that the energy break-even point of a wind turbine is (on average) reached within its first year.

The key indicator to compare the monetary cost of energy from different sources is the *Levelized Cost of Electricity* (LCOE), which gives the total cost per MWh of electricity that is produced and is introduced in section 1.2.1. Finally, in section 1.2.2, the concept of gross cost versus net cost is outlined in order to argue that discussion of energy cost should involve more than only comparing the LCOE of different energy sources.

1.2.1 Levelized Cost of Electricity

The lifetime averaged costs of electricity are usually given in terms of Levelized Cost of Electricity. The LCOE, usually given as €/MWh, is computed from the sum of the CAPEX and OPEX divided by the lifetime energy output as is shown in figure 1.1, where:

- CAPEX, or capital expenditure, is the total capital investment made. For an offshore wind turbine, this would thus include the rotor-nacelle-assembly, support structure (tower and foundation), installation, electrical infrastructure, cost of capital and all other project related costs.
- OPEX, or operational expenditure, is the discounted sum of all operations, maintenance, fuel and other variable costs. Note that fuel costs are nonexistent for renewable sources such as hydro, solar and wind energy.
- The lifetime energy output (LEP), is the total amount of electricity produced over the lifetime.

From this relation one can thus deduce that there are three parameters to manipulate in order to reduce the LCOE of wind energy; either reduce the CAPEX and OPEX and/or increase the lifetime energy production. It should be noted that these are not fully independent parameters.

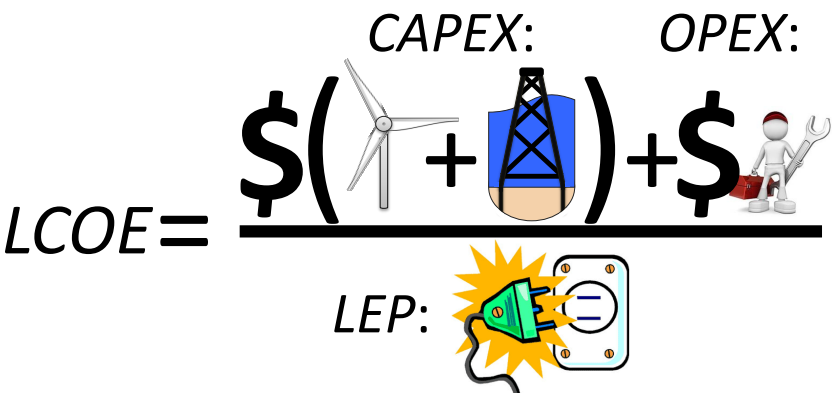

Figure 1.1: *LCOE of wind energy as a function of the capital expenditure (CAPEX), operational expenditure (OPEX) and the lifetime energy production (LEP).*

If one wants to increase the energy output by installing the turbine at a location with high winds, this will also induce higher forces on the structure of the turbine. This in turn leads to a heavier and more expensive supporting structure, thereby increasing the CAPEX. On the other hand, if one wants to lower the CAPEX by choosing cheaper materials and/or components, it is likely that the turbine would require more maintenance (increased OPEX) and/or break down more often (lowered energy production). It is therefore the job of engineers to find a design that is an optimal trade-off of these different aspects, which would results in the lowest LCOE possible.

In a 2012 study [97] using data from German and Spanish wind farms it was found that the LCOE of onshore wind varies between 65 €/MWh and 81 €/MWh, depending on the specific investments and the number of full-load hours. Comparing this with the price of electricity of 60 - 70 €/MWh for a mix of fossil and nuclear energy in Germany shows that onshore wind energy is almost at the same cost level as traditional sources of electricity. Due to the higher capital expenditures and operational expenditures required for offshore wind energy, its LCOE ranges between 105 €/MWh and 165 €/MWh. In addition, a 2013 study [197] showed that in the interior part of the U.S. power purchase agreements have been signed at the same price levels as the wholesale electricity prices. This clearly indicates that onshore wind energy is becoming competitive with traditional sources of energy. Hence, it is evident that the LCOE of offshore wind needs to be decreased at an increased pace in order to become competitive and independent of government support schemes.

1.2.2 Gross cost versus net cost of energy

Although the LCOE introduced in section 1.2.1 is the most often used indicator to determine the cost of different sources of energy, it only looks at the direct costs and gives no indication of the associated macro-economical gains or losses. Hence, it is an indicator of the gross costs of energy. If one would not only look at the micro-economic analysis, but also at the macro-economic aspects such as job creation, contribution to the gross domestic product and energy security, one would find the "net" cost of different energy sources. In a recent study performed by Ernst & Young [48], the net costs of two different energy generation technologies, (onshore) Wind Turbines (WT) and Combined Cycle Gas Turbines (CCGT), were compared in six European countries. Even though the LCOE of wind generated energy was higher than CCGT generated energy, it was shown that the former resulted in more jobs created per € invested, more Gross Value Added per MWh generated and resulted in higher tax returns. It was found that the "net" costs of wind energy were therefore lower in all countries investigated (except for the

United Kingdom due to its large share of domestic gas) than the "net" cost of CCGT generated electricity.

Hence, the answer to the questions posed at the beginning of the section depends on one's view on the matter. If one would compare the different technologies using the LCOE, the answer would obviously be that wind energy is currently too expensive, but if one would include the "net" cost and macro-economic effects in the discussion the answers are less straightforward.

1.3 Offshore wind energy: trends and challenges

As was mentioned in section 1.2, the LCOE of offshore wind energy is still too high in order to be able to directly compete with the traditional sources of electricity. Hence, a continuous effort is required to bring down the LCOE using a combination of innovation and optimizing existing technologies. Nonetheless, offshore wind energy offers a number of benefits in comparison to onshore wind. As the number of onshore wind turbines started to increase in the 1980's and 90's, so did the opposition to the large numbers of wind turbines populating the landscape. People started protesting against the noise emitted by the turbines and the fact that they were "polluting" the landscape. Moving the turbines offshore prevented these protests, but also had a number of other benefits. As the wind speeds are more constant and higher offshore, more and less fluctuating amounts of energy are produced. In addition to this, as space is practically unlimited offshore, large wind farms composed of more than a hundred turbines can be developed. This allows for large scale development of renewable energy, a goal many European countries have committed to.

Due to the scarcity of land and the high population density throughout Western Europe, offshore wind offers excellent possibilities for developing large scale renewable energy. The first offshore wind farm, Vindeby, was built in 1991 in Denmark. Since then numerous more have been installed, are under construction or consented in mainly the North Sea and Baltic Sea. From

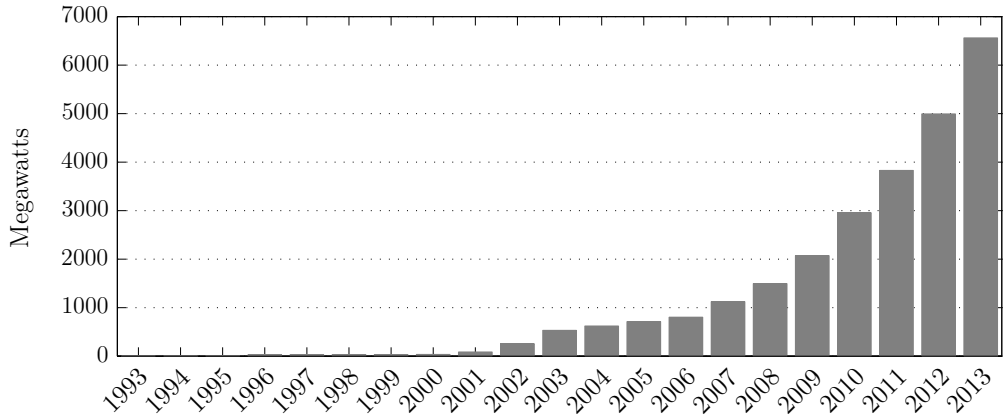

Figure 1.2: *Cumulative installed offshore wind power capacity; data from [50].*

figure 1.2 it can be seen that an almost exponential growth can be seen in the installed capacity of offshore wind power. As, in theory, there are no size constraints for offshore wind turbines, the average size of installed offshore wind turbines is growing year after year. These turbines are not only larger in terms of rated power, but are also equipped with bigger rotors in order to capture as much energy of the wind as possible. Associated trends are that these offshore wind turbines are installed in growing clusters, which are moving further offshore in deeper waters as was reported in [50]. Nonetheless, as was discussed in section 1.2, offshore wind energy is still

to expensive when compared to traditional sources of energy or onshore wind energy. As such, the wind industry has committed to an ambitious cost saving target of roughly 40% in 2020 compared to 2012 levels, which has even been formalized in the Dutch "Energy Agreement" [156].

It is not hard to imagine that the marine foundations supporting these bigger turbines in deeper seas are an essential part of an offshore wind turbine, as is also discussed in more detail in section 1.5. Different studies [98, 195] estimate the cost of the marine foundations to be in the order of 20% of CAPEX and the cost of the wind turbine tower to be around 12% CAPEX, showing that these components are responsible for a large part of the initial investment costs. A recent study [73] indicates that 6% to 7% of LCOE can be reduced in the support structure from a further industrialization and increased competition in this industry. Other studies have shown that material and cost can be saved by applying integrated design optimization to the entire support structure [58, 68, 95].

1.4 The role of structural dynamics in offshore wind turbine design

Offshore wind turbines require large investments, hence investors, but also their lenders and insurers, require that the turbines will remain operational for the investment period. Therefore, offshore wind turbines have to operate and generate energy reliably for many years under the influence of harsh environmental loading. In order to verify the design lifetime of the turbine, the wind turbine manufacturer has to account for all possible loading scenario's that could occur during the lifetime. This is not a simple task as a turbine is a slender, highly flexible, high-tech piece of machinery, that is constantly excited by different types of stochastic and harmonic loading. During its lifetime, stochastic wind forces act on the rotor and tower, waves are a constant source of excitation on the marine (or offshore) foundation. This is augmented by harmonic loading resulting from mass unbalance of the rotor (1P, or rotational frequency of the rotor), the aerodynamic effect of blades passing the tower (3P) and all their harmonic multiples, varying loads on the blades due to gravity and wind shear and many other types of loading. In addition, a turbine is an actively controlled machine that tries to maximize the wind energy it converts to electric energy, which is done by constantly modifying the pitch of the blades and the yaw angle of the rotor. These changing operational conditions influence the loading on the turbine. To summarize, an offshore wind turbine is a flexible, non-stationary system that is excited by various types of complex loading, which again depend on the state of the system.

1.4.1 Wind turbine simulations

In order to quantify the effect of the loading on the structural integrity of the wind turbine, different tools and design methods have been developed by wind turbine manufactures and research institutes worldwide. The backbone of these methods are the aero-servo-elastic simulation tools [14,121], based on (nonlinear) finite element models or (flexible) multi-body models, that take all the different types of loading and control actions into account, such as:

- Aero-elastic coupling, i.e. the dependency of the aerodynamic loads on the structural deformations and vice versa.
- Rotational effects of the rotor, resulting in the above described harmonic loading.
- Controller dynamics and changing system properties due to the controller actions.

In addition to this many aero-elastic codes have been extended to allow simulating offshore wind turbines [101, 119, 143, 190], where one also has to take into account:

- Hydrodynamic loading caused by waves and currents.
- Soil-structure interaction, which becomes important for offshore wind turbines.

Incorporating all these effects results in nonlinear wind turbine models that are evaluated using simulations in the time domain. As several thousands of different load cases need to be evaluated for certifying the design of an offshore wind turbine, computation time is obviously an important aspect.

1.4.2 Validating models and their inputs using measurements

Another approach for characterizing the dynamic behavior of wind turbine structures is by using measurements from actual installed turbines or their components. This however brings new challenges, as one has to deal with all the complexities which arise from operational wind turbines. These include among others nonlinearities due to the aerodynamic coupling, gyroscopic effects and harmonics as a result of the large rotations and a non-stationary system resulting from active control of the turbine. At the same time it should be ensured that accurate measurements are obtained. Nonetheless, if successful, the rewards are also significant as one can gain insights into the actual dynamic characteristics of the system and the excitations working on it. Some of the first known results from applying modal analysis for identifying the structural parameters (eigenfrequencies, damping ratios and eigenmodes) of wind turbines were published already in 1983 by Carne [18]. A more common approach when using experimental modal analysis (EMA) methods is to validate components of a wind turbine, such as for instance the blades [66], instead of the entire installed wind turbine.

In general, when the modal properties have to be identified from large structures in operation, such as buildings, bridges and wind turbines, there are (very) limited possibilities to accurately control and measure the input excitations. This renders the experimental modal analysis methods useless, as one requires the transfer of measured input(s) to output(s) for estimating the structural parameters. Therefore, Operational Modal Analysis (OMA) methods have been developed that are able to identify the modal parameters using output-only measurements (as is also shown in appendix C). The use of (and research into) OMA techniques in the field of wind turbine engineering has taken a giant leap since the first reported (successful) attempts in 1993 [87]. It has since then been applied for the identification of different onshore [114, 116, 200] and offshore [38, 39, 167] wind turbines.

An alternative approach for estimating the eigenfrequencies and damping ratios of offshore wind turbines is by evaluating the measurement signals obtained after a so called “rotor stop”. By pitching the blades out of the wind at a relatively high speed, a sudden loss of trust forces causes a response similar to an inverse step function. In [30, 180] this approach is used for determining the first eigenfrequencies and associated modal damping ratios. Similar measurements were already successfully performed onshore for the purpose of model validation [110]. Here the turbine was excited by suddenly releasing an applied static load at the tower top. Note however, that in this case the static force could be controlled and measured as is required in an EMA method.

Finally there is the field of structural health monitoring [70, 148], which aims at identifying structural damage by detecting changes in the measured signals. This, however, is beyond the scope of this thesis.

1.5 Design of an offshore wind turbine support structure

In general one can distinguish between the two main substructures of an offshore wind turbine: the rotor-nacelle-assembly (RNA) and its support structure. The RNA is an off-the-shelve component, but as the environmental conditions are usually different for every offshore site, support structures for offshore wind turbines are custom engineered. When designing an offshore wind turbine there is usually a clear design split between the two main components of the support structure: the foundation and tower. In general one could state that the design of an offshore wind turbine (OWT) support structure involves the following parties:

- The **wind turbine manufacturer** (WTM) is responsible for the detailed design of the RNA and the tower, modeling the aerodynamics and turbine controller, and performing the aero-elastic simulations with the integrated OWT model.
- The **foundation designer's** (FD) responsibility is the design of the offshore foundation, perform the associated soil modeling and determine the site specific wave loads acting on the foundation.
- Finally, there is an independent **certification body** to check and certify the models, computational procedures, obtained loads and support structure design.

As was mentioned earlier, thousands of aero-elastic simulations are performed by the turbine manufacturer for design and certification purposes, thereby taking into account the global dynamics of the complete structure. These results are then used by both parties to verify the designs and update the initial designs. This loop is repeated until a satisfactory design is found and all design criteria are met. In section 1.5.1 the most important design criteria are introduced. Next, in section 1.5.2 some of the different types of foundation structures are introduced. Finally, in section 1.5.3 a more detailed description of the design loop is given.

1.5.1 Design criteria

Usually OWTs are designed to operate reliably for 20-25 years. Therefore, they have to be able to withstand all the loads during this period. In order to ensure this lifetime, a number of design criteria have to be met [36]. The most important ones for the design of the support structure are briefly described in this section.

- **Fatigue limit state** (FLS): Cyclic loading well below the yield strength of the material can still cause failure of the structure after a number of cycles, this is called fatigue failure. Therefore, the structural design criteria for the FLS are based on the cumulative fatigue damage of the structure under repeated cyclic loading, as measured by the Palmgren-Miner rule [109]. In general, the Miner-sum is scaled such that unity implies the formation or initiation of cracks. By designing the structure such that the Miner-sum over the entire design lifetime is smaller (or equal) to one, a high degree of certainty is obtained that the structure has sufficient fatigue life.
- **Ultimate limit state** (ULS), also referred to as ultimate strength, relates to the failure of the wind turbine due to the loss of structural integrity under ultimate loading conditions. This loss of integrity may be related to, for instance, yielding or fracturing of structural members, instability of the structure due to buckling and collapse of platting or stiffening structures. Hence, by fulfilling the ULS one ensures that the structure is able to withstand the ultimate loads that can occur in its lifetime.

- **First natural frequency**: Finally, in order to ensure that the first natural frequencies are not (heavily) excited by the dominant harmonic excitations of the rotor at 1P and 3P (for 3 bladed turbines, P being the rotor rotational frequency), they must be outside of the bandwidth of these harmonic excitations. Hence, if the first eigenfrequencies are chosen to be *lower* than the 1P frequency band the design is generally referred to as soft-soft. If they are chosen to be *in between* the 1P and 3P rotational frequencies the support structure is said to be soft-stiff. And finally, if the first eigenfrequencies are *higher* than the 3P frequency band one refers to the design as stiff-stiff [165]. As the wave force spectrum is in the low frequency range below 1P, one generally wants to avoid this bandwidth as well. Therefore a soft-soft support structure is in practice not used for offshore wind turbines. The stiff-stiff design requires a very stiff (and thus generally more expensive) support structure and is thus also an uncommon choice. Hence, one mostly uses a soft-stiff design for offshore wind turbines. Note that this requirement is highly associated to the FLS loads, as exciting the first modes will obviously lead to an increase in fatigue loads on the structure.

1.5.2 Common types of offshore foundation structures

Different types of marine foundations exist for installing wind turbines offshore, as is shown in figures 1.3 and 1.4. These different foundation types can be classified according to the water depths they are suited for.

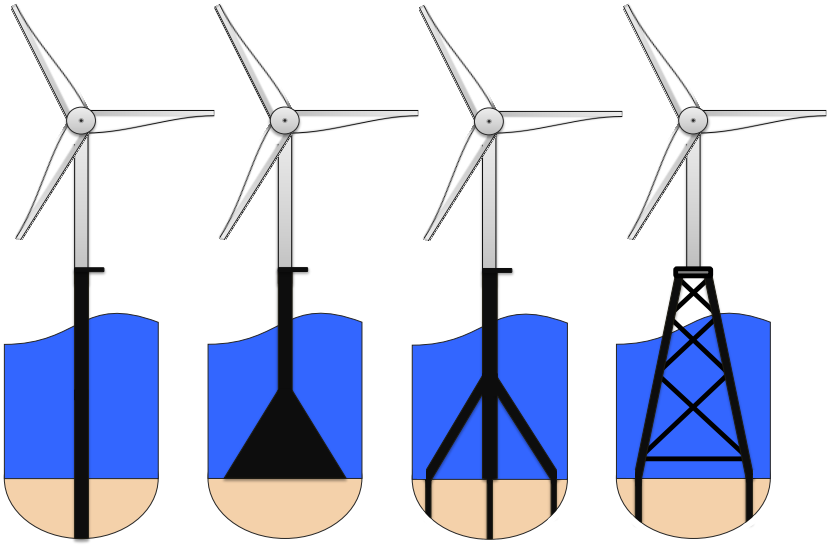

Figure 1.3: *Different bottom-fixed foundation types for offshore wind turbines. From left to right: gravity based, monopile, tripod and jacket.*

Shallow waters: up to approximately 35 meters
The largest part of all offshore wind turbines is currently installed in water depths up to 35 meters. In this range of water depths, the most commonly used types of marine foundations are the following:

- **Gravity based foundation**. This type of foundation is simply placed on the seabed and use its self weight to create a stable support for the wind turbine. The added weight for stability often comes in the form of sand, rocks or iron. Note that the gravity based

foundation requires a stable seabed and it is only economically feasible in very shallow waters. This type of offshore foundation is therefore rarely used nowadays. Nonetheless, at the end of 2013 they still accounted for 12% of all foundations installed [50].

- A **monopile** is a long steel tubular structure with a large diameter that is hammered or vibrated into the seabed. Due to the fact that monopiles are relatively simple to produce and install, they are the most commonly used foundation type and currently constitute up to 76% of all installed offshore wind turbine foundations [50]. In order to extend their feasibility to larger wind turbines and greater water depths, so called "XL-monopiles", with diameters up to 10 meters, are currently under development.

Medium water depths: approximately 30 to 80 meters

As the current trends in the offshore wind industry are to install larger wind turbines in deeper waters, the foundation solutions for shallow waters can become economically and/or technically infeasible. Therefore, in the range beyond 30 meters the most commonly used foundation structures are listed here:

- **Tripods** are offshore foundations consisting of a central vertical tube, connected to three legs that form a wide base at the seabed. Here they are often connected to small diameter piles that are driven into the soil in order to anchor the tripods to the seabed. The large base provides a stable footing that is able to cope with large overturning moments. Approximately 5% of the currently installed marine foundations are tripods.
- **Jackets**, which make up for 6% of installed foundations, are multi-membered constructions generally built from three or four legs that are connected by (cross-) bracing. As jackets are composed of many tubular elements that are (in general) connected in the welded nodes, the production costs of jackets are relatively high. The legs of the jacket can be connected to small diameter soil-piles or suction buckets [17] to anchor the structure to the seabed. Due to the "transparant" nature of jackets, they are less sensitive to wave loading as some of the other foundation types. The large footprint and cross-braced structure provides, in the static sense, a stiff foundation structure. An often neglected side effect is that these features can also result in localized dynamics (brace modes) in the structure itself.

Note that these foundations are generally classified as multi-membered offshore foundations.

Deep waters: 80 meters and beyond

Foundation solutions that are being developed for water depths greater than 80 meters, are floating foundations [6]. Even though many different floating concepts are under development, only the three types shown in figure are briefly outlined.

- A **spar-buoy** is a large, but slender, cylindrical buoy that floats upright. It uses ballast to lower the center of gravity below the center of buoyancy to make the structure stable and is secured to the seabed using mooring-lines. The first floating MW-scale wind turbine, Hywind, was commissioned in 2009 and is supported by a spar-buoy [157].
- **Semi-submersibles** are partly submerged structures with a wide base to provide a stable supporting base for the wind turbine. Semi-subs are kept in place by mooring-lines that

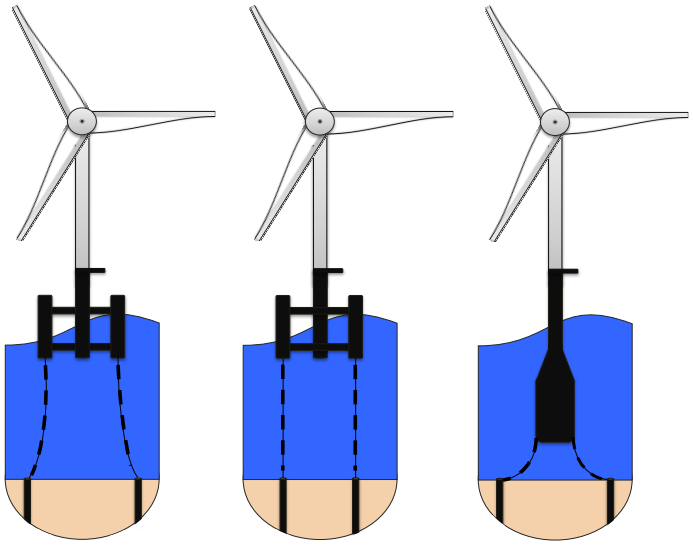

Figure 1.4: *Different floating foundation types for offshore wind turbines. From left to right: semi-submersible, tension leg platform and floating spar buoy.*

are anchored in the seabed. The WindFloat turbine is the first multi-MW wind turbine installed on a semi-submersible [142].

- A **tension leg platform** (TLP) is a vertically moored floating structure. A TLP has very large buoyancy, generally 2-3 times the vertical weight of the system. A high restoring force and hence vertical stiffness is obtained from tensioning the mooring lines. There are plans to install the first TLP based multi-megawatt offshore wind turbine by the end of 2014 [2, 6].

Note that these types of foundations are all still in a testing or prototyping phase. Hence, the work presented in this thesis is mainly focussed on bottom-fixed multi-membered foundations.

1.5.3 Design process with multiple parties

As was already introduced at the beginning of this section, the design of an offshore wind turbine support structure is in general a process that involves multiple parties. For the sake of simplicity, the role of the certification body will be disregarded in the rest of this thesis. In order to design the support structure, both the FD and WTM require the environmental conditions of the site. The WTM requires, among others, the information of the wind climate and the FD needs the water depth, wave climate and soil properties in order to start the design of the support structure. The typical design cycle is summarized in figure 1.5 and can be described as follows:

1. An initial foundation design is created by the FD based on the wave climate, soil properties, water depth and the initial or generic wind turbine loads provided by the WTM. This initial design and the associated wave loads are then passed to the WTM. Note that for the more complex types of foundations, these are often equivalent monopile or reduced models and generalized wave loads in order to save computational time in the integrated simulations, as is described in for instance [12, 175].

2. The model of the foundation is integrated in the aero-elastic model of the WTM, such that the full OWT is modeled.

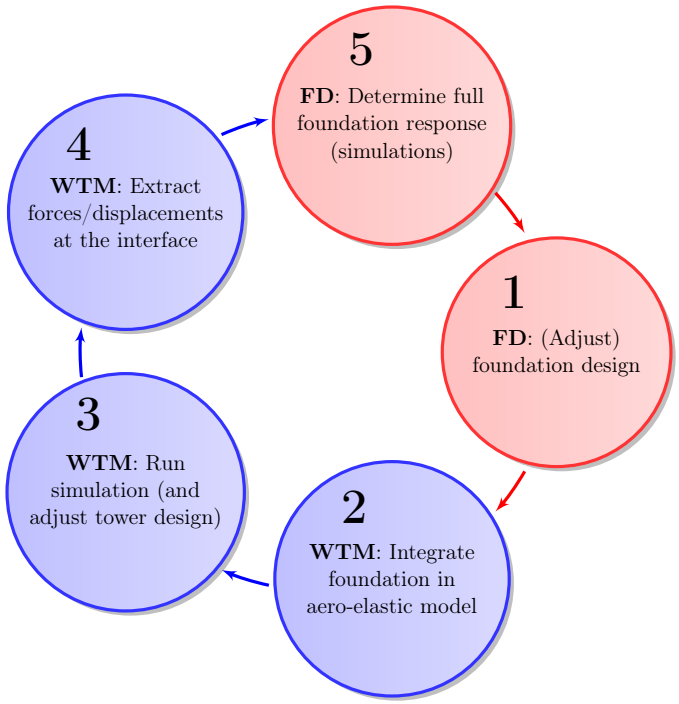

Figure 1.5: *Schematic overview of the design cycle of an OWT support structure.*

3. The WTM performs simulations for the full set of load cases, which include among others different wind and wave loading conditions, extreme conditions and emergency situations. These simulations are performed using the aero-elastic model, in which the dynamics of the turbine and controller as well as the influence of the wind is included. Note that the wave loads are also applied during these simulations. This step will be discussed in more detail in section 7.1.1. An overview and comparison of different aero-elastic simulation tools is given in [119, 124, 190]. As a second step, the WTM checks whether the current tower design meets the design criteria and if this is not the case or if it is too conservative, the tower design is updated.

4. From the results, the WTM extracts the forces and/or displacements at the interface between the tower and foundation. These results are then passed to the FD.

5. These interface forces and/or displacements and the synchronized wave loads are applied on the detailed foundation model. After this, the FD can run a number of simulations on the detailed model in order to determine whether the foundation design fulfills the design criteria. This is usually done with one of the methods described in section 7.2. If the design criteria are not met or if the design is too conservative, the foundation design is updated and a new design loop is started.

From figure 1.5 one can see that within one design cycle there are two one-way interfaces between the FD and WTM. Obviously, these sequential interactions can cause slow convergence of the design process and might introduce inaccuracies depending on how the information is exchanged and subsequently used. There are usually a number of reasons why these interfaces could lead to difficulties in the project:

- Firstly, both the foundation and aero-elastic models are often considered intellectual property and **confidential**, therefore many parties are not willing to share these models.
- Secondly, each party only wants to take **responsibility** and bear the risks on its own part of the project. Hence, a too close collaboration could lead to one party becoming

liable for the risks and responsibilities of the other.

- Finally, there is also the inability to easily share models, as for instance software packages and modeling approaches used by the different parties could be **incompatible**.

Hence, in order to overcome these issues, parties usually prefer to exchange only interface data and reduced or equivalent models. Note that the data exchange interface may also be chosen differently, e.g. by exchanging displacements at several (or possibly all) nodal locations in the foundation structure or even by exchanging foundation loads as obtained directly by the WTM. The latter however is currently not the standard practice in industry.

1.6 Thesis goal, outline and contributions

To briefly summarize the issues identified in the previous sections: the current trend in offshore wind energy is to install ever larger turbines in deeper waters further offshore. As a result, monopile foundations become uneconomical and more complex, multi-membered, types of foundations (e.g. jackets, tripods) are preferred. For design and certification purposes thousands of aero-elastic simulations are performed, taking into account the global dynamics of the complete structure. However, dynamic models of complex foundation require many more degrees of freedom (DoFs) than monopile models, leading to excessive computation times. In addition, as different parties are responsible for subcomponents of the support structure, the design of the support structure is an iterative process that requires large amounts of data to be exchanged between the different parties. Therefore, a framework of computational procedures is required that ensures fast and accurate results over the entire design loop, while minimizing the amount of data transfer between the different parties. Hence, from the problem statement given here, the following research objective was defined:

"Development of simulation procedures, based on the dynamic substructuring methodology, for the integrated analysis of offshore wind turbines with multi-membered support structures."

To achieve this goal, two subtasks were defined:

1. *Develop and implement modeling and computational strategies based on substructuring, to efficiently include models of complex foundations in aero-elastic simulations of offshore wind turbines.*

2. *To demonstrate the use of these strategies in the load calculation process of multi-membered offshore wind turbine foundations and evaluate their performance in terms of computational efficiency and accuracy.*

Hence, the first subtask focusses on the development of numerical substructuring methods that can be applied in the time domain aero-elastic simulations. The main goal in this part is to provide a set of numerical substructuring tools that enable one to find accurate coupled responses of a wind turbine on a complex marine foundation structure. As the internal loads in the structures are not a direct output of these simulations, one needs an additional process step to obtain the ultimate and fatigue loads in both the turbine and foundation elements, which is the focuss of the second subtask. Note that although the focuss is on bottom-fixed multi-membered foundations, a number of methods proposed in this work are also suited for the integrated analysis of floating offshore wind turbines.

1.6.1 Outline of the thesis

The thesis has been divided into two parts, as is visualized in figure 1.6, corresponding to the division of the thesis objective into two subtasks.

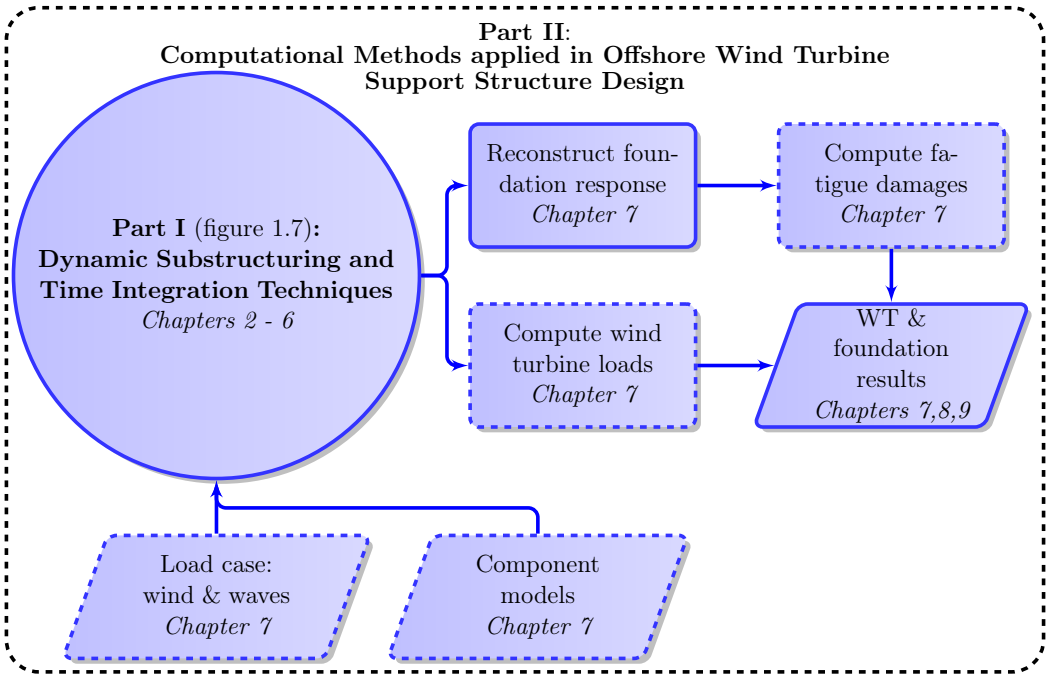

Figure 1.6: *Overview of the thesis structure. Part I, consisting of chapters 2 to 6, contains the theory of the different computational strategies proposed. In Part II, consisting of chapters 7 to 9, these approaches are demonstrated using a realistic test case. The different items enclosed by dashed borders indicate topics only partially discussed in this thesis.*

Outline of Part I: Dynamic Substructuring and Time Integration Techniques
In Part I the computational strategies to include linear and nonlinear models of complex foundations in the aero-elastic simulations of the integrated offshore wind turbine are introduced. In the different chapters in this part (chapters 2 to 6) multiple approaches are presented that are all based on the dynamic substructuring concept, as is also visualized in figure 1.7.

- **Chapter 2** starts with an introduction and classification of dynamic substructuring methods. The most common class of substructuring techniques, the family of Component Mode Synthesis methods, is outlined and some of its techniques are discussed in more detail. Finally, a brief summary of stiffness-based assembly methods is given, which are used for connecting reduced and unreduced component models.
- In **chapter 3** two time integration approaches are outlined. Firstly, the family of Newmark methods, suited for integrating second-order ordinary differential equations, is outlined. Secondly, it is presented how to apply the convolution product and impulse response functions for obtaining time responses of dynamic systems.
- **Chapter 4** introduces two monolithic multi-domain time integration schemes. These methods can be employed for coupling two or more (similar) time integration schemes in order to obtain the coupled responses of composed dynamical systems.
- A framework for the recently introduced Impulse Based Substructuring approach is presented in **chapter 5**. This framework employs both the Newmark scheme and convolution

product, which are introduced in chapter 3, to obtain coupled substructure responses in the time domain.

- In **chapter 6** it is presented how to efficiently deal with forces on the internal DoFs in a dynamic substructuring analysis. It is shown that one can use three different approaches for applying wave forces on the reduced foundation models used in the aero-elastic simulations.

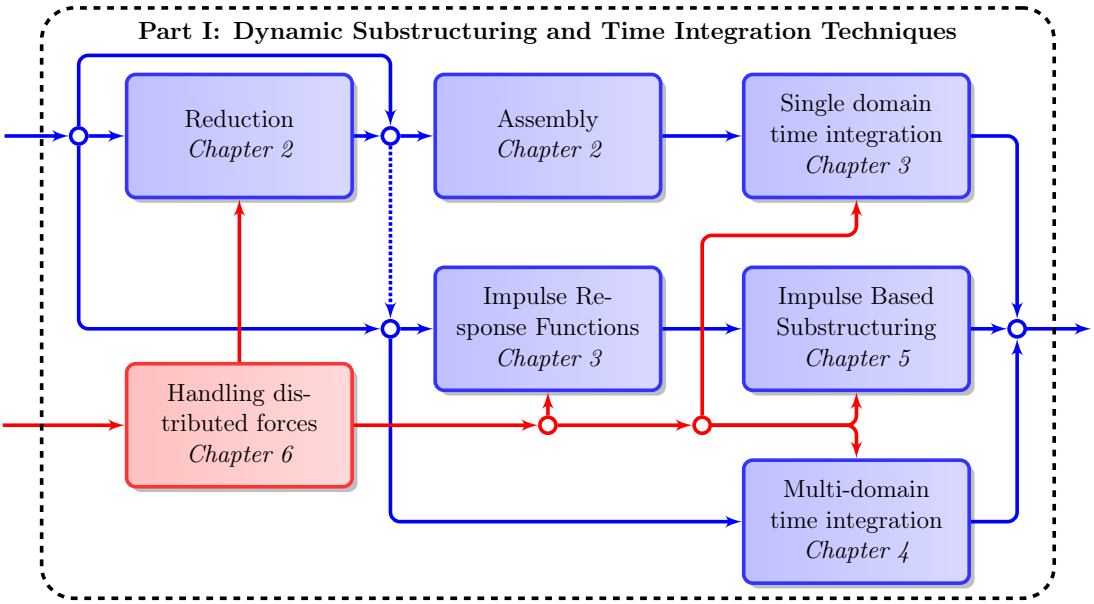

Figure 1.7: *Graphical outline of Part I of the thesis. Blue lines are associated to all types of models, whereas red lines are associated to forces (and the methods for handling these in a DS framework).*

Outline of Part II: Computational Methods applied in Offshore Wind Turbine Support Structure Design

In part II of the thesis the simulation strategies presented in part I are subsequently demonstrated using a realistic test case of an offshore wind turbine. In addition, different methods applied for obtaining the loads and fatigue damages in the foundation structure are outlined.

- In **chapter 7** the use of different Component Mode Synthesis methods, for integrating the wind turbine and foundation model in aero-elastic simulations, are evaluated. Secondly different methods are introduced and evaluated, in order to reconstruct the full foundation response from the generalized results obtained.

- The same load case as introduced in chapter 7 is used in **chapter 8** to demonstrate the different methods for efficiently dealing with forces exciting the internal DoFs of reduced components.

- In **chapter 9** the same load case as applied in chapters 7 and 8 is used to demonstrate the Impulse Based Substructuring method in load calculation procedures for offshore wind turbines.

1.6.2 Thesis contributions

A number of practical and scientific contributions have resulted from the work performed during this project.

- Firstly, a general framework for the Impulse Based Substructuring method is formulated. Although the basic method was already proposed in [139], it has been extended such that it is mature enough to be used in engineering practice. It has also been proven that the exact same characteristics can be obtained as the generalized-α time integration scheme in terms of stability and accuracy.
- A collection of methods is proposed that enables to efficiently and accurately include the effects of forces acting on the internal degrees of freedom of reduced substructure models in a dynamic substructuring analysis.
- Two different monolithic multi-domain time integration techniques, which are based on the generalized-α scheme, are proposed that allow to couple time simulations in different modeling environments.
- An evaluation of the load calculation processes for the design of offshore wind turbine foundations is performed, involving different types of reduced models and post-processing analyses. From this evaluation an overview of accurate and inaccurate computational procedures is distilled, thereby serving as a reference for future procedures for the design of jacket foundations for offshore wind turbines.
- In cooperation with Sven Voormeeren, Jørgen Thirstrup Petersen and Anders Riis Sørensen from Siemens Wind Power the in-house aero-elastic wind turbine simulation code BHawC is modified such that complex foundation types can be integrated as reduced models.
- A module is added to BHawC, with the help of Peter Fisker Skjoldan, that allows to couple the aero-elastic simulations in BHawC with time simulations of arbitrary (linear and nonlinear) foundation models performed in MatLab.
- Finally, a list of publications resulting from this work is given in appendix D.

Part I

Dynamic Substructuring and Time Integration Techniques

2

Dynamic Substructuring and Component Mode Synthesis

"Divide et impera"

– Trajano Boccalini

2.1 What is Dynamic Substructuring?

"Divide and rule": an ancient tactic often successfully applied in a vast range of domains; from economics to warfare and politics. This knowledge must have triggered Schwarz in 1890 to apply the strategy to a mathematical problem [149]. He divided a complex domain in two simple parts (a circle and a rectangle) in order to find a solution for the associated differential equations of the combined domains. Since the analytical solutions where known in both subdomains, the solutions on the interfaces were used in an iterative way to converge to the solution for the complex domain. This idea of *domain decomposition* can be seen as the ancestor of dynamic substructuring, where the subdomains are in fact the components of the total structure.

The developments of the substructuring ideas came two decades after the development of the *finite element method* (FEM), which can be traced back to Hrennikoff [76] and Courant [22]. It was triggered by the desire of the engineers and scientists at those times, to build better, and thus bigger, numerical models to describe the dynamics of the more complex structures. The size of these models were, however, always limited by the amount of computing recourses available. By dividing large and complex structures, such as aeroplanes and spacecraft, into several smaller, simpler substructures (or components), one could still obtain the components dynamics. Using this a priori knowledge of the component dynamics, allowed one to create much compacter models of the global structure. This substructuring approach to dynamic analysis has several advantages:

- It allows the evaluation of structures that would otherwise be to large and/or complex to be simulated or measured as a whole.
- Experimentally obtained substructures (measurements) can be combined with numerical or analytical substructures, in order to compute the dynamic behavior of the total structure.

- Local dynamic behavior and its influence on the global behavior can be determined more easily. This allows for local optimization of the design, but also for model simplification by eliminating local subsystem behavior which has no significant impact on the assembled system.
- It allows sharing and combining of substructures from different project groups.

As was introduced in chapter 1, an offshore wind turbine is made up of a number of distinct main components. In addition to this, the design of the entire wind turbine is divided among multiple parties. This obviously requires efficient and accurate methods for combining the different component model into a single integrated offshore wind turbine model. Hence, the dynamic substructuring paradigm is a perfectly suited approach here.

Within the field of dynamic substructuring one generally identifies a number of classes. The basic idea and history of these different classes of substructuring methods will briefly be described in sections 2.1.2 to 2.1.3 and an outline of the rest of the section is given in 2.1.4.

Note that this chapter is based on work presented in [166, 175, 183, 186]

2.1.1 Frequency Based Substructuring

The first class of substructuring methods are the Frequency Based Substructuring (FBS) methods. The FBS methods allow for the assembly of Frequency Response Functions (FRFs) of substructures that were either measured or obtained from numerical and analytical models. Bishop and Johnson [10] are in 1960 among the first to describe the idea of finding the admittances FRFs of a multi-degree-of-freedom (MDOF) system from its component admittances.

From the 1980's onward, experimental substructuring caught the attention of the experimental society. Due to much improved measurement hardware and experimental techniques, measurements could now be used in substructuring analysis. In 1984 Crowley *et al.* [28] presented a method for the direct assembly of FRFs called SMURF (Structural Modification Using experimental frequency Response Functions), which did not get much attention from the engineering community. Jetmundsen *et al.* [88] proposed an alternative method, which is often referred to as the classical frequency based substructuring method (FBS). Almost two decades later, De Klerk *et al.* [34] proposed to write the frequency based substructuring approaches using the dual assembly formalism, which became known as LM-FBS (Lagrange Multiplier Frequency Based Substructuring). For a more extended historical overview of substructuring methods, the reader is referred to [35].

Frequency Based Substructuring methods are for instance used in the automobile industry, where one is unable to model a car body with all its details. By measuring the FRFs of an actual car body and coupling these with different sources of noise, accurate estimates of transfer of these disturbances can be obtained [29, 31, 155].

2.1.2 Component Mode Synthesis

The most commonly used substructuring techniques are those found in the class of the *Component Mode Synthesis* (CMS) methods. The development of these methods resulted from the desire to create ever larger and detailed FE models in the aeronautic and aerospace industries in the 50's and 60's. As with all the dynamic substructuring methods, the first step is to divide a structure into multiple components. The second step is to reduce the component FE models using Ritz vectors [132] that are used as a reduced basis in describing the displacements of the

physical nodes of the structure. Afterwards, one reassembles the reduced components in order to obtain a compact representation of the composed system.

The first ideas for finite element model reduction and dynamic substructuring were published by Hurty [79, 80] and Gladwell [63] in the 1960's. Gladwell proposed to use so called *branch modes* for the reduction. Firstly, a number of constraints are applied, such that only one substructure can vibrate while the rest is either fixed or vibrating as a rigid body. The resulting system is called a *branch* of the total system and the vibration modes found in this configuration are then referred to as *branch modes*. These branch modes can now be used as a Rayleigh-Ritz basis [129] for the full structure. Hurty proposed to use a combination of vibration modes, rigid body modes and static modes, which were all employed in a computer program created shortly after by Bamford [8].

Following Hurty and Gladwell the classical CMS methods were introduced soon after: Guyan proposed his static reduction method in 1965 [67], Craig followed with his approach in 1968 [24], MacNeal in 1971 [103] and Rubin in 1975 [144]. These methods have become standard in the field of structural dynamics for evaluating the dynamic behavior of large structures and the methods proposed by Guyan and Craig are integrated in many commercially available FE codes.

Even though, many of the breakthroughs in the field of Component Mode Synthesis originate from the 60's and 70's, it is still an active research field. Relatively recently, the dual counterpart of the Craig-Bampton method was proposed [136] and one that combines both into a single mixed reduction basis [186]. In addition, different research groups are trying to extend the methods to allow for nonlinear substructures [81, 94, 99, 108, 193], but no standard methods, such as the traditional superlements, have been established yet.

2.1.3 Impulse Based Substructuring

Finally, one can distinguish a third class of substructuring methods, the so called *Impulse Based Substructuring* (IBS) method. It uses the same concepts as in frequency based substructuring approaches (i.e. admittance representation of the components and dual assembly) but considers for the substructures directly the impulse response functions (IRFs) in the time domain measured for the input and interface degrees of freedom, instead of the modal properties or the FRFs. The IBS method, that allows to assemble the IRFs of different substructures, was first named as such by Rixen in [139] and [141].

Similar ideas were published by Dowell in 1971 [42], 1972 [43] and 1982 [44]. These methods use the principle of mode superposition of free modes per component, or other analytical solutions per component for given interface forces and use the compatibility equation to find the dual interface problem. Klein [96] has taken a similar approach for solving a substructured problem. Holl and Irschik introduce their paper [75] as an extension of this earlier work and use modal superposition and the Duhamel integral to compute the response of the linear subsystems. Also Gordis [64, 65] introduced the idea of describing the individual components as IRFs and couple these to find the coupled responses.

In [168, 169, 172] the method is extended to allow for the coupling of IRFs with linear and nonlinear FE models. The same concept was already used by Wolf [198] for coupling finite element models and infinite domains in the field of soil-structure interaction. Here, the fundamentals for both "stiffness" and "flexibility" based coupling were described, nonetheless Wolf only described how to couple two substructures, of which one was the infinite domain.

Like with any substructuring method, IBS also introduces some practical challenges. Firstly, it was found in [138, 162, 164] that due to the imperfect impulse resulting from hammer measurements, direct use of the measured response is not possible in an experimental IBS analysis. Hence, in [162] and [164] a number of possible solutions to this are proposed and tested. In addition to this, systems with low damping require long impulse response functions to capture the full response and the associated convolution product will be increasingly expensive to solve. Different approaches, such as windowing and truncating the IRFs [140] or splitting the high and low frequency response [163], have been proposed recently.

2.1.4 Chapter Outline

As in the process for designing OWT support structures a large number of transient response simulations are performed, the current thesis focusses on the substructuring methods in the time domain. As the Impulse Based Substructuring method is discussed in chapter 5, the current chapter focusses on the Component Mode Synthesis methods that will be used in this work. In additions to this, one of the most important aspects required to use the dynamic substructuring doctrine, namely the assembly of substructure models, is handled in this chapter as well.

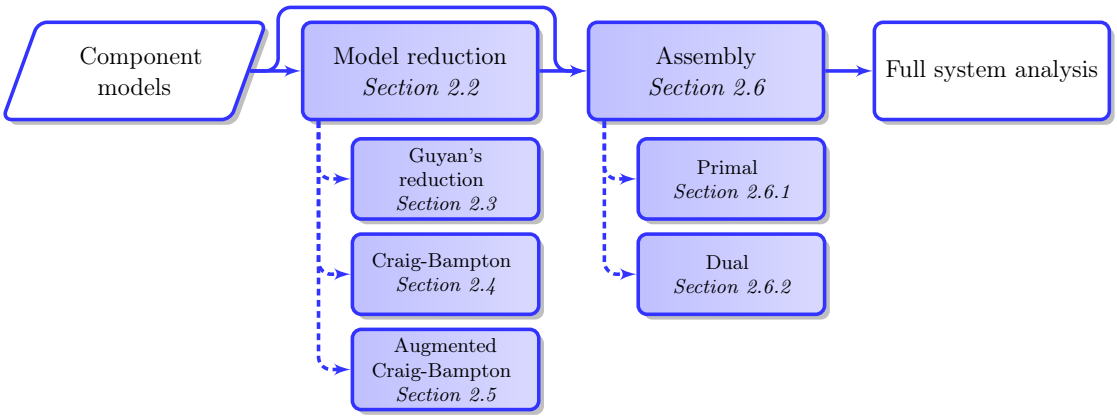

Figure 2.1: *Outline of chapter 2.*

The outline of the remainder of this chapter is given in figure 2.1. Here one can clearly identify the three steps required in the CMS methodology: firstly obtaining the component models, secondly performing the reduction and finally the assembly of the (reduced) substructure models. Obviously, if one wants to include a full component model in the assembly, the reduction step can be left out.

Firstly, in section 2.2 the general formulation and underlying concept of the different CMS methods is given. Also some of the different modes that are commonly used for constructing a reduction basis are introduced. In sections 2.3, 2.4 and 2.5 the different reduction methods that are used throughout the thesis are introduced. As one also needs to be able to reassemble all the different (reduced) component models into a single structure again, assembly methods are the topic of section 2.6. Note that only the *primal* (section 2.6.1) and *dual* (section 2.6.2) assembly methods will be outlined in this work.

2.2 The concept of Component Mode Synthesis

In the field of structural dynamics one often uses finite element models which were built to assess deformations and stress concentrations in structures. These models are often too refined

and have several hundreds of thousands (or even millions) of degrees of freedom. Finding a static solution for these models does not pose any problems, since there are many efficient solvers to handle this. Solving dynamic problems, such as computing vibration modes, harmonic and/or transient responses, requires solving many static-like problems and results in much longer computation times. Often the dynamic behaviour of a structure can be well described using a coarser mesh. Sometimes though, further coarsening of the mesh will result in errors due to the fact that the finite elements are deformed beyond acceptable aspect ratios to fit the detailed geometry of the structure. In addition, a coarser mesh can lead to a crude overestimation of eigenfrequencies, since by reducing the number of DoF for the structure to deform in, the structure is "artificially stiffened". And finally, remeshing the structure could be very costly and difficult, especially for complex structures.

A more elegant approach would be to reduce the number of DoFs without modifying the mesh. Such methods exist and are known as *component model reduction methods*. The basic idea behind reduction methods in structural dynamics is in fact a modal superposition, where the nodal displacements are written in terms of Ritz vectors [132] (or simply modes) and their associated modal amplitudes; these methods are referred to as *Component Mode Synthesis* (CMS).[1] Hence, by regarding the undamped equations of motion of a single substructure, denoted by $\star^{(s)}$,

$$\begin{bmatrix} \boldsymbol{M}^{(s)}_{[bb]} & \boldsymbol{M}^{(s)}_{[bi]} \\ \boldsymbol{M}^{(s)}_{[ib]} & \boldsymbol{M}^{(s)}_{[ii]} \end{bmatrix} \begin{bmatrix} \ddot{\boldsymbol{u}}^{(s)}_{[b]} \\ \ddot{\boldsymbol{u}}^{(s)}_{[i]} \end{bmatrix} + \begin{bmatrix} \boldsymbol{K}^{(s)}_{[bb]} & \boldsymbol{K}^{(s)}_{[bi]} \\ \boldsymbol{K}^{(s)}_{[ib]} & \boldsymbol{K}^{(s)}_{[ii]} \end{bmatrix} \begin{bmatrix} \boldsymbol{u}^{(s)}_{[b]} \\ \boldsymbol{u}^{(s)}_{[i]} \end{bmatrix} = \begin{bmatrix} \boldsymbol{f}^{(s)}_{[b]} \\ \boldsymbol{f}^{(s)}_{[i]} \end{bmatrix} + \begin{bmatrix} \boldsymbol{g}^{(s)}_{[b]} \\ \boldsymbol{0} \end{bmatrix}, \tag{2.1}$$

where $\boldsymbol{M}$ and $\boldsymbol{K}$ are respectively the mass and stiffness matrices and $\boldsymbol{u}$ and $\ddot{\boldsymbol{u}}$ are the displacements and accelerations. Note that for the sake of simplity the superscript denoting the substructure s will be dropped in the remainder of this section. In Eq. (2.1) one can distinguish between the internal DoFs, denoted by $\star_{[i]}$, and the coupling (or boundary) DoFs, denoted by $\star_{[b]}$. The latter of these are excited directly by the coupling forces, $\boldsymbol{g}_{[b]}$, that originate from the neighboring structures. Hence, it is essential that these connecting forces are represented well by the reduction basis. One therefore includes static modes ($\boldsymbol{\psi}$) in the reduction basis, which represent the static deformation caused by coupling forces originating from the neighboring substructures and also a number of vibration modes ($\boldsymbol{\phi}$) to describe the dynamic response of the system. Hence, the displacements at all the nodes of the structure are approximated by:

$$\boldsymbol{u} = \sum_{k=1}^{n_{[b]}} \boldsymbol{\psi}_k q_{[b],k} + \sum_{j=1}^{n_\phi} \boldsymbol{\phi}_j \eta_j = \boldsymbol{R} \begin{bmatrix} \boldsymbol{q}_{[b]} \\ \boldsymbol{\eta} \end{bmatrix} = \boldsymbol{R}\boldsymbol{q}, \tag{2.2}$$

where $\boldsymbol{\eta}$ and $\boldsymbol{q}_{[b]}$ respectively denote the modal amplitudes of the vibration modes and those of the static modes. The different modes are columns in the reduction matrix $\boldsymbol{R}$. If one uses a total of r modes for the reduction, then $\boldsymbol{R}$ has a dimension $n \times r$, where n are the number of DoFs of the full problem. For an efficient reduction it is required that the reduced set of DoFs is very small in comparison to the original set of DoFs ($r << n$). By substituting Eq. (2.2) into the original set of DoFs, one finds

$$\boldsymbol{M}\boldsymbol{R}\ddot{\boldsymbol{q}} + \boldsymbol{K}\boldsymbol{R}\boldsymbol{q} = \boldsymbol{f} + \boldsymbol{g} + \boldsymbol{r}, \tag{2.3}$$

which means that one tries to find a solution for the full problem in the subspace spanned by the reduction basis. As one will thus find an approximation of the exact solution, a residual

[1] Model reduction methods are also applied in other fields, such as mathematics, control engineering and electrical engineering. Here one typically wants to obtain an accurate input-output description of the system to be reduced. On the other hand, in the field of structural dynamics one is typically interested in obtaining an accurate result for the entire displacement field in order to allow for stress analysis. For an overview of model order reduction techniques applied in these other fields of engineering, see for instance [5, 127, 147].

force ($\boldsymbol{r}$) is introduced that is in a subspace orthogonal to the reduction basis, such that

$$\boldsymbol{R}^T\boldsymbol{r} = \boldsymbol{0}. \tag{2.4}$$

Therefore, by projecting Eq. (2.3) onto the projection basis, which is often referred to as *Galerkin projection*, on directly solves the problem in the reduced subspace,

$$\tilde{\boldsymbol{M}}\ddot{\boldsymbol{q}} + \tilde{\boldsymbol{K}}\boldsymbol{q} = \boldsymbol{R}^T\boldsymbol{f} + \boldsymbol{R}^T\boldsymbol{g}, \tag{2.5}$$

where:

$$\begin{aligned} \tilde{\boldsymbol{M}} &= \boldsymbol{R}^T\boldsymbol{M}\boldsymbol{R}, \\ \tilde{\boldsymbol{K}} &= \boldsymbol{R}^T\boldsymbol{K}\boldsymbol{R}. \end{aligned} \tag{2.6}$$

All kinds of static and vibration "modes" can be used to create a reduction basis, such as attachment modes, constraint modes, rigid body modes and normal modes, but also different types of pseudo-modes can be added. Some of the more commonly employed modes are introduced next. Firstly in sections 2.2.1 and 2.2.2 two types of static modes, the constraint and attachment modes, are introduced. In section 2.2.3 the rigid body modes are introduced and finally in sections 2.2.4 and 2.2.5 the free- and fixed interface vibration modes are presented.

2.2.1 Constraint modes

A constraint mode is the static deformation shape due to a unit displacement applied to one of the boundary DoFs, while the remaining boundary DoFs are restrained and no forces are applied at the internal DoFs. The set of constraint modes thus contains the substructure's static response to applied interface displacements. The computation of the constraint modes starts with splitting the DoFs into boundary DoFs ($\boldsymbol{u}_{[b]}$) and internal DoFs ($\boldsymbol{u}_{[i]}$), as is done in Eq. (2.1). Now, by assuming that there are no external forces exciting the internal part of the structure, the second line that describes the internal response in (2.1) then writes:

$$\boldsymbol{M}_{[ii]}\ddot{\boldsymbol{u}}_{[i]} + \boldsymbol{M}_{[ib]}\ddot{\boldsymbol{u}}_{[b]} + \boldsymbol{K}_{[ii]}\boldsymbol{u}_{[i]} + \boldsymbol{K}_{[ib]}\boldsymbol{u}_{[b]} = \boldsymbol{0}. \tag{2.7}$$

By neglecting the inertia forces in (2.7), the remaining "static" part can be condensed on the boundary DoFs $\boldsymbol{u}_{[b]}$:

$$\boldsymbol{u}_{[i],stat} = -\boldsymbol{K}_{[ii]}^{-1}\boldsymbol{K}_{[ib]}\boldsymbol{u}_{[b]}, \tag{2.8}$$

and forms the static condensation matrix, whose columns contain so-called constraint modes. These constraint modes represent the static response of the internal DoFs ($\boldsymbol{u}_{[i]}$) for unit displacements of the boundary DoFs ($\boldsymbol{u}_{[b]}$). The original set of degrees of freedom $\boldsymbol{u}$ are reduced to a set of boundary DoFs ($\boldsymbol{u}_{[b]}$), such that:

$$\begin{bmatrix} \boldsymbol{u}_{[b]} \\ \boldsymbol{u}_{[i]} \end{bmatrix} = \boldsymbol{\Psi}_C\boldsymbol{u}_{[b]} = \begin{bmatrix} \boldsymbol{I} \\ -\boldsymbol{K}_{[ii]}^{-1}\boldsymbol{K}_{[bi]} \end{bmatrix}\boldsymbol{u}_{[b]}, \tag{2.9}$$

where the constraint modes are denoted by $\boldsymbol{\Psi}_C$. Using these constraint modes, interface compatibility between substructures can easily be enforced, since the original set of interface DoFs ($\boldsymbol{u}_{[b]}$) are retained.

2.2.2 Attachment modes

Attachment modes are defined as the displacements due to a unit force applied at one of the interface DoFs ($\boldsymbol{u}_{[b]}$). Attachment modes are therefore columns of the associated flexibility matrix ($\boldsymbol{G}$).

$$\begin{aligned} &\boldsymbol{K}^{+}\boldsymbol{f} = \boldsymbol{G}\boldsymbol{f} = \boldsymbol{u}, \\ &\boldsymbol{f} = \begin{bmatrix} 0 & 0 & \dots & 1 \end{bmatrix}^{T}. \end{aligned} \tag{2.10}$$

Here, $\boldsymbol{K}^{+}$ is the pseudo-inverse (or generalized inverse) of the stiffness matrix. Computing the attachment modes will be straightforward if the structure is fully constrained. As the pseudo-inverse operation is then replaced by a regular inverse operation, one only has to solve the following set of equations:

$$\boldsymbol{\Psi}_a = \boldsymbol{K}^{-1}\boldsymbol{F}. \tag{2.11}$$

Here $\boldsymbol{F}$ is a force matrix containing in each of its columns a unit force related to one of the boundary DoFs and $\boldsymbol{\Psi}_a$ are the obtained *attachment modes*. If the system is under- or unconstrained and rigid body modes are present, one will have to apply a pseudo-inverse operation in order to compute the attachment modes, as is shown in Eq. (2.10) and described in [23, 166].

2.2.3 Rigid body modes

A special type of free vibration modes are rigid body modes; if the substructure is not fully constrained a number of rigid body modes exists. Rigid body modes are modes in which the substructure shows displacements without deformations, such that

$$\boldsymbol{K}\boldsymbol{\Phi}_r = \boldsymbol{0}, \tag{2.12}$$

or in other words: it displaces as a rigid body. In addition to the global rigid body displacements (displacements of the total structure), a structure could for instance also contain mechanisms (i.e. hinges etc.) which will allow for parts of the structure to displace without introducing any deformations, these displacements are in fact also rigid body modes and Eq. (2.12) also holds. For systems having no mechanisms, the geometry of the substructure can be used to obtain the rigid body modes without solving an eigenvalue problem, as is described in [166].

2.2.4 Free interface vibration modes

Free vibration modes are the vibration shapes of the substructure if the interface DoFs are unconstrained. They are obtained by solving the (undamped) free vibration eigenvalue problem:

$$\left(\boldsymbol{K} - \omega_r^2\boldsymbol{M}\right)\boldsymbol{\phi}_{f,r} = \boldsymbol{0}. \tag{2.13}$$

Here, $\boldsymbol{\phi}_{f,r}$ is the r^{th} free vibration mode with its associated eigenfrequency ω_r^2. The free vibration modes thus contain information of the substructure dynamics and can be considered the "true" eigenmodes of the system. A single free interface vibration mode is denoted by $\boldsymbol{\phi}_f$ and a set of free interface vibration modes is denoted by $\boldsymbol{\Phi}_f$.

2.2.5 Fixed interface vibration modes

A second approach to include vibrational information in a reduction basis would be to use fixed interface vibration modes. These can be computed by constraining the boundary DoFs. As was shown in Eq. (2.1), the system can be partitioned into boundary DoFs ($\boldsymbol{u}_{[b]}$) and internal DoFs ($\boldsymbol{u}_{[i]}$). By constraining the boundary DoFs ($\boldsymbol{u}_{[b]} = \boldsymbol{0}$) and assuming no external forces, one obtains the constrained free vibration problem.

$$\boldsymbol{M}_{[ii]}\ddot{\boldsymbol{u}}_{[i]} + \boldsymbol{K}_{[ii]}\boldsymbol{u}_{[i]} = \boldsymbol{0}. \tag{2.14}$$

This can be solved as an eigenvalue problem:

$$\left(\boldsymbol{K}_{[ii]} - \omega^2_{[i],j}\boldsymbol{M}_{[ii]}\right)\boldsymbol{\phi}_{[i],j} = \boldsymbol{0}. \tag{2.15}$$

The result is the set of eigenmodes and eigenfrequencies of the substructure constrained at its boundary DoFs. A single fixed interface vibration mode will be denoted by $\boldsymbol{\phi}_{[i]}$, a set of fixed interface vibration modes by $\boldsymbol{\Phi}_{[i]}$.

2.2.6 Reduction methods; a matter of mixing modes

As was introduced in section 2.2, one builds the reduction basis from a selection of deformation shapes. The most commonly used deformation shapes are the different modes that are described in this section. As is shown in figure 2.2, one finds different reduction methods by mixing different types of modes in a single reduction basis.

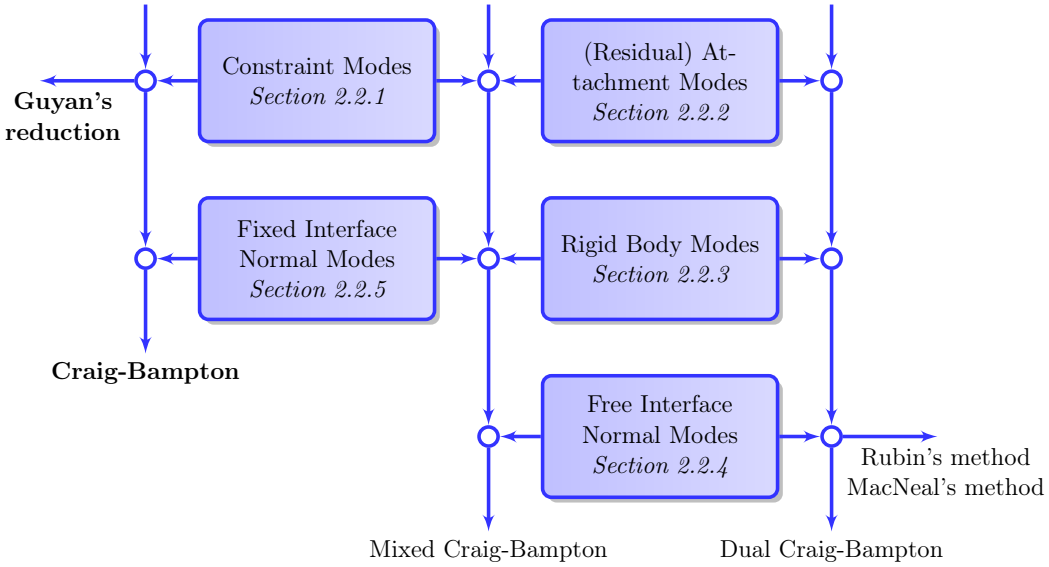

Figure 2.2: *Different combinations of modes lead to the different CMS methods; the bold methods are discussed in this thesis.*

The only prerequisite is that the reduction basis contains at least one type of static modes, in order to allow for a coupling to the neighboring substructures. In addition, in order to improve the conditioning of the reduced matrices, it is required that the columns of the reduction basis are either mass or stiffness orthogonalized. The underlined methods; Guyan's reduction and Craig-Bampton are discussed respectively in sections 2.3 and 2.4.

The Dual Craig-Bampton [136] method employs residual attachment modes, rigid body modes and free interface normal modes in order to build the reduction basis. As attachment modes are defined, as was stated in section 2.2.2, as the displacement field due to a unit force at an interface DoFs, the reduced boundary DoFs are in fact interface *forces* instead of *displacements*. This means that for the assembly of the reduced substructures one has to "assemble" the forces on the interface, as is presented in [186].

The Mixed Craig-Bampton [186] method can be regarded as a generalization of the Craig-Bampton and Dual Craig-Bampton methods. The method is derived by dividing the substructure degrees of freedom into a set of internal DOFs, free interface DoFs and fixed interface DoFs using a simple but effective selection scheme. Based on this selection a reduction basis is computed consisting of vibration modes, constraint modes and residual flexibility modes, which leads to relatively sparse reduced matrices.

Rubin's method [144] and MacNeal's method [103] employ the same ingredients as the Dual Craig-Bampton method, but instead of directly using the attachment modes in the reduction basis, they are transformed in order to allow for displacement boundary DoFs. By this transformation the sparsity of the reduced matrices is lost, but the assembly process is highly simplified, thereby leading to *superelements* that allow for an easy assembly in FE models.

For a more detailed introduction to Component Mode Synthesis, the reader is referred to [23, 25, 166, 181].

2.3 Guyan reduction

One of the oldest reduction methods is the *Guyan-Irons reduction* [67,83], nonetheless it is best known as Guyan reduction. The dynamic equations that govern the system are:

$$\boldsymbol{M}\ddot{\boldsymbol{u}} + \boldsymbol{K}\boldsymbol{u} = \boldsymbol{f}. \tag{2.16}$$

In order to reduce the system, the degrees of freedom $\boldsymbol{u}$ are split into internal DoFs ($\boldsymbol{u}_{[i]}$) and interface (or boundary) DoFs ($\boldsymbol{u}_{[b]}$). By assuming no external forces are applied to the internal DoFs $\boldsymbol{u}_{[i]}$ and neglecting the substructures internal inertia forces, the internal DoFs can be condensed on the boundary DoFs using the constraint modes described in section 2.2.1.

$$\begin{bmatrix} \boldsymbol{u}_{[i]} \\ \boldsymbol{u}_{[b]} \end{bmatrix} = \boldsymbol{\Psi}_C \boldsymbol{u}_{[b]}. \tag{2.17}$$

Substitution of (2.17) into (2.16) and projection onto the reduction basis will lead to the reduced dynamic equations, which are now only a function of the boundary DoFs, such that:

$$\tilde{\boldsymbol{M}}\ddot{\boldsymbol{u}}_{[b]} + \tilde{\boldsymbol{K}}\boldsymbol{u}_{[b]} = \tilde{\boldsymbol{f}}_{[b]}, \tag{2.18}$$

where:

$$\begin{aligned} \tilde{\boldsymbol{K}} &= \boldsymbol{\Psi}_C^T \boldsymbol{K} \boldsymbol{\Psi}_C = \boldsymbol{K}_{[bb]} - \boldsymbol{K}_{[bi]}\boldsymbol{K}_{[ii]}^{-1}\boldsymbol{K}_{[ib]}, \\ \tilde{\boldsymbol{M}} &= \boldsymbol{\Psi}_C^T \boldsymbol{M} \boldsymbol{\Psi}_C = \boldsymbol{M}_{[bb]} - \boldsymbol{M}_{[bi]}\boldsymbol{K}_{[ii]}^{-1}\boldsymbol{K}_{[ib]} - \boldsymbol{K}_{[bi]}\boldsymbol{K}_{[ii]}^{-1}\boldsymbol{M}_{[ib]} + \boldsymbol{K}_{[bi]}\boldsymbol{K}_{[ii]}^{-1}\boldsymbol{M}_{[ii]}\boldsymbol{K}_{[ii]}^{-1}\boldsymbol{K}_{[ib]}, \\ \tilde{\boldsymbol{f}}_{[b]} &= \boldsymbol{\Psi}_C^T \boldsymbol{f}_{[b]}. \end{aligned} \tag{2.19}$$

Since in the derivation of the condensed stiffness the inertia forces are neglected, the exact solution is found if this technique is applied to static problems. If it is applied to dynamic

problems, an approximate solution is found. This is due to the fact that the internal inertia forces of the substructure are statically condensed on the interface and only contribute in a quasi-static manner. This approximation is valid as long as the spectrum of the excitations is much lower than the lowest eigenfrequency ($\omega^{(s)}$) of the substructure. Or in other words, the reduction method can only be used if the response of the structure is quasi-static. Nonetheless, Guyan reduction is still used extensively nowadays, due to its simplicity and the fact that the method is integrated in many commercial FE codes.

If the structure is to be excited by a certain harmonic, or a force spectrum with a relatively narrow bandwidth, one could perform the reduction around a certain frequency (ω_p). Here, instead of neglecting the inertia forces in the reduction step, one incorporates these around a specific frequency ω_p. The harmonic response at a specific frequency can be found by transforming the equations of motion into the frequency domain,

$$-\omega^2 \boldsymbol{M}\boldsymbol{u} + \boldsymbol{K}\boldsymbol{u} = \boldsymbol{Z}(\omega)\boldsymbol{u} = \boldsymbol{f}(\omega), \tag{2.20}$$

where $\boldsymbol{Z}(\omega)$ is the dynamic stiffness. Instead of using the static stiffness matrix ($\boldsymbol{K}$), one now employs the dynamic stiffness matrix ($\boldsymbol{Z}(\omega)$) to condense the internal degrees of freedom onto the boundary DoFs, as was presented in [102].

$$\boldsymbol{u}_{[i]} = -\boldsymbol{Z}_{[ii]}^{-1}(\omega_p)\boldsymbol{Z}_{[ib]}(\omega_p)\boldsymbol{u}_{[b]} = \boldsymbol{\Psi}_C(\omega_p)\boldsymbol{u}_{[b]}. \tag{2.21}$$

Using the static condensation of (2.21) in (2.17) and (2.19), will lead to the reduced set of equations. By taking into account the dynamic stiffness at ω_p in the condensation process, the exact behavior of the substructure will no longer be found for a static problem ($\omega = 0$), but for a harmonic problem at $\omega = \omega_p$.

Due to the easy assembly of the reduced matrices in the finite element method, the Guyan reduced components are classified as so called *superelements*.

2.4 The Craig-Bampton method

The Craig-Bampton method [24] can be seen as an extension of Guyan's reduction. Instead of reducing with only constraint modes, the Craig-Bampton method also includes information on the internal dynamics and thereby creates a more complete basis for the reduction. This vibrational information is the set of fixed-vibration modes; the substructure is fixed at its boundary DoFs and an analysis is done in order to obtain the eigenmodes (see section 2.2.5). Again, splitting the total set of DoFs $\boldsymbol{u}$ into the boundary DoFs $\boldsymbol{u}_{[b]}$ and internal DoFs $\boldsymbol{u}_{[i]}$, results in the following:

$$\begin{bmatrix} \boldsymbol{M}_{[bb]} & \boldsymbol{M}_{[bi]} \\ \boldsymbol{M}_{[ib]} & \boldsymbol{M}_{[ii]} \end{bmatrix} \begin{bmatrix} \ddot{\boldsymbol{u}}_{[b]} \\ \ddot{\boldsymbol{u}}_{[i]} \end{bmatrix} + \begin{bmatrix} \boldsymbol{K}_{[bb]} & \boldsymbol{K}_{[bi]} \\ \boldsymbol{K}_{[ib]} & \boldsymbol{K}_{[ii]} \end{bmatrix} \begin{bmatrix} \boldsymbol{u}_{[b]} \\ \boldsymbol{u}_{[i]} \end{bmatrix} = \begin{bmatrix} \boldsymbol{f}_{[b]} \\ \boldsymbol{0} \end{bmatrix} + \begin{bmatrix} \boldsymbol{g}_{[b]} \\ \boldsymbol{0} \end{bmatrix}, \tag{2.22}$$

where $\boldsymbol{g}_{[b]}$ are the connection forces to the neighboring substructures. The constraint modes are computed as described in section 2.2.1. The internal DoFs ($\boldsymbol{u}_{[i]}$) are now described in terms of constraint modes ($\boldsymbol{\Psi}_C$) and fixed-interface vibration modes ($\boldsymbol{\Phi}_{[i]}$):

$$\boldsymbol{u}_{[i]} = \boldsymbol{\Psi}_{C,[i]}\boldsymbol{u}_{[b]} + \boldsymbol{\Phi}_{[i]}\boldsymbol{\eta}.$$

The reduction basis in matrix form will then be:

$$\begin{bmatrix} \boldsymbol{u}_{[b]} \\ \boldsymbol{u}_{[i]} \end{bmatrix} = \begin{bmatrix} \boldsymbol{u}_{[b]} \\ \boldsymbol{\Psi}_{C,[i]}\boldsymbol{u}_{[b]} + \boldsymbol{\Phi}_{[i]}\boldsymbol{\eta} \end{bmatrix} = \begin{bmatrix} \boldsymbol{I} & \boldsymbol{0} \\ \boldsymbol{\Psi}_{C,[i]} & \boldsymbol{\Phi}_{[i]} \end{bmatrix} \begin{bmatrix} \boldsymbol{u}_{[b]} \\ \boldsymbol{\eta} \end{bmatrix} = \boldsymbol{R} \begin{bmatrix} \boldsymbol{u}_{[b]} \\ \boldsymbol{\eta} \end{bmatrix}. \tag{2.23}$$

Using the reduction matrix $\boldsymbol{R}$ to reduce the original set of equations (Eq. (2.22)), we obtain:

$$\begin{aligned} \tilde{\boldsymbol{K}} &= \boldsymbol{R}^T \boldsymbol{K} \boldsymbol{R}, \\ \tilde{\boldsymbol{M}} &= \boldsymbol{R}^T \boldsymbol{M} \boldsymbol{R}. \end{aligned} \tag{2.24}$$

Here $\tilde{\boldsymbol{M}}$ and $\tilde{\boldsymbol{K}}$ are the reduced mass and stiffness matrices, which are given in more detail below:

$$\begin{aligned} \tilde{\boldsymbol{K}} &= \begin{bmatrix} \tilde{\boldsymbol{K}}_{[bb]} & \boldsymbol{0} \\ \boldsymbol{0} & \boldsymbol{\Omega}^2_{[i]} \end{bmatrix}, \\ \tilde{\boldsymbol{K}}_{bb} &= \boldsymbol{K}_{[bb]} - \boldsymbol{K}_{[bi]} \boldsymbol{K}^{-1}_{[ii]} \boldsymbol{K}_{[ib]}, \\ \tilde{\boldsymbol{M}} &= \begin{bmatrix} \tilde{\boldsymbol{M}}_{[bb]} & \tilde{\boldsymbol{M}}_{[b\zeta]} \\ \tilde{\boldsymbol{M}}_{[\zeta b]} & \boldsymbol{I} \end{bmatrix}, \\ \tilde{\boldsymbol{M}}_{[bb]} &= \boldsymbol{M}_{[bb]} - \boldsymbol{M}_{[bi]} \boldsymbol{K}^{-1}_{[ii]} \boldsymbol{K}_{[ib]} - \boldsymbol{K}_{[bi]} \boldsymbol{K}^{-1}_{[ii]} \boldsymbol{M}_{[ib]} + \boldsymbol{K}_{[bi]} \boldsymbol{K}^{-1}_{[ii]} \boldsymbol{M}_{[ii]} \boldsymbol{K}^{-1}_{[ii]} \boldsymbol{K}_{[ib]}, \\ \tilde{\boldsymbol{M}}_{[\zeta b]} &= \boldsymbol{\Phi}^T_{[i]} \left(\boldsymbol{M}_{[ib]} - \boldsymbol{M}_{[ii]} \boldsymbol{K}^{-1}_{[ii]} \boldsymbol{K}_{[ib]} \right) = \tilde{\boldsymbol{M}}^T_{[b\zeta]}. \end{aligned} \tag{2.25}$$

One of the advantages of the Craig-Bampton method is the straightforward reduction; both the constraint modes and the fixed interface modes can easily be computed. Secondly, in the reduced system the original interface DoFs ($\boldsymbol{u}_{[b]}$) are retained, thereby allowing for easy assembly of the reduced substructures as superelements in regular FE packages. Due to the fact that the method is integrated in many finite element packages and the advantages given, the Craig-Bampton method is one of the most popular reduction methods. One can easily add, remove or replace substructures, without having to redo an analysis on the full model. A disadvantage of Craig-Bampton reduction is that if the interface of the substructure is changed (for example due to connecting more components), the entire reduction basis changes and has to be recomputed.

2.5 Augmented Craig-Bampton method

A Craig-Bampton superelement is able to accurately represent the response of the full model, as long as the loading is applied at the retained interface DoFs and the spectral content of the loading is lower than that of the superelement. However, in engineering practice this is often not the case and large parts of structures can be subject to distributed external forces. In order to overcome this issue, this loading can be taken into account in the construction of the reduction basis by augmenting the basis with specialized forced response vectors. This procedure is often referred to as *modal truncation augmentation* (MTA) [40,41,133]. Whereas MTAs are generally used in CMS to improve the substructure response to interface forces and thereby provide a better overall vibration model [41,135], here the MTAs are only used to improve the response to loads applied on a substructure.

To this end, the loading on the internal DoFs is firstly described as a summation of spatial force distribution vectors $\boldsymbol{\chi}_{[i],j}$, multiplied by their corresponding force amplitudes $\theta_{[i],j}(t)$:

$$\boldsymbol{f}_{[i]}(t) = \sum_{j=1}^{n_p} \boldsymbol{\chi}_{[i],j} \theta_{[i],j}(t) = \boldsymbol{X}_{[i]} \boldsymbol{\theta}_{[i]}. \tag{2.26}$$

In order to ensure that the external forces are captured well by the reduced models, one can compute the static response of the structure to these force shapes and augment the reduction basis with these pseudo modes (or modal truncation augmentation vectors, MTAs in short),

as was proposed in [183]. In order to improve the conditioning of the reduced matrices, it is required that the MTAs are orthogonal to the fixed interface modes, which are already included in the reduction basis, such that:

$$\bar{\boldsymbol{\Phi}}_{MTA} = \boldsymbol{T}\boldsymbol{K}_{[ii]}^{-1}\boldsymbol{X}_{[i]}, \tag{2.27}$$

Here $\boldsymbol{T}$ is the following orthogonal projector:

$$\boldsymbol{T} = \boldsymbol{I} - \boldsymbol{\Phi}_{[i]}\boldsymbol{\Phi}_{[i]}^{T}\boldsymbol{M}_{[ii]}. \tag{2.28}$$

To further improve the numerical robustness and retain the sparsity of the reduced matrices, the MTA vectors are mutually orthogonalized by solving the eigenvalue problem defined as:

$$\left(\bar{\boldsymbol{\Phi}}_{MTA}^{T}\boldsymbol{K}_{[ii]}\bar{\boldsymbol{\Phi}}_{MTA}\right)\boldsymbol{y} = \boldsymbol{\sigma}^{2}\left(\bar{\boldsymbol{\Phi}}_{MTA}^{T}\boldsymbol{M}_{[ii]}\bar{\boldsymbol{\Phi}}_{MTA}\right)\boldsymbol{y}, \tag{2.29}$$

where $\boldsymbol{\sigma}^2$ is a diagonal matrix containing the "pseudo-frequencies" corresponding to the MTAs. These frequencies are always higher than those of the fixed interface vibration modes and provide an indication of the frequency range in which the MTA's provide a dynamic correction.[2] The orthonormalized MTAs are computed by:

$$\boldsymbol{\Phi}_{MTA} = \bar{\boldsymbol{\Phi}}_{MTA}\boldsymbol{y}, \tag{2.30}$$

and have the following properties:

$$\begin{aligned} \boldsymbol{\Phi}_{MTA}^{T}\boldsymbol{M}_{[ii]}\boldsymbol{\Phi}_{MTA} &= \boldsymbol{I}, \\ \boldsymbol{\Phi}_{MTA}^{T}\boldsymbol{K}_{[ii]}\boldsymbol{\Phi}_{MTA} &= \boldsymbol{\sigma}^{2}. \end{aligned} \tag{2.31}$$

After including the MTA vectors in the reduction basis, the solution of the internal DoFs using the Augmented Craig-Bampton method can now be represented by:

$$\begin{bmatrix} \boldsymbol{u}_{[b]} \\ \boldsymbol{u}_{[i]} \end{bmatrix} = \begin{bmatrix} \boldsymbol{I} & \boldsymbol{0} & \boldsymbol{0} \\ \boldsymbol{\Psi}_C & \boldsymbol{\Phi}_{[i]} & \boldsymbol{\Phi}_{MTA} \end{bmatrix} \begin{bmatrix} \boldsymbol{u}_{[b]} \\ \boldsymbol{\eta} \\ \boldsymbol{\zeta} \end{bmatrix} = \boldsymbol{R} \begin{bmatrix} \boldsymbol{u}_{[b]} \\ \boldsymbol{\eta} \\ \boldsymbol{\zeta} \end{bmatrix}. \tag{2.32}$$

By again projecting the full model on the reduction basis, the set of equations of motion is reduced to $N_{[b]} + N_{\phi} + N_{MTA}$. An efficient reduction basis can be constructed using this approach. For a more detailed discussion of the method the reader is referred to [181, 183].

Finally note that in the case that a quasi-static response of the structure is expected, one can eliminate the fixed interface modes from the reduction basis given in Eq. (2.32) to obtain an *Augmented Guyan's reduction*. In that case, the orthogonal projector $\boldsymbol{T}$ is eliminated from Eq. (2.27).

2.6 Assembly of substructure models

As was mentioned in section 2.1.4, an essential technique for enabling the substructuring paradigm outlined in this chapter is the (re-) assembly of the different substructures. In this work only the Guyan reduction, Craig-Bampton and Augmented Craig-Bampton methods are considered, which all result in reduced structures that can be considered as *superelements*.

[2] The MTAs found here can be considered as first order MTAs. By also including higher order MTAs one is in fact constructing a Krylov sequence. Therefore a strong link exist between the modal truncation augmentation techniques and moment matching methods [5].

Therefore, only the assembly methods for the so called *stiffness formulation* are discussed. The reader is referred to [186] for a more general framework regarding assembly of reduced and unreduced components.

The derivation for the stiffness based assembly is started by considering the discrete set of linear equations of motion of a single substructure s, that can be either reduced or unreduced and is attached to neighboring substructures,

$$\boldsymbol{M}^{(s)}\ddot{\boldsymbol{q}}^{(s)} + \boldsymbol{K}^{(s)}\boldsymbol{q}^{(s)} = \boldsymbol{f}^{(s)} + \boldsymbol{g}^{(s)}, \tag{2.33}$$

where $\boldsymbol{g}^{(s)}$ denote the connection forces and $\boldsymbol{q}^{(s)}$ denotes the (generalized) set of displacements DoFs. The system of equations is again partitioned into the set of boundary DoFs, which in this formulation will always be the displacements of the boundary nodes, $\boldsymbol{u}_{[b]}^{(s)}$, and a set of internal generalized DoFs $\boldsymbol{q}_{[i]}^{(s)}$ (which are nodal displacement DoFs $\boldsymbol{u}_{[i]}^{(s)}$ for an unreduced substructure), according to

$$\boldsymbol{q}^{(s)} = \begin{bmatrix} \boldsymbol{u}_{[b]}^{(s)} \\ \boldsymbol{q}_{[i]}^{(s)} \end{bmatrix}, \quad \boldsymbol{g}^{(s)} = \begin{bmatrix} \boldsymbol{g}_{[b]}^{(s)} \\ \boldsymbol{0} \end{bmatrix}.$$

Note that for an unreduced substructure, the set of partitioned equations is given in Eq. (2.1). By definition the vector of connection forces $\boldsymbol{g}$ is zero at the internal subsystem DoFs, while $\boldsymbol{g}_{[b]}^{(s)}$ is similar to the local Lagrange multipliers used for instance in the algebraic FETI method [117]. Between the substructures one can define the intermediate interface displacement field $\boldsymbol{u}_{[\gamma]}$, to govern the compatibility of substructural displacements at the interface. This condition then writes:

$$\boldsymbol{u}_{[b]}^{(s)} - \boldsymbol{L}_{[b]}^{(s)}\boldsymbol{u}_{[\gamma]} = \boldsymbol{0}. \tag{2.34}$$

Here $\boldsymbol{L}_{[b]}^{(s)}$ is a Boolean matrix localizing the DoFs from the global intermediate displacement field corresponding to the substructure boundary DoFs. As a result, we end up with a three field formulation of the substructuring problem, having as independent unknowns the substructure DoFs field $\boldsymbol{q}^{(s)}$, the field of interface connection forces $\boldsymbol{g}_{[b]}^{(s)}$ and the intermediate interface displacement field $\boldsymbol{u}_{[\gamma]}$. Taking a variational approach we can now obtain the assembled equations. To this end, we can set up the Lagrangian of this problem as:

$$\mathcal{L}\left(\boldsymbol{q}^{(s)}, \boldsymbol{g}_{[b]}^{(s)}, \boldsymbol{u}_{[\gamma]}\right) = \sum_s \left(\frac{1}{2}\boldsymbol{q}^{(s)^T}\boldsymbol{K}^{(s)}\boldsymbol{q}^{(s)} - \boldsymbol{f}^{(s)^T}\boldsymbol{q}^{(s)} + \boldsymbol{g}_{[b]}^{(s)^T}\left(\boldsymbol{L}_{[b]}^{(s)}\boldsymbol{u}_{[\gamma]} - \boldsymbol{u}_{[b]}^{(s)}\right)\right). \tag{2.35}$$

Note that the above considers the static problem only. To include the inertia terms, one needs to go back to the variational principle in terms of the Hamiltonian [62]; these details will not be treated here. However, since in Eq. (2.34) we choose to express the compatibility condition in terms of displacements (instead of accelerations) the coupling between substructure will occur in the assembled stiffness matrix. The assembled mass matrix is hence not of primary interest, but for completeness it is included in the derivation.

$$\begin{bmatrix} \boldsymbol{M}_{[ii]} & \boldsymbol{M}_{[ib]} & \boldsymbol{0} & \boldsymbol{0} \\ \boldsymbol{M}_{[bi]} & \boldsymbol{M}_{[bb]} & \boldsymbol{0} & \boldsymbol{0} \\ \boldsymbol{0} & \boldsymbol{0} & \boldsymbol{0} & \boldsymbol{0} \\ \boldsymbol{0} & \boldsymbol{0} & \boldsymbol{0} & \boldsymbol{0} \end{bmatrix} \begin{bmatrix} \ddot{\boldsymbol{q}}_{[i]} \\ \ddot{\boldsymbol{u}}_{[b]} \\ \boldsymbol{g}_{[b]} \\ \boldsymbol{u}_{[\gamma]} \end{bmatrix} + \begin{bmatrix} \boldsymbol{K}_{[ii]} & \boldsymbol{K}_{[ib]} & \boldsymbol{0} & \boldsymbol{0} \\ \boldsymbol{K}_{[bi]} & \boldsymbol{K}_{[bb]} & -\boldsymbol{I} & \boldsymbol{0} \\ \boldsymbol{0} & -\boldsymbol{I} & \boldsymbol{0} & \boldsymbol{L}_{[b]} \\ \boldsymbol{0} & \boldsymbol{0} & \boldsymbol{L}_{[b]}^T & \boldsymbol{0} \end{bmatrix} \begin{bmatrix} \boldsymbol{q}_{[i]} \\ \boldsymbol{u}_{[b]} \\ \boldsymbol{g}_{[b]} \\ \boldsymbol{u}_{[\gamma]} \end{bmatrix} = \begin{bmatrix} \boldsymbol{f}_{[i]} \\ \boldsymbol{f}_{[b]} \\ \boldsymbol{0} \\ \boldsymbol{0} \end{bmatrix}, \tag{2.36}$$

where,

$$\begin{aligned}
\boldsymbol{K}_{[ii]} &= \operatorname{diag}\left(\boldsymbol{K}_{[ii]}^{(1)} \cdots \boldsymbol{K}_{[ii]}^{(N_s)}\right), & \boldsymbol{M}_{[ii]} &= \operatorname{diag}\left(\boldsymbol{M}_{[ii]}^{(1)} \cdots \boldsymbol{M}_{[ii]}^{(N_s)}\right), \\
\boldsymbol{K}_{[ib]} &= \operatorname{diag}\left(\boldsymbol{K}_{[ib]}^{(1)} \cdots \boldsymbol{K}_{[ib]}^{(N_s)}\right) = \boldsymbol{K}_{[bi]}^{T}, & \boldsymbol{M}_{[ib]} &= \operatorname{diag}\left(\boldsymbol{M}_{[ib]}^{(1)} \cdots \boldsymbol{M}_{[ib]}^{(N_s)}\right) = \boldsymbol{M}_{[bi]}^{T}, \\
\boldsymbol{K}_{[bb]} &= \operatorname{diag}\left(\boldsymbol{K}_{[bb]}^{(1)} \cdots \boldsymbol{K}_{[bb]}^{(N_s)}\right), & \boldsymbol{M}_{[bb]} &= \operatorname{diag}\left(\boldsymbol{M}_{[bb]}^{(1)} \cdots \boldsymbol{M}_{[bb]}^{(N_s)}\right),
\end{aligned}$$

and

$$\boldsymbol{q}_{[i]} = \begin{bmatrix} \boldsymbol{q}_{[i]}^{(1)} \\ \vdots \\ \boldsymbol{q}_{[i]}^{(N_s)} \end{bmatrix}, \quad \boldsymbol{u}_{[b]} = \begin{bmatrix} \boldsymbol{u}_{[b]}^{(1)} \\ \vdots \\ \boldsymbol{u}_{[b]}^{(N_s)} \end{bmatrix}, \quad \boldsymbol{g}_{[b]} = \begin{bmatrix} \boldsymbol{g}_{[b]}^{(1)} \\ \vdots \\ \boldsymbol{g}_{[b]}^{(N_s)} \end{bmatrix}, \quad \boldsymbol{L}_{[b]}^{T} = \begin{bmatrix} \boldsymbol{L}_{[b]}^{(1)^T} \\ \vdots \\ \boldsymbol{L}_{[b]}^{(N_s)^T} \end{bmatrix},$$

and N_s is the total number of substructures. In Eq. (2.36) one can recognize the compatibility condition in the third row, which is given in Eq. (2.34) and governs the compatibility between the $\boldsymbol{u}_{[b]}^{(s)}$ and $\boldsymbol{u}_{[\gamma]}$. The last row is the equilibrium condition on the interface, stating that the sum of the substructure connection forces must be zero. Note that the equilibrium condition is not explicitly included in the Lagrangian, but follows from the compatibility condition. However, these assembled equations of motion still contain the full three fields, which is for most cases inefficient from a computational point of view.[3] Therefore, it is desired to simplify the equations. The two most common approaches to do this, the so called *primal* and *dual* assembly methods, are discussed next.

2.6.1 Primal assembly

The most common method for simplifying the three-field formulation given in Eq. (2.36) is by means of primal assembly. By realizing that one forces compatibility between the substructure boundary DoFs $\boldsymbol{u}_{[b]}^{(s)}$ and the unique set of interface displacements $\boldsymbol{u}_{[\gamma]}$, the compatibility can be enforced *a priori* by a simple substitution.

$$\boldsymbol{u}_{[b]}^{(s)} = \boldsymbol{L}_{[b]}^{(s)} \boldsymbol{u}_{[\gamma]}. \tag{2.37}$$

Which results in the following transformation matrix:

$$\begin{bmatrix} \boldsymbol{q}_{[i]} \\ \boldsymbol{u}_{[b]} \\ \boldsymbol{g}_{[b]} \\ \boldsymbol{u}_{[\gamma]} \end{bmatrix} = \begin{bmatrix} \boldsymbol{I} & \boldsymbol{0} & \boldsymbol{0} \\ \boldsymbol{0} & \boldsymbol{L}_{[b]} & \boldsymbol{0} \\ \boldsymbol{0} & \boldsymbol{0} & \boldsymbol{I} \\ \boldsymbol{0} & \boldsymbol{I} & \boldsymbol{0} \end{bmatrix} \begin{bmatrix} \boldsymbol{q}_{[i]} \\ \boldsymbol{u}_{[\gamma]} \\ \boldsymbol{g}_{[b]} \end{bmatrix}. \tag{2.38}$$

By substituting the transformation matrix, given in Eq. (2.38) into Eq. (2.36), the compatibility issue is solved a priori. By pre-multiplying the result of the transformation by the same matrix, one also satisfies the equilibrium condition, given in the last line of Eq. (2.36), a priori and obtains the following:

$$\begin{bmatrix} \boldsymbol{M}_{[ii]} & \boldsymbol{M}_{[ib]}\boldsymbol{L}_{[b]} \\ \boldsymbol{L}_{[b]}^{T}\boldsymbol{M}_{[bi]} & \boldsymbol{L}_{[b]}^{T}\boldsymbol{M}_{[bb]}\boldsymbol{L}_{[b]} \end{bmatrix} \begin{bmatrix} \ddot{\boldsymbol{q}}_{[i]} \\ \ddot{\boldsymbol{u}}_{[\gamma]} \end{bmatrix} + \begin{bmatrix} \boldsymbol{K}_{[ii]} & \boldsymbol{K}_{[ib]}\boldsymbol{L}_{[b]} \\ \boldsymbol{L}_{[b]}^{T}\boldsymbol{K}_{[bi]} & \boldsymbol{L}_{[b]}^{T}\boldsymbol{K}_{[bb]}\boldsymbol{L}_{[b]} \end{bmatrix} \begin{bmatrix} \boldsymbol{q}_{[i]} \\ \boldsymbol{u}_{[\gamma]} \end{bmatrix} = \begin{bmatrix} \boldsymbol{f}_{[i]} \\ \boldsymbol{L}_{[b]}^{T}\boldsymbol{f}_{[b]} \end{bmatrix}. \tag{2.39}$$

[3] The three-field formulation might have some advantages for instance in formulating contact problems between non-matching grids [154].

Note that the result (for the stiffness matrix) can easily be verified by substituting Eq. (2.37) directly into the Lagrangian, given in Eq. (2.35). This will cause that the term related to the compatibility condition is canceled in the Lagrangian.

The above equations form the so called *primal* assembled system and represent the most compact form of the assembled equations of motion using a minimum number of DoFs. Note that this type of assembly is the way individual finite elements are traditionally assembled in a finite element method. Furthermore primal assembly is almost always used for the assembly of the reduced components that are outlined in sections 2.3 to 2.5. These can be assembled using the same method as simple single finite elements, thereby obtaining their name of *superelements*.

2.6.2 Dual assembly

In the primal assembly method compatibility was a priori enforced, thereby also resulting in a priori satisfying the equilibrium condition. In the *dual* approach the equilibrium condition is a priori satisfied, by realizing that the interface forces at a single, matching, interface need to be equal and opposite. Therefore, a unique field of interface force intensities $\boldsymbol{\lambda}$ can be introduced, such that

$$\boldsymbol{g}_{[b]}^{(s)} = -\boldsymbol{B}_{[b]}^{(s)^T}\boldsymbol{\lambda}, \tag{2.40}$$

where $\boldsymbol{B}_{[b]}^{(s)}$ is a signed Boolean matrix locating the substructure interface DoFs. The minus sign is chosen to emphasize that, whereas $\boldsymbol{g}^{(s)}$ is seen as an external force for the substructure, $\boldsymbol{\lambda}$ is considered an internal force. Due to the construction of the Boolean matrices it holds that [35]

$$\boldsymbol{B}_{[b]}\boldsymbol{L}_{[b]} = \boldsymbol{0}. \tag{2.41}$$

Hence this choice for the interface connection forces satisfies the interface equilibrium for any $\boldsymbol{\lambda}$. This choice gives rise to the following transformation:

$$\begin{bmatrix} \boldsymbol{q}_{[i]} \\ \boldsymbol{u}_{[b]} \\ \boldsymbol{g}_{[b]} \\ \boldsymbol{u}_{[\gamma]} \end{bmatrix} = \begin{bmatrix} \boldsymbol{I} & \boldsymbol{0} & \boldsymbol{0} & \boldsymbol{0} \\ \boldsymbol{0} & \boldsymbol{I} & \boldsymbol{0} & \boldsymbol{0} \\ \boldsymbol{0} & \boldsymbol{0} & -\boldsymbol{B}_{[b]}^T & \boldsymbol{0} \\ \boldsymbol{0} & \boldsymbol{0} & \boldsymbol{0} & \boldsymbol{I} \end{bmatrix} = \begin{bmatrix} \boldsymbol{q}_{[i]} \\ \boldsymbol{u}_{[b]} \\ \boldsymbol{\lambda} \\ \boldsymbol{u}_{[\gamma]} \end{bmatrix}. \tag{2.42}$$

Substituting the transformation matrix (Eq. (2.42)) into the three-field formulation, given in Eq. (2.36), the equilibrium issue is solved a priori by replacing the local interface forces by a unique global set of interface force intensities. In order to obtain a symmetric system of equation, the resulting set is post-multiplied with the transposed transformation matrix. Due to the relationship given in Eq. (2.41) the global intermediate displacement field $\boldsymbol{u}_{[\gamma]}$ is also eliminated, resulting in the dual assembled equations of motion:

$$\begin{bmatrix} \boldsymbol{M}_{[ii]} & \boldsymbol{M}_{[ib]} & \boldsymbol{0} \\ \boldsymbol{M}_{[bi]} & \boldsymbol{M}_{[bb]} & \boldsymbol{0} \\ \boldsymbol{0} & \boldsymbol{0} & \boldsymbol{0} \end{bmatrix} \begin{bmatrix} \ddot{\boldsymbol{q}}_{[i]} \\ \ddot{\boldsymbol{u}}_{[b]} \\ \boldsymbol{\lambda} \end{bmatrix} + \begin{bmatrix} \boldsymbol{K}_{[ii]} & \boldsymbol{K}_{[ib]} & \boldsymbol{0} \\ \boldsymbol{K}_{[bi]} & \boldsymbol{K}_{[bb]} & \boldsymbol{B}_{[b]}^T \\ \boldsymbol{0} & \boldsymbol{B}_{[b]} & \boldsymbol{0} \end{bmatrix} \begin{bmatrix} \boldsymbol{q}_{[i]} \\ \boldsymbol{u}_{[b]} \\ \boldsymbol{\lambda} \end{bmatrix} = \begin{bmatrix} \boldsymbol{f}_{[i]} \\ \boldsymbol{f}_{[b]} \\ \boldsymbol{0} \end{bmatrix}. \tag{2.43}$$

Note that the result is again confirmed by directly substituting Eq. (2.40) into the Lagrangian (Eq. (2.35)) and performing the further derivation. The above system is called the *dual* assembled system, since the unknowns defining the interface problem are forces which are mathematically dual to the original displacement unknowns. In the dual assembled form, the coupling between the different substructures is explicitly enforced by the Lagrange multipliers and the compatibility equation given in the last line of Eq. (2.43). Note that dual assembly approaches

were already considered in the early days of finite element theory, but only became popular in the 1990s as a way to implement efficient solvers on parallel processing computers. This led to the family of parallel solvers known as FETI (Finite Elements Tearing and Interconnecting) [53]. In addition to this, the dual formulation, and the use of Lagrange multipliers, is applied in various methods that are introduced in chapters 4 and 5.

2.7 Summary

The current chapter dealt briefly with three different, but highly related, topics; an introduction and classification of dynamic substructuring techniques, an introduction into Component Mode Synthesis methods and on the assembly of substructures. Firstly, the introduction and a brief historical overview of the concept of dynamic substructuring were given. The methods were classified among the three main classes of dynamic substructuring; Frequency Based Substructuring, Component Mode Synthesis and the latest addition to the family; Impulse Based Substructuring.

Secondly, the concepts of Component Mode Synthesis were presented in section 2.2. In this section some of the most common ingredients for a reduction basis were introduced and it was shown how combining these modes lead to the classical (and more recent) CMS methods. In sections 2.3 to 2.5, Guyan's reduction, the Craig-Bampton and the Augmented Craig-Bampton methods were presented, whose relationship to each other is best visualized in figure 2.3. Here, a flowchart leads to one to the reduction method of choice by merely answering two questions. The first question is whether the first fixed-interface eigenfrequency ($\omega_{[i]}$) is higher in frequency than the spectral bandwidth of the external and connection forces ($\omega^{\boldsymbol{f}+\boldsymbol{g}}$). If this is the case, a Guyan's reduction will suffice, if not, a number of fixed-interface modes need to be included in the reduction basis to account for the dynamic response of the substructure. Secondly, if forces are applied at the internal DoFs of the structure ($\boldsymbol{f}_{[i]} \neq \boldsymbol{0}$), MTA's need to be added to the reduction basis in order to account for this loading.

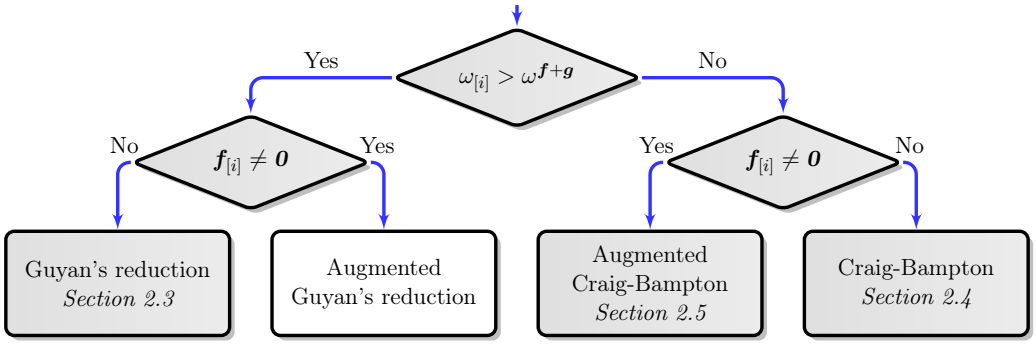

Figure 2.3: *Stepping plan towards the correct reduction method. Note that the method in the white block, the Augmented Guyan's reduction, is not explicitly discussed in this thesis.*

Finally, a brief introduction to the most common stiffness-based assembly methods, which are essential for enabling the dynamic substructuring methodology, has been given in section 2.6. The primal and dual assembly methods have both been given and can be used for the assembly of individual finite elements, but also *superelements*, in finite element models.

3

Integration by Time Stepping and Convolution

"Nature laughs at the difficulties of integration."

– Pierre-Simon Laplace

3.1 Introduction

As was noted in chapter 1, the design of an offshore wind turbine requires one to determine the responses and associated structural loading for a large number of different load cases, which are all related to certain combinations of environmental conditions and/or emergency situations. Time integration methods are essential for obtaining these responses, as they allow to compute the transient response of complex engineering structures, such as wind turbines.

For as long as differential equations have existed, people have had the desire to approximate these using numerical methods. Leonard Euler was the first to come with an explicit numerical method that resulted in a first order approximation [49]. Similar methods were generalized by Martin Wilhelm Kutta and Carl David Tolmé Runge around 1900 into the family of Runge-Kutta methods [145]. For a more detailed overview of time stepping schemes used for solving ordinary differential equations (ODEs), the reader is referred to [77].

The outline of the chapter is such that in sections 3.2 and 3.3 the most popular methods for transient simulations in the field of structural dynamics, Newmark's method and the generalized-α method, are presented. Both are methods for solving second-order differential equations, such as the equations of motion of a mechanical system. Using impulse response functions and the convolution product in order to obtain the transient response of linear dynamic systems, is the subject of section 3.4. It is demonstrated in section 3.5 how to discretize the impulse response functions and associated convolution product, in order to obtain the exact same characteristics in terms of accuracy and stability as a generalized-α time integration method. In order to improve the computational efficiency, a number of ideas are introduced in section 3.6 for limiting the size of the convolution product that one has to solve. Finally, in section 3.7, a summary of the chapter is given.

This chapter is based on work presented in [141, 168, 169, 172].

3.2 Family of Newmark time integration methods

The equations of motion of a linear(ized) mechanical system are second-order ordinary differential equations,

$$\boldsymbol{M}\ddot{\boldsymbol{q}}(t) + \boldsymbol{C}\dot{\boldsymbol{q}}(t) + \boldsymbol{K}\boldsymbol{q}(t) = \boldsymbol{f}(t),$$

where $\boldsymbol{q}(t)$ denotes a (generalized) set of DoF and $\dot{\boldsymbol{q}}(t)$, $\ddot{\boldsymbol{q}}(t)$ respectively denote the first and second time derivatives, which are all a function of time. Note that throughout the remainder of this section, the explicit time dependence is dropped in the equations. In order to solve these using the time integration methods for first-order differential equations, as were briefly mentioned in section 3.1, requires that they are transformed to a state-space notation. In the state-space notation new variables are introduced that describe the state of the system, such that $\boldsymbol{x}_1 = \boldsymbol{q}$ and $\boldsymbol{x}_2 = \dot{\boldsymbol{q}}$, thereby resulting in the following:

$$\begin{bmatrix} \dot{\boldsymbol{x}}_1 \\ \dot{\boldsymbol{x}}_2 \end{bmatrix} = \begin{bmatrix} \boldsymbol{0} & \boldsymbol{I} \\ -\boldsymbol{M}^{-1}\boldsymbol{K} & -\boldsymbol{M}^{-1}\boldsymbol{C} \end{bmatrix} \begin{bmatrix} \boldsymbol{x}_1 \\ \boldsymbol{x}_2 \end{bmatrix} + \begin{bmatrix} \boldsymbol{0} \\ \boldsymbol{M}^{-1} \end{bmatrix} \boldsymbol{f}.$$

This approach comes at the cost of doubling the number of variables and equations to solve for, which is undesirable from a computational point of view.

In order to overcome this, Newmark introduced in 1959 a single-step method, which is known as the *Newmark-β method* [112], that allowed for the direct time stepping of second-order differential equations. Newmark's method, and its derivatives, have become popular in the field of structural dynamics for obtaining the dynamic time response of large structural systems.

3.2.1 Newmark's time approximation

In the Newmark scheme, the state $(\ddot{\boldsymbol{q}}_n, \dot{\boldsymbol{q}}_n, \boldsymbol{q}_n)$ of a system at time $t_n = t_{n-1} + h$ is found from a Taylor series expansion around the known state of the system at t_{n-1} [62], such that:

$$\begin{aligned} \dot{\boldsymbol{q}}_n &= \dot{\boldsymbol{q}}_{n-1} + \int_{t_{n-1}}^{t_n} \ddot{\boldsymbol{q}}(\tau) d\tau, \\ \boldsymbol{q}_n &= \boldsymbol{q}_{n-1} + h\dot{\boldsymbol{q}}_{n-1} + \int_{t_{n-1}}^{t_n} (t_n - \tau)\ddot{\boldsymbol{q}}(\tau) d\tau. \end{aligned} \tag{3.1}$$

The approximation in the time discretization of Newmark is then introduced by approximating the integral by numerical quadrature. Firstly, by expressing the accelerations at t_{n-1} and t_n again as a Taylor expansion in the the time interval $\tau = [t_{n-1}, t_n]$,

$$\begin{aligned} \ddot{\boldsymbol{q}}_{n-1} &= \ddot{\boldsymbol{q}}(\tau) + \boldsymbol{q}^{(3)}(\tau)(t_{n-1} - \tau) + \boldsymbol{q}^{(4)}(\tau)\frac{(t_{n-1} - \tau)^2}{2} + \cdots, \\ \ddot{\boldsymbol{q}}_n &= \ddot{\boldsymbol{q}}(\tau) + \boldsymbol{q}^{(3)}(\tau)(t_n - \tau) + \boldsymbol{q}^{(4)}(\tau)\frac{(t_n - \tau)^2}{2} + \cdots. \end{aligned} \tag{3.2}$$

Now applying the quadrature using $(1-\gamma)$ and γ and $(1-2\beta)$ and 2β as interpolation functions, gives

$$\begin{aligned} \ddot{\boldsymbol{q}}(\tau) &= (1-\gamma)\ddot{\boldsymbol{q}}_{n-1} + \gamma\ddot{\boldsymbol{q}}_n + \boldsymbol{q}^{(3)}(\tau)(\tau - h\gamma - t_{n-1}) + \mathcal{O}(h^2\boldsymbol{q}^{(4)}), \\ \ddot{\boldsymbol{q}}(\tau) &= (1-2\beta)\ddot{\boldsymbol{q}}_{n-1} + 2\beta\ddot{\boldsymbol{q}}_n + \boldsymbol{q}^{(3)}(\tau)(\tau - h2\beta - t_{n-1}) + \mathcal{O}(h^2\boldsymbol{q}^{(4)}), \end{aligned} \tag{3.3}$$

which represent the accelerations at the interval $\tau = [t_{n-1}, t_n]$. Finally, substituting these in Eq. (3.1) and neglecting all the higher order derivatives gives the Newmark time discretization:

$$\begin{aligned} \dot{\boldsymbol{q}}_n &= \dot{\boldsymbol{q}}_{n-1} + (1-\gamma)h\ddot{\boldsymbol{q}}_{n-1} + \gamma h\ddot{\boldsymbol{q}}_n = \dot{\check{\boldsymbol{q}}}_n + \gamma h\ddot{\boldsymbol{q}}_n, \\ \boldsymbol{q}_n &= \boldsymbol{q}_{n-1} + h\dot{\boldsymbol{q}}_{n-1} + \left(\frac{1}{2} - \beta\right) h^2\ddot{\boldsymbol{q}}_{n-1} + \beta h^2\ddot{\boldsymbol{q}}_n = \check{\boldsymbol{q}}_n + \beta h^2\ddot{\boldsymbol{q}}_n. \end{aligned} \tag{3.4}$$

Here, $\dot{\check{\boldsymbol{q}}}_n$ and $\check{\boldsymbol{q}}_n$ are the *predictors*, which contain the effect of the previous state (at t_{n-1}) of the system on the current state. The error of the time discretization can be determined for both the displacements ($\epsilon^{\boldsymbol{q}}_{n-1}$) and velocities ($\epsilon^{\dot{\boldsymbol{q}}}_{n-1}$) by considering the neglected higher order derivatives:

$$\begin{aligned} \epsilon^{\dot{\boldsymbol{q}}}_{n-1} &= \left(\beta - \tfrac{1}{6}\right) h^3\boldsymbol{q}^{(3)}(\tau) + \mathcal{O}\left(h^4\boldsymbol{q}^{(4)}\right), \\ \epsilon^{\boldsymbol{q}}_{n-1} &= \left(\gamma - \tfrac{1}{2}\right) h^2\boldsymbol{q}^{(3)}(\tau) + \mathcal{O}\left(h^3\boldsymbol{q}^{(4)}\right). \end{aligned} \tag{3.5}$$

By varying the β and γ time integration parameters, one can find the full family of Newmark single-step methods, each with its own specifications in terms of accuracy and stability. For a full analysis on the stability and accuracy characteristics of the Newmark method, the reader is referred to [62]. In table 3.1 the characteristics of a small selection of different Newmark schemes is given.

Algorithm	β	γ	Stability limit ωh	Amplitude error $\rho - 1$	Periodicity error $\frac{\Delta T}{T}$
Central Difference	0	$\frac{1}{2}$	2	0	$\frac{-\omega^2 h^2}{24}$
Fox & Goodwin	$\frac{1}{12}$	$\frac{1}{2}$	2.45	0	$\mathcal{O}(h^3)$
Average Constant Acceleration	$\frac{1}{4}$	$\frac{1}{2}$	∞	0	$\frac{\omega^2 h^2}{12}$

Table 3.1: *Overview of the characteristics of a number of selected schemes within the Newmark family of time integration methods.*

3.2.2 Using Newmark's method in structural dynamics

The Newmark time approximation allows one to step the equations of motion of a system in time to determine the transient response of a system. In order to find the response of a structure, governed by the following set of linear equations of motion,

$$\boldsymbol{M}\ddot{\boldsymbol{q}} + \boldsymbol{C}\dot{\boldsymbol{q}} + \boldsymbol{K}\boldsymbol{q} = \boldsymbol{f}, \tag{3.6}$$

the Newmark time discretization (Eq. (3.4)) is substituted into Eq. (3.6):

$$\boldsymbol{S}\ddot{\boldsymbol{q}}_n = \boldsymbol{f} - \boldsymbol{C}\dot{\check{\boldsymbol{q}}}_n + \boldsymbol{K}\check{\boldsymbol{q}}_n. \tag{3.7}$$

Here, the only unknowns are the accelerations $\ddot{\boldsymbol{q}}_n$ at t_n. The matrix:

$$\boldsymbol{S} = \left(\boldsymbol{M} + \gamma h\boldsymbol{C} + \beta h^2\boldsymbol{K}\right),$$

is also referred to as the *effective stiffness matrix*. The effective stiffness matrix is constant in case a fixed time step is used, as the structural matrices are independent of the state of the system. Hence, it only needs to be factorized once, such that Eq. (3.7) can be solved efficiently by forward-backward substitutions.

A similar implicit scheme is used to solve nonlinear equations of motion, although one could also choose to apply an explicit scheme, as is discussed in [62]. The nonlinear equations of motion to solve are the following:

$$\boldsymbol{M}(\boldsymbol{q})\ddot{\boldsymbol{q}} + \boldsymbol{p}(\boldsymbol{q}, \dot{\boldsymbol{q}}) = \boldsymbol{f}. \tag{3.8}$$

In Eq. (3.8) the nonlinearity is both in the state-dependent mass matrix, $\boldsymbol{M}(\boldsymbol{q})$, and in a nonlinear force term, $\boldsymbol{p}(\boldsymbol{q}, \dot{\boldsymbol{q}})$, that represents the internal elastic and damping forces of the system. Unlike the procedure found for the linear system, Eq. (3.8) cannot be solved in one step. Hence, the solution for Eq. (3.8) will have to be obtained in an iterative procedure. Firstly, the equations of motion are written in a time-discrete residual form for $t = t_n$,

$$\boldsymbol{r}_n = \boldsymbol{M}(\boldsymbol{q}_n)\ddot{\boldsymbol{q}}_n + \boldsymbol{p}(\boldsymbol{q}_n, \dot{\boldsymbol{q}}_n) - \boldsymbol{f}_n = \boldsymbol{0}, \tag{3.9}$$

where $\boldsymbol{r}_n$ is the residual term that denotes the force error on the equilibrium. The Newmark relations, given in Eq. (3.4) can be rewritten to the following:

$$\begin{aligned} \ddot{\boldsymbol{q}}_n &= \frac{1}{\beta h^2}\left(\boldsymbol{q}_n - \check{\boldsymbol{q}}_n\right), \\ \dot{\boldsymbol{q}}_n &= \dot{\check{\boldsymbol{q}}}_n + \frac{\gamma}{\beta h^2}\left(\boldsymbol{q}_n - \check{\boldsymbol{q}}_n\right). \end{aligned} \tag{3.10}$$

By substituting Eq. (3.10) into Eq. (3.9), the set of displacements $\boldsymbol{q}_n$ is the only unknown left in the residual equation:

$$\boldsymbol{r}(\boldsymbol{q}_n) = \boldsymbol{0}. \tag{3.11}$$

The Newton-Raphson method is applied in this work in order to solve this set of nonlinear equations. In the Newton-Raphson method, one successively solves a number of linear (-ized) problems in order to find a solution for the underlying nonlinear problem. Hence, a first order Taylor approximation is made around the current state $\boldsymbol{q}_n^k$, found from iteration k, in order to perform the next iteration and to find the state $\boldsymbol{q}_n^{k+1}$;

$$\boldsymbol{r}(\boldsymbol{q}_n^{k+1}) \approx \boldsymbol{r}(\boldsymbol{q}_n^k) + \boldsymbol{r}'(\boldsymbol{q}_n^k)\left(\boldsymbol{q}_n^{k+1} - \boldsymbol{q}_n^k\right), \tag{3.12}$$

where the Jacobian or iteration matrix ($\boldsymbol{S}$) is used,

$$\boldsymbol{r}'(\boldsymbol{q}_n^k) = \left[\frac{\partial \boldsymbol{r}}{\partial \boldsymbol{q}}\right]_{\boldsymbol{q}_n^k} = \boldsymbol{S}(\boldsymbol{q}_n^k).$$

The iteration matrix can be interpreted again as an effective stiffness matrix, similarly to the one found for the linear case:

$$\boldsymbol{S}(\boldsymbol{q}) = \frac{\partial \boldsymbol{M}}{\partial \boldsymbol{q}}\ddot{\boldsymbol{q}} + \boldsymbol{M}\frac{\partial \ddot{\boldsymbol{q}}}{\partial \boldsymbol{q}} + \frac{\partial \boldsymbol{p}}{\partial \dot{\boldsymbol{q}}}\frac{\partial \dot{\boldsymbol{q}}}{\partial \boldsymbol{q}} - \frac{\partial \boldsymbol{f}}{\partial \dot{\boldsymbol{q}}}\frac{\partial \dot{\boldsymbol{q}}}{\partial \boldsymbol{q}} + \frac{\partial \boldsymbol{p}}{\partial \boldsymbol{q}} - \frac{\partial \boldsymbol{f}}{\partial \boldsymbol{q}}. \tag{3.13}$$

Here, one can identify the tangent stiffness matrix ($\boldsymbol{K}_t$) and tangent damping matrix ($\boldsymbol{C}_t$):

$$\boldsymbol{K}_t = \frac{\partial \boldsymbol{p}}{\partial \boldsymbol{q}} - \frac{\partial \boldsymbol{f}}{\partial \boldsymbol{q}}, \quad \boldsymbol{C}_t = \frac{\partial \boldsymbol{p}}{\partial \dot{\boldsymbol{q}}} - \frac{\partial \boldsymbol{f}}{\partial \dot{\boldsymbol{q}}},$$

and due to the Newmark relations, one finds that:

$$\frac{\partial \ddot{\boldsymbol{q}}}{\partial \boldsymbol{q}} = \frac{1}{\beta h^2}, \quad \frac{\partial \dot{\boldsymbol{q}}}{\partial \boldsymbol{q}} = \frac{\gamma}{\beta h}.$$

As the residual should be equal to zero, this is substituted in Eq. (3.12), after which the process can be written as a simple iterative scheme,

$$\boldsymbol{S}\Delta\boldsymbol{q}_n = -\boldsymbol{r}_n, \tag{3.14}$$

where $\Delta\boldsymbol{q}_n$ is the update required for the displacements. By taking into account Eq. (3.10), the update on the displacements is used to update the displacement, velocity and acceleration fields;

$$\begin{aligned} \boldsymbol{q}_n &\leftarrow \boldsymbol{q}_n + \Delta\boldsymbol{q}_n, \\ \dot{\boldsymbol{q}}_n &\leftarrow \dot{\boldsymbol{q}}_n + \frac{\gamma}{\beta h}\Delta\boldsymbol{q}_n, \\ \ddot{\boldsymbol{q}}_n &\leftarrow \ddot{\boldsymbol{q}}_n + \frac{1}{\beta h^2}\Delta\boldsymbol{q}_n. \end{aligned} \tag{3.15}$$

A new residual is found by substituting the updated state of the system in Eq. (3.9). This iterative process is continued until convergence[1], after which one continues to the next time step and the iterative Newton-Raphson process is restarted.

3.3 Generalized-α time integration method

Since a model is usually build to be accurate in a certain frequency range of interest, it could be that the higher modes of the model are in fact spurious modes. These spurious modes are not actual modes of the system, but can be a direct result of the spatial discretization using, for instance, finite elements. In addition, in for instance multibody dynamics, the constraints between different bodies introduce eigenfrequencies at infinity that destabilize even unconditionally stable time integration methods, such as the constant average acceleration Newmark method. Hence, as one is usually mainly interested in the low frequency response of a model, it is in general advantageous to have some numerical dissipation on the high frequency response of a system, that is dominated by these spurious modes. This added numerical damping is also able to stabilize the simulations for multibody models. Many different methods have been proposed that result in single-step second-order accuracy time integration methods that allow for added high-frequency numerical damping with little low-frequency damping; a small selection is found in [20, 72, 74, 196, 199].

3.3.1 Introducing numerical damping by modifying the dynamic equilibrium

The generalized-α method [20] is briefly outlined in this section. The difference between the Newmark and generalized-α methods is that the latter modifies the time discrete residual equation (Eq. (3.9)) by applying a weighted averaging over the elastic, damping, inertial and external forces between the last two time instants, such that

$$\begin{aligned} \boldsymbol{r}_n = (1-\alpha_m)\boldsymbol{M}\ddot{\boldsymbol{q}}_n + \alpha_m\boldsymbol{M}\ddot{\boldsymbol{q}}_{n-1} + (1-\alpha_f)\boldsymbol{p}\left(\boldsymbol{q}_n, \dot{\boldsymbol{q}}_n\right) + \\ \alpha_f\boldsymbol{p}\left(\boldsymbol{q}_{n-1}, \dot{\boldsymbol{q}}_{n-1}\right) - (1-\alpha_f)\boldsymbol{f}_n + \alpha_f\boldsymbol{f}_{n-1}, \end{aligned} \tag{3.16}$$

[1] In practice one would iterate until the norm of the residual is smaller than a preset force-normalized tolerance.

where, α_f controls the weight for averaging the elastic, damping and external forces and α_m controls the weight for averaging the inertial forces, such that these parameters control the amount of numerical damping of the time integration scheme.[2] Nonetheless, the process for time stepping the equations of motion, as described in section 3.2.2, remains the same. It should be noted here, that the change in the residual equation, as given in Eq. (3.16), also effects the Jacobian matrix found for the iterative Newton-Raphson process.

$$\boldsymbol{S}(\boldsymbol{q}) = (1-\alpha_m)\left(\frac{\partial \boldsymbol{M}}{\partial \boldsymbol{q}}\ddot{\boldsymbol{q}} + \boldsymbol{M}\frac{\partial \ddot{\boldsymbol{q}}}{\partial \boldsymbol{q}}\right) + (1-\alpha_f)\left(\frac{\partial \boldsymbol{p}}{\partial \dot{\boldsymbol{q}}}\frac{\partial \dot{\boldsymbol{q}}}{\partial \boldsymbol{q}} - \frac{\partial \boldsymbol{f}}{\partial \dot{\boldsymbol{q}}}\frac{\partial \dot{\boldsymbol{q}}}{\partial \boldsymbol{q}} + \frac{\partial \boldsymbol{p}}{\partial \boldsymbol{q}} - \frac{\partial \boldsymbol{f}}{\partial \boldsymbol{q}}\right) \tag{3.17}$$

If the parameters are chosen such that $\alpha_m \leq \alpha_f \leq \frac{1}{2}$, $\beta = \frac{1}{4}(1-\alpha_m+\alpha_f)^2$ and $\gamma = \frac{1}{2}-\alpha_m+\alpha_f$ the result is an unconditionally stable second-order scheme. Clearly, if $\alpha_m = 0$, on finds the HHT-α method [72], if $\alpha_f = 0$ the method is equal to the WBZ-α scheme [199] and if both parameters are equal to zero the method reduces to Newmark's constant average acceleration scheme.

Now, let ρ^∞ be the user-defined value of the spectral radius in the high-frequency limit. This spectral radius is a measure of numerical dissipation; a smaller spectral radius corresponds to a greater numerical dissipation. It can be shown that the combination of α-parameters that minimizes the low frequency dissipation for a given spectral radius in the high-frequency limit (see [20] for a detailed analysis), can be found from:

$$\alpha_m = \frac{2\rho^\infty - 1}{\rho^\infty + 1}, \quad \alpha_f = \frac{\rho^\infty}{\rho^\infty + 1}. \tag{3.18}$$

This choice in time integration parameters will result, for linear systems, in an unconditionally stable, second-order accurate time integration algorithm that possesses an optimal combination of high-frequency and low-frequency numerical dissipation.

Arnold and Brüls [7] proposed an algorithm based on the generalized-α method and proved that their method is second order accurate and unconditionally stable for nonlinear systems. As this algorithm is equal to the generalized-α method for the case of a constant mass matrix, this indirectly proves that the generalized-α method is, in this specific case, also for nonlinear systems an unconditionally stable method.

3.3.2 Block matrix and array representation for linear systems

In the case of linear systems the modified equilibrium is also obtained by applying a weighted averaging over the elastic, damping, inertial and external forces between the last two time instants, such that Eq. (3.6) is modified to:

$$\begin{aligned}(1-\alpha_m)\boldsymbol{M}\ddot{\boldsymbol{q}}_n + (1-\alpha_f)\left(\boldsymbol{C}\dot{\boldsymbol{q}}_n + \boldsymbol{K}\boldsymbol{q}_n\right) = \\ (1-\alpha_f)\boldsymbol{f}_n + \alpha_f \boldsymbol{f}_{n-1} - \alpha_m \boldsymbol{M}\ddot{\boldsymbol{q}}_{n-1} - \alpha_f\left(\boldsymbol{C}\dot{\boldsymbol{q}}_{n-1} + \boldsymbol{K}\boldsymbol{q}_{n-1}\right).\end{aligned} \tag{3.19}$$

Now the analytical solution of the first two time steps of the generalized-α is rewritten in a matrix-vector format. By substituting Eq. (3.1) into Eq. (3.19), one finds Eq. (3.20) for the

[2] Although it seems peculiar to modify the equilibrium equation like in Eq. (3.16), it is worth noting that the method remains physically consistent since the exact dynamic equilibrium is retrieved when the time step is set to zero.

first time steps,

$$\left[\begin{array}{ccc:ccc} \boldsymbol{I} & \boldsymbol{0} & \boldsymbol{0} & & & \\ \boldsymbol{0} & \boldsymbol{I} & \boldsymbol{0} & & & \\ \boldsymbol{K} & \boldsymbol{C} & \boldsymbol{M} & & & \\ \hdashline -\boldsymbol{I} & -h\boldsymbol{I} & -h^2(\frac{1}{2}-\beta)\boldsymbol{I} & \boldsymbol{I} & \boldsymbol{0} & -h^2\beta\boldsymbol{I} \\ \boldsymbol{0} & -\boldsymbol{I} & -h(1-\gamma)\boldsymbol{I} & \boldsymbol{0} & \boldsymbol{I} & -h\gamma\boldsymbol{I} \\ \alpha_f\boldsymbol{K} & \alpha_f\boldsymbol{C} & \alpha_m\boldsymbol{M} & (1-\alpha_f)\boldsymbol{K} & (1-\alpha_f)\boldsymbol{C} & (1-\alpha_m)\boldsymbol{M} \end{array}\right] \left[\begin{array}{c} \boldsymbol{q}_0 \\ \dot{\boldsymbol{q}}_0 \\ \ddot{\boldsymbol{q}}_0 \\ \hdashline \boldsymbol{q}_1 \\ \dot{\boldsymbol{q}}_1 \\ \ddot{\boldsymbol{q}}_1 \end{array}\right] = \left[\begin{array}{c} \boldsymbol{q}_0 \\ \dot{\boldsymbol{q}}_0 \\ \boldsymbol{f}_0 \\ \hdashline \boldsymbol{0} \\ \boldsymbol{0} \\ (1-\alpha_f)\boldsymbol{f}_1 + \alpha_f\boldsymbol{f}_0 \end{array}\right], \tag{3.20}$$

where $\boldsymbol{I}$ is the identity matrix ($N \times N$). If one carefully scrutinizes (3.20), it can be seen that the first two lines can be read as constraints on the displacements and velocities, as they have to be identical to the given initial conditions. The third line is the equation of motion, the unknowns being the initial accelerations. The fourth and fifth lines, now represent the Newmark time discretization and thus make the displacements and velocities of the next time steps dependent on the past displacements, velocities and accelerations and on the current (unknown) accelerations. These unknown accelerations are computed using the equation of motion given in the sixth line. It can be shown that all future time steps can be written in a way identical to the first time step (t_1), such that the generalized-α method can be written in a block-matrix notation.

$$\left[\begin{array}{ccccc} \boldsymbol{A} & & & & \\ \boldsymbol{N} & \boldsymbol{Q} & & & \\ & \boldsymbol{N} & \boldsymbol{Q} & & \\ & & \ddots & \ddots & \\ & & & \boldsymbol{N} & \boldsymbol{Q} \end{array}\right] \left[\begin{array}{c} \boldsymbol{z}_0 \\ \boldsymbol{z}_1 \\ \boldsymbol{z}_2 \\ \vdots \\ \boldsymbol{z}_n \end{array}\right] = \left[\begin{array}{c} \check{\boldsymbol{f}}_0^\star \\ \check{\boldsymbol{f}}_1 \\ \check{\boldsymbol{f}}_2 \\ \vdots \\ \check{\boldsymbol{f}}_n \end{array}\right], \tag{3.21}$$

where,

$$\check{\boldsymbol{f}}_i = \left[\begin{array}{c} \boldsymbol{0} \\ \boldsymbol{0} \\ (1-\alpha_f)\boldsymbol{f}_i + \alpha_f\boldsymbol{f}_{i-1} \end{array}\right],\ \check{\boldsymbol{f}}_0^\star = \left[\begin{array}{c} \boldsymbol{q}_0 \\ \dot{\boldsymbol{q}}_0 \\ \boldsymbol{f}_0 \end{array}\right],\ \boldsymbol{N} = \left[\begin{array}{ccc} -\boldsymbol{I} & -h\boldsymbol{I} & -h^2(\frac{1}{2}-\beta)\boldsymbol{I} \\ \boldsymbol{0} & -\boldsymbol{I} & -h(1-\gamma)\boldsymbol{I} \\ \alpha_f\boldsymbol{K} & \alpha_f\boldsymbol{C} & \alpha_m\boldsymbol{M} \end{array}\right],$$
$$\boldsymbol{A} = \left[\begin{array}{ccc} \boldsymbol{I} & \boldsymbol{0} & \boldsymbol{0} \\ \boldsymbol{0} & \boldsymbol{I} & \boldsymbol{0} \\ \boldsymbol{K} & \boldsymbol{C} & \boldsymbol{M} \end{array}\right],\ \boldsymbol{Q} = \left[\begin{array}{ccc} \boldsymbol{I} & \boldsymbol{0} & -h^2\beta\boldsymbol{I} \\ \boldsymbol{0} & \boldsymbol{I} & -h\gamma\boldsymbol{I} \\ (1-\alpha_f)\boldsymbol{K} & (1-\alpha_f)\boldsymbol{C} & (1-\alpha_m)\boldsymbol{M} \end{array}\right],\ \boldsymbol{z}_i = \left[\begin{array}{c} \boldsymbol{q}_i \\ \dot{\boldsymbol{q}}_i \\ \ddot{\boldsymbol{q}}_i \end{array}\right].$$

Note that on the left-hand-side of Eq. (3.21) one finds a repeating pattern of identical block-matrices. As the generalized-α time integration can be characterized by a lower-block diagonal matrix, one can easily use forward substitutions in order to solve the time integration, which would then be exactly the same as solving it in a time stepping manner. One can thus find the response at time t_n as

$$\boldsymbol{z}_n = \left(-\boldsymbol{Q}^{-1}\boldsymbol{N}\right)^n \boldsymbol{A}^{-1}\check{\boldsymbol{f}}_0^\star + \sum_{i=1}^{n}\left(-\boldsymbol{Q}^{-1}\boldsymbol{N}\right)^{n-i}\boldsymbol{Q}^{-1}\check{\boldsymbol{f}}_i. \tag{3.22}$$

From Eq. (3.22) one can clearly identify the superposition of the response due to the initial conditions (first term) and the forced response term (second term). Note that one would in

practice never obtain the time response from this direct equation. It is however employed in section 3.5 to find a discretization of the impulse response functions and associated convolution product that is equivalent to the generalized-α method.[3]

3.4 Using Impulse Response Functions and convolution for integration

As the name implies, Impulse Response Functions (IRFs) describe the response of the system at hand to a unit impulse force over time. Hence, they give the input-output relationship of a system or structure. As any arbitrary force function of time can be expressed as subsequent force impulses over time, IRFs can be used to determine the time response of a system [62].

3.4.1 Using impulse response functions for transient analysis

As impulse response functions give a direct input-output relationship, they only exist for structures operating in the linear regime. In order to introduce the concept of using IRFs for obtaining the time response of a system, it is chosen to start from the equation of motion of a linear dynamic finite element model:

$$\boldsymbol{M}\ddot{\boldsymbol{u}}(t) + \boldsymbol{C}\dot{\boldsymbol{u}}(t) + \boldsymbol{K}\boldsymbol{u}(t) = \boldsymbol{f}(t), \tag{3.23}$$

where, $\boldsymbol{u}(t)$, $\dot{\boldsymbol{u}}(t)$, $\ddot{\boldsymbol{u}}(t)$ respectively denote the nodal displacement, velocity and acceleration DoFs. By applying the Laplace transform to Eq. (3.23), one finds

$$s^2\boldsymbol{M}\mathcal{U} - s\boldsymbol{M}\boldsymbol{u}(0) - \boldsymbol{M}\dot{\boldsymbol{u}}(0) + s\boldsymbol{C}\mathcal{U} - \boldsymbol{C}\boldsymbol{u}(0) + \boldsymbol{K}\mathcal{U} = \mathcal{F}, \tag{3.24}$$

where $\mathcal{U}(s) = \mathfrak{L}(\boldsymbol{u}(t))$ and $\mathcal{F}(s) = \mathfrak{L}(\boldsymbol{f}(t))$. Hence, solving for $\mathcal{U}(s)$ and taking the inverse Laplace gives the response of the system in the time domain:

$$\boldsymbol{u}(t) = \dot{\boldsymbol{Y}}(t)\boldsymbol{M}\boldsymbol{u}_0 + \boldsymbol{Y}(t)\left(\boldsymbol{M}\dot{\boldsymbol{u}}_0 + \boldsymbol{C}\boldsymbol{u}_0\right) + \int_{\tau=0}^{t} \boldsymbol{Y}(t-\tau)\boldsymbol{f}(\tau)d\tau, \tag{3.25}$$

where $\dot{\boldsymbol{Y}}(t)$ is the first time derivative of the impulse response function $\boldsymbol{Y}(t)$ and can be interpreted as the impulse response function in terms of velocities. From Eq. (3.25) one can easily identify the particular solution, due to the external force, in the last term and the homogeneous solution due to the initial conditions in the first two terms. Note that the last term in Eq. (3.25) is a convolution product and is often referred to as *Duhamel's integral*. A disadvantage of the solution given in Eq. (3.25) is that one also needs to compute (and store) the first time derivative of the IRFs, in the case of nonzero initial displacements.

Instead of using the solution given in Eq. (3.25), the total response can be regarded as a superposition of a relative response $\boldsymbol{v}(t)$ and the initially applied displacements $\boldsymbol{u}_0$:

$$\boldsymbol{u}(t) = \boldsymbol{v}(t) + \boldsymbol{u}_0, \tag{3.26}$$

where $\boldsymbol{v}(t)$ is by definition characterized by zero initial displacements ($\boldsymbol{v}_0 = \boldsymbol{0}$). Substituting Eq. (3.26) into the linear equations of motion of a general dynamic system, gives

$$\boldsymbol{M}\ddot{\boldsymbol{v}}(t) + \boldsymbol{C}\dot{\boldsymbol{v}}(t) + \boldsymbol{K}\boldsymbol{v}(t) = \boldsymbol{f}(t) - \boldsymbol{K}\boldsymbol{u}_0. \tag{3.27}$$

[3] Note that the last term in Eq. (3.22) can in fact already be interpreted as a discretized convolution product.

Using the Laplace transform once more, one finds that

$$\boldsymbol{u}(t) = \boldsymbol{u}_0 + \boldsymbol{Y}(t)\boldsymbol{M}\dot{\boldsymbol{u}}_0 + \int_{\tau=0}^{t} \boldsymbol{Y}(t-\tau)\left(\boldsymbol{f}(\tau) - \boldsymbol{K}\boldsymbol{u}_0\right) d\tau, \tag{3.28}$$

which is equivalent to Eq. (3.25). It should be noted that in the form given in Eq. (3.28) the time derivative of the IRFs is no longer required. By comparing Eqs. (3.25) and (3.28) one can see that the response to the initial displacement is now performed by

$$\boldsymbol{u}_0 - \int_{\tau=0}^{t} \boldsymbol{Y}(t-\tau)\left(\boldsymbol{K}\boldsymbol{u}_0\right) d\tau,$$

where,

$$\int_{\tau=0}^{t} \boldsymbol{Y}(t-\tau) d\tau$$

is the response to a unit step load.

One can again apply the change of variable and regard the total response as a superposition of a relative response $\boldsymbol{v}(t)$ and the initially applied displacements $\boldsymbol{u}_0$ and velocities $\dot{\boldsymbol{u}}_0$:

$$\boldsymbol{u}(t) = \boldsymbol{v}(t) + \boldsymbol{u}_0 + \dot{\boldsymbol{u}}_0 t. \tag{3.29}$$

Note that the relative response $\boldsymbol{v}(t)$ is characterized by zero initial conditions and thus represents the response of the system initially at rest. Substituting this into the linear equations of motion of a general dynamic system, gives:

$$\boldsymbol{M}\ddot{\boldsymbol{v}}(t) + \boldsymbol{C}\dot{\boldsymbol{v}}(t) + \boldsymbol{K}\boldsymbol{v}(t) = \boldsymbol{f}(t) - \boldsymbol{K}\left(\boldsymbol{u}_0 + \dot{\boldsymbol{u}}_0 t\right) - \boldsymbol{C}\dot{\boldsymbol{u}}_0. \tag{3.30}$$

Again, from employing the Laplace transform, the following response is found:

$$\boldsymbol{u}(t) = \boldsymbol{u}_0 + \dot{\boldsymbol{u}}_0 t + \int_{\tau=0}^{t} \boldsymbol{Y}(t-\tau)\left(\boldsymbol{f}(\tau) - \boldsymbol{K}\left(\boldsymbol{u}_0 + \dot{\boldsymbol{u}}_0 \tau\right) - \boldsymbol{C}\dot{\boldsymbol{u}}_0\right) d\tau. \tag{3.31}$$

In this final form it can be observed that both the initial velocities and displacements influence the forcing term in the convolution integral. Hence, it is easily deduced that the response due to the initial velocities is handled in a different way, such that:

$$\boldsymbol{Y}(t)\boldsymbol{M}\dot{\boldsymbol{u}}_0 = \dot{\boldsymbol{u}}_0 t + \int_{\tau=0}^{t} \boldsymbol{Y}(t-\tau)\left(-\boldsymbol{K}\dot{\boldsymbol{u}}_0 \tau - \boldsymbol{C}\dot{\boldsymbol{u}}_0\right) d\tau.$$

Finally note that Eqs. (3.25), (3.28) and (3.31) are analytically fully equivalent.

3.4.2 Starting the transient analysis from a quasi-static equilibrium

For time simulations of operating systems, it is often beneficial to start the time integration scheme from an initial quasi-static equilibrium, instead of from the undeformed state. The latter choice leads to high initial accelerations and hence, large transient effects that are not related to the steady-state operation of the system. By choosing to start from an initial deformed state,

no high initial accelerations are present, hence limiting the transient effects due to a start of the time simulations.

Hence, the initial conditions would then follow from:

$$\dot{\boldsymbol{u}}_0 = \boldsymbol{0}, \quad \boldsymbol{K}\boldsymbol{u}_0 = \boldsymbol{f}_0.$$

Substituting these initial condition into Eq. (3.28), gives that

$$\boldsymbol{u}(t) = \boldsymbol{u}_0 + \int_{\tau=0}^{t} \boldsymbol{Y}(t-\tau)\left(\boldsymbol{f}(\tau) - \boldsymbol{f}_0\right) d\tau, \tag{3.32}$$

the term that deals with the initial velocities disappears. As the total solution given in Eq. (3.32) can now be interpreted as the combination of a static response and dynamic fluctuations due to the dynamic part of the force, this is what one would (mechanically) expect. In order to determine the initial deformation one can take the inverse of the stiffness matrix, or one can directly obtain the static flexibility from the IRFs. If we would apply a constant (unit) force (a step function) in the convolution product given in Eq. (3.28) with the initial conditions equal to zero, we would obtain

$$\boldsymbol{u}(t) = \int_{\tau=0}^{t} \boldsymbol{Y}(t-\tau)\mathbf{1}_{[j]} d\tau, \tag{3.33}$$

where $\mathbf{1}_{[j]}$ is a vector with a unit coefficient for DoF j. Hence, by taking the constant $\mathbf{1}_{[j]}$ out of the integral an making a change of variable such that $\tau_2 = t - \tau$, one obtains:

$$\boldsymbol{u}(t) = \int_{\tau_2=t}^{0} -\boldsymbol{Y}(\tau_2) d\tau_2 \mathbf{1}_{[j]} = \int_{\tau_2=0}^{t} \boldsymbol{Y}(\tau_2) d\tau_2 \mathbf{1}_{[j]}. \tag{3.34}$$

If t goes to infinity, the dynamic response will damp out and only the static response remains:

$$\boldsymbol{u}(\infty) = \int_{\tau_2=0}^{\infty} \boldsymbol{Y}(\tau_2) d\tau_2 \mathbf{1}_{[j]} = \boldsymbol{K}^{-1}\mathbf{1}_{[j]}. \tag{3.35}$$

Hence, we can obtain the static flexibility matrix $\boldsymbol{K}^{-1}$ by simply integrating the IRFs from $t = 0$ to infinity:

$$\boldsymbol{K}^{-1} = \int_{\tau_2=0}^{\infty} \boldsymbol{Y}(\tau_2) d\tau_2. \tag{3.36}$$

Note that in the discussing above it is assumed that the system is constrained in order to eliminate all the possible rigid body modes. In chapter 5 it is discussed how to initialize the simulations in the Impulse Based Substructuring method, where a single, uncoupled, substructure could be free-floating. In this case, the response from a unit step function is now a combination of a flexible response and rigid body accelerations, such that

$$\boldsymbol{u}(t) = \int_{\tau=0}^{t} \boldsymbol{Y}(t-\tau)\mathbf{1}_j d\tau = \int_{\tau=0}^{t} \boldsymbol{Y}^{flex}(t-\tau)\mathbf{1}_j d\tau + \int_{\tau=0}^{t} \boldsymbol{Y}^{rig}(t-\tau)\mathbf{1}_j d\tau, \tag{3.37}$$

where $\boldsymbol{Y}^{flex}$, $\boldsymbol{Y}^{rig}$ respectively denote the flexible and rigid body impulse response functions of the system. These can be obtained by using orthogonal projectors,

$$\begin{cases} \boldsymbol{Y}^{flex} = \left(\boldsymbol{I} - \boldsymbol{R}\left(\boldsymbol{R}^T\boldsymbol{R}\right)^{-1}\boldsymbol{R}^T\right)\boldsymbol{Y} \\ \boldsymbol{Y}^{rig} = \boldsymbol{R}\left(\boldsymbol{R}^T\boldsymbol{R}\right)^{-1}\boldsymbol{R}^T\boldsymbol{Y} \end{cases}, \tag{3.38}$$

where $\boldsymbol{R}$ denote the rigid body modes. If t goes to infinity, the flexible dynamic response will damp out and only the static response and rigid body displacements (which increase over time) will remain:

$$\lim_{t\to\infty} \int_{\tau=0}^{t} \boldsymbol{Y}^{flex}(t-\tau)\mathbf{1}_j d\tau = \boldsymbol{K}^{+}\mathbf{1}_{\boldsymbol{j}}. \tag{3.39}$$

Hence, after a change of variable, the static flexibility matrix $\boldsymbol{K}^{+}$ is again obtained from simply integrating the IRFs from $t = 0$ to infinity:

$$\boldsymbol{K}^{+} = \int_{\tau=0}^{\infty} \boldsymbol{Y}^{flex}(\tau)d\tau. \tag{3.40}$$

In practice however, one would truncate the IRFs at a certain point in time, such that $\boldsymbol{Y}^{flex}(t_k) \approx \boldsymbol{0}$. Obviously, the choice of the truncation time t_k will affect the "quality" of the flexibility matrices found (from Eqs. (3.36) and (3.40)). Truncation of IRFs is discussed in more detail in section 3.6.

3.4.3 Obtaining the impulse responses from models and experiments

Substructure IRFs can be obtained directly from impact measurements, or from numerical models that are available. Here however, the discussion is limited to IRFs obtained from numerical models. For a more detailed discussion on obtaining IRFs from impact measurements, the reader is referred to [138, 162, 164].

The most direct approach for obtaining IRFs from numerical models is to use time integration techniques (such as the generalized-α method outlined in section 3.3). Note that, although one will introduce a time discretization error, this can be controlled using the time step size and specific time integration parameters, as is shown in section 3.5. Computing the IRFs of the substructures can be seen as obtaining an *exact reduced* representation of the substructure dynamics as one only requires the IRFs of the input and output DoF for the analysis: no approximation of the dynamics is used, except for the error inherent to the time discretization.

A second approach is to obtain the set of IRFs from a modal synthesis in the time domain, as is shown in Eq. (3.41),

$$\boldsymbol{Y}^{(s)}(t) = \sum_{m=1}^{k} \boldsymbol{R}_m^{(s)} e^{\lambda_m^{(s)} t} + \bar{\boldsymbol{R}}_m^{(s)} e^{\bar{\lambda}_m^{(s)} t}, \tag{3.41}$$

where k denotes the highest mode of the system, which is equal to infinity for continuous models. In addition, $\lambda_m^{(s)}$ are complex eigenvalues (the poles) and $\boldsymbol{R}_m^{(s)}$ are the residues of the system, computed from the normal modes ($\boldsymbol{\phi}_m^{(s)}$) and the associated scaling factor ($Q_m^{(s)}$)

$$\boldsymbol{R}_m^{(s)} = Q_m^{(s)} \boldsymbol{\phi}_m^{(s)} \boldsymbol{\phi}_m^{(s)^T}. \tag{3.42}$$

Note that $\bar{\lambda}_m^{(s)}$ and $\bar{\boldsymbol{R}}_m^{(s)}$ are the associated complex conjugates. This approach is equal to applying a continuous inverse Fourier transform to the pole/residue model [13], that is used to synthesize FRFs from modal parameters. Note that if the modal basis is truncated, an approximation of the true IRF is found.

3.4.4 The impulse response due to a distributed load

In many engineering problems, such as for instance the dynamic study of an offshore foundation under wave loading, the structure is excited by a distributed load. If this is now seen from a modeling perspective, this area will consist of a large number of nodes in a finite element model, and the number of entries in the matrix containing the required IRFs would grow quadratically with respect to the size of the force loaded area. In order to overcome this issue, we describe these forces as a summation of space distributions of the force ($\boldsymbol{\chi}_i$), multiplied by their corresponding force amplitudes ($\theta_i(t)$):

$$\boldsymbol{f}(t) = \sum_{j=1}^{n_p} \boldsymbol{\chi}_j \theta_j(t) = \boldsymbol{X}\boldsymbol{\theta}. \tag{3.43}$$

We thus assume that separation of variable can be applied to the force $\boldsymbol{f}(t)$, which is dependent on both time (t) and location. Note that the same concept was used in section 2.5, in order to compute the MTAs for the Augmented Craig-Bampton method. By substituting Eq. (3.43) into Eq. (3.28) with zero initial conditions, the impulse response describes the response of a structure due to a distributed load;

$$\boldsymbol{u}(t) = \int_0^t \boldsymbol{Y}(t-\tau)\boldsymbol{X}\boldsymbol{\theta}(\tau)d\tau. \tag{3.44}$$

Suppose that the system contains a large number (p) of force loaded DoFs (inputs) with only N response DoFs of interest (outputs), such that $N << p$. In Eq. (3.44) $\boldsymbol{Y}(t)$ is a $N \times p$ sized continuous time matrix, hence computing the needed IRFs and evaluating the convolution integral will be computationally expensive. Using the shape distributions of the load to reduce the size of the impulse response function, leads to:

$$\boldsymbol{u}(t) = \int_0^t \boldsymbol{Y}_{\boldsymbol{X}}(t-\tau)\boldsymbol{\theta}(\tau)d\tau, \tag{3.45}$$

where,

$$\boldsymbol{Y}_{\boldsymbol{X}}(t) = \boldsymbol{Y}(t)\boldsymbol{X}, \tag{3.46}$$

is computed as the impulse response associated to the load distributions. This step reduces the size of the impulse response function matrix from $N \times p$ to $N \times p_\chi$, where p_χ equals the number of force shape distribution functions and $p_\chi << p$. An approach for obtaining these force shapes is discussed in chapter 6.

3.5 Discretization of the convolution product

Obviously, the direct computation of the IRFs using time integration methods, such as the generalized-α method, result in time discretized impulse response functions. But also the IRFs

obtained from either measurements or analytical models are time sampled versions of the underlying time continuous (experimental or numerical) models. Hence, the continuous convolution product given in Eq. (3.28) needs to be discretized as well.

The purpose of this section is to be able to use IRFs as a sort of "superelements in time" that can fulfill the same role as the traditional superelements, that were outlined in chapter 2. In order to control the accuracy of the resulting response and to guarantee the stability of the proposed Impulse Based Substructuring scheme (presented in chapter 5), the discretization of both the IRFs as well as the convolution product needs to be consistent with the generalized-α method.

Hence, in the remainder of the section it is assumed that the IRFs are obtained from a direct time integration of finite element models using the generalized-α method, that was summarized in section 3.3. Note that in section 3.3.2 a direct expression for a response, computed using the generalized-α method, was found. This allows to prove that the IRFs and the convolution product can be made fully equivalent to a direct time integration using the generalized-α scheme.

3.5.1 Computing the Impulse Response Functions

Several approaches exist to compute IRFs using time integration, as was presented in [141], but as the goal is to ensure that the discretization is consistent with a generalized-α time integration, only the relevant approaches are shown in this section. In the first approach, the impulse response due to an initial impulse at t_0 is computed, which can be summarized by;

$$\check{\boldsymbol{f}}_0^\star = \left[\begin{array}{ccc} \boldsymbol{0} & \boldsymbol{0} & \frac{\mathbf{1}_{[j]}}{h}^T \end{array} \right]^T, \quad \check{\boldsymbol{f}}_{i\neq 0} = \left[\begin{array}{ccc} \boldsymbol{0} & \boldsymbol{0} & \boldsymbol{0} \end{array} \right]^T, \tag{3.47}$$

where $\mathbf{1}_{[j]}$ is a vector with a unit coefficient for DoF j. Substituting Eq. (3.47) into Eq. (3.22) leads to the impulse response function due to an initial impulse at t_0,

$$\left[\begin{array}{c} {}^0\ddot{\boldsymbol{Y}}_{[j],n} \\ {}^0\dot{\boldsymbol{Y}}_{[j],n} \\ {}^0\boldsymbol{Y}_{[j],n} \end{array} \right] = \left(\left(-\boldsymbol{Q}^{-1}\boldsymbol{N}\right)^n \boldsymbol{A}^{-1} + H_{n-1}\alpha_f \left(-\boldsymbol{Q}^{-1}\boldsymbol{N}\right)^{n-1} \boldsymbol{Q}^{-1} \right) \left[\begin{array}{c} \boldsymbol{0} \\ \boldsymbol{0} \\ \frac{\mathbf{1}_{[j]}}{h} \end{array} \right], \tag{3.48}$$

where $H_{n-1} = H(n-1)$ is the discrete Heaviside step function and ${}^0\ddot{\boldsymbol{Y}}_{[j],n}$, ${}^0\dot{\boldsymbol{Y}}_{[j],n}$, ${}^0\boldsymbol{Y}_{[j],n}$ are the IRFs respectively in terms of accelerations, velocities and displacements.

A second approach consists in applying a unit impulse at the first time step (t_1), by substituting the initial conditions given in Eq. (3.49) into Eq. (3.22),

$$\check{\boldsymbol{f}}_0^\star = \left[\begin{array}{ccc} \boldsymbol{0} & \boldsymbol{0} & \boldsymbol{0} \end{array} \right]^T, \quad \check{\boldsymbol{f}}_1 = \left[\begin{array}{ccc} \boldsymbol{0} & \boldsymbol{0} & \frac{\mathbf{1}_{[j]}}{h}^T \end{array} \right]^T, \quad \check{\boldsymbol{f}}_{i\neq 1} = \left[\begin{array}{ccc} \boldsymbol{0} & \boldsymbol{0} & \boldsymbol{0} \end{array} \right]^T, \tag{3.49}$$

one obtains the unit impulse responses due to an impulse at t_1. Now shifting the obtained response back in time, such that the response at t_1 is shifted to t_0 and so on, one will obtain:

$$\left[\begin{array}{c} {}^1\ddot{\boldsymbol{Y}}_{[j],n} \\ {}^1\dot{\boldsymbol{Y}}_{[j],n} \\ {}^1\boldsymbol{Y}_{[j],n} \end{array} \right] = \left((1-\alpha_f) \left(-\boldsymbol{Q}^{-1}\boldsymbol{N}\right)^n \boldsymbol{Q}^{-1} + H_{n-1}\alpha_f \left(-\boldsymbol{Q}^{-1}\boldsymbol{N}\right)^{n-1} \boldsymbol{Q}^{-1} \right) \left[\begin{array}{c} \boldsymbol{0} \\ \boldsymbol{0} \\ \frac{\mathbf{1}_{[j]}}{h} \end{array} \right]. \tag{3.50}$$

The two different impulse response functions (Eq. (3.48) and Eq. (3.50)) will be used to derive the consistent discretization of the convolution product in section 3.5.2. Note that the IRFs given in Eq. (3.48) and Eq. (3.50) are in practice simply computed using classical time-stepping, and that the direct equations shown here have only as purpose to analyze the equivalence between discrete convolutions and discrete time-integration.

3.5.2 Discretization of the convolution product

One can easily verify, by substituting Eq. (3.48) and Eq. (3.50), that the discretization chosen in Eq. (3.51) will result in the same nodal response as the one computed using Eq. (3.22), assuming that the system is initially at rest:

$$\begin{aligned}
\ddot{\boldsymbol{u}}_n &= h\left[{}^0\ddot{\boldsymbol{Y}}_n\right]\boldsymbol{f}_0 + h\sum_{i=1}^{n}\left[{}^1\ddot{\boldsymbol{Y}}_{n-i}\right]\boldsymbol{f}_i,\\
\dot{\boldsymbol{u}}_n &= h\left[{}^0\dot{\boldsymbol{Y}}_n\right]\boldsymbol{f}_0 + h\sum_{i=1}^{n}\left[{}^1\dot{\boldsymbol{Y}}_{n-i}\right]\boldsymbol{f}_i,\\
\boldsymbol{u}_n &= h\left[{}^0\boldsymbol{Y}_n\right]\boldsymbol{f}_0 + h\sum_{i=1}^{n}\left[{}^1\boldsymbol{Y}_{n-i}\right]\boldsymbol{f}_i.
\end{aligned} \tag{3.51}$$

In order to be able to compute the response of a system from non-zero initial conditions, Eq. (3.51) is substituted in the discretized form of Eq. (3.31),[4] this becomes

$$\begin{aligned}
\ddot{\boldsymbol{u}}_n &= h\left[{}^0\ddot{\boldsymbol{Y}}_n\right]\bar{\boldsymbol{f}}_0 + h\sum_{i=1}^{n}\left[{}^1\ddot{\boldsymbol{Y}}_{n-i}\right]\bar{\boldsymbol{f}}_i,\\
\dot{\boldsymbol{u}}_n &= \dot{\boldsymbol{u}}_0 + h\left[{}^0\dot{\boldsymbol{Y}}_n\right]\bar{\boldsymbol{f}}_0 + h\sum_{i=1}^{n}\left[{}^1\dot{\boldsymbol{Y}}_{n-i}\right]\bar{\boldsymbol{f}}_i,\\
\boldsymbol{u}_n &= \boldsymbol{u}_0 + \dot{\boldsymbol{u}}_0 t_n + h\left[{}^0\boldsymbol{Y}_n\right]\bar{\boldsymbol{f}}_0 + h\sum_{i=1}^{n}\left[{}^1\boldsymbol{Y}_{n-i}\right]\bar{\boldsymbol{f}}_i,
\end{aligned} \tag{3.52}$$

where

$$\bar{\boldsymbol{f}}_i = \boldsymbol{f}_i - \boldsymbol{K}\left(\boldsymbol{u}_0 + \dot{\boldsymbol{u}}_0 t_i\right) - \boldsymbol{C}\dot{\boldsymbol{u}}_0.$$

From further examining Eq. (3.52) a number of special cases can be identified. Firstly, if one would apply the Average Constant Acceleration variant of the Newmark method ($\alpha_m = 0$, $\alpha_f = 0$, $\beta = 1/4$, $\gamma = 1/2$), it can be shown [141] that the discretization given in Eq. (3.52) can be simplified to

$$\boldsymbol{u}_n = \boldsymbol{u}_0 + \dot{\boldsymbol{u}}_0 t_n + h\sum_{i=0}^{n-1}\left[{}^0\boldsymbol{Y}_{n-i}\right]\left(\bar{\boldsymbol{f}}_i + \bar{\boldsymbol{f}}_{i+1}\right), \tag{3.53}$$

where one only requires the impulse response function due to an initial impulse (Eq. (3.48)) in order to find the response of the structure.

A second special case is found if one would start the time integration from an initial static equilibrium, such that the initial condition are equal to Eq. (3.54);

$$\boldsymbol{u}_0 = \boldsymbol{K}^{-1}\boldsymbol{f}_0, \quad \dot{\boldsymbol{u}}_0 = \boldsymbol{0}. \tag{3.54}$$

Substituting these conditions into Eq. (3.52) gives

$$\begin{cases} \bar{\boldsymbol{f}}_0 = \boldsymbol{f}_0 - \boldsymbol{K}\boldsymbol{K}^{-1}\boldsymbol{f}_0 = \boldsymbol{0} \\ \bar{\boldsymbol{f}}_i = \boldsymbol{f}_i - \boldsymbol{f}_0 \end{cases}, \tag{3.55}$$

[4] Note that although Eqs. (3.25) and (3.28) are in the analytical form fully equivalent to Eq. (3.31), this is not per definition true for the discretized versions. As the discretization given in Eq. (3.51) is consistent for systems initially at rest, it thus represents the response of $\boldsymbol{v}$ in Eq. (3.29), thereby automatically leading the the analytic form given in Eq. (3.31). Nonetheless, one could also choose to discretize according to for instance Eq. (3.28), but in that case the response due to the initial conditions is no longer consistent with the generalized-α method that has nonzero initial velocities.

thereby simplifying Eq. (3.52) to

$$\boldsymbol{u}_n = \boldsymbol{u}_0 + h \sum_{i=1}^{n} \left[{}^1\boldsymbol{Y}_{n-i}\right] \bar{\boldsymbol{f}}_i, \tag{3.56}$$

where the term from the impulse response function due to an initial impulse (Eq. (3.48)) drops out of the equation. Therefore, one only needs to compute the impulse response function for an impulse applied at time t_1 (and shifted as explained in section 3.5.1). In addition, the original system matrices are no longer needed to correct the forcing term for the initial conditions, as one can simply use the force at t_0, as is shown in Eq. (3.55). Finally, it is noted that the static flexibility matrix required to determine $\boldsymbol{u}_0$ can be obtained directly from the IRFs, as is shown in section 3.4.2.

3.6 Notes on windowing and truncating Impulse Response Functions

A clear disadvantage of using impulse response functions and the convolution product for time integration is that one is required to compute the convolution product from t_0 to t_n. In the case of long time simulations, or those using very small time steps, the computational effort required for solving the convolution product could become unacceptably large. Several approaches exist that can help to speed up computations. The most common approach would be to employ the *Fast Fourier Transform* (FFT) to allow for efficiently solving the convolution product in the frequency domain, as is for instance discussed in [125]. In this work however, a different idea is used, which is outlined in the remainder of this section.

3.6.1 Truncating IRFs of non-floating substructures

An approach presented in [140] is to truncate the convolution product of a non-floating substructure at a certain time t_k. If one assumes that $n > k$ and the response is started from zero initial condition, the convolution product given in Eq. (3.52), can be written as follows:

$$\boldsymbol{u}_n = h \left[{}^0\boldsymbol{Y}_n\right] \boldsymbol{f}_0 + h \sum_{i=m}^{n} \left[{}^1\boldsymbol{Y}_{n-i}\right] \boldsymbol{f}_i + h \sum_{j=1}^{m-1} \left[{}^1\boldsymbol{Y}_{n-j}\right] \boldsymbol{f}_j, \tag{3.57}$$

where $m = n - k$. Now, if k is chosen such that:

$$h \sum_{i=m}^{n} \left[{}^1\boldsymbol{Y}_{n-i}\right] \boldsymbol{f}_i \gg h \sum_{j=1}^{m-1} \left[{}^1\boldsymbol{Y}_{n-j}\right] \boldsymbol{f}_j, \tag{3.58}$$

an accurate approximation of Eq. (3.57) is obtained from:

$$\boldsymbol{u}_n \approx h \left[{}^0\boldsymbol{Y}_n\right] \boldsymbol{f}_0 + h \sum_{i=(n-k)}^{n} \left[{}^1\boldsymbol{Y}_{n-i}\right] \boldsymbol{f}_i. \tag{3.59}$$

The convolution product is truncated here, such that one neglects the forcing history that was applied on the structure between t_0 and $t_{(n-k)-1}$. Thereby limiting the size of the convolution product, such that the normal "growth" of the computational effort required for solving the convolution product is eliminated.

The truncation can be interpreted as applying a rectangular window on the IRFs in order to set these to zero after t_k, that can be defined as:

$$w^{rect}(t) = \begin{cases} 1 & \text{for } t < t_k \\ 0 & \text{for } t \geq t_k \end{cases} .$$

The truncation time t_k can be determined by stating that the amplitude of all IRFs have reached an oscillatory amplitude that is ϵ_k-times the maximum value over time.

Especially for systems with high damping, this approach will result in a significant increase in computational speed. As the response of such a system will decay relatively fast, the value for k is assumed to be small and hence, the convolution product required also remains small. Note that although the IRFs due to an impulse at t_0 have not been truncated in Eq. (3.59), this can easily be done. However, as no convolution product is solved using this term, the computational gain is relatively small. Obviously, by truncating this term as well, one can save computational time in the process of computing the IRFs.

3.6.2 Truncation in case of floating substructures

Due to the rigid body motion that is present in the IRFs of floating substructures, the statement in Eq. (3.58) no longer holds. Nonetheless, as was outlined in section 3.4.2, the flexible response will (in the case of damping) decay over time. Hence, one can split the total response into a flexible part and a rigid part, as is also shown in Eq. (3.37),

$$\boldsymbol{u}_n = \boldsymbol{u}_n^{flex} + \boldsymbol{u}_n^{rigid}.$$

The flexible response can now be approximated again, by applying the truncation:

$$\boldsymbol{u}_n^{flex} \approx h \left[{}^0\boldsymbol{Y}_n^{flex} \right] \boldsymbol{f}_0 + h \sum_{i=(n-k)}^{n} \left[{}^1\boldsymbol{Y}_{n-i}^{flex} \right] \boldsymbol{f}_i. \tag{3.60}$$

The rigid response can be determined using modal reduction, as was shown in [163], by describing the rigid response in terms of the (mass normalized) rigid body modes ($\boldsymbol{R}$) and associated amplitudes ($\boldsymbol{\alpha}_n$):[5]

$$\boldsymbol{u}_n^{rigid} = \boldsymbol{R}\boldsymbol{\alpha}_n.$$

Substituting this coordinate transformation into the general equation of motion of a linear dynamic system (as given in Eq. (3.6)) one obtains the following equations of motion for the rigid body motions:

$$\ddot{\boldsymbol{\alpha}}_n + \boldsymbol{R}^T\boldsymbol{C}\boldsymbol{R}\dot{\boldsymbol{\alpha}}_n = \boldsymbol{R}^T\boldsymbol{f}_n. \tag{3.61}$$

This can then easily be solved using the generalized-α time stepping scheme. As the discretization of the convolution product is equivalent to the generalized-α method, the only approximation that is made, is the approximation due to the truncation in Eq. (3.60). It should be noted that there are different approaches for time stepping the rigid body response. It was shown in [140], that one can also apply a recursive algorithm to obtain the rigid body response.

[5] Note that this technique was also generalized to non-rigid body modes [163]. In that case one can write the total response as a superposition of a low frequent (and low damped) response, which is described by a compact modal model, and a high frequent response resulting from the IRFs. As the higher modes generally have high damping ratios, their response will quickly damp out and one only requires relatively short IRFs.

3.6.3 Smoothing the truncated IRFs by means of windowing

Forcing the impulse response to zero, as is done in the truncation steps presented in the previous two subsections can seriously perturb the dynamic response of the system found from Eq. (3.59), as one enforces that the response due to the forces before t_{n-k} is equal to zero. Physically, this can be interpreted as actually introducing "spurious" impulses in order to cancel the impulse response due to those forces in the past. It was shown in [140] that a "too crude" truncation leads to instabilities in response computed using the Impulse Based Substructuring method.

In order to smoothen this transition, one can apply a window to the IRFs that are truncated. By applying for instance an exponential window,

$$w^{exp}(t) = e^{-\lambda t},$$

one would artificially add a damping term to the response such that a faster decay is obtained. In figure 3.1(a) it can be seen that by doing so, one can significantly alter the original signal. In [140] a "cosine" window was used (shown in figure 3.1(b)),

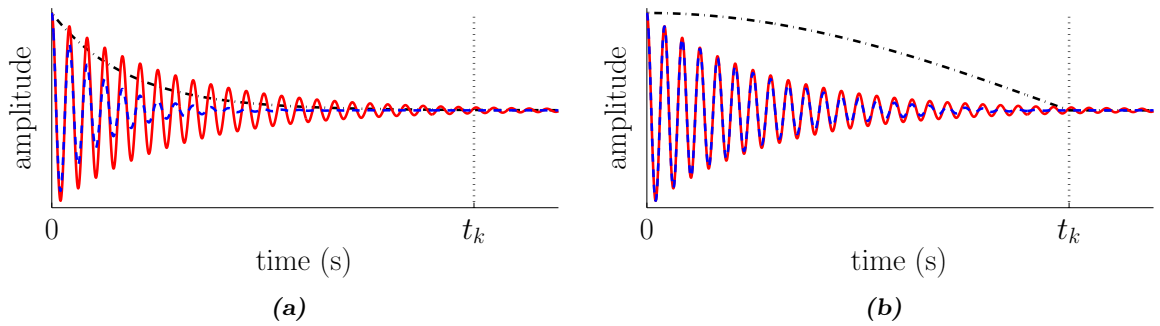

Figure 3.1: *Visualization of different windows: Original signal: (—), window function (- ·), windowed signal (- -); **(a)** Exponential window; **(b)** Cosine window.*

$$w^{cos}(t) = \begin{cases} cos\frac{\pi t}{2t_k} & \text{for } t < t_k \\ 0 & \text{for } t \geq t_k \end{cases},$$

which has the benefit of not introducing to much damping at the beginning of the impulse response, thereby not perturbing the dynamical properties of the system too much. Nonetheless, no mechanical interpretation, as was given for the exponential window, can be given for this type of window. It was demonstrated in [140] that the window can indeed be successfully used to smoothen truncated IRFs, but no analysis on the effects in terms of loss of accuracy and/or stability has been performed.

A third window that is briefly mentioned here is a combination of a rectangular and cosine window;

$$w^{com}(t) = \begin{cases} 1 & \text{for } t < t_w \\ cos\frac{\pi(t-t_w)}{2(t_k-t_w)} & \text{for } t_w \geq t < t_k \\ 0 & \text{for } t \geq t_k \end{cases}.$$

Here one starts with the rectangular window up to a certain time t_w, after which a cosine window is applied to force the response to zero at t_k. This combination allows retaining a large part of the original system, by only adding extra (non-physical) artificial damping at the end. It is also clearly seen, that this window induced the least changes (w.r.t. the previous windows)

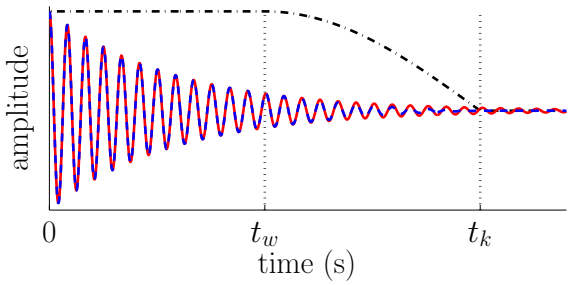

Figure 3.2: *Visualization of the composed window: Original signal: (—), window function (- ·), windowed signal (– –).*

to the original response in time. Hence, in order to find t_w and t_k one states that the amplitudes of all IRFs have reached oscillatory amplitudes that are ϵ_w-times and ϵ_k-times the maximum value over time.

3.7 Summary

In this chapter a number of procedures have been outlined that allow finding the transient response of linear and nonlinear models. Firstly, in section 3.2 the family of Newmark time integration methods has been outlined. Here, the time continuous equations of motion are discretized by means of a Taylor expansion, thereby allowing one to directly solve linear and nonlinear second-order differential equation. By varying the integration parameters of the time dicretization, one finds the different members of the Newmark family. A further generalization of this approach is found in the generalized-α scheme, where an extra two parameters are introduced. These parameters allow one to add high-frequency numerical damping. Both methods can be tuned using the time integration parameters, to result in a second order, unconditionally stable time integration method.

A second approach that can be used for obtaining the transient response of linear systems, is by means of impulse response functions and the convolution product, as is discussed in section 3.4. Using the Laplace domain the time continuous response of a linear system, starting from arbitrary initial conditions, can be determined. In addition, it was shown that IRFs due to a distributed impulse can be obtained and used to efficiently handle distributed forces that are applied on large sections of the substructure models. Finally, it was shown that one is can directly obtain the flexibility matrix from the IRFs, thereby eliminating the need for the structural stiffness matrix if one wants to start the time integrations from an initial quasi-static equilibrium.

In section 3.5 it was proven that one can discretize the IRFs and the convolution product such that these are fully equivalent to a generalized-α method. In order to do so, the IRFs need to be obtained from a time integration using the generalized-α method. The transient response obtained using the convolution product presented in section 3.5.2 is then shown to be fully equivalent to obtaining the transient response using the generalized-α method.

Finally, the concepts of truncating and windowing the IRFs are briefly outlined in section 3.6. These methods allow one to limit the size of the convolution product that needs to be solved, without altering the found response too much. Nonetheless, an approximation will be obtained from solving the transient problem using these truncated and windowed IRFs. It should be noted that no analysis has been performed to determine the errors introduced by these approaches.

4

Monolithic Multi-Domain Time Stepping Schemes

"A big computer, a complex algorithm and a long time does not equal science."

– Robert Gentleman

4.1 Introduction

The forced response of large nonlinear models is in practice quite expensive to obtain using the time integration methods introduced in chapter 3. This especially becomes an issue if one has to perform these simulations for a large number of load cases. As these time integrations involve solving a nonlinear static-like problem at each time step, the simulations could take up to several days to solve. In a lot of cases however, the global nonlinearity of the model could be relatively mild or parts of the model can be assumed to behave linearly and the strong nonlinearities, that require many iterations to solve, are localized in a small number of regions of the model. Examples of this could be interfaces with friction, localized large deformations or multi-physical phenomena.

Traditional methods for efficiently solving these kinds of problems, often include reduction of the linear parts of the structure using Component Mode Synthesis techniques, as outlined in chapter 2 and visualized in figure 4.1.

By reducing the linear parts, one can significantly limit the size of the total problem that needs to be solved. If large parts of the system can not be linearized, due to for instance large deformations, this is not an option however. Nonetheless, several advances have been made in reducing certain types of nonlinearities [160, 191, 192].

The common feature of all these approaches is that one follows the traditional Dynamic Substructuring steps; starting from component modeling and reduction and finally reassembling the different components into a single domain. In order to obtain the response of the system, one performs time integration on the entire reassembled domain. In this chapter two alternative approaches, which are both still based on a "divide and conquer" strategy, are outlined. The common feature of these methods is that, instead of reassembling the different (reduced or unreduced) domains into a single one, one directly applies the time-stepping schemes to

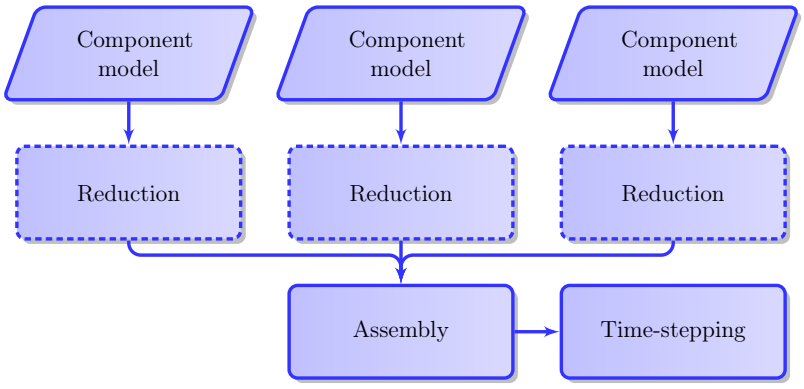

Figure 4.1: *Typical work flow for performing time integrations on a dynamic model that is assembled from multiple (reduced and/or unreduced) substructures.*

the substructures and assures that the individual time stepping schemes lead to the coupled response, as is visualized in figure 4.2.

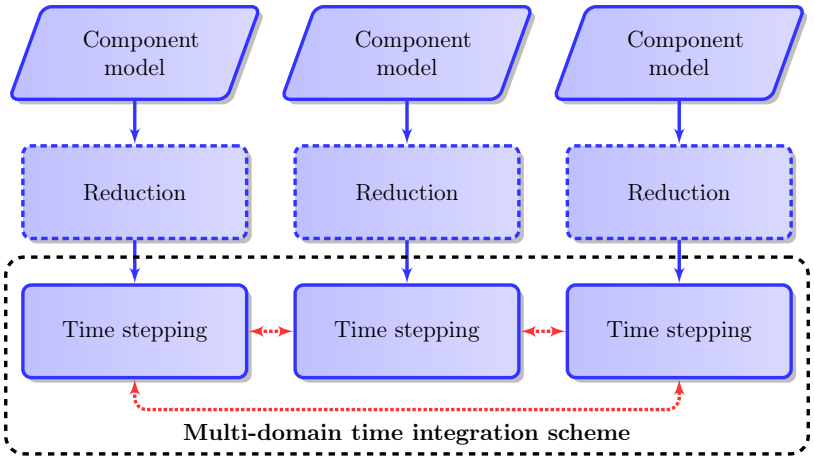

Figure 4.2: *Conceptual view of coupled multi-domain time integration. Again, one can employ reduced or unreduced models in this approach.*

4.1.1 Methods for the partitioned analysis for mechanical systems

Different approaches have been presented for obtaining methods that are able to perform a partitioned analysis of coupled structures [56]. In addition, there has been a some interest in developing methods for performing these partitioned analyses using different Newmark-based integration schemes that have different time integration parameters per substructure [15,16,104, 105]. This concept is visualized in figure 4.3a, where a smaller time scale is used for substructure A then for B. The method visualized is in fact a co-simulation method, where the different domains exchange information at t_{n-1}, to individually proceed to t_n. As this step is now based on "old" information of the previous time step and not on the results obtained at t_n, the effect of the neighboring domains will always be one time step "too late". As an extension of this, there are also methods that are able to deal with subdomains that are both non-matching in time and space [21,54]. Hence, in these methods one also has to deal with non-matching grids, or even moving grids.

The methods introduced in this chapter however, assume that one uses the same time integration

method with consistent time step size and integration parameters for all substructures, as is seen in figure 4.3b and 4.3c. An example of a staggered scheme is given in figure 4.3b, where the numbers denote the order of the steps. In this example one uses the result of substructure A at t_n, to determine the effect on subdomain B at t_{n-1}, with the result that substructure A is a time step behind in its response, see for more details on staggered schemes [55, 56, 123].

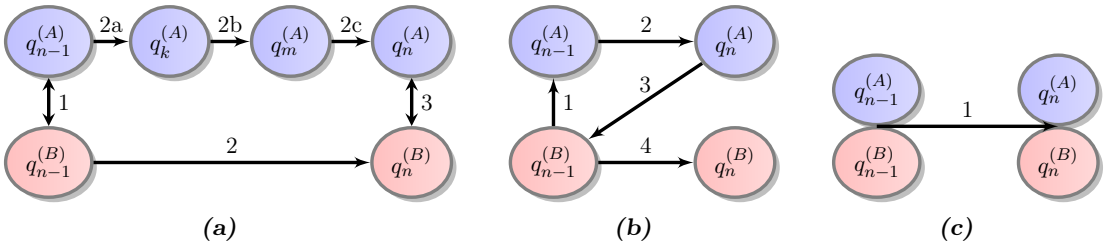

Figure 4.3: *Different types of partitioned time integration methods;* ***(a)*** *Multi-time co-simulation;* ***(b)*** *Staggered scheme;* ***(c)*** *Monolithic approach.*

The methods that are presented in this chapter are based on the concept shown in figure 4.3(c) and are thus monolithic approaches. In a monolithic approach one solves at each time step the exact coupled problem. The benefit of this, is that it is easier to end up with a stable method in comparison to the multi-time, multi-space and staggered approaches [107]. However, this often comes at the price of less efficient computational procedures.

4.1.2 Coupling different simulation packages by means of monolithic time integration

The goal of the methods introduced in this chapter is primarily to allow for a coupling between multiple simulation packages and to improve the computational speed of the time stepping procedures is in fact only a secondary objective. For instance, most of the wind turbine simulation codes were developed for simulating onshore wind turbines. Together with the development of offshore wind farms, came the developments in modeling these offshore wind turbines (for an overview see [190]). As most turbine are installed on monopile foundations, this type of foundation model is generally included [143]. Due to more challenging offshore conditions, other types of foundations structures, such as jackets, start to become more popular and need to be included in the offshore wind turbine simulations [124]. Also the floating types of foundations are being investigated and need to be included [90, 91, 142].

At the same time, a large number of commercially available simulation software suites are available that can simulate the coupled hydro-elastic behavior of offshore foundations. These packages were mainly developed to serve the oil and gas market, but can be employed in offshore wind engineering as well. Therefore, instead of integrating all these models into the existing aero-elastic simulation packages, one could also allow for coupling the existing aero-elastic modeling tools to the existing hydro-elastic simulation tools, as is for instance proposed in [92]. This concept of coupling multiple software packages has also been used in order to couple controller models to the aero-elastic simulations tools [9]. Therefore, using these ideas would create an extremely flexible modeling and simulation environment and that is exactly what the methods proposed in this chapter should facilitate.

4.1.3 Chapter outline

In this chapter two monolithic multi-domain time integration methods are presented. Firstly, a sequential time stepping scheme in given in section 4.2. Two options for initializing the time

stepping procedure are given in section 4.3. Note the the method presented in these sections has also been integrated in the Siemens in-house aero-elastic simulation code BHawC as part of this research, and a verification study of the method and its implementation are given in Appendix A. Secondly, a parallel time integration approach is presented in section 4.4, for which also two options for initialization are given in section 4.5. As both methods employ Lagrange multipliers in order to facilitate the communication between the different subdomain time stepping schemes, some remarks on the nature and stability of these Lagrange multipliers are given in section 4.6. Finally, the summary of this chapter is given in section 4.7.

This chapter is based on work presented in [170, 173].

4.2 A monolithic sequential multi-domain time integration method

The time integration schemes presented in this chapter are all based on the generalized-α method, which is outlined in section 3.3, and the dual assembly paradigm that was discussed in section 2.6.2. Hence, applying these concepts on a system that is composed of N_s (nonlinear) substructures results in the following coupled set of time discretized equations of motion,

$$\begin{cases} \boldsymbol{r}_n = (1-\alpha_m)\boldsymbol{M}\ddot{\boldsymbol{u}}_n + \alpha_m \boldsymbol{M}\ddot{\boldsymbol{u}}_{n-1} + (1-\alpha_f)\left(\boldsymbol{p}_n + \boldsymbol{B}^T\boldsymbol{\lambda}_n - \boldsymbol{f}_n\right) \\ \qquad\qquad\qquad\qquad +\alpha_f\left(\boldsymbol{p}_{n-1} + \boldsymbol{B}^T\boldsymbol{\lambda}_{n-1} - \boldsymbol{f}_{n-1}\right) \\ \boldsymbol{B}\boldsymbol{u}_n = \boldsymbol{0} \end{cases}, \tag{4.1}$$

where

$$\begin{aligned} \boldsymbol{M} &= \text{diag}\left(\boldsymbol{M}^{(1)}, \ldots, \boldsymbol{M}^{(N_s)}\right), \\ \boldsymbol{B} &= \text{row}\left(\boldsymbol{B}^{(1)}, \ldots, \boldsymbol{B}^{(N_s)}\right), \\ \boldsymbol{f}_n &= \text{col}\left(\boldsymbol{f}_n^{(1)}, \ldots, \boldsymbol{f}_n^{(N_s)}\right), \\ \boldsymbol{p}_n &= \text{col}\left(\boldsymbol{p}_n^{(1)}\left(\boldsymbol{u}_n^{(1)}, \dot{\boldsymbol{u}}_n^{(1)}\right), \ldots, \boldsymbol{p}_n^{(N_s)}\left(\boldsymbol{u}_n^{(N_s)}, \dot{\boldsymbol{u}}_n^{(N_s)}\right)\right), \\ \boldsymbol{r}_n &= \text{col}\left(\boldsymbol{r}_n^{(1)}, \ldots, \boldsymbol{r}_n^{(N_s)}\right), \\ \boldsymbol{u}_n &= \text{col}\left(\boldsymbol{u}_n^{(1)}, \ldots, \boldsymbol{u}_n^{(N_s)}\right). \end{aligned}$$

Again, $\boldsymbol{M}$ denotes the mass matrix, $\boldsymbol{B}$ is a signed Boolean operator, $\boldsymbol{p}_n$, $\boldsymbol{f}_n$ respectively denote the set of (nonlinear) internal and external forces, $\boldsymbol{r}_n$ denotes the residual force error and $\boldsymbol{u}_n$ is the set of displacement DoFs. In a dual assembled system, the coupling between the substructures is facilitated by the Lagrange multipliers that enforce compatibility between the different substructures. Several approaches can now be chosen to solve the system of equations. One could chose to solve the coupled equations of motion as a single domain using the standard generalized-α method, as outlined in section 3.3. Or one could solve the systems by means of partitioned time integrations, as is presented in section 4.2.1 for the case of two substructures. In section 4.2.3 this idea is extended to a structure decomposed into multiple substructures.

This method has been integrated, as part of this research, in the Siemens in-house aero-elastic code BHawC. A verification study of the method and implementation is given in Appendix A.

4.2.1 Derivation of the sequential approach using only two substructures

Suppose that, for the sake of illustration, one wants to compute the response of a wind turbine on a jacket type of foundation structures, as illustrated in figure 4.4. As there are only two

substructures, the coupled set of residual equations Eq. (4.1) is written explicitly per substructure, as is shown in Eq. (4.2). Here, the wind turbine model is denoted by $\star^{(A)}$ and the jacket

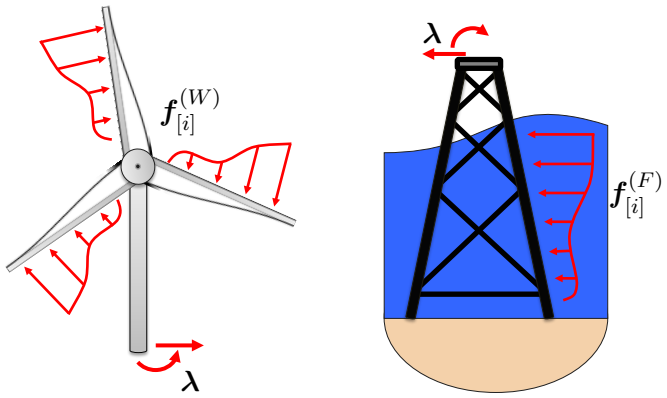

Figure 4.4: *Wind turbine and foundation model, with annotations for the applied and interface forces.*

model is denoted by $\star^{(B)}$, such that:

$$\begin{cases} \boldsymbol{r}_n^{(A)} = (1-\alpha_m)\boldsymbol{M}_n^{(A)}\ddot{\boldsymbol{u}}_n^{(A)} + \alpha_m \boldsymbol{M}_{n-1}^{(A)}\ddot{\boldsymbol{u}}_{n-1}^{(A)} + (1-\alpha_f)\left(\boldsymbol{p}_n^{(A)} + \boldsymbol{B}^{(A)^T}\boldsymbol{\lambda}_n - \boldsymbol{f}_n^{(A)}\right) \\ \qquad\qquad +\alpha_f\left(\boldsymbol{p}_{n-1}^{(A)} + \boldsymbol{B}^{(A)^T}\boldsymbol{\lambda}_{n-1} - \boldsymbol{f}_{n-1}^{(A)}\right) \\ \boldsymbol{r}_n^{(B)} = (1-\alpha_m)\boldsymbol{M}^{(B)}\ddot{\boldsymbol{u}}_n^{(B)} + \alpha_m \boldsymbol{M}^{(B)}\ddot{\boldsymbol{u}}_{n-1}^{(B)} + (1-\alpha_f)\left(\boldsymbol{p}_n^{(B)} + \boldsymbol{B}^{(B)^T}\boldsymbol{\lambda}_n - \boldsymbol{f}_n^{(B)}\right) \\ \qquad\qquad +\alpha_f\left(\boldsymbol{p}_{n-1}^{(B)} + \boldsymbol{B}^{(B)^T}\boldsymbol{\lambda}_{n-1} - \boldsymbol{f}_{n-1}^{(B)}\right) \\ \boldsymbol{B}\boldsymbol{u}_n = \boldsymbol{0} \end{cases}, \tag{4.2}$$

where $\ddot{\boldsymbol{u}}_n^{(s)}, \dot{\boldsymbol{u}}_n^{(s)}, \boldsymbol{u}_n^{(s)}$ are respectively the unknown accelerations, velocities and displacements and $\boldsymbol{\lambda}_n$ are the unknown interface forces. In order to solve these, initial estimates are used that are iteratively updated, such that:

$$\begin{aligned} \boldsymbol{u}_n^{(s)} &\leftarrow \boldsymbol{u}_n^{(s)} + \Delta\boldsymbol{u}_n^{(s)}, \\ \dot{\boldsymbol{u}}_n^{(s)} &\leftarrow \dot{\boldsymbol{u}}_n^{(s)} + \frac{\gamma}{\beta h}\Delta\boldsymbol{u}_n^{(s)}, \\ \ddot{\boldsymbol{u}}_n^{(s)} &\leftarrow \ddot{\boldsymbol{u}}_n^{(s)} + \frac{1}{\beta h^2}\Delta\boldsymbol{u}_n^{(s)}, \\ \boldsymbol{\lambda}_n &\leftarrow \boldsymbol{\lambda}_n + \Delta\boldsymbol{\lambda}_n. \end{aligned} \tag{4.3}$$

Note that, due to the rotor, the mass matrix of the wind turbine is configuration dependent. The residual force vectors, $\boldsymbol{r}_n^{(s)}$ (for $s = A, B$), can be regarded as an error on the equilibrium and should be set to zero. Here, the same approach as in section 3.2.2 for solving the nonlinear part is used. Therefore, the original Newmark relations, given in Eq. (3.4), are rearranged, to give

$$\begin{aligned} \ddot{\boldsymbol{u}}_n^{(s)} &= \frac{1}{h^2\beta}\left(\boldsymbol{u}_n^{(s)} - \check{\boldsymbol{u}}_n^{(s)}\right), \\ \dot{\boldsymbol{u}}_n^{(s)} &= \check{\dot{\boldsymbol{u}}}_n^{(s)} + \frac{\gamma}{h\beta}\left(\boldsymbol{u}_n^{(s)} - \check{\boldsymbol{u}}_n^{(s)}\right), \end{aligned} \tag{4.4}$$

where the only unknowns on the right hand side are the unknown displacements ($\boldsymbol{u}_n^{(s)}$). Hence, direct relations between the unknown accelerations ($\ddot{\boldsymbol{u}}_n^{(s)}$), velocities ($\dot{\boldsymbol{u}}_n^{(s)}$) and displacements

($\boldsymbol{u}_n^{(s)}$) are obtained. After substituting Eq. (4.4) into the second line of Eq. (4.2) the only unknowns left are the displacements and interface forces at t_n:

$$\begin{cases} \boldsymbol{r}_n^{(A)}\left(\boldsymbol{u}_n^{(A)}, \boldsymbol{\lambda}_n\right) = \check{\boldsymbol{r}}_n^{(A)}\left(\boldsymbol{u}_n^{(A)}\right) + (1-\alpha_f)\boldsymbol{B}^{(A)^T}\Delta\boldsymbol{\lambda}_n = \boldsymbol{0} \\ \boldsymbol{r}_n^{(B)}\left(\boldsymbol{u}_n^{(B)}, \boldsymbol{\lambda}_n\right) = \check{\boldsymbol{r}}_n^{(B)}\left(\boldsymbol{u}_n^{(B)}\right) + (1-\alpha_f)\boldsymbol{B}^{(B)^T}\Delta\boldsymbol{\lambda}_n = \boldsymbol{0} \\ \boldsymbol{B}\boldsymbol{u}_n = \boldsymbol{0} \end{cases} . \tag{4.5}$$

In Eq. (4.5) the total residual is divided into a part of the residual that is only a function of its own displacement ($\check{\boldsymbol{r}}_n^{(s)}(\boldsymbol{u}_n^{(s)})$) and a part that is only dependent on the unknown changes in the interface forces. Applying the Newton-Raphson method to this set of equations, gives to following linear problem to solve:

$$\begin{bmatrix} \boldsymbol{S}^{(A)} & \boldsymbol{0} & \boldsymbol{B}^{(A)^T} \\ \boldsymbol{0} & \boldsymbol{S}^{(B)} & \boldsymbol{B}^{(B)^T} \\ \boldsymbol{B}^{(A)} & \boldsymbol{B}^{(B)} & \boldsymbol{0} \end{bmatrix} \begin{bmatrix} \Delta\boldsymbol{u}_n^{(A)} \\ \Delta\boldsymbol{u}_n^{(B)} \\ (1-\alpha_f)\Delta\boldsymbol{\lambda}_n \end{bmatrix} = \begin{bmatrix} -\boldsymbol{r}_n^{(A)} \\ -\boldsymbol{r}_n^{(B)} \\ \boldsymbol{0} \end{bmatrix}, \tag{4.6}$$

where the substructure Jacobian matrices are found from:

$$\boldsymbol{S}^{(s)} = \frac{\partial \check{\boldsymbol{r}}_n^{(s)}}{\partial \boldsymbol{u}^{(s)}} = (1-\alpha_m)\left(\frac{\partial \boldsymbol{M}^{(s)}}{\partial \boldsymbol{u}^{(s)}}\ddot{\boldsymbol{u}}^{(s)} + \boldsymbol{M}^{(s)}\frac{1}{\beta h^2}\right) + (1-\alpha_f)\left(\frac{\gamma}{\beta h}\boldsymbol{C}_t^{(s)} + \boldsymbol{K}_t^{(s)}\right), \tag{4.7}$$

where

$$\boldsymbol{C}_t^{(s)} = \frac{\partial \boldsymbol{p}^{(s)}}{\partial \dot{\boldsymbol{u}}^{(s)}} - \frac{\partial \boldsymbol{f}^{(s)}}{\partial \dot{\boldsymbol{u}}^{(s)}}, \quad \boldsymbol{K}_t^{(s)} = \frac{\partial \boldsymbol{p}^{(s)}}{\partial \boldsymbol{u}^{(s)}} - \frac{\partial \boldsymbol{f}^{(s)}}{\partial \boldsymbol{u}^{(s)}}.$$

The update on the displacements of the foundation structure (B), can be written as a function of the residual ($\boldsymbol{r}_n^{(B)}$) and update on the interface forces ($\Delta\boldsymbol{\lambda}_n$),

$$\Delta\boldsymbol{u}_n^{(B)} = -\boldsymbol{S}^{(B)^{-1}}\left(\boldsymbol{r}_n^{(B)} + (1-\alpha_f)\boldsymbol{B}^{(B)^T}\Delta\boldsymbol{\lambda}_n\right) = \Delta\hat{\boldsymbol{u}}_n^{(B)} - (1-\alpha_f)\boldsymbol{S}^{(B)^{-1}}\boldsymbol{B}^{(B)^T}\Delta\boldsymbol{\lambda}_n, \tag{4.8}$$

where $\Delta\hat{\boldsymbol{u}}_n^{(B)}$ can be regarded as the update of the associate "uncoupled" problem. Substituting this in the compatibility equation, given in the last line of Eq. (4.6) and rewriting this, gives a direct expression for the update on interface forces:

$$\Delta\boldsymbol{\lambda}_n = \left((1-\alpha_f)\boldsymbol{B}^{(B)}\boldsymbol{S}^{(B)^{-1}}\boldsymbol{B}^{(B)^T}\right)^{-1}\begin{bmatrix} \boldsymbol{B}^{(A)} & \boldsymbol{B}^{(B)} \end{bmatrix}\begin{bmatrix} \Delta\boldsymbol{u}_n^{(A)} \\ \Delta\hat{\boldsymbol{u}}_n^{(B)} \end{bmatrix}. \tag{4.9}$$

Obviously, the update on the displacements for the wind turbine substructure A ($\Delta\boldsymbol{u}_n^{(A)}$) is still unknown, such that one cannot directly determine the Lagrange multipliers. However, by substituting Eq. (4.9) into the first line of Eq. (4.5) one would find that the only unknown in the residual equation is the set of displacements:

$$\boldsymbol{r}_n^{(A)}\left(\boldsymbol{u}_n^{(A)}\right) = \boldsymbol{0}. \tag{4.10}$$

An update on the displacements can thus be found from solving a single Newton-Raphson step:

$$\Delta\boldsymbol{u}_n^{(A)} = -\hat{\boldsymbol{S}}^{(A)^{-1}}\left(\boldsymbol{r}_n^{(A)} + \boldsymbol{B}^{(A)^T}\left((1-\alpha_f)\boldsymbol{B}^{(B)}\boldsymbol{S}^{(B)^{-1}}\boldsymbol{B}^{(B)^T}\right)^{-1}\boldsymbol{B}^{(B)}\Delta\hat{\boldsymbol{u}}_n^{(B)}\right), \tag{4.11}$$

where,

$$\hat{\boldsymbol{S}}^{(A)} = \frac{\partial \boldsymbol{r}^{(A)}}{\partial \boldsymbol{u}^{(A)}} = \frac{\partial \hat{\boldsymbol{r}}^{(A)}}{\partial \boldsymbol{u}^{(A)}} + \frac{\partial \boldsymbol{B}^{(A)^T}\boldsymbol{\lambda}}{\partial \boldsymbol{u}^{(A)}} = \boldsymbol{S}^{(A)} + \boldsymbol{B}^{(A)^T}\left(\boldsymbol{B}^{(B)}\boldsymbol{S}^{(B)^{-1}}\boldsymbol{B}^{(B)^T}\right)^{-1}\boldsymbol{B}^{(A)} \quad (4.12)$$

Here, one can easily recognize the condensation of the foundation structure onto the interface DoFs of the wind turbine model. The last term of Eq. (4.12) can thus be interpreted as the effective equivalent interface stiffness of the foundation model and is thus equal to the inverse of the Schur complement ($\bar{\boldsymbol{S}}^{(B)}_{[bb]}$) of $\boldsymbol{S}^{(B)}$:

$$\boldsymbol{S}^{(B)}_{int} = \left(\boldsymbol{B}^{(B)}\boldsymbol{S}^{(B)^{-1}}\boldsymbol{B}^{(B)^T}\right)^{-1} = \bar{\boldsymbol{S}}^{(B)}_{[bb]}. \quad (4.13)$$

In addition, the last term on the right hand side of Eq. (4.11) can be interpreted as the interface forces that would be found by substituting a zero displacement update for subsystem A into Eq. (4.9), such that

$$\Delta\hat{\boldsymbol{\lambda}}_n = \left((1-\alpha_f)\boldsymbol{B}^{(B)}\boldsymbol{S}^{(B)^{-1}}\boldsymbol{B}^{(B)^T}\right)^{-1}\begin{bmatrix}\boldsymbol{B}^{(A)} & \boldsymbol{B}^{(B)}\end{bmatrix}\begin{bmatrix}\boldsymbol{0} \\ \Delta\hat{\boldsymbol{u}}^{(B)}_n\end{bmatrix}. \quad (4.14)$$

Here $\Delta\hat{\boldsymbol{\lambda}}_n$ can thus be interpreted as blocked force.[1] Hence, the result that is found from Eq. (4.11) includes the effect of the neighboring structure, such that $\Delta\boldsymbol{u}^{(A)}_n$ obtained from Eq. (4.11) is equal to the one found from directly solving Eq. (4.6). By now substituting $\Delta\boldsymbol{u}^{(A)}_n$ into Eq. (4.9), one can obtain the update on the Lagrange multipliers. These are required for solving Eq. (4.8) from which the update on the displacements is obtained for subsystem B. Using the updates for the increments, the predictors and interface forces are corrected, obtained from Eq. (4.3) and a new residual is computed. The updated state of the system is substituted in Eq. (4.2) to update the residuals. These are now used to check for convergence; if the system has converged a new time step is started, if not, another iteration is performed.

It should be noted here that it is assumed that all the substructure Jacobians, $\boldsymbol{S}^{(s)}$, are non-singular matrices. This is in general true for substructures that can have unconstrained rigid body motion, assuming that the mass and/or damping of the structure is distributed on all the nodes. If one uses the same concepts to partition static problems, the tangent stiffness matrices will be singular under the same conditions and one will have to take care of the rigid body displacements, as is shown in section 4.3.

4.2.2 Practical implementation of the sequential approach

The derivation presented in section 4.2.1 does not directly constitute a partitioned time integration scheme. Nonetheless, all the underlying formulas are given and thereby form the basics of the partitioned sequential time integration method. In order to do so in a structured manner, a number of steps are defined, which are shown in figure 4.5. By following the black arrows, one finds the different steps that constitute the coupled time stepping scheme and will be briefly outlined.

1. Each new time step is started with a predictor step for both substructures.
2. Compute the residual of subsystem B using the state ($\boldsymbol{u}^{(B)}_n, \dot{\boldsymbol{u}}^{(B)}_n, \ddot{\boldsymbol{u}}^{(B)}_n$) of the subsystem.

[1] In order to efficiently deal with distributed loading on the internal DoF of reduced substructures ($\boldsymbol{f}_{[i]}$), one can use the concept of blocked forces to transform the internal loading to interface, such that the resulting responses of the neighboring substructures is exact. This is presented in section 6.3.

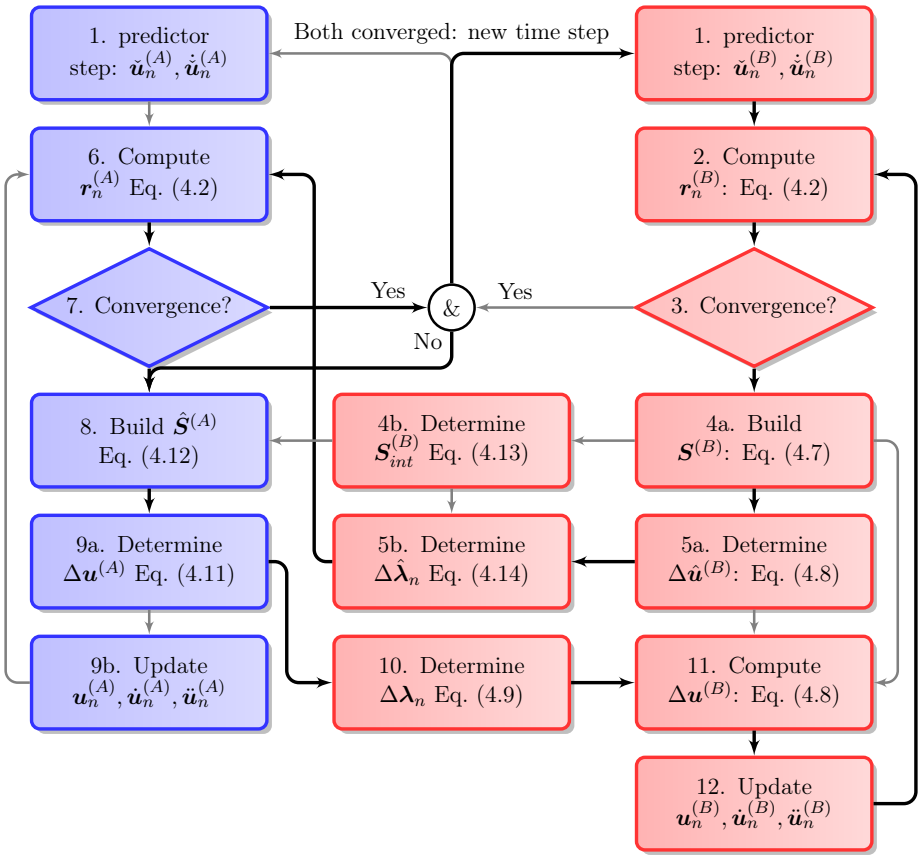

Figure 4.5: *Workflow of the sequential approach using two subsystems.*

3. Check for convergence for substructure B.

4. Firstly, in step 4a the (local) Jacobian matrix of substructure B is build (see Eq. (4.7)). Following this, in step 4b the Jacobian matrix is condensed to the interface DoF ($\boldsymbol{S}_{int}^{(B)}$), as is shown in Eq. (4.13).

5. In step 5a the "uncoupled" response is computed from Eq. (4.8). This result and the condensed Jacobian, $\boldsymbol{S}_{int}^{(B)}$, are now used to compute the blocked force $\Delta\hat{\boldsymbol{\lambda}}_n$ using Eq. (4.14) in step 5b.

6. Compute the residual of subsystem A using the state $(\boldsymbol{u}_n^{(A)}, \dot{\boldsymbol{u}}_n^{(A)}, \ddot{\boldsymbol{u}}_n^{(A)})$ of the subsystem and the forcing effect of subsystem B onto substructure A using the blocked force $\Delta\hat{\boldsymbol{\lambda}}_n$, as is shown in Eq. (4.11).

7. Check convergence for substructure A. If both substructures are converged, a new time step is started and one starts at step 1 again. If one of the substructures has not converged yet, the process is continued.

8. The (local) Jacobian matrix of substructure A is obtained and the condensed interface Jacobian of substructure $\boldsymbol{S}_{int}^{(B)}$ is assembled using Eq. (4.12). Substructure B is now effectively condensed onto the interface of substructure A.

9. Using the residual computed in step 6 and the total Jacobian obtained in step 8, the update on the displacements for substructure A is computed in step 9a. As the effective stiffness and forces from substructure B are condensed onto substructure A, one finds the *global* update for subsystem A, as can be seen in Eq. (4.11). Next, in step 9b, one updates

the state $(\boldsymbol{u}_n^{(A)}, \dot{\boldsymbol{u}}_n^{(A)}, \ddot{\boldsymbol{u}}_n^{(A)})$ of substructure A.

10. Using the global update for subsystem A, one can compute the actual update on the Lagrange multipliers using Eq. (4.9).

11. The update on the Lagrange multipliers are now used to obtain the "coupled" update $(\Delta\boldsymbol{u}^{(B)})$ on the displacements for substructure B using Eq. (4.8)

12. Finally, the state of subsystem B $(\boldsymbol{u}_n^{(B)}, \dot{\boldsymbol{u}}_n^{(B)}, \ddot{\boldsymbol{u}}_n^{(B)})$ is updated and a new iteration is started from step 2 onwards.

From figure 4.5 and the overview of the different steps given, it is easily seen that the proposed method is a sequential method. Hence, each iteration is a loop that starts by obtaining the uncoupled response for substructure B, after which one exchanges the effective interface stiffness matrix and interface forces to substructure A. Here the global problem is solved, which is used to compute the interface forces and update subsystem B. Nonetheless, if the number of interface DoF are relatively small, the amount of information that needs to be exchanged is limited. A clear advantage with respect to the methods introduced at the beginning of the chapter is that in this approach, one does not alter the underlying steps and equations of the generalized-α, but simply solves these equation in a different manner. Thereby maintaining all the characteristics in terms of accuracy and stability of the original generalized-α method, that was outlined in section 3.3.

4.2.3 Remarks on extending the sequential approach to multiple substructures

The sequential monolithic time integration approach presented in sections 4.2.1 and 4.2.2 requires to condense one substructure on the other. The resulting scheme is not too complex in the case of two substructures, but if one wants to extend the approach to multiple substructures, which could all be linked to each other, this is less straightforward.

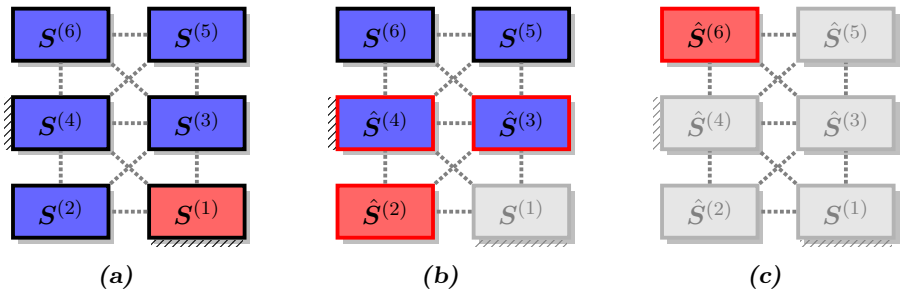

Figure 4.6: *Frontal approach on a substructure level. The red box indicates the* front*, blue boxes are uncondensed substructures and a red border indicates that a neighboring structure (or multiple substructures) has been condensed on the interface. A grey box denotes a condensed substructure.* ***(a)*** *Substructure 1 is the active front and has to be condensed onto substructures 2, 3 and 4.* ***(b)*** *Substructure 1 is eliminated, thereby moving the front to substructure 2, which has to be condensed onto substructures 3 and 4.* ***(c)*** *After a number of condensation steps, the front arrives at substructure 6, thereby allowing to solve the global problem in subdomain 6.*

A similar approach is used in the so called *frontal solvers*, first introduced by Irons [84]. Here, large finite element models are solved by assembling only a small subset of elements at a time and eliminates the equations by means of a Gauss elimination. This subset of elements is then referred to as the *front* and serves as a transition region between the set of elements already condensed (i.e. eliminated) and those still unaffected. The approach taken in sections 4.2.1 and

4.2.2 can be considered as a frontal solver, which involves only two subsets. Hence, the concept of a frontal solver is used here to extend the approach to multiple substructures.

This idea is visualized in figure 4.6. Here, the different substructures (or subdomains) and their interconnections are shown. In this frontal approach one thus condenses in a number of steps all the different substructures onto the last one. This last subdomain thus contains all the effects of the neighboring subsystems (in terms of mass, damping, stiffness and loading). By solving the response in this substructure one thus finds the coupled response. By stepping from substructure to substructure in the reversed order, the obtained results can be used in all the different subdomains to find the local coupled response.

4.3 Initialization of the sequential multi-domain time integration scheme

The two most common approaches for initializing time stepping schemes are presented for the sequential method in this section. The first approach, discussed in section 4.3.1, is to compute the initial accelerations, using either a given set of initial conditions or simply for a partitioned system that is initially at rest. The second approach, given in section 4.3.2, is to use the forces at t_0 to compute an initial static equilibrium from which the time stepping will proceed.

4.3.1 Starting from initial accelerations

The accelerations at the first time step at t_0 for a decomposed system can simply be found by substituting the initial force $\boldsymbol{f}_0^{(s)}$ and initial conditions $\dot{\boldsymbol{u}}_0^{(s)}, \boldsymbol{u}_0^{(s)}$ into Eq. (3.20).[2] In case one uses the partitioned time scheme presented in the previous section, the coupled problem one has to solve at the initial time step becomes:

$$\begin{bmatrix} \boldsymbol{M}^{(A)} & \boldsymbol{0} & \boldsymbol{B}^{(A)^T} \\ \boldsymbol{0} & \boldsymbol{M}^{(B)} & \boldsymbol{B}^{(B)^T} \\ \boldsymbol{B}^{(A)} & \boldsymbol{B}^{(B)} & \boldsymbol{0} \end{bmatrix} \begin{bmatrix} \ddot{\boldsymbol{u}}_0^{(A)} \\ \ddot{\boldsymbol{u}}_0^{(B)} \\ \boldsymbol{\lambda}_0 \end{bmatrix} = \begin{bmatrix} \boldsymbol{f}_0^{(A)} - \boldsymbol{p}_0^{(A)} \\ \boldsymbol{f}_0^{(B)} - \boldsymbol{p}_0^{(B)} \\ \boldsymbol{0} \end{bmatrix}, \tag{4.15}$$

where, the nonlinear force term $\boldsymbol{p}^{(s)}(\dot{\boldsymbol{u}}_0^{(s)}, \boldsymbol{u}_0^{(s)})$ can now be regarded as a constant force, since the initial conditions are given. Note that, as the accelerations need to be compatible, the compatibility condition is enforced using the accelerations here. For solving Eq. (4.15) the same approach is used as in the sequential partitioned time integration scheme. Thus one first solves for the "uncoupled" response of system B ($\ddot{\hat{\boldsymbol{u}}}_0^{(B)}$), which is found from the following:

$$\ddot{\boldsymbol{u}}_0^{(B)} = \boldsymbol{M}^{(B)^{-1}} \left(\boldsymbol{f}_0^{(B)} - \boldsymbol{p}_0^{(B)} - \boldsymbol{B}^{(B)^T} \boldsymbol{\lambda}_0 \right) = \ddot{\hat{\boldsymbol{u}}}_0^{(B)} - \boldsymbol{M}^{(B)^{-1}} \boldsymbol{B}^{(B)^T} \boldsymbol{\lambda}_0. \tag{4.16}$$

Now the forcing effect of substructure B onto substructure A is computed:

$$\hat{\boldsymbol{\lambda}}_0 = \left(\boldsymbol{B}^{(B)} \boldsymbol{M}^{(B)^{-1}} \boldsymbol{B}^{(B)^T} \right)^{-1} \begin{bmatrix} \boldsymbol{B}^{(A)} & \boldsymbol{B}^{(B)} \end{bmatrix} \begin{bmatrix} \boldsymbol{0} \\ \ddot{\hat{\boldsymbol{u}}}_0^{(B)} \end{bmatrix}. \tag{4.17}$$

Note again, that this force can be interpreted as a constraint force (or blocked force) and is therefore the force that is needed to set $\ddot{\hat{\boldsymbol{u}}}_0^{(B)}$ equal to zero. This force contains the forcing effect of substructure B on substructure A, as was already discussed in section 4.2.1. Hence,

[2] Obviously, the compatibility condition also applies to the initial conditions given, such that $\boldsymbol{B}\dot{\boldsymbol{u}}_0 = \boldsymbol{0}$ and $\boldsymbol{B}\boldsymbol{u}_0 = \boldsymbol{0}$.

by both condensing the added mass effects and added force effects (as given in Eq. (4.17)) onto the interface of substructure A, the initial accelerations for this substructure are determined:

$$\ddot{\boldsymbol{u}}_0^{(A)} = \left(\boldsymbol{M}^{(A)} + \boldsymbol{B}^{(A)^T} \left(\boldsymbol{B}^{(B)} \boldsymbol{M}^{(B)^{-1}} \boldsymbol{B}^{(B)^T} \right)^{-1} \boldsymbol{B}^{(A)} \right)^{-1} \left(\boldsymbol{f}_0^{(A)} - \boldsymbol{p}_0^{(A)} + \boldsymbol{B}^{(A)^T} \hat{\boldsymbol{\lambda}}_0 \right). \quad (4.18)$$

As the compatibility condition between the substructures should be satisfied, one can compute the interface forces needed to enforce this condition from:

$$\boldsymbol{\lambda}_0 = \left(\boldsymbol{B}^{(B)} \boldsymbol{M}^{(B)^{-1}} \boldsymbol{B}^{(B)^T} \right)^{-1} \left[\begin{array}{cc} \boldsymbol{B}^{(A)} & \boldsymbol{B}^{(B)} \end{array} \right] \left[\begin{array}{c} \ddot{\boldsymbol{u}}_0^{(A)} \\ \ddot{\boldsymbol{u}}_0^{(B)} \end{array} \right]. \quad (4.19)$$

Substituting these into Eq. (4.16) allows one to determine the initial accelerations for substructure B.

4.3.2 Computing the initial quasi-static equilibrium

One often wants to limit the high accelerations that arise from starting the time integration from a set of initial accelerations, as was given in section 4.3. An option to minimize the transient effects related to this, is to start the simulations from an initial quasi-static equilibrium. For the initial time step, the static equivalent of Eq. (4.2) needs to solved;

$$\left\{ \begin{array}{l} \boldsymbol{r}_0^{(A)} = \boldsymbol{p}_0^{(A)} + \boldsymbol{B}^{(A)^T} \boldsymbol{\lambda}_0 - \boldsymbol{f}_0^{(A)} \\ \boldsymbol{r}_0^{(B)} = \boldsymbol{p}_0^{(B)} + \boldsymbol{B}^{(B)^T} \boldsymbol{\lambda}_0 - \boldsymbol{f}_0^{(B)} \\ \boldsymbol{B}\boldsymbol{u}_0 = \boldsymbol{0} \end{array} \right. . \quad (4.20)$$

As the nonlinear forces, $\boldsymbol{p}_0^{(s)}$, are still a function of the (unknown) initial displacements, $\boldsymbol{u}_0^{(s)}$, the coupled set of static equations is to be solved using the Newton-Raphson scheme to find corrections on the initial estimates, such that:

$$\begin{array}{l} \boldsymbol{u}_0^{(s)} \leftarrow \boldsymbol{u}_0^{(s)} + \Delta \boldsymbol{u}_0^{(s)}, \\ \boldsymbol{\lambda}_0 \leftarrow \boldsymbol{\lambda}_0 + \Delta \boldsymbol{\lambda}_0. \end{array} \quad (4.21)$$

Hence, the corrections are found from solving the static equivalent of Eq. (4.6) in each iteration step:

$$\left[\begin{array}{ccc} \boldsymbol{K}_t^{(A)} & \boldsymbol{0} & \boldsymbol{B}^{(A)^T} \\ \boldsymbol{0} & \boldsymbol{K}_t^{(B)} & \boldsymbol{B}^{(B)^T} \\ \boldsymbol{B}^{(A)} & \boldsymbol{B}^{(B)} & \boldsymbol{0} \end{array} \right] \left[\begin{array}{c} \Delta \boldsymbol{u}_0^{(A)} \\ \Delta \boldsymbol{u}_0^{(B)} \\ \Delta \boldsymbol{\lambda}_0 \end{array} \right] = \left[\begin{array}{c} -\boldsymbol{r}_0^{(A)} \\ -\boldsymbol{r}_0^{(B)} \\ \boldsymbol{0} \end{array} \right]. \quad (4.22)$$

The tangent stiffness matrices $\boldsymbol{K}_t^{(s)}$ are given in Eq. (4.7). Solving this will be straightforward in the case that all the substructures have sufficient boundary conditions to constrain the rigid body motion, as one could simply follow the steps given in section 4.2.1. Here however, it is assumed that the assembled structure is adequately constrained, but that some of the substructures can have rigid body modes. This is a problem commonly encountered in *Finite Element Tearing and Interconnecting* (FETI) methods as well [53,134]. In that case the solution for substructure B would write

$$\Delta \boldsymbol{u}_0^{(B)} = \boldsymbol{K}_t^{(B)^+} \left(-\boldsymbol{r}_0^{(B)} - \boldsymbol{B}^{(B)^T} \Delta \boldsymbol{\lambda}_0 \right) - \boldsymbol{R}^{(B)} \Delta \boldsymbol{\alpha}_0^{(B)}, \quad (4.23)$$

where $\boldsymbol{K}_t^{(B)^+}$ is the generalized inverse of $\boldsymbol{K}_t^{(B)}$ and $\boldsymbol{R}^{(B)}$ are the rigid body modes that span the null space of $\boldsymbol{K}_t^{(B)}$.[3] Hence, the response of the subsystem is a combination of flexible

[3] For a detailed explanation on the generalized inverse, the reader is referred to [52].

deformations and rigid displacements. The amplitudes of the rigid body modes, $\Delta\boldsymbol{\alpha}_0^{(B)}$, are found from the fact that the external forces and interface forces must be self-equilibrated:

$$\boldsymbol{R}^{(B)^T}\left(\boldsymbol{f}_0^{(B)} - \boldsymbol{B}^{(B)^T}\boldsymbol{\lambda}_0\right) = \boldsymbol{0}. \tag{4.24}$$

Therefore, any update on the interface forces should comply with this condition. Hence, substituting Eq. (4.23) into the compatibility equation of Eq. (4.22) and taking into account Eq. (4.24) leads to the set of equations to solve for obtaining the interface forces and rigid body amplitudes, assuming the displacements $\Delta\boldsymbol{u}_0^{(A)}$ are known, such that:

$$\begin{bmatrix} \boldsymbol{F}_I^{(B)} & \boldsymbol{R}_{[b]}^{(B)} \\ \boldsymbol{R}_{[b]}^{(B)^T} & \boldsymbol{0} \end{bmatrix} \begin{bmatrix} \Delta\boldsymbol{\lambda}_0 \\ \Delta\boldsymbol{\alpha}_0^{(B)} \end{bmatrix} = \begin{bmatrix} -\boldsymbol{B}^{(B)}\boldsymbol{K}_t^{(B)^+}\boldsymbol{r}_0^{(B)} + \boldsymbol{B}^{(A)}\Delta\boldsymbol{u}_0^{(A)} \\ \boldsymbol{R}^{(B)^T}\left(\boldsymbol{f}_0^{(B)} - \boldsymbol{B}^{(B)^T}\boldsymbol{\lambda}_0\right) \end{bmatrix}, \tag{4.25}$$

where

$$\boldsymbol{R}_{[b]}^{(B)} = \boldsymbol{B}^{(B)}\boldsymbol{R}^{(B)}, \quad \boldsymbol{F}_I^{(B)} = \boldsymbol{B}^{(B)}\boldsymbol{K}_t^{(B)^+}\boldsymbol{B}^{(B)^T}. \tag{4.26}$$

Obviously, the residual of subsystem A is also a function of the displacements and the interface forces:

$$\boldsymbol{r}^{(A)}\left(\boldsymbol{u}_0^{(A)}, \boldsymbol{\lambda}_0\right) = \boldsymbol{p}^{(A)}(\boldsymbol{u}_0^{(A)}) + \boldsymbol{B}^{(A)^T}\boldsymbol{\lambda}_0 - \boldsymbol{f}_0^{(A)}. \tag{4.27}$$

Hence a relationship expressing the interface forces as a function of the displacements has to be obtained, thereby effectively condensing the linearized subsystem B into the residual of subsystem A. Therefore, an orthogonal projector,

$$\boldsymbol{P}^{(B)} = \boldsymbol{I} - \boldsymbol{R}_{[b]}^{(B)}\left(\boldsymbol{R}_{[b]}^{(B)^T}\boldsymbol{R}_{[b]}^{(B)}\right)^{-1}\boldsymbol{R}_{[b]}^{(B)^T}, \tag{4.28}$$

is defined to eliminate $\Delta\boldsymbol{\alpha}_0$ from equation Eq. (4.25) and used to divide the interface forces into a part that is in the space of the rigid body modes and a part that is in the space of the tangential stiffness matrix:

$$\Delta\boldsymbol{\lambda}_0 = \boldsymbol{P}^{(B)}\Delta\bar{\boldsymbol{\lambda}}_0 + \Delta\check{\boldsymbol{\lambda}}_0. \tag{4.29}$$

Substituting Eq. (4.29) into Eq. (4.25) and introducing the orthogonal projector gives:

$$\begin{cases} \Delta\check{\boldsymbol{\lambda}}_0 = \boldsymbol{R}_{[b]}^{(B)}\left(\boldsymbol{R}_{[b]}^{(B)^T}\boldsymbol{R}_{[b]}^{(B)}\right)^{-1}\boldsymbol{R}^{(B)^T}\left(\boldsymbol{f}_0^{(B)} - \boldsymbol{B}^{(B)^T}\boldsymbol{\lambda}_0\right) \\ \Delta\bar{\boldsymbol{\lambda}}_0 = \left(\boldsymbol{P}^{(B)^T}\boldsymbol{F}_I^{(B)}\boldsymbol{P}^{(B)}\right)^+\boldsymbol{P}^{(B)^T}\left(-\boldsymbol{B}^{(B)}\boldsymbol{K}_t^{(B)^+}\boldsymbol{r}_0^{(B)} + \boldsymbol{B}^{(A)}\Delta\boldsymbol{u}_0^{(A)}\right. \\ \qquad\qquad\qquad\qquad\qquad\qquad\left. -\boldsymbol{B}^{(B)}\boldsymbol{K}_t^{(B)^+}\boldsymbol{B}^{(B)^T}\Delta\check{\boldsymbol{\lambda}}_0\right) \end{cases} \tag{4.30}$$

By substituting Eqs. (4.29) and (4.30) into Eq. (4.27), the residual is no longer explicitly dependent on the interface forces ($\boldsymbol{\lambda}_0$). Hence, one needs to solve:

$$\check{\boldsymbol{K}}_t^{(A)}\Delta\boldsymbol{u}_0^{(A)} = -\boldsymbol{r}_0^{(A)} - \boldsymbol{B}^{(A)^T}\Delta\hat{\boldsymbol{\lambda}}_0, \tag{4.31}$$

where the last term on the right hand side in Eq. (4.31) can again be interpreted as the forcing effect of substructure B onto substructure A, such that:

$$\Delta\hat{\boldsymbol{\lambda}}_0 = \left(\boldsymbol{P}^{(B)^T}\boldsymbol{F}_I^{(B)}\boldsymbol{P}^{(B)}\right)^+\boldsymbol{P}^{(B)^T}\left(-\boldsymbol{B}^{(B)}\boldsymbol{K}_t^{(B)^+}\boldsymbol{r}_0^{(B)} - \boldsymbol{B}^{(B)}\boldsymbol{K}_t^{(B)^+}\boldsymbol{B}^{(B)^T}\Delta\check{\boldsymbol{\lambda}}_0\right)$$

and $\check{\boldsymbol{K}}_t^{(A)}$ is the iteration (or Jacobian) matrix. The iteration matrix $\check{\boldsymbol{K}}_t^{(A)}$ is obtained for the static case by computing the derivative of the residual with respect to the displacements, taking into account the stiffness felt from the neighboring substructure:

$$\check{\boldsymbol{K}}_t^{(A)} = \boldsymbol{K}_t^{(A)} + \boldsymbol{B}^{(A)^T} \boldsymbol{P}^{(B)} \left(\boldsymbol{P}^{(B)^T} \boldsymbol{F}_I^{(B)} \boldsymbol{P}^{(B)} \right)^+ \boldsymbol{P}^{(B)^T} \boldsymbol{B}^{(A)}. \tag{4.32}$$

Note that the derivation was started with the assumption that the total system does not have any rigid body modes, but that the individual subsystems can. Therefore, by condensing substructures onto each other, the tangential stiffness matrix, $\check{\boldsymbol{K}}_t^{(A)}$, is nonsingular. As the update on subsystem A is computed now, the result can be substituted in Eq. (4.30) to obtain the update on the Lagrange multipliers. This is needed in turn to determine the rigid body displacements of substructure B, using Eq. (4.25), and finally obtaining the update of its total displacement field using Eq. (4.23). By now updating the states of the subsystems and the Lagrange multipliers using Eq. (4.21), one is able to update residuals in Eq. (4.20) and continue this process until all components have converged.

As is seen, the quasi-static initialization process is similar to the time stepping scheme proposed in section 4.2.1, where a number of additional steps are required in order to handle singular tangential stiffness matrices.

4.4 A parallel scheme for monolithic multi-domain time integration

The sequential scheme that was presented in section 4.2, has some advantages, but also has a number of disadvantages. One of the biggest disadvantages is that the approach is not so straightforward to extend to multiple substructures and in addition the method, due to its sequential nature, can not easily be made parallel. The method presented in this section is by construction a parallel method and can also be easily extended to multiple substructures. As the proposed time integration scheme can be interpreted as a further development of the *Finite Element Tearing and Interconnecting* (FETI) method [53], the FETI method is first briefly outlined in section 4.4.1. Finally, in section 4.4.2 the parallel time integration scheme is presented. This approach is based on the idea of solving the nonlinearities on a local level, by iterating on the substructure level, instead of the global system level.

4.4.1 Finite Element Tearing and Interconnecting

The derivation of the FETI method starts again from the dual assembled equations of motion in the residual form, that are given in Eq. (4.1). In order to solve these, the Newton-Raphson scheme is used again, such that at each iteration one has to solve:

$$\begin{bmatrix} \boldsymbol{S} & \boldsymbol{B}^T \\ \boldsymbol{B} & \boldsymbol{0} \end{bmatrix} \begin{bmatrix} \Delta \boldsymbol{u}_n \\ (1-\alpha_f)\Delta \boldsymbol{\lambda}_n \end{bmatrix} = \begin{bmatrix} -\boldsymbol{r}_n \\ \boldsymbol{0} \end{bmatrix}, \tag{4.33}$$

which is, in the case of two substructures, exactly the same as Eq. (4.6). Here however, a different approach is taken, as the first line of Eq. (4.33) is substituted in the compatibility equation given in the last line and rewritten to directly obtain the update on the Lagrange multipliers,

$$(1-\alpha_f)\Delta \boldsymbol{\lambda}_n = -\left(\boldsymbol{B}\boldsymbol{S}^{-1}\boldsymbol{B}^T \right)^{-1} \boldsymbol{B}\boldsymbol{S}^{-1}\boldsymbol{r}_n, \tag{4.34}$$

such that the global interface problem is solved. By more closely examining Eq. (4.34) and recalling the fact that $\boldsymbol{S}$ is a per-substructure block diagonal matrix, one can recognize in the last term the response of the structure if it is unaware of its neighbors:

$$\Delta\hat{\boldsymbol{u}}_n^{(s)} = \boldsymbol{S}^{(s)^{-1}}\boldsymbol{r}_n^{(s)}. \tag{4.35}$$

By solving each of the local domains independently on its "own" CPU core, the method can very efficiently by implemented in a parallel computer environment. Such that Eq. (4.34) can aso be rewritten according to[4]:

$$(1-\alpha_f)\Delta\boldsymbol{\lambda}_n = -\left(\boldsymbol{B}\boldsymbol{S}^{-1}\boldsymbol{B}^T\right)^{-1}\boldsymbol{B}\Delta\hat{\boldsymbol{u}}_n. \tag{4.36}$$

By substituting the result from Eq. (4.34) into the first line of Eq. (4.33), one can solve for the local domains:

$$\Delta\boldsymbol{u}_n^{(s)} = -\boldsymbol{S}^{(s)^{-1}}\left(\boldsymbol{r}_n^{(s)} + (1-\alpha_f)\boldsymbol{B}^{(s)^T}\Delta\boldsymbol{\lambda}_n\right) = \Delta\hat{\boldsymbol{u}}_n^{(s)} - (1-\alpha_f)\boldsymbol{S}^{(s)^{-1}}\boldsymbol{B}^{(s)^T}\Delta\boldsymbol{\lambda}_n. \tag{4.37}$$

After which the state of the system is updated again using Eq. (4.3). Note that the scheme here, starts with a *tearing* step, given in Eq. (4.35), where one solves to local problems without considering the compatibility condition. As a direct result of this, the interfaces will no longer be compatible and gaps between the substructures could occur. In Eq. (4.36) the interface forces that are needed for enforcing this compatibility are computed. Finally, in the *interconnecting* step, these forces are applied for closing the interface gaps. These three steps, given in Eqs. (4.35), (4.36) and Eq. (4.37) constitute the FETI method and are also shown in figure 4.7.

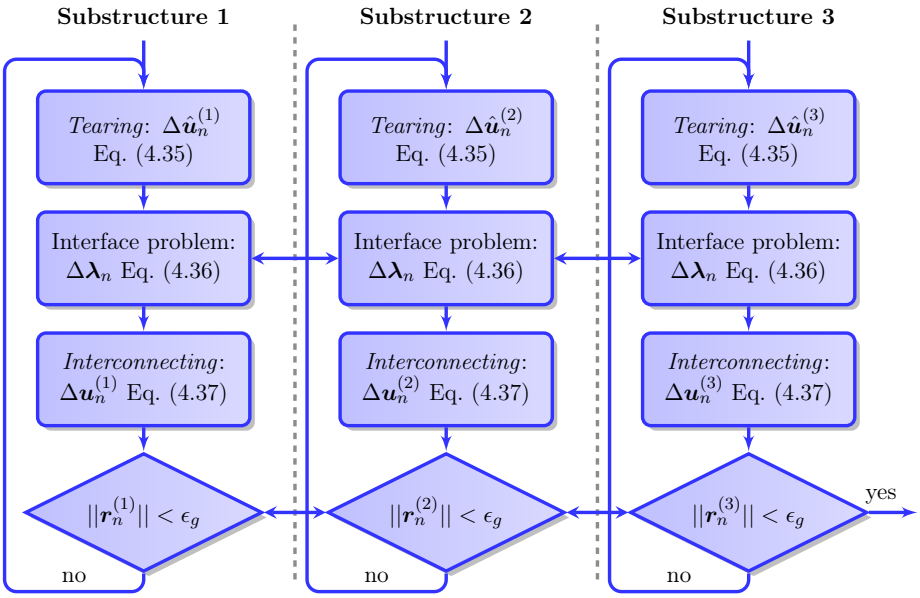

Figure 4.7: *Systematic overview of the FETI method.*

From figure 4.7 it can be seen that the iterations are performed on a global level. Therefore, all the different subdomains have to perform the same amount of iterations, which could reduce the efficiency of the method if all the (strong) nonlinearities are within a single substructure. In this case the strong nonlinear substructure dictates the number of iterations that all the weakly nonlinear or linear substructures need to perform as well.

[4]Note that in a parallel implementation of FETI, the interface problem given in Eq. (4.36) is not solved using a factorization, but rather using an iterative solver like the Preconditioned Conjugate Gradient.

4.4.2 A monolithic parallel multi-domain time integration method

The method presented here modifies the FETI procedure in a similar manner as was proposed in [27, 120]. In this method one handles the nonlinearities on the local domains, where the Lagrange multipliers are considered as external forces in the local domain, rather than internal forces that enforce compatibility. In order to attain such a procedure, iterations on two levels are introduced. Firstly, iterations are performed on the global level, that take into account the compatibility condition that needs to be fulfilled. Secondly, an iteration loop on the substructure level is introduced, where the interface forces are regarded as given external forces. Similar approaches, that are often referred to as semi-explicit, usually perform only one iteration at the global level, as is also recently presented in [150].

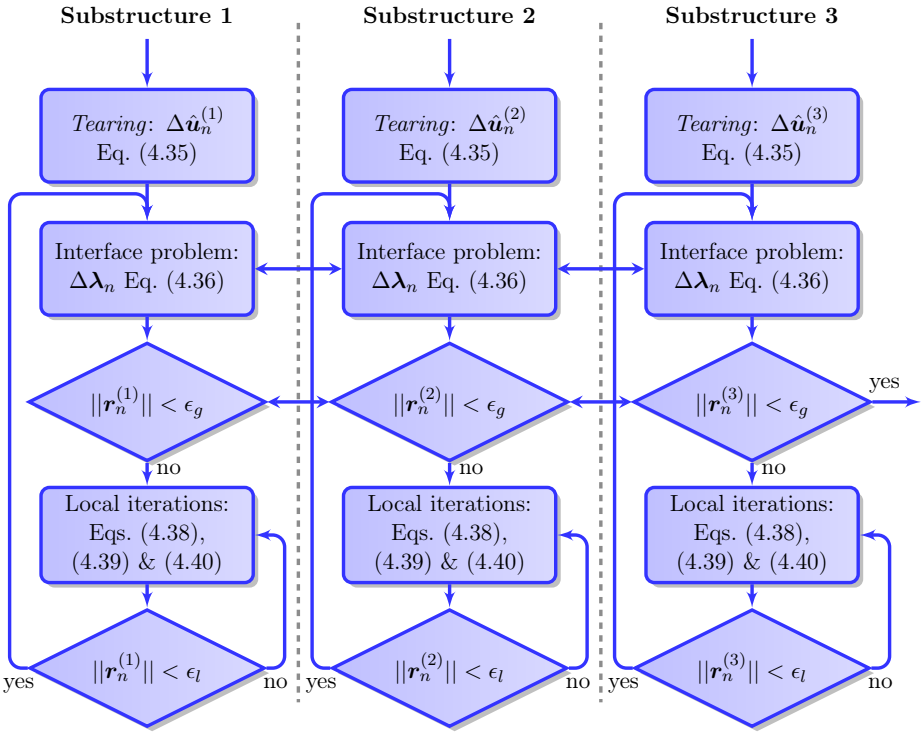

Figure 4.8: *Systematic overview of the parallel monolithic multi-domain time integration method.*

Hence, the procedure, which is illustrated in figure 4.8, is started again by first performing the *tearing* step given in Eq. (4.35). Using these results the update on the Lagrange multipliers is computed using Eq. (4.36) and update the Lagrange multipliers, such that $\boldsymbol{\lambda}_n = \boldsymbol{\lambda}_n + \Delta\boldsymbol{\lambda}_n$. This results in now substituted in the local problems, such that one wants to solve the following:

$$\begin{aligned}\boldsymbol{r}_n^{(s)} = (1-\alpha_m)\boldsymbol{M}^{(s)}\ddot{\boldsymbol{u}}_n^{(s)} + \alpha_m\boldsymbol{M}^{(s)}\ddot{\boldsymbol{u}}_{n-1}^{(s)} + (1-\alpha_f)\left(\boldsymbol{p}_n^{(s)} + \boldsymbol{B}^{(s)^T}\boldsymbol{\lambda}_n - \boldsymbol{f}_n^{(s)}\right) \\ +\alpha_f\left(\boldsymbol{p}_{n-1}^{(s)} + \boldsymbol{B}^{(s)^T}\boldsymbol{\lambda}_{n-1} - \boldsymbol{f}_{n-1}^{(s)}\right).\end{aligned} \tag{4.38}$$

Note that the Lagrange multipliers are now considered as *given* external forces applied to the interface. The substructure increments $\Delta\boldsymbol{u}_n^{(s)}$ are now computed by performing a Newton-Raphson iteration on the local substructure level:

$$\Delta\boldsymbol{u}_n^{(s)} = -\boldsymbol{S}^{(s)^{-1}}\boldsymbol{r}_n^{(s)}. \tag{4.39}$$

Now the state of the individual substructures is updated using Eq. (4.40):

$$\begin{aligned} \boldsymbol{u}_n^{(s)} &\leftarrow \boldsymbol{u}_n^{(s)} + \Delta\boldsymbol{u}_n^{(s)}, \\ \dot{\boldsymbol{u}}_n^{(s)} &\leftarrow \dot{\boldsymbol{u}}_n^{(s)} + \frac{\gamma}{\beta h}\Delta\boldsymbol{u}_n^{(s)}, \\ \ddot{\boldsymbol{u}}_n^{(s)} &\leftarrow \ddot{\boldsymbol{u}}_n^{(s)} + \frac{1}{\beta h^2}\Delta\boldsymbol{u}_n^{(s)}. \end{aligned} \tag{4.40}$$

This in turn allows to find the new residual, by substituting the new state in Eq. (4.38). This local iteration process is continued individually for each substructure until it has reached a certain local force-normalized convergence criterion (ϵ_l). In this section it is chosen to write the equations explicitly per substructure, as one component could require more iterations then the others. Therefore, different substructures will require a different number of iterations per substructure. In fact, if one of the substructures is linear, it will have converged in a single iteration. In this process, the effect of the neighboring substructures is obviously only taken into account by means of the given Lagrange multipliers, so one has to perform an *interconnect* step again in order to enforce compatibility. Therefore, as soon as all of the local iterations have converged, the results are used to correct the Lagrange multipliers using Eq. (4.36). In a next step, the Lagrange multipliers are used to update the local residuals in Eq. (4.38). This process is continued until the local residuals are all smaller than certain global force-normalized convergence criterion (ϵ_g).

An essential extra parameter introduced in this scheme is the local (force normalized) convergence criterion (ϵ_l). Obviously, if one sets an extremely high value for ϵ_l, only one local iteration will be performed and one actually ends up with the FETI scheme outlined in section 4.4.1. On the other hand, setting an extreme strict tolerance setting can results in an unnecessary amount of local iterations, thereby limiting the efficiency again. A simple test study, given in Appendix B, has been carried out using this approach.

4.5 Initializing the parallel monolithic multi-domain time integration

In this section the two most common methods for initializing the time integration scheme of section 4.4 are presented. Similar to the outline of section 4.3, the approach of initial accelerations is given in section 4.5.1 and starting the time integration from an initial quasi-static equilibrium is presented in section 4.5.2.

4.5.1 Starting time stepping using the initial accelerations

The simplest approach would be to start the time integration from initial accelerations, as one then only needs to solve the following dual assembled linear problem:

$$\begin{bmatrix} \boldsymbol{M} & \boldsymbol{B}^T \\ \boldsymbol{B} & \boldsymbol{0} \end{bmatrix} \begin{bmatrix} \ddot{\boldsymbol{u}}_0 \\ \boldsymbol{\lambda}_0 \end{bmatrix} = \begin{bmatrix} \boldsymbol{f}_0 - \boldsymbol{p}_0 \\ \boldsymbol{0} \end{bmatrix}. \tag{4.41}$$

By substituting the initial conditions $(\dot{\boldsymbol{u}}_0, \boldsymbol{u}_0)$ Eq. (4.41), the nonlinear force $\boldsymbol{p}(\dot{\boldsymbol{u}}_0, \boldsymbol{u}_0)$, simply becomes a constant force. Therefore, one can determine the initial accelerations and Lagrange multipliers from applying only one FETI-like step in order to solve Eq. (4.41). Firstly, the initial accelerations found from the uncoupled problem are computed,

$$\ddot{\boldsymbol{u}}_0 = \boldsymbol{M}^{-1}(\boldsymbol{f}_0 - \boldsymbol{p}_0), \tag{4.42}$$

which are substituted in the interface problem in order to determine the Lagrange multipliers as a second step:

$$\boldsymbol{\lambda}_0 = \left(\boldsymbol{B}\boldsymbol{M}^{-1}\boldsymbol{B}^T\right)^{-1}\boldsymbol{B}\ddot{\hat{\boldsymbol{u}}}_0. \tag{4.43}$$

Finally, substituting the Lagrange multipliers, found into the first line of Eq. (4.41), allows to find the initial accelerations from the following:

$$\ddot{\boldsymbol{u}}_0 = \boldsymbol{M}^{-1}\left(\boldsymbol{f}_0 - \boldsymbol{p}_0 - \boldsymbol{B}^T\boldsymbol{\lambda}_0\right) = \ddot{\hat{\boldsymbol{u}}}_0 - \boldsymbol{M}^{-1}\boldsymbol{B}^T\boldsymbol{\lambda}_0. \tag{4.44}$$

Even though the initialization step presented here is relatively cheap and simple to compute, it does induce high accelerations and transient effects at the start of the simulations, which is generally not desirable. In addition it requires factorizing the substructure mass matrices ($\boldsymbol{M}^{(s)}$), which is not needed for the rest of the simulation.

4.5.2 Starting the time integration from an initial quasi-static equilibrium

The second initialization approach presented is to start the simulations from an initial quasi-static equilibrium. This requires one to solve the following initial problem, found from enforcing $\ddot{\boldsymbol{u}}_0 = \dot{\boldsymbol{u}}_0 = \boldsymbol{0}$:

$$\begin{cases} \boldsymbol{r}_0 = \boldsymbol{p}_0 + \boldsymbol{B}^T\boldsymbol{\lambda}_0 - \boldsymbol{f}_0 \\ \boldsymbol{B}\boldsymbol{u}_0 = \boldsymbol{0} \end{cases}, \tag{4.45}$$

where, $\boldsymbol{p}_0 = \boldsymbol{p}(\boldsymbol{u}_0)$ is the nonlinear force that is a function of the initial displacements. Therefore, this approach, unlike the one given in section 4.5.1, requires one to solve a static set of nonlinear equations. Hence, the strategy that is applied for solving the dynamic equations of motion in section 4.4.2 is also used here in order to solve the initial static problem. By linearizing around the initial set of displacement a first update on the displacements can be computed:

$$\begin{bmatrix} \boldsymbol{K}_t & \boldsymbol{B}^T \\ \boldsymbol{B} & \boldsymbol{0} \end{bmatrix}\begin{bmatrix} \Delta\boldsymbol{u}_0 \\ \Delta\boldsymbol{\lambda}_0 \end{bmatrix} = \begin{bmatrix} -\boldsymbol{r}_0 \\ \boldsymbol{0} \end{bmatrix}. \tag{4.46}$$

It is again assumed here that the total structure has sufficient boundary conditions that constrain all rigid body motion, but that this is not necessarily the case for the individual substructures. Therefore, the update per substructure yields

$$\Delta\boldsymbol{u}_0^{(s)} = \boldsymbol{K}_t^{(s)^+}\left(-\boldsymbol{r}_0^{(s)} - \boldsymbol{B}^{(s)^T}\Delta\boldsymbol{\lambda}_0\right) - \boldsymbol{R}^{(s)}\Delta\boldsymbol{\alpha}_0^{(s)}, \tag{4.47}$$

which is a combination of flexible deformations induced by the external and interface forces and a contribution due to the rigid body displacements and rotations. The amplitudes of the rigid body modes, $\Delta\boldsymbol{\alpha}_0^{(s)}$, are found from the fact that the external forces and interface forces must be self-equilibrated:

$$\boldsymbol{R}^{(s)^T}\left(\boldsymbol{f}_0^{(s)} - \boldsymbol{B}^{(s)^T}\boldsymbol{\lambda}_0\right) = \boldsymbol{0}. \tag{4.48}$$

Therefore, any update on the interface forces should comply to this condition. Hence, substituting Eq. (4.47) into the compatibility equation of Eq. (4.46) and taking into account Eq. (4.48) leads to the set of equations to solve for obtaining the interface forces and rigid body amplitudes;

$$\begin{bmatrix} \boldsymbol{F}_I & \boldsymbol{R}_{[b]} \\ \boldsymbol{R}_{[b]}^T & \boldsymbol{0} \end{bmatrix}\begin{bmatrix} \Delta\boldsymbol{\lambda}_0 \\ \Delta\boldsymbol{\alpha}_0 \end{bmatrix} = \begin{bmatrix} -\boldsymbol{B}\boldsymbol{K}_t^+\boldsymbol{r}_0 \\ \boldsymbol{R}^T\left(\boldsymbol{f}_0 - \boldsymbol{B}^T\boldsymbol{\lambda}_0\right) \end{bmatrix}, \tag{4.49}$$

where

$$\boldsymbol{R}_{[b]} = \boldsymbol{B}\boldsymbol{R}, \quad \boldsymbol{F}_I = \boldsymbol{B}\boldsymbol{K}_t^+\boldsymbol{B}^T. \tag{4.50}$$

Using the obtained updates from Eq. (4.49), the set of interface forces and rigid body amplitudes is updated:

$$\begin{cases} \boldsymbol{\lambda}_0 \leftarrow \boldsymbol{\lambda}_0 + \Delta\boldsymbol{\lambda}_0, \\ \boldsymbol{\alpha}_0 \leftarrow \boldsymbol{\alpha}_0 + \Delta\boldsymbol{\alpha}_0. \end{cases} \tag{4.51}$$

The interface forces are now regarded as a set of given external forces, such the nonlinearities are solved at the local level. The local substructure residuals are computed,

$$\boldsymbol{r}_0^{(s)} = \boldsymbol{p}_0^{(s)} + \boldsymbol{B}^{(s)^T}\boldsymbol{\lambda}_0 - \boldsymbol{f}_0^{(s)}, \tag{4.52}$$

and are solved for on the substructure level. Note that the external and interface forces are self-equilibrated and that the (internal) nonlinear force is also not dependent on the rigid body displacements of the substructure. Therefore, one can solve for the local flexible response of the individual substructures ($\boldsymbol{u}_{0,flex}$) by means of local Newton-Raphson iterations, up to a certain force normalized criterion ϵ_l. The total response is then found by adding the rigid body displacements:

$$\boldsymbol{u}_0^{(s)} = \boldsymbol{u}_{0,flex}^{(s)} - \boldsymbol{R}^{(s)}\boldsymbol{\alpha}_0^{(s)}. \tag{4.53}$$

As the local displacement fields are not per definition compatible, the global interface problem is solved, using the local displacement fields from Eq. (4.53), in order to update the Lagrange multipliers and rigid body amplitudes:

$$\begin{bmatrix} \boldsymbol{F}_I & \boldsymbol{R}_{[b]} \\ \boldsymbol{R}_{[b]}^T & \boldsymbol{0} \end{bmatrix} \begin{bmatrix} \Delta\boldsymbol{\lambda}_0 \\ \Delta\boldsymbol{\alpha}_0 \end{bmatrix} = \begin{bmatrix} \boldsymbol{u}_0 \\ \boldsymbol{0} \end{bmatrix}. \tag{4.54}$$

This result is substituted in Eq. (4.51) to update the Lagrange multipliers and rigid body amplitudes. This process is continued until the residuals have become smaller than the global force normalized convergence criterion ϵ_g. Note that this process, that avoids most of the startup transient effects, involves solving a nonlinear static problem, which is more expensive from a computational point-of-view than computing the initial accelerations.

4.6 Remarks on the use of Lagrange multipliers in time integration

In this section the choice of applying the generalized-α averaging onto the Lagrange multipliers is discussed in section 4.6.1. In addition, in section 4.6.2, some remarks are made on the stability of the Lagrange multipliers in monolithic partitioned time integration methods presented in the chapter.

4.6.1 Averaging of the interface force in the generalized-α scheme

Note that as the Lagrange multipliers can be interpreted as instantaneous (interface) forces that enforce the imposed compatibility conditions, Eq. (4.1) could also have been written as:

$$\begin{cases} \boldsymbol{r}_n = (1-\alpha_m)\boldsymbol{M}\ddot{\boldsymbol{u}}_n + \alpha_m\boldsymbol{M}\ddot{\boldsymbol{u}}_{n-1} + (1-\alpha_f)\left(\boldsymbol{p}_n - \boldsymbol{f}_n\right) \\ \qquad\qquad\qquad\qquad\qquad\qquad +\alpha_f\left(\boldsymbol{p}_{n-1} - \boldsymbol{f}_{n-1}\right) + \boldsymbol{B}^T\boldsymbol{\lambda}_{\alpha_f} \quad , \\ \boldsymbol{B}\boldsymbol{u}_n = \boldsymbol{0} \end{cases} \tag{4.55}$$

where $\boldsymbol{\lambda}_{\alpha_f}$ is the array of interface forces at t_{α_f}. The time instance t_{α_f} is found from a weighted average between t_{n-1} and t_n, according to $t_{\alpha_f} = \alpha_f t_{n-1} + (1-\alpha_f)t_n$, as is shown in figure **??**. Note that in this formulation one truly considers the interface forces as instantaneous forces

Figure 4.9: *Visualization of the time instances t_{α_m} and t_{α_f} introduced by the generalized-α method.*

that enforce the compatibility condition, whereas in Eq. (4.1) one considers these as the forces required at t_{n-1} and t_n, such that their weighted average leads to satisfying the compatibility condition. Note that, as all the subdomains in Eqs. (4.1) and (4.55) have the exact same time discretization, one could regard this as a conforming time grid.[5] Therefore, if the subdomain interfaces are compatible at t_{n-1} and t_n, this is also holds for the time in between ($\tau = [t_{n-1}, t_n]$).

As Eqs. (4.1) and (4.55) describe the exact same coupled system of equations, which will thus lead to the exact same response in terms of accelerations, velocities and displacements, one can "subtract" these two sets of equations from each other to find:

$$\boldsymbol{\lambda}_{\alpha_f} = (1-\alpha_f)\boldsymbol{\lambda}_n + \alpha_f \boldsymbol{\lambda}_{n-1}. \tag{4.56}$$

Hence, in the approaches presented in the chapter one can choose to either obtain the coupling forces ($\boldsymbol{\lambda}$) at the same time instances as the external force contributions ($t_i = 0 \dots t_n$), or regard these as instantaneous force contributions occurring at the interpolated time steps (t_{α_f}). In this work the preference is given to regarding these as additional external force on the substructure level, thereby determining them at the physical time steps, instead of at the "fictitious" time instance t_{α_f}.

4.6.2 Remarks on time integration stability in the presence of Lagrange multipliers

The Lagrange multipliers, that have been introduced to enforce the compatibility between the different substructures in Eq. (4.1), are often found to be destabilizing in direct time integration of dually assembled systems, as they introduce eigenvalues at infinity. Several solutions are proposed to stabilize the Lagrange multipliers. Farhat *et al.* proposed three different approaches in [51] and analyzed the resulting time integration schemes for linear problems. As also mentioned in section 3.3, Arnold and Brüls [7] proposed an algorithm based on the generalized-α method and proved second order accuracy for both the accelerations and Lagrange multipliers. This algorithm is equal to the generalized-α method for the case of a constant mass matrix and would thereby also prove the accuracy of the proposed sequential method for this specific case.

Nonetheless it is believed that in both algorithms proposed in this chapter, the Lagrange multipliers should not have any destabilizing effects. In differential algebraic systems, the instability can be interpreted as coming from infinite frequencies related to the algebraic conditions that act as an additional dynamic with zero mass on the Lagrange multipliers [51]. However, in the way the integration is performed here, the dynamics of the Lagrange multipliers is not accounted for in the time stepping and only the dynamics of the displacements is included in the time stepping algorithms. Indeed the Lagrange multipliers appear only as instantaneous values that enforce compatibility. Therefore the instability sometimes encountered for differential algebraic equations will not be of concern here. Hence, an instability of the coupled simulations could only occur in the case that one of the subsystems would become unstable, which would obviously also result in an apparent instable growth of the Lagrange multipliers.

[5] This can be regarded as analog to conforming finite element discretizations; where one uses matching nodes and the same interpolations functions for neighboring finite elements.

4.7 Summary

In this chapter two different monolithic multi-domain time integration methods have been presented. The first approach introduced is a sequential scheme, which is similar to applying the idea of a frontal solver for monolithically solving the coupled dynamic problems. In section 4.2 the approach has been derived for two substructures only. It could be verified that one would find the same response as one would find from solving the coupled subsystems in a single domain using the generalized-α scheme. Thereby, one ensures that the characteristics of the underlying generalized-α method are retained in this sequential monolithic multi-domain time integration method. It has also been discussed that one can use the concept of a frontal solver in order to generalize the method to allow for more than two subdomains in the time integration.

In order to initialize the sequential scheme at t_0, two approaches starting either from initial accelerations or a quasi-static equilibrium are presented in section 4.3. An extra challenge in the latter of the two methods is that some of the individual substructures can have rigid body modes, such that the substructure stiffness matrices can be singular.

The second approach presented in section 4.4 can be interpreted as an extension on the existing FETI methods. The FETI methods solve the nonlinear problem on the global level, thereby linearizing on the full system level, solving the interface problem and successively the linearized local domains. The proposed parallel monolithic multi-domain time integration method solves for the local nonlinear problems, by linearizing on the local domains and solving the linear interface problem on the global level. The result of the global step is then used to solve for the nonlinearities on a *per* substructure basis, which is finally used to update the global linear interface problem. This method has several benefits over the sequential approach as it allows a simple parallel implementation, it can easily be extended to multiple subdomains and is easy to implement. The different initialization approaches have been presented for the parallel monolithic multi-domain time integration method in section 4.5.

Finally, a brief discussion on the use of Lagrange multipliers in these monolithic time integration methods has been given in section 4.6. Here it is firstly shown that, in case of a generalized-α method, it is irrelevant whether the Lagrange multipliers are considered at the time steps t_n and t_{n-1} or as instantaneous internal forces at $t_{\alpha_f} = (1 - \alpha_f)t_n + \alpha_f t_{n-1}$. In addition it has been argued that the use of Lagrange multipliers in the methods presented here, should not affect the stability of these time integration schemes.

5

Impulse Based Substructuring

"Want het groote geschiedt niet bij impulsie alleen en is een aaneenschakeling van kleine dingen die tot elkaar gebragt zijn."

– Vincent van Gogh

5.1 Introduction to Impulse Based Substructuring

Apart from the Frequency Based Substructuring techniques and the Component Mode Synthesis methods introduced in chapter 2, a third class of substructuring techniques, Impulse Based Substructuring, has been introduced recently [139, 141]. The assembly procedure computes the time response of a system by evaluating per substructure the convolution product between the impulse response functions and the applied forces, including the interface forces that are computed to satisfy the interface compatibility.

An outline on using impulse response functions for time simulation purposes is given in chapter 3. The findings from that chapter are used here in order to derive the Impulse Based Substructuring schemes. This chapter outlines the basic principle of the method and shows that the theory can be easily applied when the impulse response functions are computed through direct time integration of a numerical model. In section 5.2 it is shown how to couple different substructure IRFs in order to obtain the total system response in time. The IBS method is extended in section 5.3, thereby allowing one to directly couple nonlinear finite element models using the generalized-α time integration method. In addition, in section 5.4 it is shown how to initialize the IBS method. Finally, the Impulse Based Substructuring technique is summarized in section 5.5.

This chapter is based on work presented in [141, 168, 169, 172].

5.2 Coupling Impulse Response Functions

Let us again assume that the global structure has been decomposed into a number (N_s) of substructures. All the substructure models are modeled as IRFs, as is described in section 3.4.1 and Eq. (3.31). Hence, in order to couple the substructures the dual assembly paradigm, that is outlined in section 2.6.2, is employed in order to obtain the classical formulation of the Impulse Based Substructuring method:

$$\begin{cases} \boldsymbol{u}(t) = \boldsymbol{u}_0 + \dot{\boldsymbol{u}}_0 t + \int_{\tau=0}^{t} \boldsymbol{Y}(t-\tau)\left(\boldsymbol{f}(\tau) - \boldsymbol{K}\left(\boldsymbol{u}_0 + \dot{\boldsymbol{u}}_0\tau\right) - \boldsymbol{C}\dot{\boldsymbol{u}}_0 - \boldsymbol{B}^{(s)^T}\boldsymbol{\lambda}(\tau)\right) d\tau \\ \sum_{s=1}^{N_s} \boldsymbol{B}^{(s)}\boldsymbol{u}^{(s)}(t) = \boldsymbol{0} \end{cases} . \tag{5.1}$$

In practice however, the IRFs will not be continuous in time and are either sampled from the analytical model or experiment or are obtained through direct time integration, as is discussed in section 3.4.3. In order to use the discrete IRFs, the convolution product is discretized in time as well, as is introduced in section 3.5. Hence, if one substitutes the result from this into Eq. (5.1), the discrete version of the IBS method is obtained:

$$\begin{cases} \boldsymbol{u}_n^{(s)} = \boldsymbol{u}_0^{(s)} + \dot{\boldsymbol{u}}_0^{(s)} t_n + h\left[{}^0\boldsymbol{Y}_n^{(s)}\right]\left(\bar{\boldsymbol{f}}_0^{(s)} - \boldsymbol{B}^{(s)^T}\boldsymbol{\lambda}_0\right) \\ \qquad\qquad + h\sum_{i=1}^{n}\left[{}^1\boldsymbol{Y}_{n-i}^{(s)}\right]\left(\bar{\boldsymbol{f}}_i^{(s)} - \boldsymbol{B}^{(s)^T}\boldsymbol{\lambda}_i\right) \\ \sum_{s=1}^{N_s} \boldsymbol{B}^{(s)}\boldsymbol{u}_n^{(s)} = \boldsymbol{0} \end{cases} , \tag{5.2}$$

where $\bar{\boldsymbol{f}}_i^{(s)} = \boldsymbol{f}_i^{(s)} - \boldsymbol{K}^{(s)}\left(\boldsymbol{u}_0^{(s)} + \dot{\boldsymbol{u}}_0^{(s)} t_i\right) + \boldsymbol{C}^{(s)}\dot{\boldsymbol{u}}_0^{(s)}$. In this dual assembled form (Eq. (5.2)), the solution at time t_n is determined by the time history of external and interface forces from t_0 to t_n, such that the only unknowns are the interface forces at t_n,

$$\begin{cases} \boldsymbol{u}_n^{(s)} = \hat{\boldsymbol{u}}_n^{(s)} - h\left[{}^1\boldsymbol{Y}_0^{(s)}\right]\boldsymbol{B}^{(s)^T}\boldsymbol{\lambda}_n \\ \sum_{s=1}^{N_s} \boldsymbol{B}^{(s)}\boldsymbol{u}_n^{(s)} = \boldsymbol{0} \end{cases} , \tag{5.3}$$

where,

$$\begin{aligned} \hat{\boldsymbol{u}}_n^{(s)} = \boldsymbol{u}_0^{(s)} + \dot{\boldsymbol{u}}_0^{(s)} t_n + h\left[{}^0\boldsymbol{Y}_n^{(s)}\right]\left(\bar{\boldsymbol{f}}_0^{(s)} - \boldsymbol{B}^{(s)^T}\boldsymbol{\lambda}_0\right) \\ + h\sum_{i=1}^{n-1}\left[{}^1\boldsymbol{Y}_{n-i}^{(s)}\right]\left(\bar{\boldsymbol{f}}_i^{(s)} - \boldsymbol{B}^{(s)^T}\boldsymbol{\lambda}_i\right) + h\left[{}^1\boldsymbol{Y}_0^{(s)}\right]\bar{\boldsymbol{f}}_n^{(s)}. \end{aligned} \tag{5.4}$$

Here, $\hat{\boldsymbol{u}}_n^{(s)}$ is the predictor that contains the response due to all the known force inputs. In order to determine the unknown interface forces the first line of Eq. (5.4) is substituted in the compatibility condition given in the second line. By rewriting the result, a direct expression for $\boldsymbol{\lambda}_n$ is obtained:

$$\boldsymbol{\lambda}_n = \left(h\sum_{s=1}^{N_s}\boldsymbol{B}^{(s)}\left[{}^1\boldsymbol{Y}_0^{(s)}\right]\boldsymbol{B}^{(s)^T}\right)^{-1}\sum_{s=1}^{N_s}\boldsymbol{B}^{(s)}\hat{\boldsymbol{u}}_n^{(s)}. \tag{5.5}$$

Here, the second summation gives the compatibility error on the interface and the first term is interpreted as a global effective interface stiffness. By multiplying the two terms, one obtains the Lagrange multipliers that are required for enforcing the compatibility at t_n, which is very similar to the dual interface problem found for the LM-FBS method, that is applied in Frequency Based Substructuring [34,35]. By substituting the found $\boldsymbol{\lambda}_n$ into Eq. (5.3) one finds the coupled response. Hence, Eqs. (5.3) and (5.5) constitute the stepping algorithm for the IBS strategy. Note that for determining the Lagrange multipliers at t_0 different approaches are needed, as will be presented in section 5.4.

5.3 Coupling Impulse Response Functions and Finite Element Models

The same concepts as presented in section 5.2 can be used for coupling IRFs and FE models. Hence, the dual assembly paradigm is used to enforce the coupling between multiple substructures by means of Lagrange multipliers. Using this approach, linear and nonlinear finite element models can be coupled to IRFs in order to obtain the coupled response, as is visualized in figure 5.1. The IBS method, as presented in section 5.2, constitutes a time stepping scheme, and

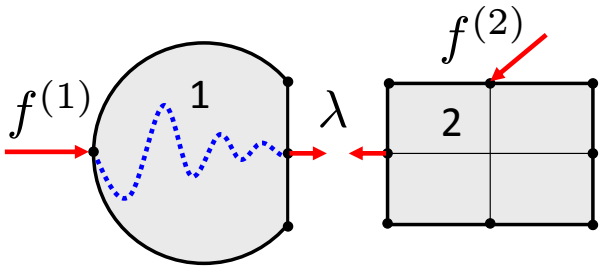

Figure 5.1: *Conceptual view of coupling IRFs (domain 1) to an FE model (domain 2).*

therefore a time stepping scheme is also required in order to simulate the time responses of the FE substructures. The method presented here will employ the generalized-α scheme, as outlined in section 3.3, to allow for the time stepping. As the convolution product can be made fully equivalent to any of the "α" (generalized-α, HHT-α, WBZ-α) and Newmark time integration methods (see section 3.5), the proposed coupling method will result in a second-order accurate and unconditionally stable time stepping scheme.

5.3.1 The IBS time stepping algorithm

The dual assembled and time discretized system of equations is given in Eq. (5.6). The variables with superscript (s) denote the substructures described by their IRFs ($s = 1 \dots N_{IRF}$), where N_{IRF} denotes the total number of substructures modeled with their IRFs. The variables with superscript (r) denote the substructures given as (nonlinear) finite element models, such that $r = (N_{IRF} + 1 \dots N_s)$, where N_s denotes the total number of substructures.

$$\begin{cases} \boldsymbol{u}_n^{(s)} = \boldsymbol{u}_0^{(s)} + \dot{\boldsymbol{u}}_0^{(s)} t_n + h \left[{}^0\boldsymbol{Y}_n^{(s)}\right] \left(\bar{\boldsymbol{f}}_0^{(s)} - \boldsymbol{B}^{(s)^T} \boldsymbol{\lambda}_0\right) \\ \qquad\qquad + h \sum_{i=1}^{n} \left[{}^1\boldsymbol{Y}_{n-i}^{(s)}\right] \left(\bar{\boldsymbol{f}}_i^{(s)} - \boldsymbol{B}^{(s)^T} \boldsymbol{\lambda}_i\right) \\ \boldsymbol{r}_n^{(r)} = (1-\alpha_m)\boldsymbol{M}^{(r)} \ddot{\boldsymbol{u}}_n^{(r)} + \alpha_m \boldsymbol{M}^{(r)} \ddot{\boldsymbol{u}}_{n-1}^{(r)} + (1-\alpha_f)\left(\boldsymbol{p}_n^{(r)} + \boldsymbol{B}^{(r)^T}\boldsymbol{\lambda}_n - \boldsymbol{f}_n^{(r)}\right) \\ \qquad\qquad + \alpha_f \left(\boldsymbol{p}_{n-1}^{(r)} + \boldsymbol{B}^{(r)^T}\boldsymbol{\lambda}_{n-1} - \boldsymbol{f}_{n-1}^{(r)}\right) \\ \boldsymbol{B}\boldsymbol{u}_n = \begin{bmatrix} \boldsymbol{B}^{(s)} & \boldsymbol{B}^{(r)} \end{bmatrix} \begin{bmatrix} \boldsymbol{u}_n^{(s)} \\ \boldsymbol{u}_n^{(r)} \end{bmatrix} = \boldsymbol{0} \ . \end{cases} \tag{5.6}$$

Here, $\boldsymbol{p}^{(r)}(\dot{\boldsymbol{u}}_n^{(r)}, \boldsymbol{u}_n^{(r)})$ is the nonlinear force vector which contains all the nonlinear stiffness and damping contributions. In addition, it can be seen that the nonlinear part of the set of equations is already written in a residual form. Also note that in the case of models with large rotations, the mass matrix $\boldsymbol{M}^{(r)}(\boldsymbol{u}_n^{(r)})$ also becomes nonlinear and needs to be accounted for in the developments, but for the sake of simplicity this is discarded throughout the rest of this section. In case more than two substructures are assembled, the matrices and vectors in Eq. (5.6) should be considered as block matrices, as is introduced at the start of section 4.2. As part of the equations of motion given in Eq. (5.6) are nonlinear, they need to be solved in an iterative manner. Even though several different nonlinear solution methods exist, it was chosen to use the full Newton-Raphson method, as was outlined in section 3.2.2. The residual force vector, $\boldsymbol{r}_n^{(r)}$, can be regarded as an error on the equilibrium and should be set to zero. Here, the same approach as in section 3.2.2 for solving the nonlinear part is used. Therefore, the original Newmark relations, given in Eq. (3.4), are recasted, to give

$$\begin{aligned} \ddot{\boldsymbol{u}}_n^{(r)} &= \frac{1}{h^2\beta}\left(\boldsymbol{u}_n^{(r)} - \check{\boldsymbol{u}}_n^{(r)}\right), \\ \dot{\boldsymbol{u}}_n^{(r)} &= \dot{\check{\boldsymbol{u}}}_n^{(r)} + \frac{\gamma}{h\beta}\left(\boldsymbol{u}_n^{(r)} - \check{\boldsymbol{u}}_n^{(r)}\right), \end{aligned} \tag{5.7}$$

where the only unknowns on the right hand side are the unknown displacements ($\boldsymbol{u}_n^{(r)}$). Hence, direct relations between the unknown accelerations ($\ddot{\boldsymbol{u}}_n^{(r)}$), velocities ($\dot{\boldsymbol{u}}_n^{(r)}$) and displacements ($\boldsymbol{u}_n^{(r)}$) are obtained. After substituting Eq. (5.7) into the second line of Eq. (5.6) the only unknowns left are the displacements and interface forces at t_n,

$$\begin{aligned} \boldsymbol{r}_n^{(r)}\left(\boldsymbol{u}_n^{(r)}, \boldsymbol{\lambda}_n\right) = \frac{1}{h^2\beta}\boldsymbol{M}^{(r)}\left((1-\alpha_m)\left(\boldsymbol{u}_n^{(r)} - \check{\boldsymbol{u}}_n^{(r)}\right) + \alpha_m \ddot{\boldsymbol{u}}_{n-1}^{(r)}\right) \\ + (1-\alpha_f)\left(\boldsymbol{p}^{(r)}\left(\boldsymbol{u}_n^{(r)}\right) + \boldsymbol{B}^{(r)^T}\boldsymbol{\lambda}_n - \boldsymbol{f}_n^{(r)}\right) + \alpha_f\left(\boldsymbol{p}_{n-1}^{(r)} + \boldsymbol{B}^{(r)^T}\boldsymbol{\lambda}_{n-1} - \boldsymbol{f}_{n-1}^{(r)}\right). \end{aligned} \tag{5.8}$$

In order to solve this nonlinear set of equations, we want to apply the Newton-Raphson method but avoiding to compute at every iteration the interface forces which requires solving the global problem. Hence, it is required to find an explicit relation between the set of displacements and the interface forces. Starting from the first line of Eq. (5.6), the response can be split in a known part, as is given in Eq. (5.4), and an unknown part:

$$\boldsymbol{u}_n^{(s)} = \hat{\boldsymbol{u}}_n^{(s)} - h\left[{}^1\boldsymbol{Y}_0^{(s)}\right]\boldsymbol{B}^{(s)^T}\boldsymbol{\lambda}_n. \tag{5.9}$$

Substituting this into the compatibility equation, given in the last line in Eq. (5.6),

$$\begin{bmatrix} \boldsymbol{B}^{(s)} & \boldsymbol{B}^{(r)} \end{bmatrix} \begin{bmatrix} \hat{\boldsymbol{u}}_n^{(s)} - h\left[{}^1\boldsymbol{Y}_0^{(s)}\right]\boldsymbol{B}^{(s)^T}\boldsymbol{\lambda}_n \\ \boldsymbol{u}_n^{(r)} \end{bmatrix} = \boldsymbol{0},$$

and rewriting this, gives us an explicit equation for $\boldsymbol{\lambda}_n$:

$$\boldsymbol{\lambda}_n = \left(h\boldsymbol{B}^{(s)} \left[{}^1\boldsymbol{Y}_0^{(s)} \right] \boldsymbol{B}^{(s)^T} \right)^{-1} \left[\begin{array}{cc} \boldsymbol{B}^{(s)} & \boldsymbol{B}^{(r)} \end{array} \right] \left[\begin{array}{c} \hat{\boldsymbol{u}}_n^{(s)} \\ \boldsymbol{u}_n^{(r)} \end{array} \right]. \tag{5.10}$$

Substituting Eq. (5.10) into Eq. (5.8) gives a direct (nonlinear) relation between the residual and the set of displacements:

$$\boldsymbol{r}_n^{(r)} \left(\boldsymbol{u}_n^{(r)} \right) = \boldsymbol{0}. \tag{5.11}$$

This is the nonlinear problem that will be solved using Newton-Raphson iterations. Hence we successively solve the following set of linear equations

$$\boldsymbol{S}^{(r)}(\boldsymbol{u}_n^{(r)}) \Delta \boldsymbol{u}^{(r)} = -\boldsymbol{r}_n^{(r)}, \tag{5.12}$$

where, $\boldsymbol{S}^{(r)}(\boldsymbol{u}_n^{(r)})$ is the iteration matrix, to obtain an update on the displacement field ($\Delta \boldsymbol{u}^{(r)}$). By taking into account the Newmark relations, given in Eq. (5.7), one computes the new state of the system from:

$$\begin{aligned} \ddot{\boldsymbol{u}}_n^{(r)} &\leftarrow \ddot{\boldsymbol{u}}_n^{(r)} + \frac{1}{\beta h^2} \Delta \boldsymbol{u}^{(r)}, \\ \dot{\boldsymbol{u}}_n^{(r)} &\leftarrow \dot{\boldsymbol{u}}_n^{(r)} + \frac{\gamma}{\beta h} \Delta \boldsymbol{u}^{(r)}, \\ \boldsymbol{u}_n^{(r)} &\leftarrow \boldsymbol{u}_n^{(r)} + \Delta \boldsymbol{u}^{(r)}, \end{aligned} \tag{5.13}$$

and determines the new residual using Eq. (5.11). This process is repeated until the residual is smaller than the set convergence criterium and requires us to compute the Jacobian (or iteration) matrix $\boldsymbol{S}^{(r)}$,

$$\begin{aligned} \boldsymbol{S}^{(r)} \left(\boldsymbol{u}_n^{(r)} \right) = \frac{\partial \boldsymbol{r}^{(r)}}{\partial \boldsymbol{u}^{(r)}} &= (1-\alpha_m) \frac{1}{\beta h^2} \boldsymbol{M}^{(r)} \\ &+ (1-\alpha_f) \left(\boldsymbol{K}_t^{(r)} + \frac{\gamma}{\beta h} \boldsymbol{C}_t^{(r)} + \boldsymbol{B}^{(r)^T} \left(h\boldsymbol{B}^{(s)} \left[{}^1\boldsymbol{Y}_0^{(s)} \right] \boldsymbol{B}^{(s)^T} \right)^{-1} \boldsymbol{B}^{(r)} \right), \end{aligned} \tag{5.14}$$

where the tangential stiffness ($\boldsymbol{K}_t^{(r)}$) and damping ($\boldsymbol{C}_t^{(r)}$) matrices are found from

$$\boldsymbol{K}_t^{(r)} = \frac{\partial \boldsymbol{p}^{(r)}}{\partial \boldsymbol{u}^{(r)}} - \frac{\partial \boldsymbol{f}^{(r)}}{\partial \boldsymbol{u}^{(r)}}, \quad \boldsymbol{C}_t^{(r)} = \frac{\partial \boldsymbol{p}^{(r)}}{\partial \dot{\boldsymbol{u}}^{(r)}} - \frac{\partial \boldsymbol{f}^{(r)}}{\partial \dot{\boldsymbol{u}}^{(r)}}.$$

Note that by including the interface forces in the residual (5.8) and subsequently using this residual to compute the Jacobian matrix in Eq. (5.14), the influence of the neighboring substructures is included in the Newton-Raphson iterations. In fact the final term in Eq. (5.14) is found by taking the Jacobian of the interface forces, given in Eq. (5.10), with respect to the displacements, as is given:

$$\frac{\partial \boldsymbol{B}^{(r)^T} \boldsymbol{\lambda}}{\partial \boldsymbol{u}^{(r)}} = \boldsymbol{B}^{(r)^T} \left(h\boldsymbol{B}^{(s)} \left[{}^1\boldsymbol{Y}_0^{(s)} \right] \boldsymbol{B}^{(s)^T} \right)^{-1} \boldsymbol{B}^{(r)}. \tag{5.15}$$

This can be physically interpreted as a condensation of the linear substructures onto the nonlinear substructures and thus results in an effective interface stiffness. After the nonlinear subsystems are converged, the interface forces, computed using Eq. (5.10), are substituted in Eq. (5.9) to update the set of displacements of all the linear IRF-substructures.

One can see from a careful examination of the time stepping approach described in this section, that the time stepping scheme presented in section 5.2 can be considered a special case. Clearly, if one would only include IRFs in the analysis presented here, the exact same method as described in section 5.2 is found. Hence, the approach described here can be regarded as a generalized framework for the IBS method for working with numerical models.

5.3.2 Implementation and comparison to a standard generalized-α time integration setup

Even though the derivation of the method involves quite some equations in section 5.3.1, the actual implementation of the method only requires a limited number of modifications to the standard generalized-α scheme. A compact schematic overview of both methods is given in figure 5.2, where it is already easy to see that the backbone, consisting of a predictor step and an iterative step, of both methods is similar.

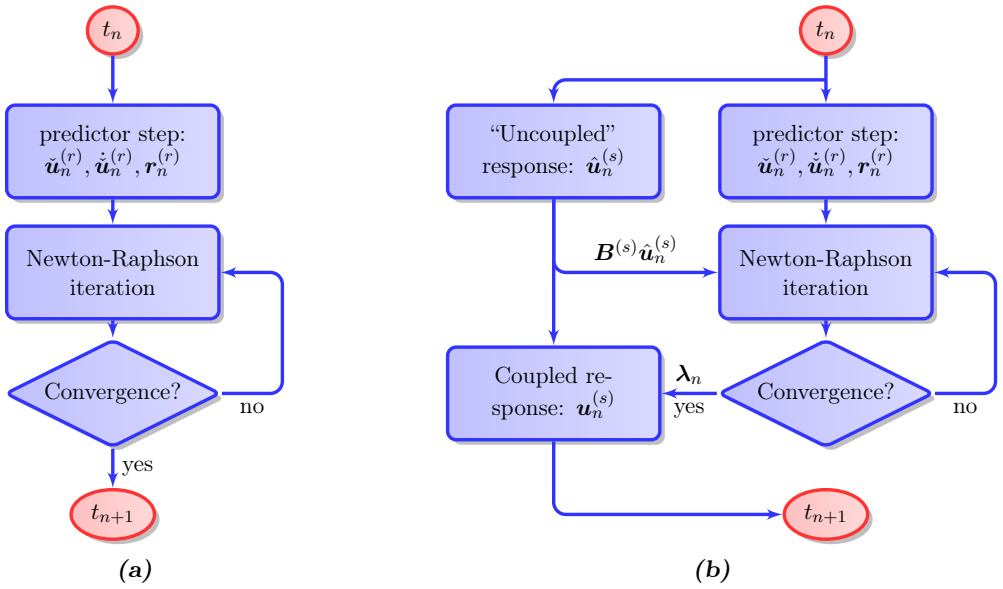

Figure 5.2: ***(a)*** *Standard generalized-α time integration scheme;* ***(b)*** *IBS time integration scheme; note that the Newton-Raphson step in the IBS scheme is slightly modified as is explained in the text of section 5.3.2.*

In the standard generalized-α scheme (figure 5.2a and section 3.3), one starts with a predictor step from which the residual is computed. In the second block, "Newton-Raphson iteration", the update of the displacements, velocities and accelerations is determined. Using this updated set of DoF, the nonlinear contributions are updated and a new residual is computed. The third block, "Convergence?", checks whether the residual is equal to zero[1] (or if other convergence criterion are met); if this is the case one moves to the next time step and repeats the same loop again, otherwise a new iteration step is performed.

In the proposed method (figure 5.2b), the basic steps remain for a large part the same. One again starts with determining the predictors and associated residual of the nonlinear substructure, but in addition one also computes the "uncoupled" response (the predictor) of the linear component using Eq. (5.9). To start the second step, "Newton-Raphson iteration", the "uncoupled" interface displacements of subsystems (s) are required to compute the interface forces using (5.10), which are added to the residuals of substructures (r) (Eq. (5.8)). Using the obtained residual the updates of the states of the substructures, the nonlinear forces, interface forces and the residuals of subsystems (r) are computed. Again this process is repeated until convergence. Afterwards, the response of the linear subsystems is updated using Eq. (5.9) and a new time step is started. As is clear, only small modifications to the Newton-Raphson step of the standard time integration scheme need to be made and, additionally, the convolution product needs to be solved in order to implement the IBS method. Finally note that in this

[1] In practice one would iterate until the norm of the residual is smaller than a preset tolerance, which is often normalized with respect to a given force quantity.

approach the linear components are only solved ones per time step, as the Newton-Raphson iterations are only performed for the nonlinear substructures in which the linear contribution are implicitly included through their interface contribution (as in a condensation approach).

5.4 Initialization of the Impulse Based Substructuring method

The impulse based substructuring algorithm that is presented in the previous two sections, describes the dynamic time stepping phase. In order to start the simulations it is required that one also consistently handles the initialization phase of the process.

5.4.1 The approach of initial accelerations

The first approach to initialize the time stepping method is by means of using initial accelerations. If one uses a standard generalized-α method, this is found by simply substituting the initial conditions and initial forces in Eq. (3.20) in order to find the accelerations at t_0. Hence, in the case of a dual assembled system, one would find for the initial time step:

$$\begin{cases} \ddot{\boldsymbol{u}}_0^{(s)} = \boldsymbol{M}^{(s)^{-1}} \left(\boldsymbol{f}_0^{(s)} - \boldsymbol{K}^{(s)} \boldsymbol{u}_0^{(s)} - \boldsymbol{C}^{(s)} \dot{\boldsymbol{u}}_0^{(s)} - \boldsymbol{B}^{(s)^T} \boldsymbol{\lambda}_0 \right) \\ \ddot{\boldsymbol{u}}_0^{(r)} = \boldsymbol{M}^{(r)^{-1}} \left(\boldsymbol{f}_0^{(r)} - \boldsymbol{p}^{(r)} \left(\boldsymbol{u}_0^{(r)}, \dot{\boldsymbol{u}}_0^{(r)} \right) - \boldsymbol{B}^{(r)^T} \boldsymbol{\lambda}_0 \right) \\ \boldsymbol{B} \ddot{\boldsymbol{u}}_0 = \boldsymbol{0} \end{cases} . \tag{5.16}$$

Note that, as the nonlinear force $\boldsymbol{p}^{(r)}$ is a function of the initial conditions, it can be considered a constant force, $\boldsymbol{p}_0^{(r)}$, for the initialization step. In addition, the compatibility condition is now enforced using the accelerations instead of the displacements.[2] Similar to the approach followed section 4.5.1, one can split Eq. (5.16) into a known part again and the unknown contribution due to the coupling forces:

$$\begin{cases} \ddot{\boldsymbol{u}}_0^{(s)} = \ddot{\tilde{\boldsymbol{u}}}_0^{(s)} - \boldsymbol{M}^{(s)^{-1}} \boldsymbol{B}^{(s)^T} \boldsymbol{\lambda}_0 \\ \ddot{\boldsymbol{u}}_0^{(r)} = \ddot{\tilde{\boldsymbol{u}}}_0^{(r)} - \boldsymbol{M}^{(r)^{-1}} \boldsymbol{B}^{(r)^T} \boldsymbol{\lambda}_0 \\ \boldsymbol{B} \ddot{\boldsymbol{u}}_0 = \boldsymbol{0} \end{cases} , \tag{5.17}$$

where the predictors are found to be:

$$\begin{cases} \ddot{\tilde{\boldsymbol{u}}}_0^{(s)} = \boldsymbol{M}^{(s)^{-1}} \left(\boldsymbol{f}_0^{(s)} - \boldsymbol{K}^{(s)} \boldsymbol{u}_0^{(s)} - \boldsymbol{C}^{(s)} \dot{\boldsymbol{u}}_0^{(s)} \right) \\ \ddot{\tilde{\boldsymbol{u}}}_0^{(r)} = \boldsymbol{M}^{(r)^{-1}} \left(\boldsymbol{f}_0^{(r)} - \boldsymbol{p}_0^{(r)} \right) \end{cases} . \tag{5.18}$$

Substituting the first two lines of Eq. (5.17) into compatibility condition given in the last line and rewriting the result leads to a direct expression for the interface forces:

$$\boldsymbol{\lambda}_0 = \left(\begin{bmatrix} \boldsymbol{B}^{(s)} & \boldsymbol{B}^{(r)} \end{bmatrix} \begin{bmatrix} \boldsymbol{M}^{(s)^{-1}} & \boldsymbol{0} \\ \boldsymbol{0} & \boldsymbol{M}^{(r)^{-1}} \end{bmatrix} \begin{bmatrix} \boldsymbol{B}^{(s)^T} \\ \boldsymbol{B}^{(r)^T} \end{bmatrix} \right)^{-1} \begin{bmatrix} \boldsymbol{B}^{(s)} & \boldsymbol{B}^{(r)} \end{bmatrix} \begin{bmatrix} \ddot{\tilde{\boldsymbol{u}}}_0^{(s)} \\ \ddot{\tilde{\boldsymbol{u}}}_0^{(r)} \end{bmatrix} . \tag{5.19}$$

Hence, substituting $\boldsymbol{\lambda}_0$ into Eq. (5.17) yields the response at the initial time step. Note that, although the accelerations are not used for time stepping the response of the linear systems by means of the convolution product, one still needs $\boldsymbol{\lambda}_0$ in Eqs. (5.2) and (5.6).

[2] Obviously, the initial conditions given need to be compatible as well, such that $\boldsymbol{B}\dot{\boldsymbol{u}}_0 = \boldsymbol{0}$, $\boldsymbol{B}\boldsymbol{u}_0 = \boldsymbol{0}$.

If one would have the IRFs in terms of accelerations for the first time step, $\left[{}^0\ddot{\boldsymbol{Y}}_0^{(s)}\right]$, one could substitute the result given in Eq. (3.52) into Eq. (5.16), in order to obtain the following:

$$\begin{cases} \ddot{\boldsymbol{u}}_0^{(s)} = h\left[{}^0\ddot{\boldsymbol{Y}}_0^{(s)}\right]\left(\boldsymbol{f}_0 - \boldsymbol{K}^{(s)}\boldsymbol{u}_0^{(s)} - \boldsymbol{C}^{(s)}\dot{\boldsymbol{u}}_0^{(s)} - \boldsymbol{B}^{(s)^T}\boldsymbol{\lambda}_0\right) \\ \ddot{\boldsymbol{u}}_0^{(r)} = \boldsymbol{M}^{(r)^{-1}}\left(\boldsymbol{f}_0^{(r)} - \boldsymbol{p}^{(r)}\left(\boldsymbol{u}_0^{(r)}, \dot{\boldsymbol{u}}_0^{(r)}\right) - \boldsymbol{B}^{(r)^T}\boldsymbol{\lambda}_0\right) \\ \boldsymbol{B}\ddot{\boldsymbol{u}}_0 = \boldsymbol{0} \end{cases} . \tag{5.20}$$

By performing all the steps described above, the interface forces are found from:

$$\boldsymbol{\lambda}_0 = \left(\begin{bmatrix} \boldsymbol{B}^{(s)} & \boldsymbol{B}^{(r)} \end{bmatrix} \begin{bmatrix} h\left[{}^0\ddot{\boldsymbol{Y}}_0^{(s)}\right] & \boldsymbol{0} \\ \boldsymbol{0} & \boldsymbol{M}^{(r)^{-1}} \end{bmatrix} \begin{bmatrix} \boldsymbol{B}^{(s)^T} \\ \boldsymbol{B}^{(r)^T} \end{bmatrix} \right)^{-1} \begin{bmatrix} \boldsymbol{B}^{(s)} & \boldsymbol{B}^{(r)} \end{bmatrix} \begin{bmatrix} \ddot{\hat{\boldsymbol{u}}}_0^{(s)} \\ \ddot{\hat{\boldsymbol{u}}}_0^{(r)} \end{bmatrix} . \tag{5.21}$$

The results found in Eq. (5.19) and Eq. (5.21) are fully equivalent, as

$$h\left[{}^0\ddot{\boldsymbol{Y}}_0^{(s)}\right] = \boldsymbol{M}^{(s)^{-1}},$$

which can easily be verified from the analysis performed in section 3.5.1. Note that, in order to avoid factorizing the substructure mass matrices, one could start from a set of truncated initial accelerations ($\ddot{\boldsymbol{u}}_0 = \boldsymbol{0}$). This can however have a negative effect on the accuracy of the obtained solutions, as is shown in [78].

5.4.2 Quasi-static initialization of the time stepping algorithm

As was already discussed in section 3.4.2, it is in general beneficial to start simulating the responses of operating systems from an initial quasi-static equilibrium instead of from the undeformed state. In addition to this, it was shown in section 3.5.2 that the convolution product can be simplified by starting the simulations from a quasi-static equilibrium.

Firstly, the quasi-static initial conditions ($\ddot{\boldsymbol{u}}_0 = \boldsymbol{0}$ and $\dot{\boldsymbol{u}}_0 = \boldsymbol{0}$) are substituted into Eq. (5.6) to obtain the initial static problem:

$$\begin{cases} \boldsymbol{K}^{(s)}\boldsymbol{u}_0^{(s)} = \boldsymbol{f}_0^{(s)} - \boldsymbol{B}^{(s)^T}\boldsymbol{\lambda}_0 \\ \boldsymbol{p}^{(r)}(\boldsymbol{u}_0^{(r)}) = \boldsymbol{f}_0^{(r)} - \boldsymbol{B}^{(r)^T}\boldsymbol{\lambda}_0 \\ \boldsymbol{B}\boldsymbol{u}_0 = \boldsymbol{0} \end{cases} . \tag{5.22}$$

Solving this will be straightforward in the case that all the substructures have sufficient boundary conditions to constrain the rigid body motion. Similar to what was done in section 4.3.2, it is assumed here that the assembled structure is adequately constrained, but that some of the substructures can have rigid body modes. Therefore, the solution for the linear substructures would write

$$\boldsymbol{u}_0^{(s)} = \boldsymbol{K}^{(s)^+}\left(\boldsymbol{f}_0^{(s)} - \boldsymbol{B}^{(s)^T}\boldsymbol{\lambda}_0\right) - \boldsymbol{R}^{(s)}\boldsymbol{\alpha}_0^{(s)}, \tag{5.23}$$

where $\boldsymbol{K}^{(s)^+}$ is the generalized inverse of $\boldsymbol{K}^{(s)}$ and $\boldsymbol{R}^{(s)}$ are the rigid body modes that span the null space of $\boldsymbol{K}^{(s)}$. Hence, the response of the subsystem is a combination of flexible deformations and rigid displacements. By recalling that one can obtain the flexibility matrix directly from the IRFs, as was given in Eq. (3.40), one can directly substitute this in Eq. (5.23), thereby resulting in:

$$\boldsymbol{u}_0^{(s)} = \sum_{i=0}^{\infty}\left[{}^1\boldsymbol{Y}_i^{(s),flex}\right]\left(\boldsymbol{f}_0^{(s)} - \boldsymbol{B}^{(s)^T}\boldsymbol{\lambda}_0\right) - \boldsymbol{R}^{(s)}\boldsymbol{\alpha}_0^{(s)}. \tag{5.24}$$

The amplitudes of the rigid body modes, $\boldsymbol{\alpha}_0^{(s)}$, are found from the fact that the external forces and interface forces must be self-equilibrated:

$$\boldsymbol{R}^{(s)^T}\left(\boldsymbol{f}_0^{(s)} - \boldsymbol{B}^{(s)^T}\boldsymbol{\lambda}_0\right) = \boldsymbol{0}. \tag{5.25}$$

Hence, substituting Eq. (5.24) into the compatibility equation of Eq. (5.22) and taking into account Eq. (5.25) leads to the set of equations to solve for obtaining the interface forces and rigid body amplitudes, assuming the displacements $\boldsymbol{u}_0^{(r)}$ are known;

$$\begin{bmatrix} \boldsymbol{F}_I & \boldsymbol{R}_{[b]}^{(s)} \\ \boldsymbol{R}_{[b]}^{(s)^T} & \boldsymbol{0} \end{bmatrix} \begin{bmatrix} \boldsymbol{\lambda}_0 \\ \boldsymbol{\alpha}_0 \end{bmatrix} = \begin{bmatrix} \boldsymbol{B}^{(s)} \sum_{i=0}^{m} \left[{}^1\boldsymbol{Y}_i^{(s),flex}\right] \boldsymbol{f}_0^{(s)} + \boldsymbol{B}^{(r)}\boldsymbol{u}_0^{(r)} \\ \boldsymbol{R}^{(s)^T}\boldsymbol{f}_0^{(s)} \end{bmatrix}, \tag{5.26}$$

where

$$\boldsymbol{R}_{[b]}^{(s)} = \boldsymbol{B}^{(s)}\boldsymbol{R}^{(s)}, \quad \boldsymbol{F}_I = \boldsymbol{B}^{(s)} \sum_{i=0}^{m} \left[{}^1\boldsymbol{Y}_i^{(s),flex}\right] \boldsymbol{B}^{(s)^T}. \tag{5.27}$$

The method for solving the coupled static problem, given in Eq. (5.22), is analogous to the approach used for solving the coupled dynamic problem in section 5.3 and related to the approach given in section 4.3.2. Firstly, the set of equations for the residual of the nonlinear part is determined:

$$\boldsymbol{r}^{(r)}\left(\boldsymbol{u}_0^{(r)}, \boldsymbol{\lambda}_0\right) = \boldsymbol{p}^{(r)}(\boldsymbol{u}_0^{(r)}) + \boldsymbol{B}^{(r)^T}\boldsymbol{\lambda}_0 - \boldsymbol{f}_0^{(r)}. \tag{5.28}$$

The residual is now still a function of the displacements and the interface forces, hence we would like to obtain a relationship expressing the interface forces as a function of the displacements, thereby effectively condensing the linear subsystems into the residual of the nonlinear subsystems. Therefore, an orthogonal projector,

$$\boldsymbol{P} = \boldsymbol{I} - \boldsymbol{R}_{[b]}^{(s)}\left(\boldsymbol{R}_{[b]}^{(s)^T}\boldsymbol{R}_{[b]}^{(s)}\right)^{-1}\boldsymbol{R}_{[b]}^{(s)^T}, \tag{5.29}$$

is defined to eliminate $\boldsymbol{\alpha}_0$ from equation Eq. (5.26) and used to divide the interface forces into a part that is in the space of the rigid body modes and a part that is in the space of the stiffness matrix,

$$\boldsymbol{\lambda}_0 = \boldsymbol{P}\bar{\boldsymbol{\lambda}}_0 + \check{\boldsymbol{\lambda}}_0. \tag{5.30}$$

Substituting Eq. (5.30) into Eq. (5.26) and introducing the orthogonal projector gives:

$$\begin{cases} \check{\boldsymbol{\lambda}}_0 = \boldsymbol{R}_{[b]}^{(s)}\left(\boldsymbol{R}_{[b]}^{(s)^T}\boldsymbol{R}_{[b]}^{(s)}\right)^{-1}\boldsymbol{R}^{(s)^T}\boldsymbol{f}_0^{(s)} \\ \bar{\boldsymbol{\lambda}}_0 = \left(\boldsymbol{P}^T\boldsymbol{F}_I\boldsymbol{P}\right)^+\boldsymbol{P}^T\left(\boldsymbol{B}^{(s)}\sum_{i=0}^{m}\left[{}^1\boldsymbol{Y}_i^{(s),flex}\right]\boldsymbol{f}_0^{(s)} + \boldsymbol{B}^{(r)}\boldsymbol{u}_0^{(r)} \right. \\ \qquad\qquad \left. -\boldsymbol{B}^{(s)}\sum_{i=0}^{m}\left[{}^1\boldsymbol{Y}_i^{(s),flex}\right]\boldsymbol{B}^{(s)^T}\check{\boldsymbol{\lambda}}_0\right) \end{cases}. \tag{5.31}$$

By substituting Eqs. (5.30) and (5.31) into Eq. (5.28), the residual is no longer explicitly dependent on the interface forces ($\boldsymbol{\lambda}_0$). In order to bring the residual to zero, the Newton-Raphson approach is used. Therefore, one successively solves:

$$\begin{aligned} &\hat{\boldsymbol{K}}_t^{(r)}\Delta\boldsymbol{u}_0^{(r)} = -\boldsymbol{r}^{(r)}(\boldsymbol{u}_0^{(r)}), \\ &\boldsymbol{u}_0^{(r)} = \boldsymbol{u}_0^{(r)} + \Delta\boldsymbol{u}_0^{(r)}, \end{aligned} \tag{5.32}$$

where $\hat{\boldsymbol{K}}_t^{(r)}$ is the iteration (or Jacobian) matrix, until the residual is smaller than a chosen threshold or convergence criterion. The iteration matrix $\hat{\boldsymbol{K}}_t^{(r)}$ is obtained for the static case by computing the derivative of the residual with respect to the displacements,

$$\hat{\boldsymbol{K}}_t^{(r)} = \frac{\partial \boldsymbol{r}^{(r)}}{\partial \boldsymbol{u}^{(r)}} = \frac{\partial \boldsymbol{p}^{(r)}}{\partial \boldsymbol{u}^{(r)}} - \frac{\partial \boldsymbol{f}^{(r)}}{\partial \boldsymbol{u}^{(r)}} + \frac{\partial \boldsymbol{B}^{(r)^T} \boldsymbol{\lambda}}{\partial \boldsymbol{u}^{(r)}}, \tag{5.33}$$

which results in the following iteration matrix:

$$\hat{\boldsymbol{K}}_t^{(r)} = \boldsymbol{K}_t^{(r)} + \boldsymbol{B}^{(r)^T} \boldsymbol{P} \left(\boldsymbol{P}^T \boldsymbol{F}_I \boldsymbol{P} \right)^+ \boldsymbol{P}^T \boldsymbol{B}^{(r)}. \tag{5.34}$$

Analogous to the iteration matrix used in section 5.3, it is clear that the stiffness of the neighboring linear substructures is condensed in the tangent stiffness matrix ($\boldsymbol{K}_t^{(r)}$) of the nonlinear part. Hence, in Eq. (5.32) we iterate on the *global* problem and thus finds the *global* $\boldsymbol{u}_0^{(r)}$. Substituting the obtained displacements into Eq. (5.26) allows one to determine the interface forces and rigid body contributions, which after substitution into Eq. (5.24), leads to the set of displacements for all the linear substructures that are described by their IRFs.

5.5 Summarizing the Impulse Based Substructuring technique

In this section a brief summary of the proposed IBS method is given, by discussing its characteristics and some of its main benefits. The IBS method is essentially a substructure coupling technique, similar to the well-established FBS techniques. By using the IRFs of linear substructures, one has already pre-computed the dynamic behavior of the subcomponents, thereby only having to take into account the effect of the external forces acting on the system.

In this work all the relevant steps that allow for applying the IBS in practice have been given throughout this work, as is visualized in figure 5.3.

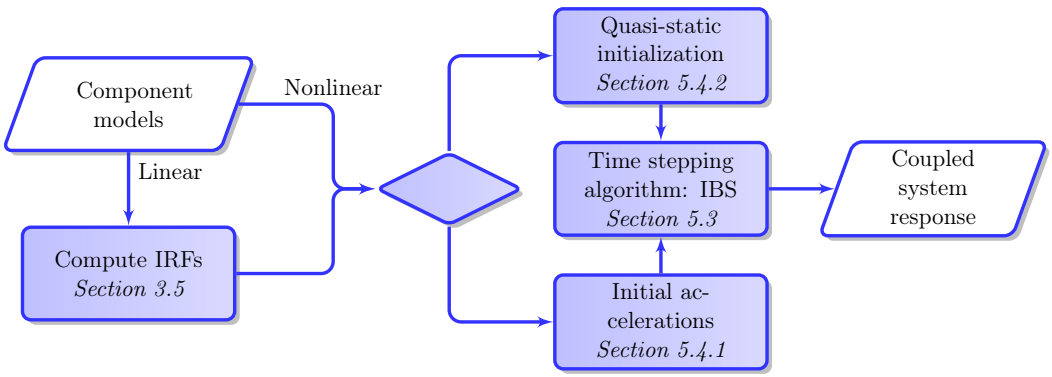

Figure 5.3: *Steps required for using Impulse Based Substructuring.*

The first step of generating the substructure IRFs is presented in chapter 3. Then, in order to initialize the Impulse Based Substructuring method, one can either apply the approach of initial accelerations or start from an initial static equilibrium, as is shown in section 5.4. Finally, in sections 5.2 and 5.3 the time stepping scheme is presented.

The biggest gain comes from the fact that one can reduce the cost per iteration since the linear substructures (described in their IRFs) are fully condensed on the interface of the nonlinear substructures (as is shown in Eq. (5.14)). Traditionally, one reduces the computational cost by representing the linear substructure in a reduced and approximated form (using for instance

CMS techniques). However, the IBS method is no reduction and approximation technique, as the linear domains are exactly accounted for. Thus, the IBS method can be seen as a dynamic condensation on the interface, but not as a reduction method in the classical sense. Another way to reach a similar result would be to:

- set up the time-stepping matrices $\boldsymbol{S}^{(s)}$ of the linear domains, which are thus constant when the time-step size is also kept constant,
- condense those $\boldsymbol{S}^{(s)}$ matrices on the interface,
- assemble the condensed matrices with the nonlinear domains.

In this case no approximation would be made, but it requires building the condensed $\boldsymbol{S}^{(s)}$ matrices on the interface which can be expensive. In the IBS method, no real condensation is needed, since the dynamics of the internal of the linear domains is implicitly included in the impulse response. The cost is thus mainly in computing the impulse response and performing the convolution products. Those costs can be kept small if the IRFs are short or if the time period to be simulated is small. If not, one can also apply truncation of the IRFs and resulting convolution product, as was shown in [140] and outlined in section 3.6.

Note that the method is currently limited to simulations with constant and equal time steps and integration parameters. This also means that the IRFs have to be generated with the exact same time steps and integration parameters in order to ensure that the method has the same stability and accuracy properties as the associated generalized-α method. An interesting idea would be to mix different time steps and integration parameters for the different subdomains, as is done for instance in [15, 104]. But in this case the accuracy and stability of the approach will not be found so easily. Hence, one has to determine under which conditions this mixing of integration parameters leads to a stable integration scheme and secondly what the accuracy of the resulting scheme will be.

To summarize the IBS method presented here offers an efficient way to include the dynamic effects of linear components on nonlinear ones. Similar to the classical substructuring techniques (like for instance Craig-Bampton) it requires sharing a minimum of information between parties responsible for different parts of a composed structure. Here only the impulse responses on the interface are required and to the contrary of CMS methods, the dynamics of the substructures undergo no approximation. Therefore the proposed method has significant advantages in ensuring that the global dynamics are efficiently and accurately computed in collaborative projects.

6

Internal Loading on Substructure Models

"Ohne Mathematik tappt man doch immer im Dunkeln."

– Werner von Siemens

6.1 Issues with distributed loading on component models

A problem often encountered in the field of dynamic substructuring is to properly determine and represent forces acting on the internal degrees of freedom of a substructure. If one uses experimental models, these forces are often not measurable as one can only measure their effects as accelerations at the discrete measurement points, or as reaction forces if the substructure is constrained in a test stand. If one would measure the constraint forces or displacements at the interfaces to other substructures, one in fact measures the excitation that the substructure on the "source" side applies on the other substructures (the "receivers"). It is shown that these constraint forces (or blocked forces) can be used, for instance, in a transfer path analysis to determine the effect of running gears on the noise in a vehicle [32, 33]. On the other hand, one can also use the free interface displacements in a frequency based substructuring (FBS) analysis to determine the effect of factory floor vibrations on high precision machinery [177].[1] Hence, by using these methods there is no need to determine the true internal forces of the source structure, which is practically impossible.

The problem of excitations on internal DoFs is also encountered when applying substructuring methods for numerical models in the time domain, such as Component Mode Synthesis (section 2.2) and the more recent Impulse based Substructuring (chapter 5), which are used to reduce the computational effort. Here, one usually distinguishes between non-retained (internal) DoFs and retained (boundary) DoFs, which are the more interesting ones as they usually serve as the interface to other substructures or act as an input for external forces. Hence, when reducing a substructure, one generally wants to retain the boundary DoFs and capture the internal DoFs in either a modal basis (in the case of CMS) or implicitly include their behavior in an impulse response function (in the case of IBS). These methods are able to significantly reduce the number

[1] Note that these methods are highly related to mobility and impedance methods [57, 61], which originate from the field of electrical engineering.

of DoFs, while leading to accurate simulation results, if the external forces are only exciting the retained DoFs. If a large part of the structure is force loaded, one can no longer include all these DoFs in the subset of retained DoFs, as this leads to unacceptably large (reduced) substructure models and cripples the effectiveness of the CMS and IBS approaches. On the other hand, if one includes the (large) set of force loaded DoFs in the non-retained nodal DoFs, one cannot guarantee that the reduction basis captures the effect of the external forces correctly.

In this chapter three different strategies are presented that allow for efficiently and accurately handling distributed loads applied on the internal DoFs. In section 6.2 this is achieved using the idea of a spectral decomposition; by applying a proper orthogonal decomposition to the time series of external forces. The approach of *equivalent blocked forces* is introduced in section 6.3, where it is analytically proven that the effect of the internal forces on the "source" side are transmitted correctly to the neighboring "receiver" substructures. In section 6.4 the *dual* of the blocked force approach is presented, which uses equivalent free interface displacements to transmit the loads on the "source" substructure to the "receiver" components. Again, it can be analytically proven that the resulting forcing effect onto the "receiver" structures is exact. Finally, in section 6.5 an overview of the three different approaches, with their advantages and disadvantages, is given. Note that all the methods presented in this chapter are only valid if both the model of the source and the loading applied to it are linear.

This chapter is based on work presented in [141, 171, 183].

6.2 Spatial reduction of external loads

The first approach, discussed in this chapter, that allows for efficiently and accurately including the distributed forces in a dynamic substructure analysis is based on the concept of a spatial reduction. In section 2.5 it was outlined how one can include modal truncation vectors to the reduction basis and in section 3.4.4 it was shown that one is also able to compute impulse response functions using a distributed force as input. In both methods however, one requires a set of shapes, $\boldsymbol{X}$ in Eqs. (2.26) and (3.43), that accurately represent the spatial distribution of the loads on the structure. In this section it is shown how one can obtain these force shapes by means of a Proper Orthogonal Decomposition (POD).

POD, which is also known as Principle Component Analysis (PCA) or the Karhunen–Loève Transform (KLT), is a mathematical data analysis method for efficient analysis of complex data [19]. The POD method is a so-called orthogonal linear transformation, transforming data dependent on n possibly correlated variables into a reduced or equal set of uncorrelated variables, called principal components.

Again, assuming that the system at hand consists of N DoFs and n_{max} time steps, the matrix containing the full force time series can be constructed,

$$\boldsymbol{F} = \begin{bmatrix} \boldsymbol{f}_0 & \boldsymbol{f}_1 & \cdots & \boldsymbol{f}_{n_{max}} \end{bmatrix}, \tag{6.1}$$

where the dimensions of $\boldsymbol{F}$ are $N \times n_{max}$. As we want to include the most important force shape distributions, a Singular Value Decomposition (SVD) is applied to $\boldsymbol{F}$:

$$\boldsymbol{F} = \boldsymbol{U}\boldsymbol{\Sigma}\boldsymbol{V}^T. \tag{6.2}$$

The matrix $\boldsymbol{U}$ is a square $(N \times N)$ matrix of left singular vectors, $\boldsymbol{\Sigma}$ is a $(N \times n_{max})$ matrix containing the singular values and $\boldsymbol{V}$ is a $(n_{max} \times n_{max})$ matrix of right singular vectors. In

addition, $\boldsymbol{U}$ and $\boldsymbol{V}$ are both orthonormal matrices, such that:

$$\boldsymbol{U}^T\boldsymbol{U} = \boldsymbol{I},$$
$$\boldsymbol{V}^T\boldsymbol{V} = \boldsymbol{I}.$$

By dividing the left singular vectors by the number of time steps (n_{max}) the proper orthogonal modes (POMs) are obtained. By doing the same for the singular value contained in $\boldsymbol{\Sigma}$ the proper orthogonal values (POVs) are obtained. The POMs can now be interpreted as time-invariant force shape distributions and the associated proper orthogonal value indicates how important the POM is in representing the total force, hence they represent the relative amount of energy captured by the corresponding POMs. The columns of the right singular vectors ($\boldsymbol{V}$) contain the time modulation of the corresponding POM of the associated POMs, normalized by the POVs.

It can be shown that, because of its formulation, the POD is optimal in a least squares sense when considering the energy in the snapshots. This means that the POMs form a vector basis that captures more energy per mode than any other set of basis vectors [93, 94]. Hence, often only few modes are needed to capture a large amount of the system's energy and these thus form an efficient reduction basis $\boldsymbol{X}$ for the applied forces.

6.3 Equivalent blocked force method

An alternative to reducing the internal forces, as presented in section 6.2, is to transform these to the boundary DoFs of the substructure as these are retained after the reduction or in the substructure IRFs. As in a substructuring analysis there is only a direct link between the different substructures through the boundary DoFs, and thus not through the internal DoFs, an equivalent force needs to be found that ensures that the boundary response of the source substructure is exact. In section 6.3.1, it will be proven that such an equivalent force does exist, which is in fact equal to the blocked interface force with an opposite sign, as is shown in section 6.3.2. In section 6.3.3 the practical application and benefits of the blocked force method are discussed.

6.3.1 Derivation of the equivalent forces needed at the interface

The DoFs of the source component are split into a set of internal DoFs and a set of boundary DoFs. If this is substituted in the block-matrix representation of the generalized-α time integration method, given in Eq. (3.21), one finds for the first two time steps the following:

$$\begin{bmatrix} \boldsymbol{A}_{[ii]} & \boldsymbol{A}_{[ib]} & \boldsymbol{0} & \boldsymbol{0} \\ \boldsymbol{A}_{[bi]} & \boldsymbol{A}_{[bb]} & \boldsymbol{0} & \boldsymbol{0} \\ \boldsymbol{N}_{[ii]} & \boldsymbol{N}_{[ib]} & \boldsymbol{Q}_{[ii]} & \boldsymbol{Q}_{[ib]} \\ \boldsymbol{N}_{[bi]} & \boldsymbol{N}_{[bb]} & \boldsymbol{Q}_{[bi]} & \boldsymbol{Q}_{[bb]} \end{bmatrix} \begin{bmatrix} \boldsymbol{z}_{[i],0} \\ \boldsymbol{z}_{[b],0} \\ \boldsymbol{z}_{[i],1} \\ \boldsymbol{z}_{[b],1} \end{bmatrix} = \begin{bmatrix} \check{\boldsymbol{f}}_{[i],0} \\ \boldsymbol{0} \\ \check{\boldsymbol{f}}_{[i],1} \\ \boldsymbol{0} \end{bmatrix}. \tag{6.3}$$

Note here that the derivation still holds if $\check{\boldsymbol{f}}_{[b],n} \neq \boldsymbol{0}$, but for clarity the forces on the interface (and non-zero initial conditions) are discarded in the current discussion. Also note that in case of using the generalized-α method for time integration, the coupling matrices $\boldsymbol{N}_{[ib]}$ and $\boldsymbol{N}_{[ib]}$ are non-zero and equal to:

$$\boldsymbol{N}_{[ib]} = \begin{bmatrix} \boldsymbol{0} & \boldsymbol{0} & \boldsymbol{0} \\ \boldsymbol{0} & \boldsymbol{0} & \boldsymbol{0} \\ \alpha_f \boldsymbol{K}_{[ib]} & \alpha_f \boldsymbol{C}_{[ib]} & \alpha_m \boldsymbol{M}_{[ib]} \end{bmatrix}, \quad \boldsymbol{N}_{[bi]} = \begin{bmatrix} \boldsymbol{0} & \boldsymbol{0} & \boldsymbol{0} \\ \boldsymbol{0} & \boldsymbol{0} & \boldsymbol{0} \\ \alpha_f \boldsymbol{K}_{[bi]} & \alpha_f \boldsymbol{C}_{[bi]} & \alpha_m \boldsymbol{M}_{[bi]} \end{bmatrix}.$$

The goal of this section is to find the equivalent interface forces that result in the exact same response for the boundary DoFs of the "source" substructure at hand. Therefore, in section 6.3.1.1 the initial time step is evaluated, such that the equivalent force is derived for this time step and it is shown that the response of the boundary DoFs is exact with respect to the original problem. In section 6.3.1.2 the same exercise is performed for t_1, where it is again shown that an equivalent interface force can be found that results in the correct response of the boundary DoFs. This result is then used to generalize the approach for all remaining time steps.

6.3.1.1 Response at the initial time step

In order to compute the response at the initial time step, Eq. (6.4) is taken from Eq. (6.3):

$$\begin{bmatrix} \boldsymbol{A}_{[ii]} & \boldsymbol{A}_{[ib]} \\ \boldsymbol{A}_{[bi]} & \boldsymbol{A}_{[bb]} \end{bmatrix} \begin{bmatrix} \boldsymbol{z}_{[i],0} \\ \boldsymbol{z}_{[b],0} \end{bmatrix} = \begin{bmatrix} \check{\boldsymbol{f}}_{[i],0} \\ \boldsymbol{0} \end{bmatrix}. \tag{6.4}$$

Note that Eq. (6.4) is referred to as being the reference problem at the initial time (t_0). Hence, the response can be found by solving the given set of equations.

For obtaining the equivalent force at t_0, the derivation is started from Eq. (6.4). Firstly, the internal forces are condensed onto the boundary DoFs, such that the following is found:

$$\left(\boldsymbol{A}_{[bb]} - \boldsymbol{A}_{[bi]}\boldsymbol{A}_{[ii]}^{-1}\boldsymbol{A}_{[ib]}\right)\boldsymbol{z}_{[b],0} = -\boldsymbol{A}_{[bi]}\boldsymbol{A}_{[ii]}^{-1}\check{\boldsymbol{f}}_{[i],0}, \tag{6.5}$$

which can be rewritten as:

$$\bar{\boldsymbol{A}}_{[bb]}\boldsymbol{z}_{[b],0} = \check{\boldsymbol{f}}_{[b],0}^{eq},$$

where $\bar{\boldsymbol{A}}_{[bb]}$ is defined as the Schur complement of matrix $\boldsymbol{A}$ and $\check{\boldsymbol{f}}_{[b],0}^{eq}$ is defined as the equivalent force at the interface. If one expands the left hand side of Eq. (6.5), the original set of equations is obtained again, but with a different loading on the right hand side, as can be seen in Eq. (6.6). It can clearly be seen that the set of loads on the internal DoFs are replaced by a set of alternative loads on the boundary DoFs;

$$\begin{bmatrix} \boldsymbol{A}_{[ii]} & \boldsymbol{A}_{[ib]} \\ \boldsymbol{A}_{[bi]} & \boldsymbol{A}_{[bb]} \end{bmatrix} \begin{bmatrix} \tilde{\boldsymbol{z}}_{[i],0} \\ \tilde{\boldsymbol{z}}_{[b],0} \end{bmatrix} = \begin{bmatrix} \boldsymbol{0} \\ -\boldsymbol{A}_{[bi]}\boldsymbol{A}_{[ii]}^{-1}\check{\boldsymbol{f}}_{[i],0} \end{bmatrix} = \begin{bmatrix} \boldsymbol{0} \\ \check{\boldsymbol{f}}_{[b],0}^{eq} \end{bmatrix}. \tag{6.6}$$

Hence, the *equivalent* problem has now been defined, which is different from the original problem given in Eq. (6.4). Therefore, the variables are changed from $\boldsymbol{z}_{[\star],0}$ to $\tilde{\boldsymbol{z}}_{[\star],0}$, where the $\tilde{\star}$ denotes the fact that one is now working with the equivalent problem. Now, by comparing the reference result, obtained from solving Eq. (6.4),

$$\begin{bmatrix} \boldsymbol{z}_{[i],0} \\ \boldsymbol{z}_{[b],0} \end{bmatrix} = \begin{bmatrix} \left(\boldsymbol{A}_{[ii]}^{-1} + \boldsymbol{A}_{[ii]}^{-1}\boldsymbol{A}_{[ib]}\bar{\boldsymbol{A}}_{[bb]}^{-1}\boldsymbol{A}_{[bi]}\boldsymbol{A}_{[ii]}^{-1}\right)\check{\boldsymbol{f}}_{[i],0} \\ -\bar{\boldsymbol{A}}_{[bb]}^{-1}\boldsymbol{A}_{[bi]}\boldsymbol{A}_{[ii]}^{-1}\check{\boldsymbol{f}}_{[i],0} \end{bmatrix}, \tag{6.7}$$

with the results obtained with the equivalent loading in Eq. (6.8),

$$\begin{bmatrix} \tilde{\boldsymbol{z}}_{[i],0} \\ \tilde{\boldsymbol{z}}_{[b],0} \end{bmatrix} = \begin{bmatrix} \boldsymbol{A}_{[ii]}^{-1}\boldsymbol{A}_{[ib]}\bar{\boldsymbol{A}}_{[bb]}^{-1}\boldsymbol{A}_{[bi]}\boldsymbol{A}_{[ii]}^{-1}\check{\boldsymbol{f}}_{[i],0} \\ -\bar{\boldsymbol{A}}_{[bb]}^{-1}\boldsymbol{A}_{[bi]}\boldsymbol{A}_{[ii]}^{-1}\check{\boldsymbol{f}}_{[i],0} \end{bmatrix}, \tag{6.8}$$

it is clear that the exact same response is found for the boundary DoFs ($\tilde{\boldsymbol{z}}_{[b],0}$), but that the response of the internal DoFs ($\tilde{\boldsymbol{z}}_{[i],0}$) differs from the reference result. Thus, the relation between the responses obtained from the reference problem and the equivalent problem is the following:

$$\begin{bmatrix} \tilde{\boldsymbol{z}}_{[i],0} \\ \tilde{\boldsymbol{z}}_{[b],0} \end{bmatrix} = \begin{bmatrix} \boldsymbol{z}_{[i],0} - \boldsymbol{A}_{[ii]}^{-1}\check{\boldsymbol{f}}_{[i],0} \\ \boldsymbol{z}_{[b],0} \end{bmatrix}. \tag{6.9}$$

As the response at the next time step is highly dependent on the current step, one has to be sure that the error made on the response of the internal DoFs from using the equivalent forces, will not affect the response of the boundary DoFs in the next time step.

6.3.1.2 Response at the next time steps

Therefore the same exercise is performed for the next time step (t_1) in Eq. (6.3), one therefore has to solve:

$$\begin{bmatrix} \boldsymbol{Q}_{[ii]} & \boldsymbol{Q}_{[ib]} \\ \boldsymbol{Q}_{[bi]} & \boldsymbol{Q}_{[bb]} \end{bmatrix} \begin{bmatrix} \boldsymbol{z}_{[i],1} \\ \boldsymbol{z}_{[b],1} \end{bmatrix} = \begin{bmatrix} \check{\boldsymbol{f}}_{[i],1} \\ \boldsymbol{0} \end{bmatrix} - \begin{bmatrix} \boldsymbol{N}_{[ii]} & \boldsymbol{N}_{[ib]} \\ \boldsymbol{N}_{[bi]} & \boldsymbol{N}_{[bb]} \end{bmatrix} \begin{bmatrix} \boldsymbol{z}_{[i],0} \\ \boldsymbol{z}_{[b],0} \end{bmatrix}. \tag{6.10}$$

The reference response at t_1 is obtained from solving Eq. (6.10). Here, one can easily see that the response of the boundary DoFs ($\boldsymbol{z}_{[b],1}$) is also a function of the response of the internal DoFs in the previous time step ($\boldsymbol{z}_{[i],0}$).

Similar to the approach followed at t_0, the next step is to start from Eq. (6.10) and, again, condense the internal DoFs on the interface DoFs,

$$\bar{\boldsymbol{Q}}_{[bb]}\boldsymbol{z}_{[b],1} = -\boldsymbol{Q}_{[bi]}\boldsymbol{Q}_{[ii]}^{-1}\left(\check{\boldsymbol{f}}_{[i],1} - \boldsymbol{N}_{[ii]}\boldsymbol{z}_{[i],0} - \boldsymbol{N}_{[ib]}\boldsymbol{z}_{[b],0}\right) - \boldsymbol{N}_{[bb]}\boldsymbol{z}_{[b],0} - \boldsymbol{N}_{[bi]}\boldsymbol{z}_{[i],0}, \tag{6.11}$$

where $\bar{\boldsymbol{Q}}_{[bb]}$ is the Schur complement of $\boldsymbol{Q}$. As the next step is to re-expand the left hand side of Eq. (6.11) to obtain the equivalent problem, it requires that the set of variables is also changed from the reference set ($\boldsymbol{z}$) to the variables of the equivalent problem ($\tilde{\boldsymbol{z}}$). Therefore, the result obtained in Eq. (6.9) is substituted into Eq. (6.11), which results in the following:

$$\begin{aligned} \bar{\boldsymbol{Q}}_{[bb]}\tilde{\boldsymbol{z}}_{[b],1} = -\boldsymbol{Q}_{[bi]}\boldsymbol{Q}_{[ii]}^{-1}\Big(\check{\boldsymbol{f}}_{[i],1} - \boldsymbol{N}_{[ii]}\left(\tilde{\boldsymbol{z}}_{[i],0} + \boldsymbol{A}_{[ii]}^{-1}\check{\boldsymbol{f}}_{[i],0}\right) - \boldsymbol{N}_{[ib]}\boldsymbol{z}_{[b],0}\Big) \\ -\boldsymbol{N}_{[bb]}\boldsymbol{z}_{[b],0} - \boldsymbol{N}_{[bi]}\left(\tilde{\boldsymbol{z}}_{[i],0} + \boldsymbol{A}_{[ii]}^{-1}\check{\boldsymbol{f}}_{[i],0}\right). \end{aligned} \tag{6.12}$$

It can easily be verified that re-expansion of the left hand side of Eq. (6.12) results in:

$$\begin{aligned} \begin{bmatrix} \boldsymbol{Q}_{[ii]} & \boldsymbol{Q}_{[ib]} \\ \boldsymbol{Q}_{[bi]} & \boldsymbol{Q}_{[bb]} \end{bmatrix} \begin{bmatrix} \tilde{\boldsymbol{z}}_{[i],1} \\ \tilde{\boldsymbol{z}}_{[b],1} \end{bmatrix} = -\begin{bmatrix} \boldsymbol{N}_{[ii]} & \boldsymbol{N}_{[ib]} \\ \boldsymbol{N}_{[bi]} & \boldsymbol{N}_{[bb]} \end{bmatrix} \begin{bmatrix} \tilde{\boldsymbol{z}}_{[i],0} \\ \boldsymbol{z}_{[b],0} \end{bmatrix} + \\ \begin{bmatrix} \boldsymbol{0} \\ -\boldsymbol{Q}_{[bi]}\boldsymbol{Q}_{[ii]}^{-1}\left(\check{\boldsymbol{f}}_{[i],1} - \boldsymbol{N}_{[ii]}\boldsymbol{A}_{[ii]}^{-1}\check{\boldsymbol{f}}_{[i],0}\right) - \boldsymbol{N}_{[bi]}\boldsymbol{A}_{[ii]}^{-1}\check{\boldsymbol{f}}_{[i],0} \end{bmatrix}. \end{aligned} \tag{6.13}$$

Hence, one can determine that the equivalent interface force, $\check{\boldsymbol{f}}_{[b],1}^{eq}$, obtained for this time step is the following:

$$\check{\boldsymbol{f}}_{[b],1}^{eq} = -\boldsymbol{Q}_{[bi]}\boldsymbol{Q}_{[ii]}^{-1}\left(\check{\boldsymbol{f}}_{[i],1} - \boldsymbol{N}_{[ii]}\boldsymbol{A}_{[ii]}^{-1}\check{\boldsymbol{f}}_{[i],0}\right) - \boldsymbol{N}_{[bi]}\boldsymbol{A}_{[ii]}^{-1}\check{\boldsymbol{f}}_{[i],0}. \tag{6.14}$$

The *equivalent* problem for t_1 has now been defined, which is different from the original problem given in Eq. (6.10).

Firstly, in order to be able to compare the reference solution with the one obtained from the equivalent problem, the reference result is again obtained from solving Eq. (6.10),

$$\begin{bmatrix} \boldsymbol{z}_{[i],1} \\ \boldsymbol{z}_{[b],1} \end{bmatrix} = \begin{bmatrix} \left(\boldsymbol{Q}_{[ii]}^{-1} + \boldsymbol{Q}_{[ii]}^{-1}\boldsymbol{Q}_{[ib]}\bar{\boldsymbol{Q}}_{[bb]}^{-1}\boldsymbol{Q}_{[bi]}\boldsymbol{Q}_{[ii]}^{-1}\right)\boldsymbol{a} - \boldsymbol{Q}_{[ii]}^{-1}\boldsymbol{Q}_{[ib]}\bar{\boldsymbol{Q}}_{[bb]}^{-1}\boldsymbol{b} \\ -\bar{\boldsymbol{Q}}_{[bb]}^{-1}\boldsymbol{Q}_{[bi]}\boldsymbol{Q}_{[ii]}^{-1}\boldsymbol{a} + \bar{\boldsymbol{Q}}_{[bb]}^{-1}\boldsymbol{b} \end{bmatrix}, \tag{6.15}$$

where,

$$\begin{aligned}\boldsymbol{a} &= \check{\boldsymbol{f}}_{[i],1} - \boldsymbol{N}_{[ii]}\boldsymbol{z}_{[i],0} - \boldsymbol{N}_{[ib]}\boldsymbol{z}_{[b],0},\\ \boldsymbol{b} &= -\boldsymbol{N}_{[bi]}\boldsymbol{z}_{[i],0} - \boldsymbol{N}_{[bb]}\boldsymbol{z}_{[b],0}.\end{aligned}$$

Secondly, the result from the equivalent problem is obtained by solving Eq. (6.13), which gives:

$$\begin{bmatrix} \tilde{\boldsymbol{z}}_{[i],1} \\ \tilde{\boldsymbol{z}}_{[b],1} \end{bmatrix} = \begin{bmatrix} \left(\boldsymbol{Q}_{[ii]}^{-1} + \boldsymbol{Q}_{[ii]}^{-1}\boldsymbol{Q}_{[ib]}\bar{\boldsymbol{Q}}_{[bb]}^{-1}\boldsymbol{Q}_{[bi]}\boldsymbol{Q}_{[ii]}^{-1}\right)\tilde{\boldsymbol{a}} - \boldsymbol{Q}_{[ii]}^{-1}\boldsymbol{Q}_{[ib]}\bar{\boldsymbol{Q}}_{[bb]}^{-1}\tilde{\boldsymbol{b}} \\ -\bar{\boldsymbol{Q}}_{[bb]}^{-1}\boldsymbol{Q}_{[bi]}\boldsymbol{Q}_{[ii]}^{-1}\tilde{\boldsymbol{a}} + \bar{\boldsymbol{Q}}_{[bb]}^{-1}\tilde{\boldsymbol{b}} \end{bmatrix}, \tag{6.16}$$

where,

$$\begin{aligned}\tilde{\boldsymbol{a}} &= -\boldsymbol{N}_{[ii]}\tilde{\boldsymbol{z}}_{[i],0} - \boldsymbol{N}_{[ib]}\tilde{\boldsymbol{z}}_{[b],0} = -\boldsymbol{N}_{[ii]}\left(\boldsymbol{z}_{[i],0} - \boldsymbol{A}_{[ii]}^{-1}\check{\boldsymbol{f}}_{[i],0}\right) - \boldsymbol{N}_{[ib]}\boldsymbol{z}_{[b],0},\\ \tilde{\boldsymbol{b}} &= \check{\boldsymbol{f}}_{[b],1}^{eq} - \boldsymbol{N}_{[bi]}\tilde{\boldsymbol{z}}_{[i],0} - \boldsymbol{N}_{[bb]}\tilde{\boldsymbol{z}}_{[b],0} = -\boldsymbol{Q}_{[bi]}\boldsymbol{Q}_{[ii]}^{-1}\left(\check{\boldsymbol{f}}_{[i],1} - \boldsymbol{N}_{[ii]}\boldsymbol{A}_{[ii]}^{-1}\check{\boldsymbol{f}}_{[i],0}\right)\\ &\qquad -\boldsymbol{N}_{[bi]}\boldsymbol{z}_{[i],0} - \boldsymbol{N}_{[ib]}\boldsymbol{z}_{[b],0}.\end{aligned}$$

Finally, from comparing the solution obtained from the equivalent loading case (Eq. (6.16)), to the solution of the original problem (Eq. (6.15)), one finds

$$\begin{bmatrix} \tilde{\boldsymbol{z}}_{[i],1} \\ \tilde{\boldsymbol{z}}_{[b],1} \end{bmatrix} = \begin{bmatrix} \boldsymbol{z}_{[i],1} - \boldsymbol{Q}_{[ii]}^{-1}\left(\check{\boldsymbol{f}}_{[i],1} - \boldsymbol{N}_{[ii]}\boldsymbol{A}_{[ii]}^{-1}\check{\boldsymbol{f}}_{[i],0}\right) \\ \boldsymbol{z}_{[b],1} \end{bmatrix}. \tag{6.17}$$

The response of the boundary DoFs is again equal to the reference solution ($\boldsymbol{z}_{[b],1}$), but the response of the internal DoFs differs from the reference solution ($\boldsymbol{z}_{[i],1}$).

As the block-matrix representation of the generalized-α method in Eq. (3.21) shows that each new time step is a repetition of the same blocks, the results obtained in this section can be generalized to:

$$\begin{aligned}\check{\boldsymbol{f}}_{[b],n}^{eq} = &-\boldsymbol{Q}_{[bi]}\left(\sum_{j=1}^{n}\left(-\boldsymbol{Q}_{[ii]}^{-1}\boldsymbol{N}_{[ii]}\right)^{n-j}\boldsymbol{Q}_{[ii]}^{-1}\check{\boldsymbol{f}}_{[i],j} + \left(-\boldsymbol{Q}_{[ii]}^{-1}\boldsymbol{N}_{[ii]}\right)^{n}\boldsymbol{A}_{[ii]}^{-1}\check{\boldsymbol{f}}_{[i],0}\right)\\ &-\boldsymbol{N}_{[bi]}\left(\sum_{j=2}^{n}\left(-\boldsymbol{Q}_{[ii]}^{-1}\boldsymbol{N}_{[ii]}\right)^{n-j}\boldsymbol{Q}_{[ii]}^{-1}\check{\boldsymbol{f}}_{[i],j} + \left(-\boldsymbol{Q}_{[ii]}^{-1}\boldsymbol{N}_{[ii]}\right)^{n-1}\boldsymbol{A}_{[ii]}^{-1}\check{\boldsymbol{f}}_{[i],0}\right),\end{aligned} \tag{6.18}$$

for the equivalent interface force for $n > 0$, which will result in the following responses at any moment in time:

$$\begin{bmatrix} \tilde{\boldsymbol{z}}_{[i],n} \\ \tilde{\boldsymbol{z}}_{[b],n} \end{bmatrix} = \begin{bmatrix} \boldsymbol{z}_{[i],n} - \sum_{j=1}^{n}\left(-\boldsymbol{Q}_{[ii]}^{-1}\boldsymbol{N}_{[ii]}\right)^{n-j}\boldsymbol{Q}_{[ii]}^{-1}\check{\boldsymbol{f}}_{[i],j} - \left(-\boldsymbol{Q}_{[ii]}^{-1}\boldsymbol{N}_{[ii]}\right)^{n}\boldsymbol{A}_{[ii]}^{-1}\check{\boldsymbol{f}}_{[i],0} \\ \boldsymbol{z}_{[b],n} \end{bmatrix}. \tag{6.19}$$

Hence, one is able to transform the forces on the internal DoFs to equivalent forces on the interface (Eq. (6.18)), that result in the exact same response on the interface.

6.3.2 Using constraint forces as equivalent forces at the interface

Although Eq. (6.18) has a clear recursive behavior from which one could easily compute $\hat{\boldsymbol{f}}_{[b],n}^{eq}$, it cannot be directly related to any physical interpretation. In this section it will be shown that the expression found for the equivalent force on the interface is equal to the force one finds by

restraining the substructure, that is loaded on its internal DoFs, on the boundary DoFs. The associated time integration equations would then write:

$$\begin{bmatrix} \boldsymbol{A}_{[ii]} & \boldsymbol{A}_{[ib]} & \boldsymbol{0} & \boldsymbol{0} \\ \boldsymbol{A}_{[bi]} & \boldsymbol{A}_{[bb]} & \boldsymbol{0} & \boldsymbol{0} \\ \boldsymbol{N}_{[ii]} & \boldsymbol{N}_{[ib]} & \boldsymbol{Q}_{[ii]} & \boldsymbol{Q}_{[ib]} \\ \boldsymbol{N}_{[bi]} & \boldsymbol{N}_{[bb]} & \boldsymbol{Q}_{[bi]} & \boldsymbol{Q}_{[bb]} \end{bmatrix} \begin{bmatrix} \boldsymbol{z}^{con}_{[i],0} \\ \boldsymbol{0} \\ \boldsymbol{z}^{con}_{[i],1} \\ \boldsymbol{0} \end{bmatrix} = \begin{bmatrix} \check{\boldsymbol{f}}_{[i],0} \\ \check{\boldsymbol{g}}_{[b],0} \\ \check{\boldsymbol{f}}_{[i],1} \\ \check{\boldsymbol{g}}_{[b],1} \end{bmatrix}, \tag{6.20}$$

where, $\check{\boldsymbol{g}}_{[b],n}$ is the array that contains the constraint forces on the clamped interface points. This force is denoted by $\boldsymbol{g}_{[b],n}$, as it can be interpreted as being a connection force that connects the source substructure to a substructure with infinite stiffness and mass. Hence, from the initial time step, one directly finds that

$$\check{\boldsymbol{g}}_{[b],0} = \boldsymbol{A}_{[bi]}\boldsymbol{A}^{-1}_{[ii]}\check{\boldsymbol{f}}_{[i],0},$$

which is equal to the negative equivalent force at the interface in Eq. (6.5). The constraint force at t_1 is again computed using Eq. (6.20), thereby resulting in:

$$\check{\boldsymbol{g}}_{[b],1} = \boldsymbol{Q}_{[bi]}\boldsymbol{Q}^{-1}_{[ii]}\left(\check{\boldsymbol{f}}_{[i],1} - \boldsymbol{N}_{[ii]}\boldsymbol{A}^{-1}_{[ii]}\check{\boldsymbol{f}}_{[i],0}\right) + \boldsymbol{N}_{[bi]}\boldsymbol{A}^{-1}_{[ii]}\check{\boldsymbol{f}}_{[i],0}.$$

Due to the repeating block-matrix pattern in Eq. (3.21), the expression can again be generalized for all time steps, such that:

$$\begin{aligned} \check{\boldsymbol{g}}_{[b],n} = \boldsymbol{Q}_{[bi]} &\left(\sum_{j=1}^{n}\left(-\boldsymbol{Q}^{-1}_{[ii]}\boldsymbol{N}_{[ii]}\right)^{n-j}\boldsymbol{Q}^{-1}_{[ii]}\check{\boldsymbol{f}}_{[i],j} + \left(-\boldsymbol{Q}^{-1}_{[ii]}\boldsymbol{N}_{[ii]}\right)^{n}\boldsymbol{A}^{-1}_{[ii]}\check{\boldsymbol{f}}_{[i],0}\right) \\ +\boldsymbol{N}_{[bi]} &\left(\sum_{j=2}^{n}\left(-\boldsymbol{Q}^{-1}_{[ii]}\boldsymbol{N}_{[ii]}\right)^{n-j}\boldsymbol{Q}^{-1}_{[ii]}\check{\boldsymbol{f}}_{[i],j} + \left(-\boldsymbol{Q}^{-1}_{[ii]}\boldsymbol{N}_{[ii]}\right)^{n-1}\boldsymbol{A}^{-1}_{[ii]}\check{\boldsymbol{f}}_{[i],0}\right) = -\check{\boldsymbol{f}}^{eq}_{[b],n}. \end{aligned} \tag{6.21}$$

Hence, one can find the equivalent force on the interface (given in Eq. (6.18)) by simply computing the constraint forces of the stand-alone substructure.[2] From a practical point of view, this is easy to implement, as most of the finite element packages are able to perform time integrations.

Even though it was found in Eq. (6.19) that an error on the internal response is introduced by applying the equivalent blocked forces at the interface, a simple correction on the erroneous internal response can be applied. By substituting the result from Eq. (6.20) into Eq. (6.19), it can be observed that the response computed using the equivalent blocked forces can be written according to:

$$\begin{bmatrix} \tilde{\boldsymbol{z}}_{[i],n} \\ \tilde{\boldsymbol{z}}_{[b],n} \end{bmatrix} = \begin{bmatrix} \boldsymbol{z}_{[i],n} - \boldsymbol{z}^{con}_{[i],n} \\ \boldsymbol{z}_{[b],n} \end{bmatrix}. \tag{6.22}$$

Therefore, the full response of the internal DoFs can be found from:

$$\boldsymbol{z}_{[i],n} = \tilde{\boldsymbol{z}}_{[i],n} + \boldsymbol{z}^{con}_{[i],n}. \tag{6.23}$$

Note that the method discussed in this section can only be applied if the "source" structure (which is force-loaded on its internal DoFs) is linear. Though, a fundamental difference with the corresponding method in the frequency domain is that the connected substructures (the "receivers") can be nonlinear. Also, as the procedure is only valid for linear systems, the time integration procedure required to compute the blocked forces is relatively cheap. The time stepping matrix (used in the generalized-α method) only needs to be factorized once and allows to find the time response at each time step by simply applying forward and backward substitutions.

[2] Note that a similar result is found in Eq. (4.14), where the forcing effect of substructure B onto A is also by means of a blocked force.

6.3.3 Practical implementation of the blocked force method

From the analysis performed in the previous sections it can thus be concluded that one can transform the loading on the internal DoFs to the interface, such that the receiver substructures do not notice this transformation. In addition it was found that this equivalent force is equal to the time series of constraint forces (with an opposite sign) that one would obtain by constraining the source substructure at its interface and performing a time integration.

From a practical point of view, this is an important result, as implementing the method in practice will be quite straightforward now. The procedure is shown in figure 6.1, where the different steps are shown from left to right. Firstly, the original problem is split into substructures (or components), which are in this case the offshore jacket structure loaded by a given set of externally applied wave forces (the "source" substructure, denoted by $\star^{(S)}$) and the wind turbine, loaded by a set of forces resulting from the (nonlinear) aero-elastic coupling (the "receiver" substructure, denoted by $\star^{(R)}$). Now, one could apply the method to transform the wave loads to equivalent forces on the interface on the offshore jacket. Hence, in the next step (*Compute constraint force*) the constrained response of the jacket is computed by time integrating:

$$\boldsymbol{M}_{[ii]}^{(S)}\ddot{\boldsymbol{u}}_{[i]}^{(S)} + \boldsymbol{C}_{[ii]}^{(S)}\dot{\boldsymbol{u}}_{[i]}^{(S)} + \boldsymbol{K}_{[ii]}^{(S)}\boldsymbol{u}_{[i]}^{(S)} = \boldsymbol{f}_{[i]}^{(S)}. \tag{6.24}$$

From the resulting accelerations, velocities and displacements, one can obtain the constraint forces at the interface for each time step. As it was shown that the constraint forces are equal to (but opposite in sign) the equivalent interface forces needed, one can directly obtain these from solving:

$$-\boldsymbol{f}_{[b]}^{eq} = \boldsymbol{M}_{[bi]}^{(S)}\ddot{\boldsymbol{u}}_{[i]}^{(S)} + \boldsymbol{C}_{[bi]}^{(S)}\dot{\boldsymbol{u}}_{[i]}^{(S)} + \boldsymbol{K}_{[bi]}^{(S)}\boldsymbol{u}_{[i]}^{(S)}. \tag{6.25}$$

As the jacket model is linear, it can be reduced using one of the classical CMS or IBS methods, thereby significantly reducing the computational effort needed for solving the final nonlinear wind turbine simulations. By finally assembling the nonlinear wind turbine model with the reduced jacket model and applying the equivalent interface force, one can compute the correct response of the turbine far more efficiently then without the reduction. In addition, if one applies one of the CMS techniques outlined in chapter 2, the full jacket response can be obtained with little extra costs. By substituting the response of the reduced model with the equivalent blocked forces ($\tilde{\boldsymbol{q}}_n^{(S)}$) in Eq. (2.2) and taking Eq. (6.23) into account, one finds that the internal response of the jacket (in terms of displacements) is easily reconstructed:

$$\boldsymbol{u}_{[i],n}^{(S)} = \boldsymbol{R}_{[i]}^{(S)}\tilde{\boldsymbol{q}}_n^{(S)} + \boldsymbol{u}_{[i],n}^{(S),con}. \tag{6.26}$$

The accuracy of the response found is obviously highly dependent on the quality of the reduction basis used. Note that the time stepping method and time steps used, should be identical to those used in Eq. (6.24) and that the used superelement has to be able to describe the dynamics of the jacket accurately.

The blocked force approach presented here has a number of advantages. Firstly, there is no approximation in the forcing effect felt by the receiver substructures. Secondly, it eliminates the need for a load case dependent reduction basis (section 2.5) or set of IRFs (section 3.4.4). Thirdly, it allows for an easy interaction between different companies or project teams, as only information on the interfaces needs to be shared. The downside is obviously, that one is required to perform an extra time integration for each loading scenario in order to determine the equivalent blocked forces. Note however, that as the method is only valid for linear systems, the time integration itself is relatively cheap when compared to a full (implicit) nonlinear time integration.

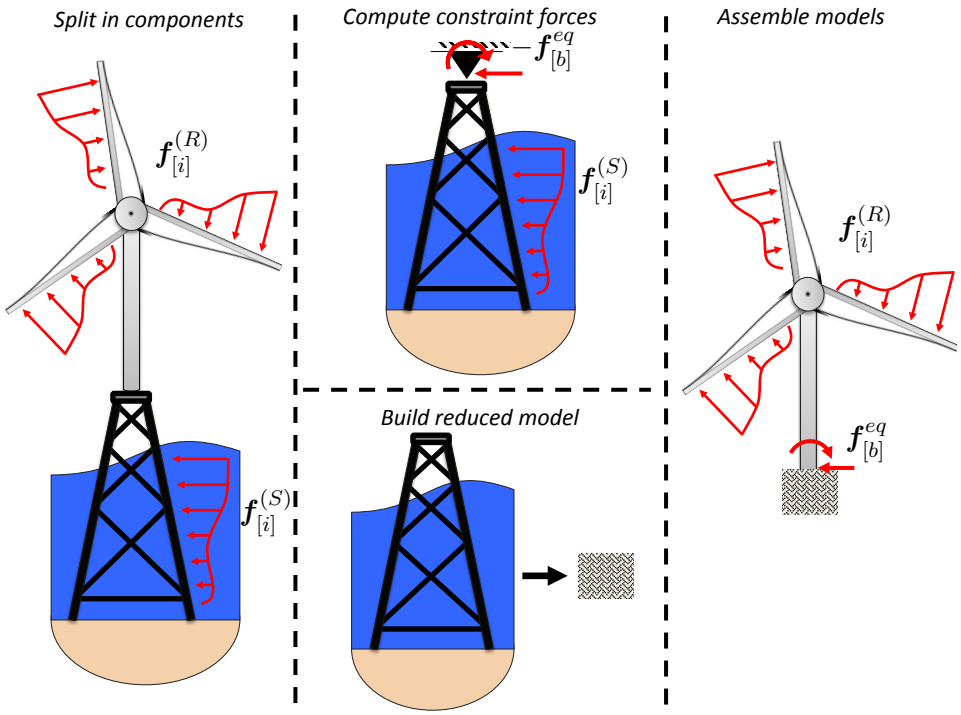

Figure 6.1: *Steps taken when using the methods of equivalent blocked forces in the time domain.*

An approach that could simplify the proposed blocked force approach is to use statically obtained blocked forces, such that one assumes that the response of the "source" substructure to the applied forces is in the quasi-static regime. In that case, one can neglect all the damping and inertia contributions and one simply has to solve the associated static problem, such that:

$$\begin{bmatrix} \boldsymbol{K}_{[ii]} & \boldsymbol{K}_{[ib]} \\ \boldsymbol{K}_{[bi]} & \boldsymbol{K}_{[bb]} \end{bmatrix} \begin{bmatrix} \boldsymbol{u}^{con}_{[i],n} \\ \boldsymbol{0} \end{bmatrix} = \begin{bmatrix} \boldsymbol{f}_{[i],n} \\ -\boldsymbol{f}^{eq}_{[b],n} \end{bmatrix}, \tag{6.27}$$

where both $\boldsymbol{u}^{con}_{[i],n}$ and $\boldsymbol{f}^{eq}_{[b],n}$ are unknowns. A strong indication of whether a (quasi-) static analysis is allowed is given by comparing the first fixed interface eigenfrequency $\omega_{[i],1}$, obtained from the following eigenvalue problem:

$$\left(\boldsymbol{K}_{[ii]} - \omega^2_{[i],j}\boldsymbol{M}_{[ii]}\right)\boldsymbol{\phi}_{[i],j} = \boldsymbol{0},$$

with the spectrum of the externally applied forces. Note however, that the forcing effect on the "receiver" substructures is no longer exact, as is the case when using the dynamically determined blocked forces.

6.4 Method of equivalent free interface displacements

The dual counterpart of the blocked force approach, presented in section 6.3, is the method that employs equivalent free interface displacements. By substituting the dual assembled set of equation of motion (see section 2.6.2) into the block matrix representation of the generalized-α time integration method, given in Eq. (3.21), one obtains:

$$\begin{bmatrix} \boldsymbol{A}^{(S)} & \boldsymbol{0} & \check{\boldsymbol{B}}^{(S)^T} & \boldsymbol{0} & \boldsymbol{0} & \boldsymbol{0} \\ \boldsymbol{0} & \boldsymbol{A}^{(R)} & \check{\boldsymbol{B}}^{(R)^T} & \boldsymbol{0} & \boldsymbol{0} & \boldsymbol{0} \\ \check{\boldsymbol{B}}^{(S)} & \check{\boldsymbol{B}}^{(R)} & \boldsymbol{0} & \boldsymbol{0} & \boldsymbol{0} & \boldsymbol{0} \\ \boldsymbol{N}^{(S)} & \boldsymbol{0} & \boldsymbol{0} & \boldsymbol{Q}^{(S)} & \boldsymbol{0} & \check{\boldsymbol{B}}^{(S)^T} \\ \boldsymbol{0} & \boldsymbol{N}^{(R)} & \boldsymbol{0} & \boldsymbol{0} & \boldsymbol{Q}^{(R)} & \check{\boldsymbol{B}}^{(R)^T} \\ \boldsymbol{0} & \boldsymbol{0} & \boldsymbol{0} & \check{\boldsymbol{B}}^{(S)} & \check{\boldsymbol{B}}^{(R)} & \boldsymbol{0} \end{bmatrix} \begin{bmatrix} \boldsymbol{z}_0^{(S)} \\ \boldsymbol{z}_0^{(R)} \\ \boldsymbol{\lambda}_0 \\ \boldsymbol{z}_1^{(S)} \\ \boldsymbol{z}_1^{(R)} \\ \boldsymbol{\lambda}_1 \end{bmatrix} = \begin{bmatrix} \check{\boldsymbol{f}}_0^{(S)} \\ \boldsymbol{0} \\ \boldsymbol{0} \\ \check{\boldsymbol{f}}_1^{(S)} \\ \boldsymbol{0} \\ \boldsymbol{0} \end{bmatrix}, \tag{6.28}$$

where $\check{\boldsymbol{B}}^{(s)} = \begin{bmatrix} \boldsymbol{B}^{(s)} & \boldsymbol{0} & \boldsymbol{0} \end{bmatrix}$, which is a signed Boolean operator that selects the displacements on the boundary DoFs, from the total set of displacements, velocities and accelerations ($\boldsymbol{z}_n^{(s)}$) and enforces the compatibility condition. Note that the "source" substructure is denoted by $\star^{(S)}$ and the receiver components by $\star^{(R)}$.

For finding the equivalent interface displacements, the same steps are taken as in section 6.3. Therefore, it is first shown that one can obtain an equivalent type of loading, that results in the exact response in the receiver substructures.

6.4.1 Condensing the internal force on the boundary degrees of freedom

The first step is to condense the source substructure on the interface, which is similar to the approach in section 6.3.1. Note that, as the interface is described here in terms of Lagrange multipliers, one condenses in fact the entire set of accelerations, velocities and displacements of the source subsystem ($\boldsymbol{z}_0^{(S)}$), and not just its internal set of DoFs, onto the interface.

6.4.1.1 Response at the initial time step

Again, starting at t_0, the following set of equations are obtained from Eq. (6.28):

$$\begin{bmatrix} \boldsymbol{A}^{(S)} & \boldsymbol{0} & \check{\boldsymbol{B}}^{(S)^T} \\ \boldsymbol{0} & \boldsymbol{A}^{(R)} & \check{\boldsymbol{B}}^{(R)^T} \\ \check{\boldsymbol{B}}^{(S)} & \check{\boldsymbol{B}}^{(R)} & \boldsymbol{0} \end{bmatrix} \begin{bmatrix} \boldsymbol{z}_0^{(S)} \\ \boldsymbol{z}_0^{(R)} \\ \boldsymbol{\lambda}_0 \end{bmatrix} = \begin{bmatrix} \check{\boldsymbol{f}}_0^{(S)} \\ \boldsymbol{0} \\ \boldsymbol{0} \end{bmatrix}. \tag{6.29}$$

Solving this set results in the reference response of both substructures ($\boldsymbol{z}_0^{(s)}$) and the associated interface forces ($\boldsymbol{\lambda}_0$) at t_0. Similar to the previous sections, the source substructure is condensed on the interface, which results in:

$$\begin{bmatrix} \boldsymbol{A}^{(R)} & \check{\boldsymbol{B}}^{(R)^T} \\ \check{\boldsymbol{B}}^{(R)} & -\check{\boldsymbol{B}}^{(S)} \boldsymbol{A}^{(S)^{-1}} \check{\boldsymbol{B}}^{(S)^T} \end{bmatrix} \begin{bmatrix} \boldsymbol{z}_0^{(R)} \\ \boldsymbol{\lambda}_0 \end{bmatrix} = \begin{bmatrix} \boldsymbol{0} \\ -\check{\boldsymbol{B}}^{(S)} \boldsymbol{A}^{(S)^{-1}} \check{\boldsymbol{f}}_0^{(S)} \end{bmatrix}. \tag{6.30}$$

By expanding the left hand side of Eq. (6.30), the original block matrix is obtained again as in Eq. (6.29),

$$\begin{bmatrix} \boldsymbol{A}^{(S)} & \boldsymbol{0} & \check{\boldsymbol{B}}^{(S)^T} \\ \boldsymbol{0} & \boldsymbol{A}^{(R)} & \check{\boldsymbol{B}}^{(R)^T} \\ \check{\boldsymbol{B}}^{(S)} & \check{\boldsymbol{B}}^{(R)} & \boldsymbol{0} \end{bmatrix} \begin{bmatrix} \tilde{\boldsymbol{z}}_0^{(S)} \\ \tilde{\boldsymbol{z}}_0^{(R)} \\ \tilde{\boldsymbol{\lambda}}_0 \end{bmatrix} = \begin{bmatrix} \boldsymbol{0} \\ \boldsymbol{0} \\ -\check{\boldsymbol{B}}^{(S)} \boldsymbol{A}^{(S)^{-1}} \check{\boldsymbol{f}}_0^{(S)} \end{bmatrix} = \begin{bmatrix} \boldsymbol{0} \\ \boldsymbol{0} \\ \boldsymbol{\delta}_{u,0} \end{bmatrix}, \tag{6.31}$$

but one can clearly see that the external load on the source substructure is replaced by a term, $\boldsymbol{\delta}_u$, that "excites" the compatibility condition. This can be physically interpreted as a gap in

the equilibrium condition, that states that $\tilde{\boldsymbol{z}}^{(S)}_{[b],0} \neq \tilde{\boldsymbol{z}}^{(R)}_{[b],0}$. Note that the *equivalent* problem is found now, which is different from the original problem given in Eq. (6.29). Hence, the variables are changed from $\boldsymbol{z}^{(s)}$ to $\tilde{\boldsymbol{z}}^{(s)}$, where the $\tilde{\star}$ denotes the fact that one is now working with the equivalent problem. Solving the responses of the equivalent problem stated in Eq. (6.31), gives:

$$\begin{bmatrix} \tilde{\boldsymbol{z}}^{(S)}_0 \\ \tilde{\boldsymbol{z}}^{(R)}_0 \\ \tilde{\boldsymbol{\lambda}}_0 \end{bmatrix} = \begin{bmatrix} -\boldsymbol{A}^{(S)^{-1}} \check{\boldsymbol{B}}^{(S)^T} \boldsymbol{\lambda}^{eq}_0 \\ -\boldsymbol{A}^{(R)^{-1}} \check{\boldsymbol{B}}^{(R)^T} \boldsymbol{\lambda}^{eq}_0 \\ \left(\check{\boldsymbol{B}} \boldsymbol{A}^{-1} \check{\boldsymbol{B}}^T\right)^{-1} \boldsymbol{B}^{(S)} \boldsymbol{A}^{(S)^{-1}} \check{\boldsymbol{f}}^{(S)}_0 \end{bmatrix} = \begin{bmatrix} \boldsymbol{z}^{(S)}_0 - \boldsymbol{A}^{(S)^{-1}} \check{\boldsymbol{f}}^{(S)}_0 \\ \boldsymbol{z}^{(R)}_0 \\ \boldsymbol{\lambda}_0 \end{bmatrix}, \tag{6.32}$$

where,

$$\check{\boldsymbol{B}} \boldsymbol{A}^{-1} \check{\boldsymbol{B}}^T = \begin{bmatrix} \check{\boldsymbol{B}}^{(S)} & \check{\boldsymbol{B}}^{(R)} \end{bmatrix} \begin{bmatrix} \boldsymbol{A}^{(S)^{-1}} & \boldsymbol{0} \\ \boldsymbol{0} & \boldsymbol{A}^{(R)^{-1}} \end{bmatrix} \begin{bmatrix} \check{\boldsymbol{B}}^{(S)^T} \\ \check{\boldsymbol{B}}^{(R)^T} \end{bmatrix}.$$

It can be seen that the substructure Boolean matrix select the part of the inverse matrix ($\boldsymbol{A}^{(s)^{-1}}$) that is related to the interface. Here it is assumed, for simplicity, that the numbering in the boundary DoFs is consistent with the numbering in $\boldsymbol{\lambda}$ (which is not always the case). Hence, these parts are in fact the inverse of the Schur complements of these matrices [122], such that one can define:

$$\left(\check{\boldsymbol{B}} \boldsymbol{A}^{-1} \check{\boldsymbol{B}}^T\right)^{-1} = \left(\bar{\boldsymbol{A}}^{(S)^{-1}}_{[bb]} + \bar{\boldsymbol{A}}^{(R)^{-1}}_{[bb]}\right)^{-1} \triangleq \mathcal{A}_{[bb]}.$$

By comparing the result obtained from Eq. (6.32) with the reference result, which can be computed from Eq. (6.29), one will find that the original response for both the interface force and the receiver substructure (R) are obtained, but that an erroneous response for the source substructure is found. This directly explains the role of the applied *interface gap* in Eq. (6.31), as this in fact corrects for the incorrect response of the source substructure in the compatibility equation.

6.4.1.2 Response at the next time steps

Obviously, the method cannot be verified by only discussing the first time step, hence also next time steps are discussed in this section. Starting from the response at t_1, the result will be generalized such that it holds for all time steps. The set of equations for the first time step can be extracted from Eq. (6.28):

$$\begin{bmatrix} \boldsymbol{Q}^{(S)} & \boldsymbol{0} & \check{\boldsymbol{B}}^{(S)^T} \\ \boldsymbol{0} & \boldsymbol{Q}^{(R)} & \check{\boldsymbol{B}}^{(R)^T} \\ \check{\boldsymbol{B}}^{(S)} & \check{\boldsymbol{B}}^{(R)} & \boldsymbol{0} \end{bmatrix} \begin{bmatrix} \boldsymbol{z}^{(S)}_1 \\ \boldsymbol{z}^{(R)}_1 \\ \boldsymbol{\lambda}_1 \end{bmatrix} = \begin{bmatrix} \check{\boldsymbol{f}}^{(S)}_1 \\ \boldsymbol{0} \\ \boldsymbol{0} \end{bmatrix} - \begin{bmatrix} \boldsymbol{N}^{(S)} \boldsymbol{z}^{(S)}_0 \\ \boldsymbol{N}^{(R)} \boldsymbol{z}^{(R)}_0 \\ \boldsymbol{0} \end{bmatrix}. \tag{6.33}$$

It is easily found that the substructure responses and interface forces at t_1 are given by:

$$\begin{bmatrix} \boldsymbol{z}^{(S)}_1 \\ \boldsymbol{z}^{(R)}_1 \\ \boldsymbol{\lambda}_1 \end{bmatrix} = \begin{bmatrix} \boldsymbol{Q}^{(S)^{-1}} \left(\check{\boldsymbol{f}}^{(S)}_1 - \boldsymbol{N}^{(S)} \boldsymbol{z}^{(S)}_0 - \check{\boldsymbol{B}}^{(S)^T} \boldsymbol{\lambda}_1\right) \\ \boldsymbol{Q}^{(R)^{-1}} \left(-\boldsymbol{N}^{(R)} \boldsymbol{z}^{(R)}_0 - \check{\boldsymbol{B}}^{(R)^T} \boldsymbol{\lambda}_1\right) \\ \mathcal{Q}_{[bb]} \left(\check{\boldsymbol{B}}^{(S)} \boldsymbol{Q}^{(S)^{-1}} \left(\check{\boldsymbol{f}}^{(S)}_1 - \boldsymbol{N}^{(S)} \boldsymbol{z}^{(S)}_0\right) - \check{\boldsymbol{B}}^{(R)} \boldsymbol{Q}^{(R)^{-1}} \boldsymbol{N}^{(R)} \boldsymbol{z}^{(R)}_0\right) \end{bmatrix}, \tag{6.34}$$

where,

$$\mathcal{Q}_{[bb]} \triangleq \left(\check{\boldsymbol{B}} \boldsymbol{Q}^{-1} \check{\boldsymbol{B}}^T\right)^{-1}.$$

In order to find the equivalent externally applied *interface gap* as was done for the first time step in Eq. (6.31), the accelerations, velocities and displacements of the source substructure are condensed on the interface problem to give:

$$\begin{bmatrix} \boldsymbol{Q}^{(R)} & \check{\boldsymbol{B}}^{(R)^T} \\ \check{\boldsymbol{B}}^{(R)} & -\bar{\boldsymbol{Q}}_{[bb]}^{(S)^{-1}} \end{bmatrix} \begin{bmatrix} \boldsymbol{z}_1^{(R)} \\ \boldsymbol{\lambda}_1 \end{bmatrix} = \begin{bmatrix} -\boldsymbol{N}^{(R)} \boldsymbol{z}_0^{(R)} \\ -\check{\boldsymbol{B}}^{(S)} \boldsymbol{Q}^{(S)^{-1}} \left(\check{\boldsymbol{f}}_1^{(S)} - \boldsymbol{N}^{(S)} \boldsymbol{z}_0^{(S)} \right) \end{bmatrix}, \tag{6.35}$$

where $\bar{\boldsymbol{Q}}_{[bb]}^{(S)}$ is defined as the Schur complement of $\boldsymbol{Q}^{(S)}$. Note that after the expansion, the set of DoFs is also changed from $\boldsymbol{z}_n^{(S)}$ into $\tilde{\boldsymbol{z}}_n^{(S)}$. Hence, substituting the relation between $\boldsymbol{z}_0^{(s)}$ and $\tilde{\boldsymbol{z}}_0^{(s)}$, as given in Eq. (6.32), into the right hand side of Eq. (6.35) gives:

$$\begin{bmatrix} \boldsymbol{Q}^{(R)} & \check{\boldsymbol{B}}^{(R)^T} \\ \check{\boldsymbol{B}}^{(R)} & -\bar{\boldsymbol{Q}}_{[bb]}^{(S)^{-1}} \end{bmatrix} \begin{bmatrix} \boldsymbol{z}_1^{(R)} \\ \boldsymbol{\lambda}_1 \end{bmatrix} = \begin{bmatrix} -\boldsymbol{N}^{(R)} \tilde{\boldsymbol{z}}_0^{(R)} \\ -\check{\boldsymbol{B}}^{(S)} \boldsymbol{Q}^{(S)^{-1}} \left(\check{\boldsymbol{f}}_1^{(S)} - \boldsymbol{N}^{(S)} \left(\tilde{\boldsymbol{z}}_0^{(S)} + \boldsymbol{A}^{(S)} \check{\boldsymbol{f}}_0^{(S)} \right) \right) \end{bmatrix}. \tag{6.36}$$

After re-expanding the left hand side of Eq. (6.36), the original block-form matrix is obtained again:

$$\begin{bmatrix} \boldsymbol{Q}^{(S)} & \boldsymbol{0} & \check{\boldsymbol{B}}^{(S)^T} \\ \boldsymbol{0} & \boldsymbol{Q}^{(R)} & \check{\boldsymbol{B}}^{(R)^T} \\ \check{\boldsymbol{B}}^{(S)} & \check{\boldsymbol{B}}^{(R)} & \boldsymbol{0} \end{bmatrix} \begin{bmatrix} \tilde{\boldsymbol{z}}_1^{(S)} \\ \tilde{\boldsymbol{z}}_1^{(R)} \\ \tilde{\boldsymbol{\lambda}}_1 \end{bmatrix} = \begin{bmatrix} -\boldsymbol{N}^{(S)} \tilde{\boldsymbol{z}}_0^{(S)} \\ -\boldsymbol{N}^{(R)} \tilde{\boldsymbol{z}}_0^{(R)} \\ -\check{\boldsymbol{B}}^{(S)} \boldsymbol{Q}^{(S)^{-1}} \left(\check{\boldsymbol{f}}_1^{(S)} - \boldsymbol{N}^{(S)} \boldsymbol{A}^{(S)} \check{\boldsymbol{f}}_0^{(S)} \right) \end{bmatrix}. \tag{6.37}$$

Note here that the right hand side is also altered due to the substitution of Eq. (6.32) and the re-expansion of the left hand side and that the equivalent externally applied *interface gap* ($\boldsymbol{\delta}_{u,1}$) is found to be the following:

$$\boldsymbol{\delta}_{u,1} = -\check{\boldsymbol{B}}^{(S)} \boldsymbol{Q}^{(S)^{-1}} \left(\check{\boldsymbol{f}}_1^{(S)} - \boldsymbol{N}^{(S)} \boldsymbol{A}^{(S)} \check{\boldsymbol{f}}_0^{(S)} \right). \tag{6.38}$$

Solving Eq. (6.37) gives the response of the equivalent problem in terms of the state of both substructures and the corresponding interface forces:

$$\begin{bmatrix} \tilde{\boldsymbol{z}}_1^{(S)} \\ \tilde{\boldsymbol{z}}_1^{(R)} \\ \tilde{\boldsymbol{\lambda}}_1 \end{bmatrix} = \begin{bmatrix} \boldsymbol{Q}^{(S)^{-1}} \left(-\boldsymbol{N}^{(S)} \boldsymbol{z}_0^{(S)} + \boldsymbol{N}^{(S)} \boldsymbol{A}^{(S)^{-1}} \check{\boldsymbol{f}}_0^{(S)} - \check{\boldsymbol{B}}^{(S)^T} \tilde{\boldsymbol{\lambda}}_1 \right) \\ \boldsymbol{Q}^{(R)^{-1}} \left(-\boldsymbol{N}^{(R)} \boldsymbol{z}_0^{(R)} - \check{\boldsymbol{B}}^{(R)^T} \tilde{\boldsymbol{\lambda}}_1 \right) \\ \mathcal{Q}_{[bb]} \left(\check{\boldsymbol{B}}^{(S)} \boldsymbol{Q}^{(S)^{-1}} \left(\check{\boldsymbol{f}}_1^{(S)} - \boldsymbol{N}^{(S)} \boldsymbol{z}_0^{(S)} \right) - \check{\boldsymbol{B}}^{(R)} \boldsymbol{Q}^{(R)^{-1}} \boldsymbol{N}^{(R)} \boldsymbol{z}_0^{(R)} \right) \end{bmatrix}. \tag{6.39}$$

From comparing this result with Eq. (6.33), one can deduce that for each time step it holds that the response of the receiver substructure and the resulting interface force is identical to the reference solution. For the source substructure, one finds that the relation between the equivalent response and the reference response is equal to:

$$\begin{cases} \tilde{\boldsymbol{z}}_n^{(S)} = \boldsymbol{z}_n^{(S)} - \sum_{j=1}^{n} \left(-\boldsymbol{Q}^{(S)^{-1}} \boldsymbol{N}^{(S)} \right)^{n-j} \boldsymbol{Q}^{(S)^{-1}} \check{\boldsymbol{f}}_j^{(S)} - \left(-\boldsymbol{Q}^{(S)^{-1}} \boldsymbol{N}^{(S)} \right)^{n} \boldsymbol{A}^{(S)^{-1}} \check{\boldsymbol{f}}_0^{(S)} \\ \tilde{\boldsymbol{z}}_n^{(R)} = \boldsymbol{z}_n^{(R)} \\ \tilde{\boldsymbol{\lambda}}_n = \boldsymbol{\lambda}_n \end{cases}. \tag{6.40}$$

And from the last line of Eq. (6.37) one can find the recursive expression that leads to the equivalent externally applied interface gap:

$$\boldsymbol{\delta}_{u,n} = -\check{\boldsymbol{B}}^{(S)} \left(\sum_{j=1}^{n} \left(-\boldsymbol{Q}^{(S)^{-1}} \boldsymbol{N}^{(S)} \right)^{n-j} \boldsymbol{Q}^{(S)^{-1}} \check{\boldsymbol{f}}_j^{(S)} + \left(-\boldsymbol{Q}^{(S)^{-1}} \boldsymbol{N}^{(S)} \right)^{n} \boldsymbol{A}^{(S)^{-1}} \check{\boldsymbol{f}}_0^{(S)} \right). \tag{6.41}$$

6.4.2 Substructure's free interface response due to external loading

As in reality, one would never explicitly solve Eq. (6.41), it will be shown that this can be computed from the (stand-alone) free interface source substructure. Starting from the generalized-α equations in block form for the source substructure, with free interfaces, at the initial and first time step, one obtains:

$$\begin{bmatrix} \boldsymbol{A}^{(S)} & \boldsymbol{0} \\ \boldsymbol{N}^{(S)} & \boldsymbol{Q}^{(S)} \end{bmatrix} \begin{bmatrix} \boldsymbol{z}_0^{(S),free} \\ \boldsymbol{z}_1^{(S),free} \end{bmatrix} = \begin{bmatrix} \check{\boldsymbol{f}}_0^{(S)} \\ \check{\boldsymbol{f}}_1^{(S)} \end{bmatrix}, \tag{6.42}$$

where the superscript $\star^{free}$ denotes the free interface response. The free response for these time steps is simply obtain by solving Eq. (6.42),

$$\begin{aligned} \boldsymbol{z}_0^{(S),free} &= \boldsymbol{A}^{(S)^{-1}} \check{\boldsymbol{f}}_0^{(S)}, \\ \boldsymbol{z}_1^{(S),free} &= \boldsymbol{Q}^{(S)^{-1}} \left(\check{\boldsymbol{f}}_1^{(S)} - \boldsymbol{N}^{(S)} \boldsymbol{A}^{(S)^{-1}} \check{\boldsymbol{f}}_0^{(S)} \right), \end{aligned}$$

and can easily be generalized to all time steps, which results in:

$$\boldsymbol{z}_n^{(S),free} = \sum_{j=1}^{n} \left(-\boldsymbol{Q}^{(S)^{-1}} \boldsymbol{N}^{(S)} \right)^{n-j} \boldsymbol{Q}^{(S)^{-1}} \check{\boldsymbol{f}}_j^{(S)} + \left(-\boldsymbol{Q}^{(S)^{-1}} \boldsymbol{N}^{(S)} \right)^{n} \boldsymbol{A}^{(S)^{-1}} \check{\boldsymbol{f}}_0^{(S)}. \tag{6.43}$$

Thus, one can obtain the equivalent interface gap, given in Eq. (6.41), from the free interface response, computed in Eq. (6.43):

$$\boldsymbol{\delta}_{u,n} = -\check{\boldsymbol{B}}^{(S)} \boldsymbol{z}_n^{(S),free}. \tag{6.44}$$

This is similar to what was found for the method which uses equivalent blocked forces (section 6.3.2). Now, one can substitute Eq. (6.43) into Eq. (6.40) to find the relation between the exact response of the different substructures and associated Lagrange multipliers and the response using equivalent loading in the form of an enforced incompatibility error:

$$\begin{bmatrix} \tilde{\boldsymbol{z}}_n^{(S)} \\ \tilde{\boldsymbol{z}}_n^{(R)} \\ \tilde{\boldsymbol{\lambda}}_n \end{bmatrix} = \begin{bmatrix} \boldsymbol{z}_n^{(S)} - \boldsymbol{z}_n^{(S),free} \\ \boldsymbol{z}_n^{(R)} \\ \boldsymbol{\lambda}_n \end{bmatrix}. \tag{6.45}$$

Note that a similar result was found for the blocked force approach in Eq. (6.22).

6.4.3 Practical implementation of approach using free interface displacements

From the derivation presented in the previous subsections one can conclude that, firstly, the effect of the forces exciting the source substructure can be transformed to an interface incompatibility in a dual assembled system, that results in the exact same response of the receiver substructures. Secondly, it was found that the interface incompatibility is equal the to free interface response of the stand-alone source substructure.

In this section the practical implementation of the method is discussed. The different steps are illustrated in figure 6.2, starting from the original dual assembled problem, which is split into the different components. The example used here is that of an offshore wind turbine, where the turbine component is denoted the receiver and the source substructure is represented by a wave excited jacket structure. As the wind turbine model is considered as nonlinear, due to the aero-elastic coupling, this model is to be retained and only the (linear) jacket structure can be

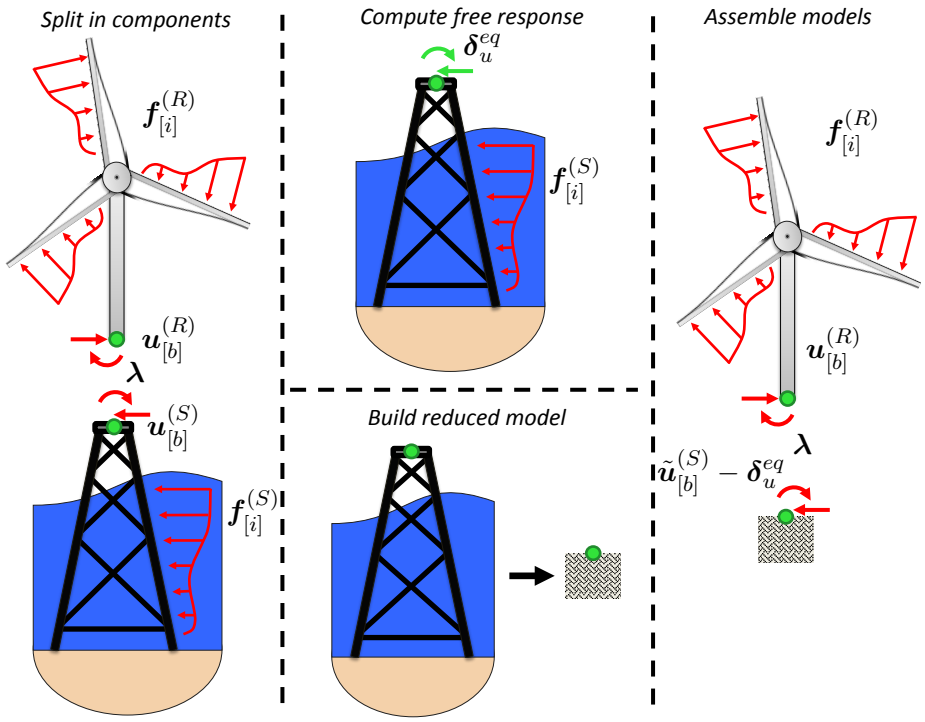

Figure 6.2: *Steps taken when using the methods of equivalent interface gap in the time domain.*

reduced. This can be done using, for instance, the Dual Craig-Bampton method [136] which was developed for dual assembled systems, or one can choose to apply the IBS method, that is presented in chapter 5. In addition to this, the equivalent interface gap needs to be computed, which can simply be obtained from the free interface response of the jacket that is excited by the wave forces:

$$\begin{cases} \boldsymbol{M}^{(S)}\ddot{\boldsymbol{u}}^{(S),free} + \boldsymbol{C}^{(S)}\dot{\boldsymbol{u}}^{(S),free} + \boldsymbol{K}^{(S)}\boldsymbol{u}^{(S),free} = \boldsymbol{f}^{(S)} \\ \boldsymbol{\delta}_u = -\boldsymbol{B}^{(S)}\boldsymbol{u}^{(S),free} \end{cases} . \tag{6.46}$$

This response can be solved using the standard generalized-α time integrations methods again, which are usually available in finite element packages.[3] By using the Boolean operator for selecting the interface response, the equivalent interface gap is obtained. In the next step, the reduced source structure (the jacket) and the unreduced nonlinear receiver component (the wind turbine) are re-assembled and excited by the equivalent interface gap on the compatibility equation, as can be seen in Eq. (6.47):

$$\begin{cases} \boldsymbol{M}^{(R)}\ddot{\boldsymbol{u}}^{(R)} + \boldsymbol{p}\left(\boldsymbol{u}^{(R)}, \dot{\boldsymbol{u}}^{(R)}\right) + \boldsymbol{B}^{(R)^T}\boldsymbol{\lambda} = \boldsymbol{f}^{(S)} \\ \tilde{\boldsymbol{M}}^{(S)}\ddot{\tilde{\boldsymbol{q}}}^{(S)} + \tilde{\boldsymbol{C}}^{(S)}\dot{\tilde{\boldsymbol{q}}}^{(S)} + \tilde{\boldsymbol{K}}^{(S)}\tilde{\boldsymbol{q}}^{(S)} + \boldsymbol{B}^{(R)^T}\boldsymbol{\lambda} = \boldsymbol{0} \\ \boldsymbol{B}\boldsymbol{u} = \boldsymbol{\delta}_u \end{cases} . \tag{6.47}$$

where, $\tilde{\boldsymbol{M}}$, $\tilde{\boldsymbol{C}}$ and $\tilde{\boldsymbol{K}}$ denote the reduced structural matrices and $\tilde{\boldsymbol{q}}^{(S)}$ is the reduced set of DoFs. As the linear subsystem is reduced, the response of the global system will now be much cheaper to compute, while the equivalent interface gap ensures that the external forces acting on the source structure are correctly taken into account. Note again that the pre-processing step in Eq. (6.46) needs to be performed with the same time integration method and parameters

[3] Note that computing the free interface response requires one to use the same time-stepping matrix as is used for computing the associated substructure IRFs, one only needs to factorize it once, thereby saving computer costs. Using the blocked force approach, requires factorizing a different time stepping matrix, as can be verified from Eq. (6.24), therefore an extra factorization of the time-stepping matrix is required.

as the final coupled problem, given in Eq. (6.47). Finally, note that even though the method is derived using a dual assembled system, one could also use the interface gap in a primal assembled system. By taking the obtained free interface displacement (Eq. (6.46)) into account in the Lagrangian given in Eq. (2.35), one can derive the associated primal assembled system of equations, however this derivation is beyond the scope of the current thesis.

One can expand (using Eq. (2.2)) the response of the reduced model, $\tilde{\boldsymbol{q}}_n^{(S)}$, that was obtained from the integrated analysis. By substituting this into Eq. (6.45), one finds that the total response of the jacket (in terms of displacements) is easily reconstructed:

$$\boldsymbol{u}_n^{(S)} = \boldsymbol{R}^{(S)}\tilde{\boldsymbol{q}}_n^{(S)} + \boldsymbol{u}_n^{(S),free}. \tag{6.48}$$

Obviously, this requires a reduced model that is spectrally converged in the frequency bandwidth of the external and interface forces.

The method employing free interface displacements has some of the same advantages (and disadvantages) as the blocked force approach. Firstly, no approximation is made in the applied forces, such as one would find from the approach presented in section 6.2. Secondly, there is no need for a load case dependent reduction basis. And thirdly, only information on the interface needs to be shared between different project groups. However, in order to obtain the free interface displacements, one needs to perform a time integration for each load case.

In addition, in case of an unconstrained source substructure the free interface displacements can grow over time, thereby resulting in ever larger incompatibilities that are enforced between the source and receiver substructures. For simulations with a long time span, this could lead to numerical errors and is a disadvantage with respect to the blocked force approach.

Finally, one can simplify the analysis by determining the static interface responses. Therefore, if the inertia and damping contributions can be neglected, one simply has to solve the associated static problem:

$$\begin{cases} \boldsymbol{K}^{(F)}\boldsymbol{u}^{(F),free} = \boldsymbol{f}^{(F)} \\ \boldsymbol{\delta}_{\boldsymbol{u}} = -\boldsymbol{B}^{(F)}\boldsymbol{u}^{(F),free} \end{cases}. \tag{6.49}$$

Again, one can only neglect the damping and inertia contributions in case the first (free interface) eigenfrequency (ω_1), which is found from:

$$\left(\boldsymbol{K} - \omega_j^2\boldsymbol{M}\right)\boldsymbol{\phi}_j = \boldsymbol{0}, \tag{6.50}$$

is much higher that the spectrum of applied forces. Note however, that in case the substructure is free-floating a static analysis could turn out to be more complex, as one has to deal with a singular stiffness matrix.

6.5 Summary

In this chapter three different strategies are presented that allow for efficient and accurate handling of distributed external forces that are applied on the internal DoFs. The first method, presented in section 6.2, is based on the concept of applying a spatial reduction to the full time series of forces. The second and third method introduced (section 6.3 and 6.4) apply a transformation, such that one obtains an equivalent loading on the interface that results in the exact response of the receiver substructures.

[4] Note in some cases one can also generate a single reduction basis for multiple load cases.

[5] Less suited due to an interface displacement that can grow over time.

	Spatial reduction	*Blocked forces*	*Free interface displacements*
Exact forcing effect on receiver components	✘	✔	✔
Load case independent reduction basis / IRFs	✘[4]	✔	✔
No extra pre-processing time integration	✔	✘	✘
Data exchange of only interface data	✘	✔	✔
Suitability for floating substructures	✔	✔	✔[5]
Applicability in primal assembled systems	✔	✔	✔
Applicability in dual assembled systems	✔	✔	✔

Table 6.1: *Characteristics of the different methods for handling distributed forces on the internal DoFs of reduced substructures*

In table 6.1 an overview of the different methods is given. The different advantages and disadvantages are given as respectively green check marks or red cross marks.

Finally, note that in case the response of the source substructure is in the quasi-static regime and its inertia and damping force contribution are allowed to be neglected, one can also compute and apply static equivalent loading to the interface. However, in this case the interface loading is approximated and one will no longer obtain the exact response of the receiver substructures.

Part II

Computational Methods applied for Offshore Wind Turbine Support Structure Design

7

Using Component Mode Synthesis for Integrated Offshore Wind Turbine Analysis

"He who loves practice without theory is like the sailor who boards ship without a rudder and compass and never knows where he may be cast."

– Leonardo da Vinci

7.1 Introduction

In section 1.5 the general process for designing offshore wind turbine support structures has been described. It was outlined that the design of a support structure usually involves multiple parties; the wind turbine manufacturer (WTM) to perform the integrated analysis and tower design and a foundation designer (FD) to design the marine foundation.

One of the more structured methods available for the FD to supply the WTM with a dynamic model that accurately represents the dynamics of the foundation is by means of the dynamic substructuring methods that are introduced in part I of this dissertation. In this chapter the Component Mode Synthesis methods, which are outlined in chapter 2, are employed in order to create compact reduced models of the foundation structure. Sharing reduced models has in practice several advantages over sharing full models. Firstly, the use of reduced models can significantly speed up simulations. Secondly, one can include the important dynamics in a reduced model, without showing any of the modeling details, which are often considered as confidential. Thirdly, it involves a lot less stored data that needs to be exchanged.

Nonetheless, one should be able to verify the accuracy of results found from using reduced models of the foundation in the aero-elastic simulations of the integrated wind turbines. In general, different reduction methods are employed in practice [69, 118, 152] and it is important to be able to make *a priori* predictions on which method will yield accurate results. In addition, the foundation designer has a number of approaches available to reconstruct the full transient jacket response from the integrated analysis, as is discussed in [12, 36, 174], which therefore need to be taken into account as well in the verification process. From the obtained foundation

response one is able to determine the internal loads and stresses in all the elements, which are required to obtain the fatigue damage induced on the elements of the foundation.

7.1.1 Integrated load calculations of offshore wind turbines

In this section some basics of the integrated analysis of an offshore wind turbine are introduced. The integrated model is required to simulate thousands of load cases in order to determine the stresses that the structural components have to endure during their lifetime. Note that these stresses are not directly obtained from these simulation, as one generally only computes the dynamic response of the structure. Hence, a post-processing step is required to compute the induced stresses from the obtained time series of nodal displacements.

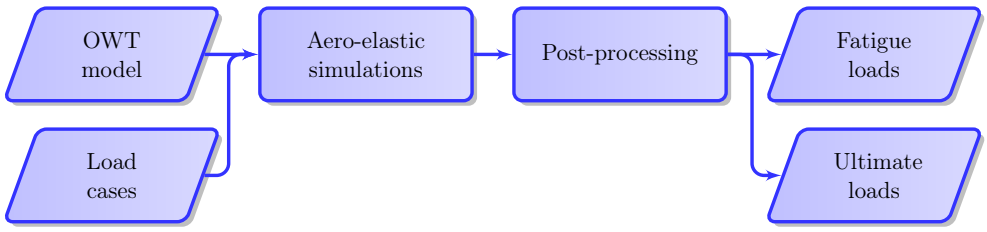

Figure 7.1: *Obtaining the ultimate and fatigue loads from the integrated offshore wind turbine analysis.*

These steps are shown in figure 7.1, where one starts on the left side with the model of the complete offshore wind turbine, which also includes the aero-dynamic properties of the blades and a controller model, and the load cases, according the the standards [82, 128], that need to be taken into account. Using these inputs, the aero-elastic simulations are performed for the hundreds or even thousands of different load cases. The obtained transient responses of the wind turbine are now post-processed in order to determine the ultimate and fatigue loads. From these ultimate and fatigue loads, one can verify whether the offshore wind turbine, thus also its support structure, is able to withstand the environmental loads for the next 20 to 25 years.

7.1.2 Integrated wind turbine analysis using reduced components

As was described in section 1.5, models of complex foundations are in general provided to the WTM as approximate or pseudo models. These models could be as simple as an approximation of the equivalent mass and stiffness at the interface, or could be more sophisticated models generated using the Component Mode Synthesis methods that are outlined in chapter 2. In this chapter the marine foundation models are reduced using these CMS methods.

In order to use these reduced components in the aero-elastic simulations a number of steps are required, as is shown in figure 7.2. As a first step, one needs to apply the reduction to the original foundation model, as is outlined in section 2.2. This reduced model then needs to be assembled into the aero-elastic model using the assembly techniques presented in section 2.6. Using this aero-elastic model, one runs the complete set of load cases. From the (generalized) simulation results obtained, one needs to reconstruct the full foundation response (section 7.2) in order to be able to determine the internal loads and stresses in the individual foundation elements. From these results, one is able to compute the ultimate and fatigue loads (and damages). Note that the ultimate loads are not considered in this work.

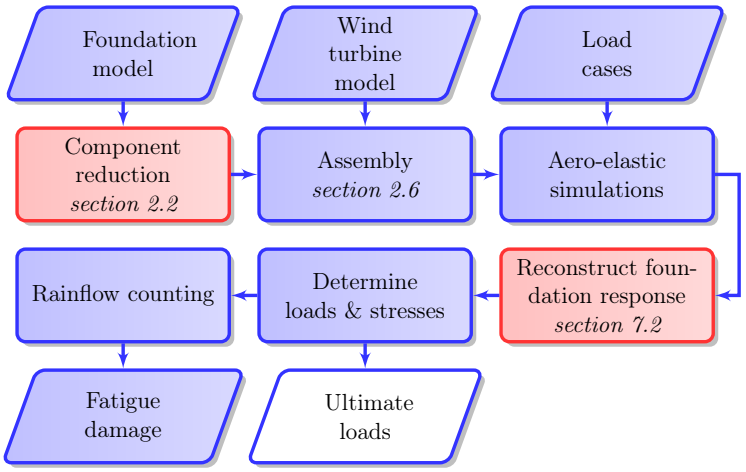

Figure 7.2: *Steps required for obtaining fatigue damage induced on the element when reduced foundation models are used. The red blocks indicate which effects are investigated in the current test case: reduction and the post-processing analysis.*

In both the reduction step and the step required for reconstructing the foundation response, a number of choices can be made as is outlined in sections 2.2 and 7.2. Firstly, the accuracy of the approximation made by using reduced components depends on the quality of the chosen reduction basis, as is also discussed in chapter 2. In the case that one would use increasingly more vibration mode shapes to build a reduction basis, the solution will converge towards the exact solution. In case all vibration modes are included one would find the exact solution, but the model size would obviously be unreduced. In general, it can be stated that the convergence of the approximation depends on:

- Convergence in the *spectral* sense: how well the excitation, from either the external or the interface forces, is represented in the frequency range of the retained modes.
- Convergence in the *spatial* sense: how well the spatial distribution of external forces is spanned by the retained modes in the reduction basis.

Therefore, one can conclude that firstly it is important that the reduced substructure is both spectrally and spatially accurate. Secondly, it is important that the reconstruction is consistent with the underlying unreduced problem and does not introduce additional computational errors.

7.1.3 Chapter outline

This chapter is organized such that in section 7.2 the different methods available for reconstructing the full foundation transient response are introduced. The case study, which uses the model of a SWT-3.6-120 wind turbine and the UpWind reference jacket, is introduced in section 7.3. In this case study, two different normal power production load cases are considered. The results of the test case are given in sections 7.4 and 7.5. Firstly, in section 7.4 the effect of the different reduced foundation models on the turbine response is evaluated. Secondly, in section 7.5 the fatigue damages computed in the jacket structure are compared to a reference solution in order to verify the accuracy of the different reduction and post-processing analysis methods. In addition, in order to quantify the sensitivity of the chosen computational approaches with respect to the flexibility of the jacket, the same exercise is performed in section 7.6 using a more flexible model of the UpWind jacket. As in a commercial design process the computational effort is also an important aspect to consider, the computational costs of the different approaches are compared in section 7.7. Finally, the summary is given in section 7.8.

This chapter is based on work presented in [174, 175].

7.2 Post-processing analysis to obtain foundation loads

An overview of the entire computational process is given in figure 7.2, where both the reduction and assembly steps have been outlined in chapter 2. Hence, the next step is to discuss how to get the response of the full foundation model from the reduced results obtained from the integrated aero-elastic simulations. This step is essential to determine the loads within the foundation, as one requires the full displacement field in order to compute stresses in the foundation elements.

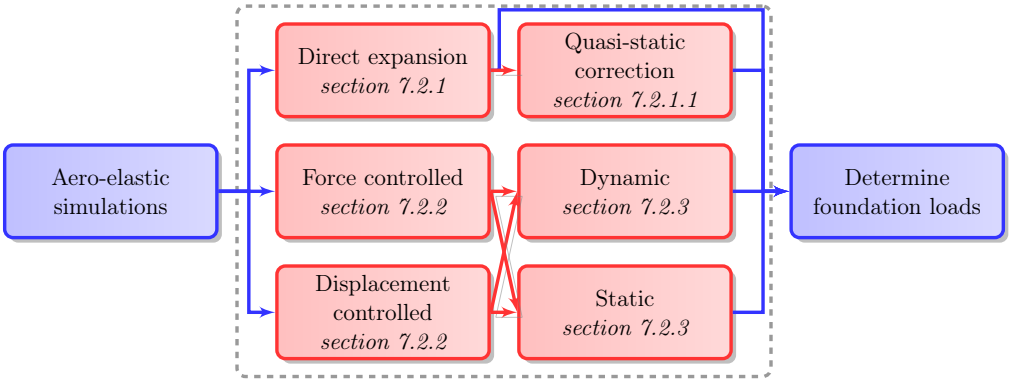

Figure 7.3: *Overview of the different post-processing options available to reconstruct the full foundation response.*

By zooming in on the "Reconstruct foundation response" step in figure 7.2, one will find different methods for reconstructing the response of the jacket, as is shown in figure 7.3. Firstly, one could use the reduction basis to expand the modal coordinates back the the full physical domain, as will be discussed in section 7.2.1. An additional quasi-static correction can be applied to the expanded results (see section 7.2.1.1). Secondly, by using the displacements or forces at the interface one can perform a post-processing analysis on the stand-alone foundation, respectively referred to as *displacement controlled* (DC) and *force controlled* (FC), which are presented in section 7.2.2. In both the displacement and force controlled approaches one can choose to include inertia and damping effects of the foundation, i.e. by solving a *dynamic* problem, or one could neglect these and solve a *static* problem, as is presented in section 7.2.3.

7.2.1 Expansion of superelement results

The easiest and most direct method for obtaining the full foundation response would be a direct expansion step using the reduction basis, i.e.:

$$\boldsymbol{u} = \boldsymbol{R}\boldsymbol{q}. \tag{7.1}$$

Note however, that by applying the reduction one in fact forces that the solution is found in the space spanned by the reduction basis. By directly expanding the obtained results, the solution thus stays in this limited solution space. In case the reduced model is not spectrally and/or spatially converged, the solution found from the reduced model can deviate significantly from the reference solution, which is obtained from the full model. A method for *a posteriori* determining the error in the reduced solution, is by determining the residual $\boldsymbol{r}$. This residual is

found by substituting the expanded solution, given in Eq. (7.1), directly in the original equations of motion, as is shown in Eq. (7.2),

$$\boldsymbol{M}^{(F)}\boldsymbol{R}^{(F)}\ddot{\boldsymbol{q}}^{(F)} + \boldsymbol{C}^{(F)}\boldsymbol{R}^{(F)}\dot{\boldsymbol{q}}^{(F)} + \boldsymbol{K}^{(F)}\boldsymbol{R}^{(F)}\boldsymbol{q}^{(F)} + \boldsymbol{B}^{(F)^T}\boldsymbol{\lambda} = \boldsymbol{f}^{(F)} + \boldsymbol{r}^{(F)}. \tag{7.2}$$

By comparing for instance the norm of the residual with the norm of the elastic or external forces, a measure of the error is obtained. Note that this does not directly relate to the error made in the displacements computed using a reduced model. In order to obtain posteriori estimates for the error on the displacements, error estimation methods have been developed (see e.g. [85, 86, 181, 182]).

7.2.1.1 Quasi-static correction

Nonetheless, one could also use the residual found from Eq. (7.2) to compute a quasi-static correction on the expanded results. The residual can be interpreted as an external force that was missing in the original analysis using the reduced component. Hence, the quasi-static deformation induced by the residual can be added to the expanded result in order to correct these results, as:

$$\boldsymbol{u} = \boldsymbol{R}\boldsymbol{q} - \boldsymbol{K}^{-1}\boldsymbol{r}. \tag{7.3}$$

This correction is mainly useful if the residual results from poor spatial convergence of the superelement, i.e. the reduction basis is not able to capture the localized deformations caused by the external loading on the non-retained (internal) DoFs. If the external loading is also relatively low frequent, like for instance wave loading, such that the response is in the quasi-static regime and inertial and damping forces can be neglected, the static correction was shown to give excellent results [36].

Note that if the residual has a broad spectral bandwidth, this can indicate that the residual is caused by a spectral mismatch of the reduced component, instead of a spatial one. Therefore, the quasi-static residual correction will lose its effectiveness, as the residual is likely to excite a dynamic response. In this case one can either perform a harmonic correction around a central frequency (or several frequencies) using a dynamic stiffness matrix, or otherwise redo the analysis with an improved reduced model.

Note that applying Eq. (7.3) is in fact equivalent to the *Mode Acceleration* (MA) method, as is described in [40,60,129,194]. The MA method also enables one to define direct relations between the modal coordinates and all types of displacement related responses, such as element forces and stresses, using so called Output Transformation Matrices (OTMs), while incorporating the quasi-static correction [59].

7.2.2 Force versus displacement controlled post-processing

Another approach for reconstructing the foundation response is to perform an additional post-processing analysis on the stand-alone foundation model, using the interface information available from the integrated simulations on the complete OWT model. As discussed in chapter 2, the reduction methods treated here retain the displacement DoFs on the interface. Hence these displacements can be used directly for the reconstruction of the full foundation response. This *displacement controlled* (DC) approach to postprocessing will be treated in section 7.2.2.1. A second option would be to use the interface (or coupling) forces between the foundation and tower to reconstruct the full foundation response. This leads to a *force controlled* (FC) post-processing method, which will be elaborated in section 7.2.2.2.

7.2.2.1 Displacement controlled approach

In the displacement controlled approach one uses the interface DoFs ($\ddot{\boldsymbol{u}}_{[b]}$,$\dot{\boldsymbol{u}}_{[b]}$,$\boldsymbol{u}_{[b]}$) obtained from the integrated analysis in order to perform a post-processing simulation on the stand-alone model of the foundation structure. Firstly, the coupled equations of motion given in Eq. (2.43) are recalled. Focusing on the foundation substructure and partitioning the equations in terms of internal and boundary DoFs, one would find:

$$\begin{aligned}\begin{bmatrix} \boldsymbol{M}^{(F)}_{[ii]} & \boldsymbol{M}^{(F)}_{[ib]} \\ \boldsymbol{M}^{(F)}_{[bi]} & \boldsymbol{M}^{(F)}_{[bb]} \end{bmatrix} \begin{bmatrix} \ddot{\boldsymbol{u}}^{(F)}_{[i]} \\ \ddot{\boldsymbol{u}}^{(F)}_{[b]} \end{bmatrix} + \begin{bmatrix} \boldsymbol{C}^{(F)}_{[ii]} & \boldsymbol{C}^{(F)}_{[ib]} \\ \boldsymbol{C}^{(F)}_{[bi]} & \boldsymbol{C}^{(F)}_{[bb]} \end{bmatrix} \begin{bmatrix} \dot{\boldsymbol{u}}^{(F)}_{[i]} \\ \dot{\boldsymbol{u}}^{(F)}_{[b]} \end{bmatrix} \\ + \begin{bmatrix} \boldsymbol{K}^{(F)}_{[ii]} & \boldsymbol{K}^{(F)}_{[ib]} \\ \boldsymbol{K}^{(F)}_{[bi]} & \boldsymbol{K}^{(F)}_{[bb]} \end{bmatrix} \begin{bmatrix} \boldsymbol{u}^{(F)}_{[i]} \\ \boldsymbol{u}^{(F)}_{[b]} \end{bmatrix} + \begin{bmatrix} \boldsymbol{0} \\ \boldsymbol{B}^{(F)^T}_{[b]} \end{bmatrix} \boldsymbol{\lambda} = \begin{bmatrix} \boldsymbol{f}^{(F)}_{[i]} \\ \boldsymbol{f}^{(F)}_{[b]} \end{bmatrix}.\end{aligned} \tag{7.4}$$

Now by substituting the known interface accelerations, velocities and displacements in Eq. (7.4) and separating the knowns and unknowns, one obtains the equations of motion for the internal DoFs:

$$\boldsymbol{M}^{(F)}_{[ii]}\ddot{\boldsymbol{u}}^{(F)}_{[i]} + \boldsymbol{C}^{(F)}_{[ii]}\dot{\boldsymbol{u}}^{(F)}_{[i]} + \boldsymbol{K}^{(F)}_{[ii]}\boldsymbol{u}^{(F)}_{[i]} = \boldsymbol{f}^{(F)}_{[i]} - \left(\boldsymbol{M}^{(F)}_{[ib]}\ddot{\boldsymbol{u}}_{[b]} + \boldsymbol{C}^{(F)}_{[ib]}\dot{\boldsymbol{u}}_{[b]} + \boldsymbol{K}^{(F)}_{[ib]}\boldsymbol{u}_{[b]}\right). \tag{7.5}$$

Note that if an unreduced foundation model has been used in the integrated OWT simulations and the resulting interface responses are used in Eq. (7.5), the exact same responses at the internal foundation DoFs are obtained. If one would choose to neglect the damping and inertia effects in the interface excitation (i.e. on the right hand side) by assuming $\ddot{\boldsymbol{u}}_{[b]} = \dot{\boldsymbol{u}}_{[b]} = \boldsymbol{0}$, an approximation would be found. A visualization of the process is given in figure 7.4, where the reduced foundation model is simply represented by a gray block that is assembled underneath the wind turbine. The interface responses ($\boldsymbol{u}_{[b]}$,$\dot{\boldsymbol{u}}_{[b]}$,$\ddot{\boldsymbol{u}}_{[b]}$) are extracted from the integrated analysis and are applied as time varying boundary conditions to the full foundation model, as is shown in Eq. (7.5).

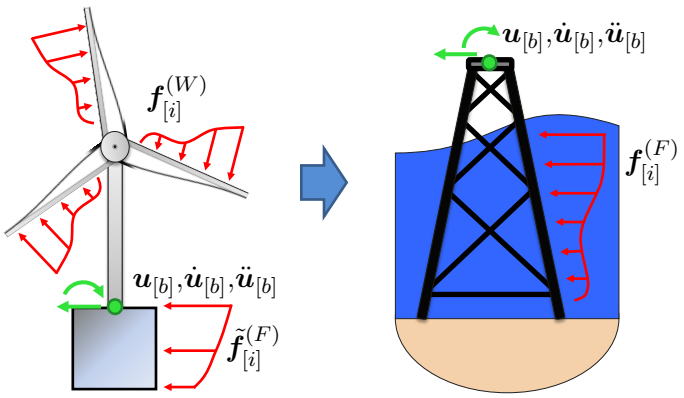

Figure 7.4: *Visualization of the displacement controlled method as presented in section 7.2.2.1.*

Two additional remarks need to be made here. Firstly, if a reduced model is used in the integrated analysis, the accuracy of the internal foundation response found from the DC-approach depends on the accuracy of the interface response. Hence, if an erroneous interface response is obtained from the integrated analysis, the reconstructed internal foundation response will also be inaccurate. Secondly, the equations given here are continuous in time, whereas in reality one has to discretize these using for instance Newmark's method [112] or the generalized-α scheme [20]. Note that, as the periodicity and amplitude error for the generalized-α method are

both dependent on the time step size and integration parameters chosen, one has to perform the DC analysis with the same time step size and integration parameters to ensure a consistent result.[1]

7.2.2.2 Force controlled approach

Instead of using the interface accelerations, velocities and displacements for reconstructing the foundation response, one can also use the interface forces. Assuming that the wind turbine and foundation models have been assembled using the primal assembly method, as outlined in section 2.6.1, one does not have direct access to the interface forces. However, these can be computed in a straightforward manner by calculating the dynamic equilibrium at the tower bottom element. This effectively yields the coupling forces between the tower and foundation, i.e. the Lagrange multipliers $\boldsymbol{\lambda}(t)$ in the dual assembled system of equations (Eq. (2.43)). Substituting these interface forces back into the second line of Eq. (7.4) and regarding these as given external forces, results in:

$$\boldsymbol{M}^{(F)}\ddot{\boldsymbol{u}}^{(F)} + \boldsymbol{C}^{(F)}\dot{\boldsymbol{u}}^{(F)} + \boldsymbol{K}^{(F)}\boldsymbol{u}^{(F)} = \boldsymbol{f}^{(F)} - \boldsymbol{B}^{(F)^T}\boldsymbol{\lambda}. \tag{7.6}$$

Hence, by using only these interface loads it is possible to reconstruct the exact dynamic response of the jacket structure as if it were part of the integrated OWT structure. Note that the interface forces contain all the dynamic excitations of the wind turbine that are "felt" by the foundation. In practice however, one would use a reduced foundation model, such that the interface forces can contain inaccuracies compared to when no reduction is applied. These inaccuracies can propagate into the foundation response found from the force controlled post-processing analysis.

A visualization of the different steps is shown in figure 7.5. The interface forces that exist between the foundation and wind turbine tower need to be determined as a second step (or are readily available in case dual assembly was used), which are then applied to the stand-alone full foundation model in order to compute its response.

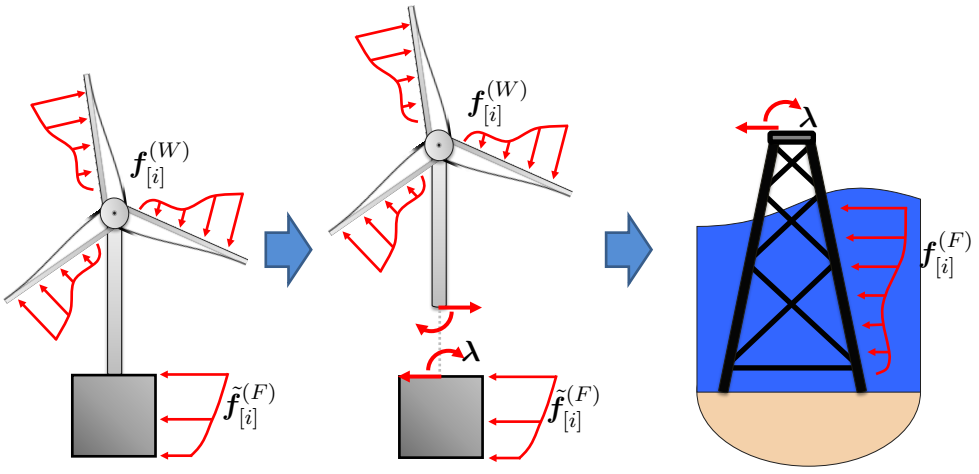

Figure 7.5: *Visualization of the force controlled method as presented in section 7.2.2.2.*

The two remarks made at the end of section 7.2.2.1 also hold here, namely i) the accuracy of

[1] Also note that one must take care of potential aliasing effects arising from directly down-sampling the interface signals.

the reconstructed response depends on the quality of the reduced foundation model and ii) one must ensure that the FC time analysis is consistent with the integrated simulations.

7.2.3 Dynamic versus quasi-static analysis

In section 7.2.2 the force and displacement controlled methods for reconstructing the full foundation response were introduced. It was explained that the resulting reconstruction runs in Eqs. (7.5) and (7.6) are dynamic equations that need to be solved in a time stepping scheme. Due to this full dynamic post-processing analysis, the entire process appears to be cumbersome and unattractive from a computational point-of-view. Nevertheless, as the foundation model is linear, it only requires factorizing the effective stiffness matrix, thereby resulting in relatively cheap post-processing simulations. However, to simplify the analysis it is often assumed in practice that the response of the foundation is in the quasi-static regime, such that the contribution of the inertia and damping forces can be neglected [152].

7.2.3.1 Quasi-static displacement controlled

From Eq. (7.5) it can be seen that the set of equations that needs to be solved in the displacement controlled method is a second order differential equation, which includes the inertia and damping terms. By neglecting these ($\dot{\boldsymbol{u}}^{(F)} = \ddot{\boldsymbol{u}}^{(F)} = \boldsymbol{0}$) a simple static problem is obtained:

$$\boldsymbol{K}^{(F)}_{[ii]}\boldsymbol{u}^{(F)}_{[i]} = \boldsymbol{f}^{(F)}_{[i]} - \boldsymbol{K}^{(F)}_{[ib]}\boldsymbol{u}_{[b]}. \tag{7.7}$$

In the above equation also the dynamic excitation forces on the right hand side, associated to $\dot{\boldsymbol{u}}_{[b]}$ and $\ddot{\boldsymbol{u}}_{[b]}$, have been neglected.[2] A priori, one can already get a good indication of whether this assumption is valid for the system at hand by computing the first eigenfrequency of the foundation model clamped at the interface from:

$$\left(\boldsymbol{K}^{(F)}_{[ii]} - \omega^{(F)^2}_{[i],1}\boldsymbol{M}^{(F)}_{[ii]}\right)\boldsymbol{\phi}^{(F)}_{[i],1} = \boldsymbol{0}, \tag{7.8}$$

where $\omega^{(F)}_{[i],1}$ is the first eigenfrequency of the foundation clamped at the interface and $\boldsymbol{\phi}^{(F)}_{[i],1}$ is the associated eigenmode. If the spectrum of the excitations is not much lower than this eigenfrequency, the component is likely to be excited dynamically and damping and inertia forces cannot be neglected. Note that, if a Guyan reduction is applied to the foundation and there would be no loading on the internal DoFs ($\boldsymbol{f}^{(F)}_{[i]} = \boldsymbol{0}$), Eq. (7.7) would be equivalent to a direct expansion using the reduction basis (section 7.2.1).

7.2.3.2 Quasi-static force controlled

Similarly, one can also choose to neglect the damping and inertia contributions in the force controlled approach. Neglecting these terms in Eq. (7.6), results in a simple static problem to solve:

$$\boldsymbol{K}^{(F)}\boldsymbol{u}^{(F)} = \boldsymbol{f}^{(F)} - \boldsymbol{B}^{(F)^T}\boldsymbol{\lambda}. \tag{7.9}$$

Again, by comparing the spectral content of the excitations (both the applied forces and interface forces) in Eq. (7.9) with the structural properties of the foundation model, one can get a

[2] Note that it was found in [36] that this has a negligible influence on the results obtained.

good indication whether the damping and inertia contributions can be neglected. By solving the corresponding eigenvalue problem, given in Eq. (7.10), one can determine the free-interface eigenfrequencies and modes of the full foundation model:

$$\left(\boldsymbol{K}^{(F)} - \omega_r^{(F)^2}\boldsymbol{M}^{(F)}\right)\boldsymbol{\phi}_r^{(F)} = \boldsymbol{0}. \tag{7.10}$$

Note that the first eigenfrequency of the foundation with fixed interfaces (see Eq. (7.8)) will always be greater (or equal) than that of the corresponding free-interface model, such that:

$$\omega_{[i],1}^{(F)} \geq \omega_1^{(F)}.$$

Therefore, the quasi-static DC approach will generally allow for excitations with a broader spectral bandwidth, compared to the quasi-static FC method.

7.3 Case study using the UpWind reference jacket

In order to evaluate the different methods discussed in the previous two sections, a case study on a representative simulation model of an OWT is treated in this chapter. The reference model consists of an SWT-3.6-120 RNA model on a tubular tower and jacket offshore foundation. The modeling of the wind turbine and the various foundation models is addressed in section 7.3.1, while section 7.3.2 briefly describes the load cases analyzed in the case study. Finally, section 7.3.3 shows the results of an eigenvalue comparison of the different OWT models before treating the time simulation results in sections 7.4 and 7.5.

7.3.1 Modeling of wind turbine and jacket foundation structures

For the case study in this chapter, an aero-elastic model is used of the SWT-3.6-120 wind turbine supported by the jacket structure initially designed for the UpWind project and subsequently used in the OC4 benchmark study [37, 188]. Four different superelements, of which the details are discussed in this section, are created from this jacket model.

7.3.1.1 Wind turbine model

The SWT-3.6-120 wind turbine is modeled in the Siemens in-house developed aero-elastic simulation tool BHawC (Bonus Horizontal axis wind turbine Code). It is constructed from Timoshenko beam elements each placed in a co-rotational frame, resulting in a fully geometrically non-linear model. In this case study, the main structural components of the wind turbine are modeled as follows:

- The model of the 58.5-meter long blades consists of 14 elements and 15 nodes each, i.e. 90 DoFs per blade.
- The tower has a length of 66 meters and is modeled by 9 elements (10 nodes), i.e. 60 DoFs.
- The nacelle and hub are modeled by various beam elements as well as specialized elements for various drivetrain components, resulting in a total nacelle-hub model of 100 DoFs.

Connecting the main components yields a wind turbine model with a total size of 406 DoFs. All element and model properties, controller parameters and other simulation settings are taken from the standard simulation model for the SWT-3.6-120.

7.3.1.2 Jacket model

The jacket foundation designed in the UpWind project consists of four main legs which are interconnected via four levels of bracings, see figure 7.6. The jacket is designed for water depths of 50 meters and has a height of 68 meters. This results in a tower top height of 84 meters above mean sea level. Based on the information in [188], the various parts of the jacket are modeled as follows:

- The main jacket structure, i.e. the four legs and cross-braces, is modeled in ANSYS using linear Timoshenko beam elements. Direct assembly of the beam elements in the tubular joints leads to an overestimation of the joint stiffness, as is shown in [12,46,189]. However, the main focuss of this work in on assessing the performance of different load calculation procedures using reduced components. Therefore, detailed modeling of the tubular joints of the jacket is not considered.
- The stiffness of the connection to the seabed is assumed to be high and is therefore modeled as rigidly clamped; this excludes any soil effects from the model.
- The connection between the turbine and jacket is realized using a concrete transition piece with a mass of 666 tons; its inertia was calculated using this mass and the specified dimensions. This transition piece rigidly connects the top elements of the jacket structure, the interface to the tower is thereby realized by a 6 DoFs coupling.
- Additional mass is modeled to account for marine growth on the structure, water contained in the free-flooded legs and the hydrodynamic mass felt from the surrounding water. These added masses are calculated as nodal point masses (with directional properties) using the ASAS software package, which is a finite element code, supplied by ANSYS, for offshore and maritime applications. These masses are thereafter added to the structural model in ANSYS.
- The damping matrix is build using a modal expansion [25]:

$$\boldsymbol{C} = \sum_{l=1}^{m} 2\epsilon_l \omega_l \boldsymbol{M} \boldsymbol{\phi}_l \boldsymbol{\phi}_l^T \boldsymbol{M}, \tag{7.11}$$

  where m represent the highest mode taken into account, ω_l and $\boldsymbol{\phi}_l$ are respectively the l^{th} eigenfrequency and (mass normalized) eigenmode and ϵ_l is the corresponding modal damping ratio. The damping ratio's are chosen as 2.5% for the first two modes and 2% for the remaining modes up to $m = 200$. The high frequency numerical damping, introduced by the generalized-α method, provides the damping for the higher modes. Note however, that the modal expansion given in Eq. (7.11) leads to a full damping matrix.

After completing the jacket model in ANSYS, it is imported in Matlab for reduction (if applicable) and subsequently stored. The total jacket model consists of 224 linear beam elements and 1062 DoFs. A plot is shown in figure 7.6, where the point masses representing the added masses are shown as red dots.

7.3.1.3 OWT models with jacket superelement

Computing the full reference solution (1462 DoFs) resulted in unacceptable computation times. Assembling the jacket model with a full damping matrix to the tower bottom node significantly compromises the efficiency of the sparse solver that is employed in BHawC. Therefore, use is made of the possibility to couple the time integrations in BHawC and MatLab using the

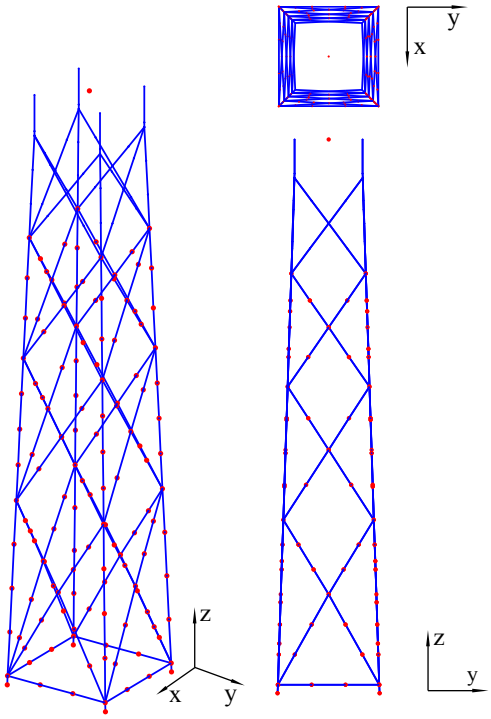

Figure 7.6: *Model of the OC4 jacket structure.*

sequential multi-domain time method presented in section 4.2 and verified in appendix A. This allows to simulate jacket model in MatLab and simultaneously simulate the wind turbine in BHawC. By using this method one ensures that the coupled response of the integrated OWT is found, while obtaining a computational speedup of approximately 70. This speedup is obtained by taking advantage of the fact that the jacket model is linear, hence it requires factorizing the effective stiffness matrix only once. The reference model is thus composed of the full jacket and wind turbine models (1062 DoFs + 406 DoFs).

Next, the jacket model is reduced according to the theory outlined in chapter 2. Four reduced jacket models are created: one using the Guyan method (section 2.3), one using the Craig-Bampton method (section 2.4) and two using the Augmented Craig-Bampton method (section 2.5). The Guyan model is included since in so-called "integrated-sequential" methods (see e.g. [118, 151, 152]), it has been proposed to use such a statically condensed model to describe the jacket foundation. The Craig-Bampton model is created using 20 fixed-interface vibration modes ($\boldsymbol{\Phi}_{[i]}$). This model is then augmented with 20 MTAs ($\boldsymbol{\Phi}_{MTA}$) to constitute the first Augmented Craig-Bampton model, while another Augmented Craig-Bampton model is included which has 180 vibration modes and again 20 MTAs. As will be seen in section 7.3.3 (and figure 7.7), the models with 20 fixed interface modes are spectrally converged up to a frequency which is (more than) twice that of the Guyan reduced and models with 180 modes can be considered as spectrally fully converged in our frequency range of interest. Hence this particular choices of modal basis allows us to study the spectral convergence of the reduction basis. The number of MTAs added to the basis was chosen to accurately represent the spatial distribution of the load, as explained next.

In order to create the MTA vectors, a POD analysis on wave load time series is performed in order to extract the most dominant wave load shape vectors, as was described in section 6.2. In total 20 spatial force distribution vectors $\boldsymbol{X}$ (see Eq. (2.26)) are extracted, resulting in 20 MTA vectors. By taking the L2-norm (per time step) of the differences between the original

applied forces ($\boldsymbol{f}(t)$) and the reduced forces ($\tilde{\boldsymbol{f}}(t)$) and dividing this by the L2-norm of the original applied forces, a qualitative measure ($\epsilon(t)$) is found for the amount of force neglected due to the reduction step,

$$\epsilon(t) = \frac{||\boldsymbol{f}(t) - \boldsymbol{X}\left(\boldsymbol{X}^T\boldsymbol{X}\right)^{-1}\boldsymbol{X}^T\boldsymbol{f}(t)||}{||\boldsymbol{f}(t)||}. \tag{7.12}$$

After the reduction step (on average) 99.5% of the L2-norm of the force was retained when adding 20 MTAs to the reduction basis of the CB20 model. For both augmented models the MTAs are obtained from the same POD analysis, although the final MTA vectors will be slightly different due to the orthogonalization with respect to the fixed interface vibration modes in the reduction basis (see Eq. 2.27). An overview of the different OWT models is given in table 7.1.

Jacket model				**Turbine model**	**Total model**	
# $\boldsymbol{\Psi}_C$	# $\boldsymbol{\Phi}_{[i]}$	# $\boldsymbol{\Phi}_{MTA}$	# DoFs	# DoFs	Total DoFs	Name
-	-	-	1062	406	1062 + 406	Ref
6	-	-	6	406	6 + 406	GR
6	20	-	26	406	26 + 406	CB20
6	20	20	46	406	46 + 406	CB2020
6	180	20	206	406	206 + 406	CB18020

Table 7.1: *Overview of simulation models of offshore turbine.*

7.3.2 Load cases

In this case study load cases have been considered according to the design load case (DLC) definition 1.2 in the IEC61400-3 standard. DLC1.2 is a fatigue relevant load case, in which the turbine is operating in normal wind conditions (i.e. normal turbulence levels and deterministic extreme operation gusts are excluded) in a normal sea state (i.e. deterministic extreme waves not included). Since jacket designs are usually governed by fatigue loads, this load case was deemed most important. Most comparisons in the next sections will therefore be expressed in terms of fatigue damage.

In this scenario wind and wave loading are aligned. Two average wind speeds v_a were considered, namely 13 and 25 m/s. These respectively correspond to the wind speeds where the turbine is operating around its nominal power (13 m/s) and where it is close to the cut-out wind speed (25 m/s). The associated significant wave heights H_s were chosen at 3.75 and 9.4 m, respectively. The wave forces are computed beforehand using ANSYS ASAS, which is done by assuming small velocities of the structure and thereby discarding the relative velocity terms in the Morison equation [111]. In total 6 seeds are considered for both wind speeds to get some statistical averaging, leading to a total of 12 simulations per model. For each of the 5 OWT models listed in table 7.1, the 630 second time simulations were solved using BHawC, which uses the generalized-α scheme with a time step of 0.02 seconds. Note that the first 30 seconds of the simulation results are discarded to remove any start-up transient effects.

7.3.3 Eigenvalue comparison

Before continuing with the time simulation results in sections 7.4 and 7.5, this section shows the results of an eigensolution comparison of the different reduced models in order to get an

estimate of their spectral convergence. The relative difference of the eigenfrequencies found from the reduced models with respect to the reference model can be computed according to

$$\epsilon_r = \frac{\tilde{\omega}_r^{(OWT)} - \omega_r^{(OWT)}}{\omega_r^{(OWT)}}, \tag{7.13}$$

where, $\tilde{\omega}_r$ denotes the r^{th} mode computed using the OWT model with a reduced foundation model. The result gives an idea of which modes of the complete OWT can be accurately described by the reduced foundation model and hence yields a direct indication of its spectral convergence.

This exercise is performed for all reduced models and the results are shown in figure 7.7. The frequencies are normalized with respect to the 20$^{\text{th}}$ eigenfrequency of the reference model. It can clearly be seen that the OWT with Guyan reduced foundation ("GR") starts to deviate already from the 20$^{\text{th}}$ mode onwards, whereas the Augmented Craig-Bampton models perform significantly better. The CB model and ACB model with 20 fixed interface modes and 20 MTA's ("CB20" and "CB2020") are accurate up to the 55$^{\text{th}}$ mode, thereby demonstrating that the MTAs, which are designed to improve spatial convergence, have limited effect on the spectral convergence. Finally, the ACB model with 180 fixed interface modes and 20 MTAs ("CB18020") has a very low error on the eigenfrequencies of the integrated OWT model in the frequency range shown.

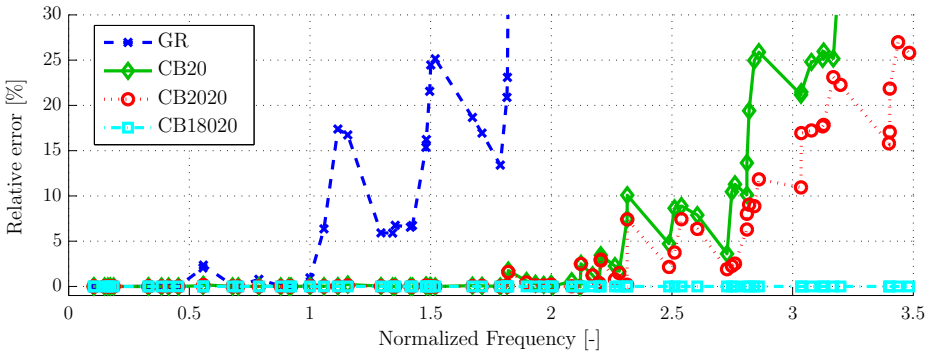

Figure 7.7: *Relative error on the eigenfrequencies for the modes up to a normalized frequency of 3.5.*

7.4 Time simulation results: wind turbine

Although the focus is on evaluating the computational procedures used for the design of the foundation structure, a brief comparison of some results obtained for the wind turbine substructure is given in this section. Therefore, the effect of using a reduced foundation on the Damage Equivalent Loads (DELs) of a number of elements in the turbine part are briefly presented here. Note that for compactness only the results for the 13 m/s simulations are shown.

In order to evaluate the effect of the reduced foundation model on the loads in the wind turbine, the resultant bending moments are determined at three locations in the structure: at the tower bottom, the tower top and the root of blade 1. The moments are computed in the local element frame as:

$$M_{res}^{el} = \sqrt{M_y^{el^2} + M_z^{el^2}}.$$

In order to quantify the effect of the reduced foundation models for a number of elements in

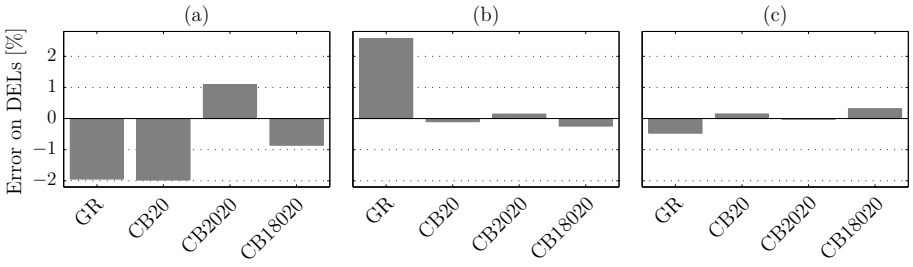

Figure 7.8: *Error on the damage equivalent loads for different elements. Result from DLC 1.2 with $v_a = 13$ m/s and $H_s = 3.75$ m.* ***(a)*** *Tower bottom element;* ***(b)*** *Tower top element;* ***(c)*** *Blade 1 root element.*

different parts of the wind turbine, the DELs have been computed for the three elements listed above. DELs are computed by applying rainflow counting [45] to the time series of resultant loads and using the associated S/N curves with the Palmgren-Miner rule [109], to compute an equivalent load that has the same effect in terms of fatigue damage. By normalizing the computed DELs with respect to the DELs from the reference solution, the errors can easily be computed and are shown in figure 7.8.

From figure 7.8 it can be concluded that the effect of reducing the foundation models on the turbine results are negligible. Furthermore, it can be seen that the error introduced by a reduced foundation decreases for elements further away from the tower-foundation interface. This appears to be in accordance with Saint-Venant's principle [146], which states that (in static problems) the effect of an introduced error tends to decrease if one moves further from the source of the error.[3]

7.5 Time simulation results: foundation

As was mentioned in the introduction, the goal of this chapter is to gain insight in the effects of reduced foundation models (which were outlined in chapter 2) and the post-processing analysis (section 7.2) on the accuracy of the fatigue damage computed in the foundation. Hence, in order to obtain the fatigue damage for each beam element a number of steps need to be performed after the full foundation response is obtained from the post-processing analysis, as shown in figure 7.9.

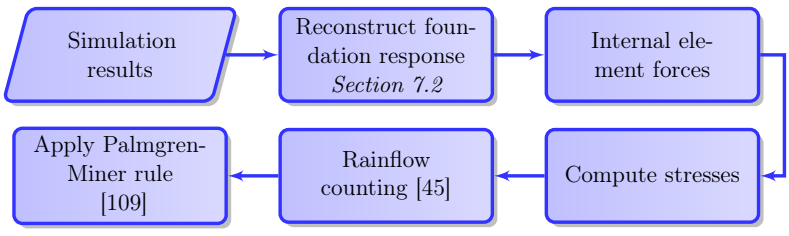

Figure 7.9: *Steps required for determining the fatigue loads of the foundation.*

Firstly, the response of the foundation needs to be computed using one of the post-processing methods presented in section 7.2. From the response of the structure, the internal forces and moments in the beam elements can be determined. From these, using the geometrical properties of the beams, the stresses in the beam can be calculated. For simplicity these stresses are lumped

[3] Note that Saint Venant's principle has only been proven valid for static problems.

to a stress intensity using the Von Misses criterion. Even though this yields conservative fatigue damage estimates, it does allow a straightforward comparison of the different models. The stress cycles are computed using rainflow counting [45] and the cumulative damage is determined from the Palmgren-Miner rule [109].

The steps in figure 7.9 have been performed for all models given in section 7.3.1 in combination with all post-processing options (section 7.2) available. By computing the relative error of the fatigue damage of each element with the corresponding reference damage a simple interpretation of the results is possible:

$$\begin{aligned} \epsilon < 0\% &: \text{ The fatigue damage is underestimated,} \\ \epsilon > 0\% &: \text{ The fatigue damage is overestimated.} \end{aligned} \tag{7.14}$$

Next, in section 7.5.1 the results for the direct expansion are discussed. After that, the quasi-static correction, outlined in section 7.2.1.1, is demonstrated in section 7.5.2. Finally, the results for the force and displacement controlled approaches are presented in section 7.5.3.

7.5.1 Direct expansion of superelement results

The results obtained using direct expansion, as presented in section 7.2.1, are given in figure 7.10. Here the relative error of the fatigue damage for all 224 beam elements that make up the jacket model are shown as a series of box-plots. The relative error percentage is given on the vertical axis and the different models can be identified on the horizontal axis. The data is summarized in a box-and-whisker plot for each model, where the horizontal line enclosed in the box represents the median (Q2 marker) of the data, the box represents the Interquartile Range (IQR) that contains the ±25% (Q3 and Q1 markers) of data points with respect to the median. The whiskers either capture the remaining 25% of the data (as can be seen at the lower whisker at "GR") or is defined as $1.5 \times$ IQR from the Q1 or Q3 markers. The data that is outside of the range spanned by the whiskers are referred to as outliers and are indicated by the + markers.

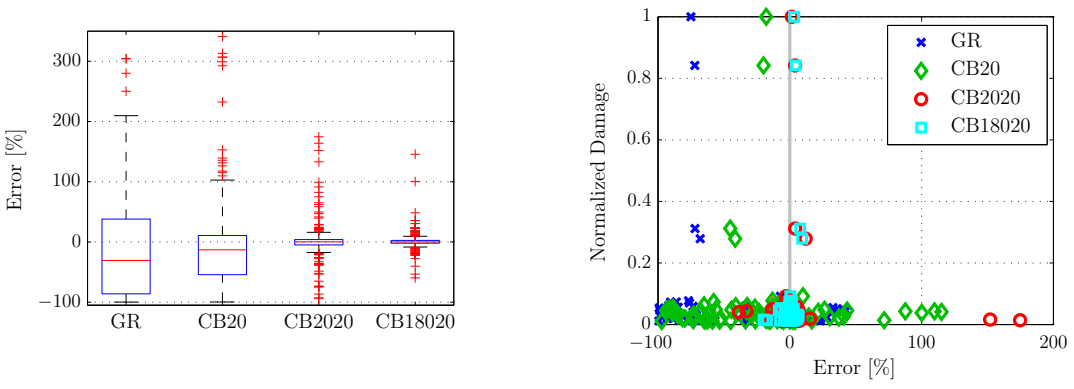

(a) *(b)*

Figure 7.10: *Relative fatigue damage errors from a direct expansion for DLC 1.2 with $v_a = 13$ m/s and $H_s = 3.75$ m.* ***(a)*** *Box-and-whisker plot of elements with an error between -100% and 250%.* ***(b)*** *Error versus normalized damage for elements with $D^{el}_{nor} > 0.01$.*

By examining the results in figure 7.10a it can be seen that by direct expansion of the "GR" model in 50% of the elements the fatigue loads are *underestimated* by at least 30% and in 25% of the elements the fatigue loading is *overestimated* by at least 40%, with a relatively large number of outliers that go up to 4500% overestimation. Even the "CB20" model shows

a relatively large spread in results with outliers up to 820%. These extreme outliers have been left out of figure 7.10a, in order to improve resolution for the two ACB models. By using more advanced reduced models, such as the "CB2020" and "CB18020", the fatigue load predictions improve significantly. This is expected as these models converge towards the full model. Nonetheless, significant errors are still found in a relatively large number of outliers. Also note the improvement that is obtained from including 20 MTAs in the "CB2020" model.

Errors could however be acceptable for elements that are not design driving. In order to determine how accurate the fatigue estimates are on the fatigue driving elements, the normalized damage of all elements is therefore determined according to:

$$D^{el}_{i,norm} = \frac{D^{el}_{i}}{D^{el}_{max}}, \text{ for } i = 1 \cdots n_{el} \tag{7.15}$$

where D^{el}_{nor} is the normalized damage that ranges from zero to one, D^{el}_{max} is the maximum cumulative damage occurring and D^{el}_{i} is the damage in element i. This normalized damage is computed using the reference results and reveals the critical elements for a certain load case. By plotting the normalized damages for the elements with $D^{el}_{nor} > 0.01$ (33 elements out of 224) versus the error on the damage obtained from the expanded results, figure 7.10b is obtained. Hence, figure 7.10a shows the distribution of all errors, whereas figure 7.10b indicates whether the errors are critical or not. By looking at figure 7.10b, one can see that the "GR" model underestimates the damage induced on the critical elements by almost 80% and the "CB20" underestimates these damages by approximately 20%.

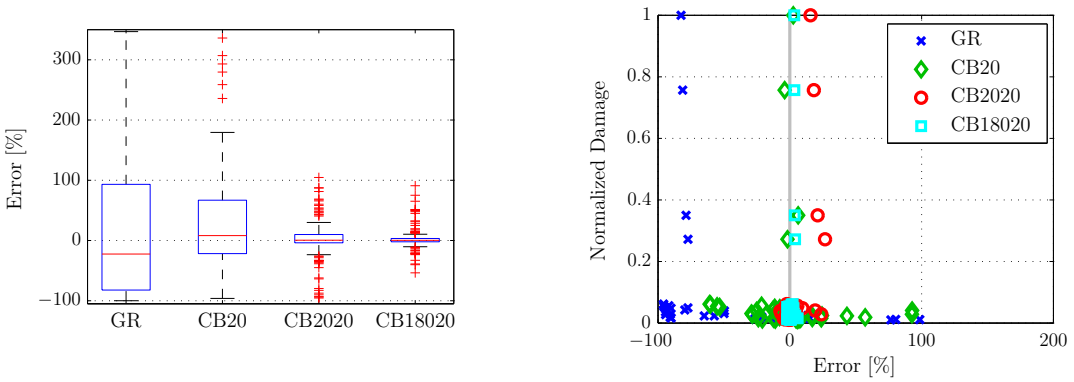

(a) **(b)**

Figure 7.11: *Relative fatigue damage errors from direct expansion for DLC 1.2 with $v_a = 25$ m/s and $H_s = 9.4$ m.* ***(a)*** *Box-and-whisker plot of elements with an error between -100% and 250%.* ***(b)*** *Error versus normalized damage for elements with $D^{el}_{nor} > 0.01$.*

Similar trends can be seen for the DLC 1.2 25 m/s load case, from which the results are shown in figure 7.11. Again, direct expansion of the "GR" and "CB20" models lead to a large spread on the fatigue damage errors (errors up to respectively 8130 % and 3140%). It is clear from figure 7.11b that the "GR" model again underestimates the fatigue damage induced by the critical elements. Note that the accuracy of the "CB2020" model is much lower in comparison to the 13 m/s wind case, as the damage on the most critical elements is now overestimated by 15-20%, whereas the "CB20" model better predicts the fatigue damages in the critical elements. Even though this is counter-intuitive it can be explained from the fact that the solutions of the reduced models will converge to the reference in the *global* sense. As it is seen that the spread in results is much lower for the "CB2020" model, it is more accurate in the global sense while resulting in some larger errors locally. The differences with respect to the other load case are due

to the fact that for this wind speed the blades are pitched relative to the 13 m/s case, leading to the same rotor torque but lower rotor thrust. The wind loading felt by the foundation is thus lower, while wave loading is more dominant due to increased significant wave height. The effect of the limited spatial convergence is therefore more pronounced. Nonetheless, the "CB18020" model still performs outstandingly. Hence, it can be concluded that one has to remain careful when dealing with results obtained from a direct expansion of the modal coordinates.

7.5.2 Improving the results from the expansion using a quasi-static correction

In section 7.2.1.1 an approach to improve the results obtained from the expansion has been presented. This approach applies a quasi-static correction using the residual, that is obtained a posteriori by substituting the expanded modal responses into the unreduced equations of motion. The results are presented in a similar manner as is done in section 7.5.1. Hence, the relative error of the fatigue damage for all the 224 beam elements are shown as a series of box-plots in figure 7.12a for the 13 m/s load case and in figure 7.13a for the 25 m/s load case. By comparing the results in these figures with the ones computed using a direct expansion

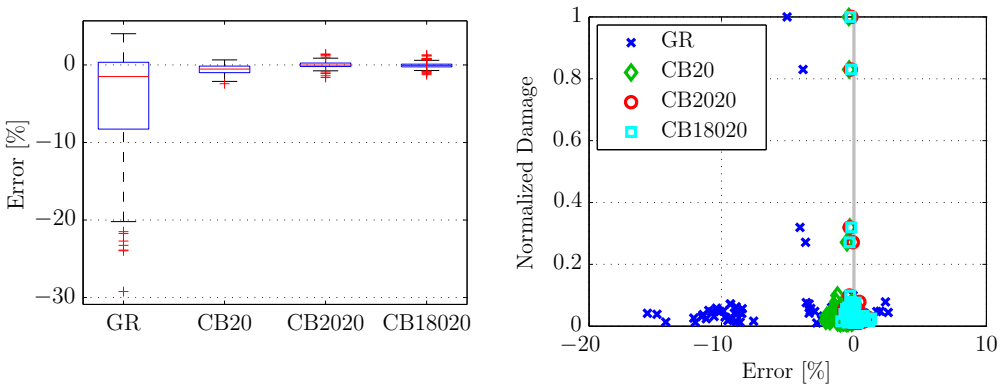

(a) ***(b)***

Figure 7.12: *Relative fatigue damage errors from improving the direct expansion using the quasi-static correction for DLC 1.2 with $v_a = 13$ m/s and $H_s = 3.75$ m.* ***(a)*** *Box-and-whisker plot of all elements.* ***(b)*** *Error versus normalized damage for elements with $D^{el}_{nor} > 0.01$.*

only (figures 7.10a and 7.11a), one can clearly see that the fatigue damage estimates have improved considerably. Firstly, it is seen that the maximum error obtained from the "CB20", "CB2020" and "CB18020" models is less than 3% for *all* elements and can thus be considered as (almost) negligible. However, the most remarkable improvement has been obtained for the fatigue damage estimates for the Guyan reduced model. Whereas this approach resulted into errors from (almost) -100% to 4500% before, the correction has reduced this to errors in the range of -30% to 5%. Nonetheless, an underestimation of 30% for the most crucial element would still be unacceptable.

In order to visualize the errors on the most crucial elements, the relative error versus the normalize damage is given in figures 7.12b and 7.13b. Again, it is clear that the "CB20, "CB2020" and "CB18020" methods result in a negligible error for the most critical elements an thus perform outstandingly. The most noticeable from these figures is again the enormous improvement of the "GR" results with respect to the results shown in figures 7.10b and 7.11b, as the underestimation of the fatigue damage for the most critical elements has been reduced to a range between 2% to 5%.

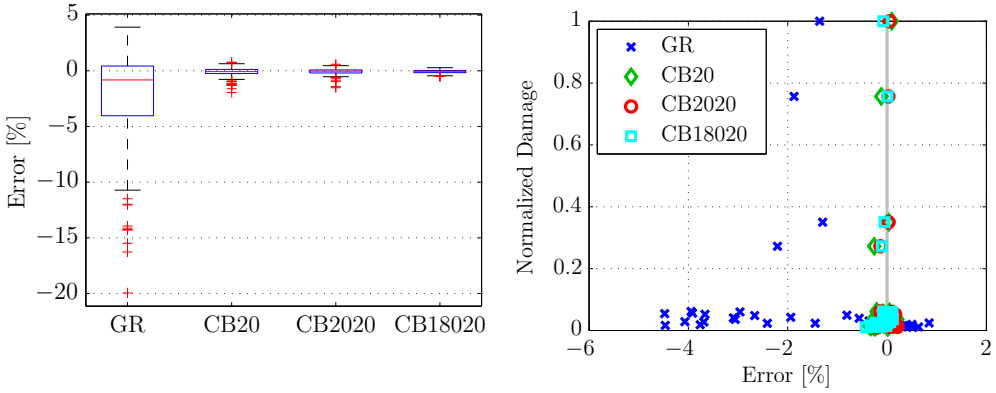

(a) *(b)*

Figure 7.13: *Relative fatigue damage errors from improving the direct expansion using the quasi-static correction for DLC 1.2 with $v_a = 25$ m/s and $H_s = 9.4$ m.* ***(a)*** *Box-and-whisker plot of all elements.* ***(b)*** *Error versus normalized damage for elements with $D^{el}_{nor} > 0.01$.*

This result is explained from the fact that the quasi-static correction mainly corrects for the lack of spatial convergence in the reduced models. As this effect is most pronounced for the "GR" model it is obvious that the improvements (in the absolute sense) due to the quasi-static correction will also be the largest here. Hence, the errors that remain after the correction step are associated to the lack of spectral convergence and these cannot be "fixed" by a simple quasi-static correction. This also explains the highly accurate results obtained (for all the elements) using all the (Augmented) Craig-Bampton models; as these models can be considered as spectrally converged (in the frequency range of the applied forces), the quasi-static correction only needs to repair for the last bits of forces that were "reduced away". Note also, that the difference between the results obtained using the CB and two ACB models is almost negligible, even though the "CB18020" model includes almost 5 times as many modes as the "CB2020" model and 10 times as many as the "CB20" model.

7.5.3 Results from force and displacement controlled approaches

The results obtained with the force and displacement controlled approaches are visualized using the same box-and-whisker plots as introduced in section 7.5.1. In order to be able to compare both methods, using both the quasi-static and dynamic approaches (as presented in section 7.2.3) all the results are given in figures 7.14 to 7.17.

The results are given here in a matrix-representation with two rows and two columns of sub-figures, where the rows show the effect of a quasi-static (1^{st} row) or dynamic (2^{nd} row) post-processing analysis and the columns represent the force (1^{st} column) and displacement (2^{nd} column) controlled approaches. The distributions of the errors are given in figures 7.14 and 7.16 for respectively the 13 m/s and 25 m/s load cases. In addition to this, in figures 7.15 and 7.17 the severity of the errors is rated again by showing these with respect to the normalized damages, in order to identify errors on design driving elements.

Again, a clear summary of the damage results is obtained. Firstly, it can be observed that the static force controlled approach will always lead to an underestimation of the actual fatigue damage. The fatigue damages of the most critical elements are underestimated by about 40% for the 13 m/s load case and approximately 17% for the 25 m/s load case. This is true even in case the interface forces are obtained from the reference model. It can thus be concluded that

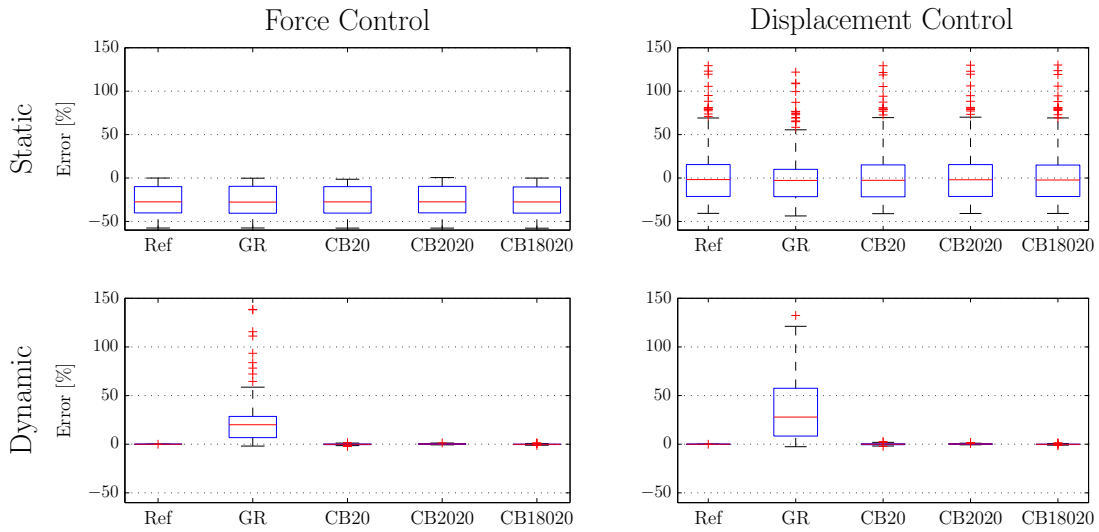

Figure 7.14: *Relative fatigue damage errors from static (1^{st} row) and dynamic (2^{nd} row) force (1^{st} column) and displacement (2^{nd} column) controlled analysis: DLC 1.2 with v_a = 13 m/s, H_s = 3.75 m.*

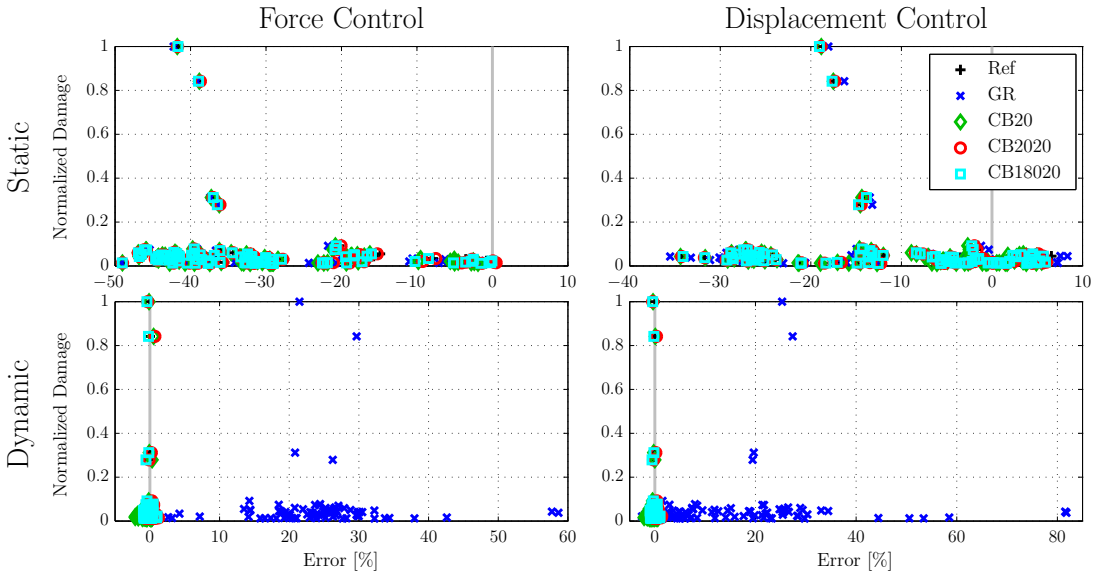

Figure 7.15: *Relative fatigue damage errors from static (1^{st} row) and dynamic (2^{nd} row) force (1^{st} column) and displacement (2^{nd} column) controlled analysis: DLC 1.2 with v_a = 13 m/s, H_s = 3.75 m for elements with $D_{nor}^{el} > 0.01$.*

the jacket response is not quasi-static and the inertia and damping forces cannot be neglected.

The static displacement controlled results show a large spread in figures 7.14 and 7.16, from roughly 50% underestimation to more than 100% overestimation for all methods. By more closely examining the results in figures 7.15 and 7.17 it can be seen that the method appears to perform better than the static force controlled approach, but that still 15-20% (13 m/s) and 5-7% (25 m/s) underestimation for the most critical elements is found. Even though a 5-7% error seems acceptable it should be noted that this error varies per load case. One therefore cannot have confidence in the accuracy level of this method. This again indicates that the assumption of a quasi-static foundation response is invalid and one should be very cautious when applying a static displacement controlled load calculation method for the design of OWT jackets.

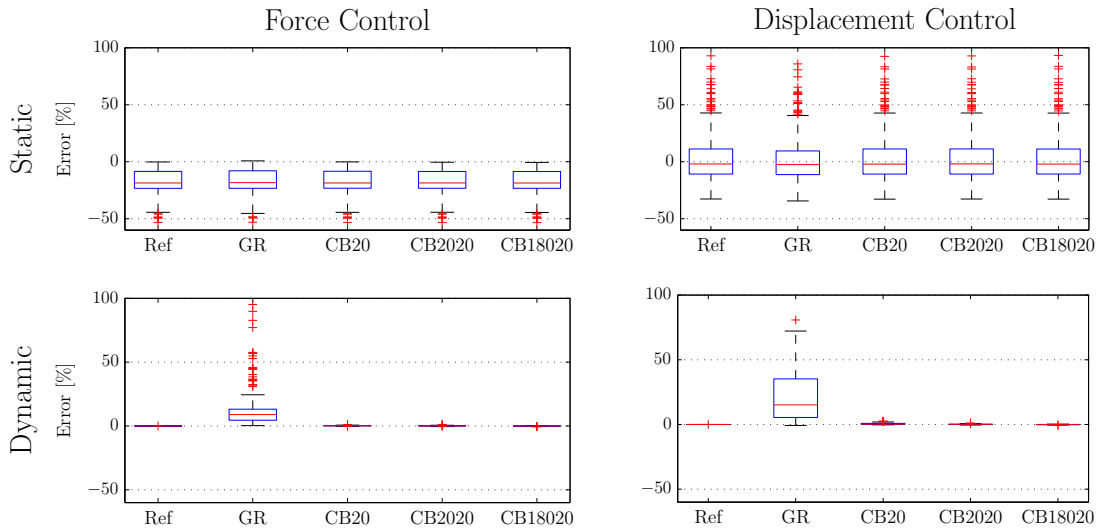

Figure 7.16: *Relative fatigue damage errors from static (1^{st} row) and dynamic (2^{nd} row) force (1^{st} column) and displacement (2^{nd} column) controlled analysis: DLC 1.2 with $v_a = 25$ m/s, $H_s = 9.4$ m.*

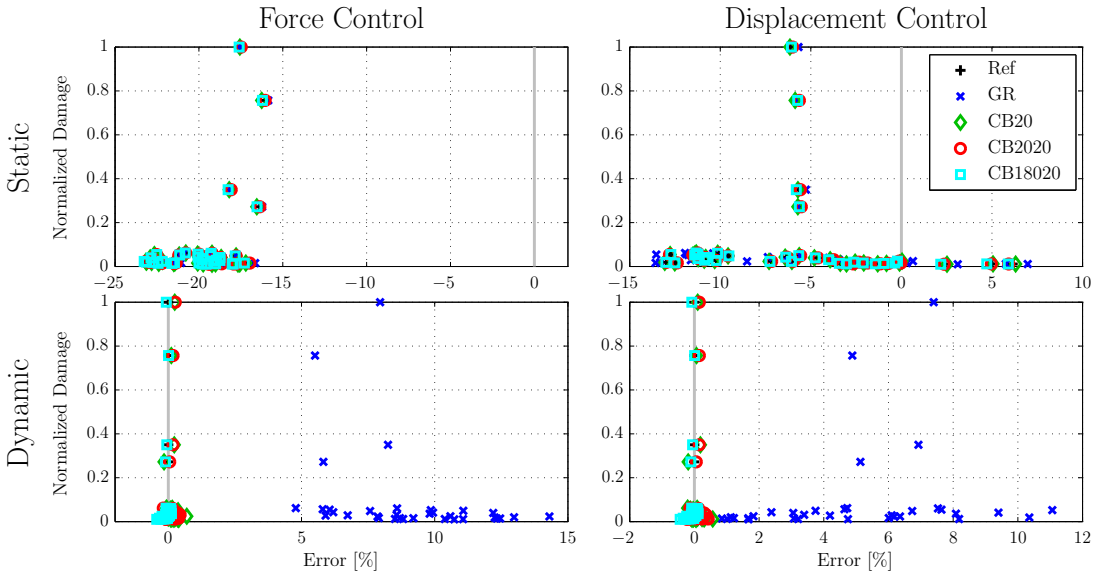

Figure 7.17: *Relative fatigue damage errors from static (1^{st} row) and dynamic (2^{nd} row) force (1^{st} column) and displacement (2^{nd} column) controlled analysis: DLC 1.2 with $v_a = 25$ m/s, $H_s = 9.4$ m for elements with $D^{el}_{nor} > 0.01$.*

No such approximations were made in the derivation of the dynamic force and displacement controlled approaches discussed in sections 7.2.2.1 and 7.2.2.2. It is therefore expected that, when used with the interface forces or motions from the reference model, the fatigue damages obtained from these post-processing methods should be equal to the reference solution. By reviewing the results in all four figures, this is easily verified. From the bottom row of plots in figures 7.14 to 7.17 it can also be seen that the use of the "CB20", "CB2020" and "CB18020" models all lead to accurate predictions for all elements when dynamic force or displacement control is applied. First and foremost, the damage of the most critical elements is highly accurate, but also the fatigue damage of the other elements is accurately obtained. Hence, it is shown that in this case the more limited spatial convergence of the "CB20" model does not affect the global OWT response. Therefore, the local jacket deformations can be accurately reconstructed using a dynamic post-processing analysis.

Finally, it can be seen that a dynamic post-processing analysis using either the force or displacement controlled approach following a Guyan reduction leads to significant overestimation of the fatigue damage. It should be noted that in figures 7.14 and 7.16 not all outliers are shown for the "GR" results. In fact, the maximum error found for the dynamic force and displacement controlled approaches are respectively over 140% and 500% for the 13 m/s load case and almost 100% and 200% for the 25 m/s load case. By reviewing the error versus normalized damage in figures 7.15 and 7.17 it is clear that for both methods one can find a 20% to 30% overestimation of the accumulated fatigue damage for the most critical elements.

Given the underestimation found when directly expanding results from the Guyan superelement in the previous section, this overestimation can be surprising. This can be explained as follows. On the one hand, due to the limited spatial convergence of the Guyan reduced model, the displacements at the internal degrees of freedom are largely underestimated when computed by direct expansion. On the other hand, the lack of spectral convergence leads to an overly stiff representation of the foundation such that in the integrated analysis the spectral content of interface signals is too high. Thereby additional dynamics in the jacket are excited in a dynamic post-processing analysis, leading to an overestimation of the loading.

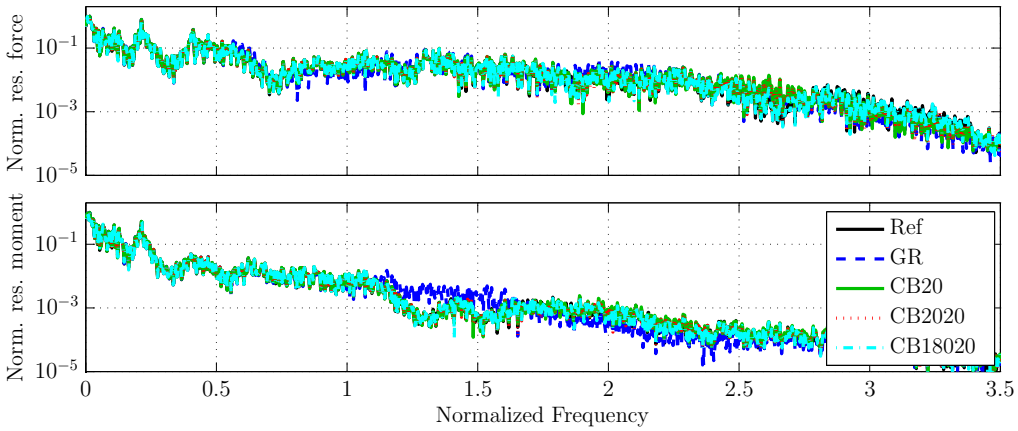

Figure 7.18: *Spectra of the detrended resultant interface forces and moments for the different models from DLC 1.2 with $v_a = 13$ m/s and $H_s = 3.75$ m.*

In figure 7.18 the normalized spectra (normalized with respect to the 20^{th} eigenfrequency of the reference system) of the (detrended) normalized resultant interface forces and moments are given. Here one can clearly distinguish the significantly higher interface moments for the "GR" model in the normalized frequency range from approximately 1.1 to 1.6. By comparing the results in figure 7.18 with those found from figure 7.7, it is clear that this range corresponds to where the eigenfrequencies of the "GR" model start to deviate from those obtained using the reference model.

7.6 Sensitivity of results with respect to the foundation's stiffness

In the test case presented in section 7.3, the turbine installed on the UpWind reference jacket is the Siemens SWT-3.6-120. However, the UpWind jacket has been designed to be used with the NREL benchmark turbine, a 5MW offshore wind turbine equipped with a 126m rotor [89], which is a significantly larger and heavier turbine (RNA: 350 tonnes versus 225 tonnes). Hence, it is expected that the foundation is also heavier and stiffer than what would be required for

the SWT-3.6-120. In order to quantify the effect of a more flexible foundation on the results of the test case introduced in section 7.3, a more compliant UpWind jacket is created.

The easiest way of lowering the stiffness, is by simply lowering the Young's modulus of the material used in the model. Therefore, the Young's modulus in the material properties has been lowered to 40% of the original modulus: from 210 GPa to 84 GPa. It was verified using a modal analysis that the design criterion on first natural frequency of the integrated offshore wind turbine structure still holds. This means that the first natural frequency is in the spectral bandwidth between the 1P and 3P frequencies, such that the forced response due to these main excitation sources is limited. Nonetheless, this does not guarantee that the jacket foundation fulfills the other main design criteria.

In figure 7.19 the (frequency normalized) eigenfrequencies of the offshore wind turbine are shown for the different reduced models. Note that the frequencies in figure 7.19 are normalized as in figure 7.7, such that one can directly compare these figures. The models are reduced again in the same manner as in the original test case, thereby resulting in the models given in table 7.2. One can easily observe from comparing figures 7.7 and 7.19, that eigenmodes are shifted

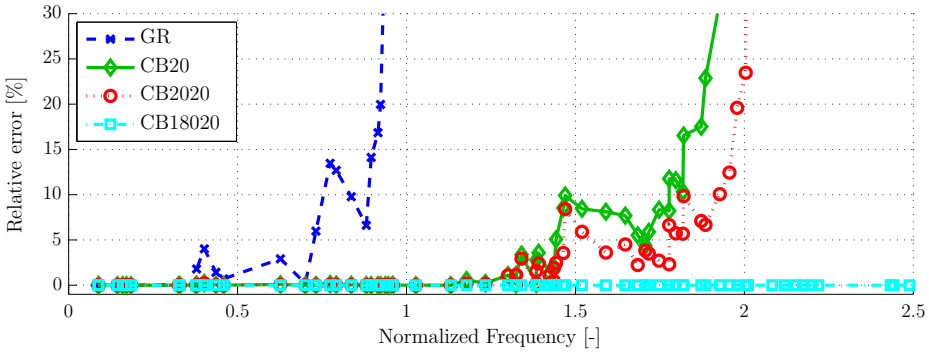

Figure 7.19: *Relative error on the eigenfrequencies of the reduced models.*

down in frequency and that the "GR" model of the more flexible jacket already starts to deviate substantially after the first 14 modes, compared to 20 modes for the original model. In addition to this, the "CB20" and "CB2020" models also start to deviate at lower (normalized) frequencies.

Jacket model				**Turbine model**	**Total model**	
# $\boldsymbol{\Psi}_C$	# $\boldsymbol{\Phi}_{[i]}$	# $\boldsymbol{\Phi}_{MTA}$	# DoFs	# DoFs	Total DoFs	Name
-	-	-	1062	406	1062 + 406	Ref
6	-	-	6	406	6 + 406	GR
6	20	-	26	406	26 + 406	CB20
6	20	20	46	406	46 + 406	CB2020
6	180	20	206	406	206 + 406	CB18020

Table 7.2: *Overview of simulation models of offshore turbine used for the sensitivity study.*

In order to quantify the effect of a more flexible foundation, only one of the two load cases presented in section 7.3 is applied. It is chosen to use the load case where the turbine is operating around its nominal power, which corresponds to an average wind speed of 13 m/s, and the significant wave heights (H_s) are chosen as 3.75 m.

The rest of this section is organized such that in section 7.6.1 the effect of the different reduced models on the damage equivalent loads in a number of elements in the turbine are shown.

In section 7.6.2 the effect of a direct expansion on the fatigue damage induced on all the elements of the more flexible jacket is shown. These results are then improved using the quasi-static correction in section 7.6.3. Finally, in section 7.6.4 the force and displacement control approaches are applied again to obtain the fatigue damages in the elements of the jacket. Here, the effect of both post-processing methods and the different reduced models are shown for the more flexible foundation.

7.6.1 Effect on the damage equivalent loads for the wind turbine component

Firstly, the error on the DELs (see section 7.4) in three different wind turbine elements: the tower bottom, tower top and root of blade 1, are shown in figure 7.20. In section 7.4 it has been found that the effect of the reduced foundations on the turbine's DELs is small for all the CMS methods applied. From figure 7.20 it can clearly be seen that this is not the case for the more flexible jacket foundation, as an overestimation of 11% on the tower bottom DEL and 5.5% on the tower top DEL is found from the "GR" model. The (Augmented) Craig-Bampton models still show an excellent performance with negligible errors on all three focus elements. It can also be seen that the error on the tower bottom resultant bending moment is larger for the "CB18020" model than for the "CB2020". Even though this is contrary to ones intuition, it should be noted that increasing the number of modes in a reduction basis ensures a convergence in the *global* and not in the *local* sense. In addition, this difference is so small that (part of) it is most likely caused by the numerical tolerances used in the time stepping scheme (as is also discussed in section 7.5).

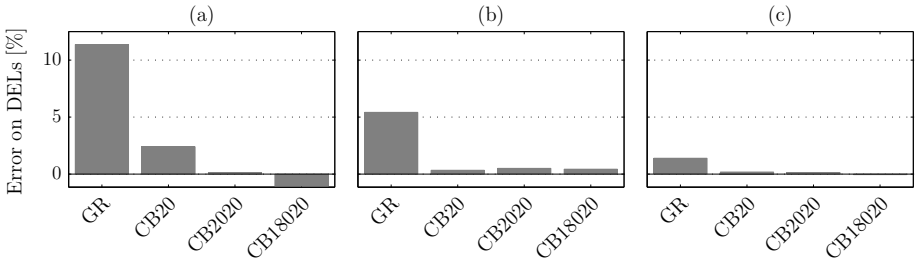

Figure 7.20: *Error on the damage equivalent loads for different elements. Result from DLC 1.2 with $v_a = 13$ m/s and $H_s = 3.75$ m.* ***(a)*** *Tower bottom element;* ***(b)*** *Tower top element;* ***(c)*** *Blade 1 root element.*

As is already explained in section 7.5, the lack of spectral convergence for the "GR" model leads to an overly stiff representation of the jacket. Therefore, this results in more pronounced high frequent deformations in the tower and hence, higher DELs in the tower elements.

This effect is also seen in the spectra of normalized interface forces and moments between the wind turbine and jacket substructures, which are given in figure 7.21. Note again that the amplitudes of the interface forces and moments are normalized and that the frequencies are normalized as in figures 7.7, 7.18 and 7.19 in order to allow for cross comparisons. From figure 7.21 it is clear that the interface forces for the "GR", "CB20" and "CB2020' models start to deviate from the reference solution around the same (normalized) frequencies as where the eigenfrequencies of these models start to differ, as is seen in figure 7.19. By comparing figures 7.18 and 7.21 it it clear that the interface forces (and moments) of the "GR" model differ already at a lower frequency. As the main part of the excitation energy in the wind and waves is relatively low-frequent, a lower frequent spectral mismatch due to the reduced models will have a stronger effect on the coupled responses, as is seen in the results presented in this section.

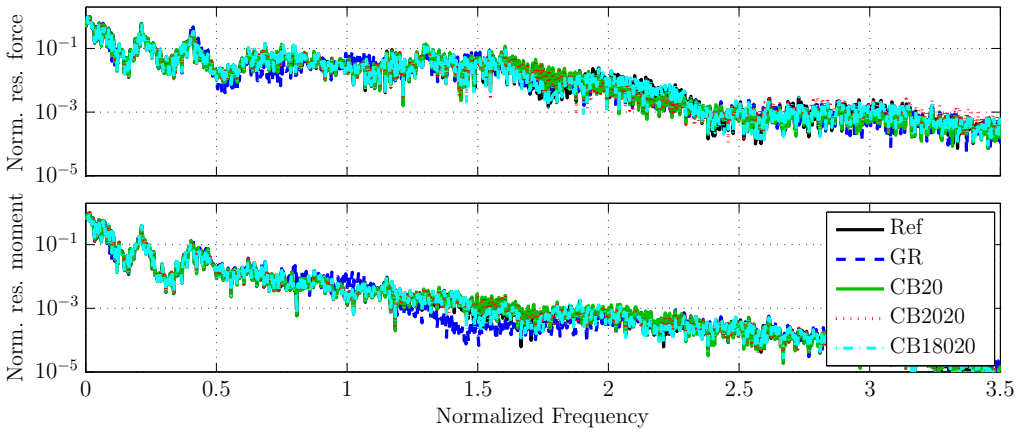

Figure 7.21: *Spectra of the detrended resultant interface forces and moments for the different models from DLC 1.2 with $v_a = 13$ m/s and $H_s = 3.75$ m.*

7.6.2 Effect on the jacket's fatigue damage estimates using direct expansion

In order to reconstruct the full nodal response of the jacket, one can (again) perform a direct expansion of the modal response of the reduced jacket, as is outlined in section 7.2.1. The results from this operation are presented using box-and-whisker plots, in figure 7.22a, as relative errors on the fatigue damage in all elements. Firstly, it is observed that a large spread in the results is obtained from directly expanding the modal coordinates associated to the Guyan reduced jacket model. One can observe that the fatigue damages in 50% of the elements are 30% to almost 100% underestimated, whereas the fatigue damages in 25% of the elements are at least

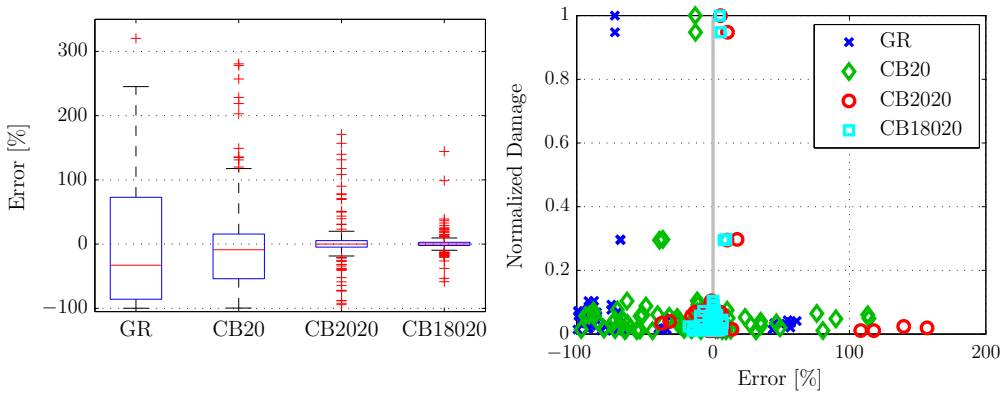

(a) ***(b)***

Figure 7.22: *Relative fatigue damage errors from direct expansion for DLC 1.2 with $v_a = 13$ m/s and $H_s = 3.75$ m.* ***(a)*** *Box-and-whisker plot of all elements with an error between -100% and 350%.* ***(b)*** *Error versus normalized damage for elements with $D^{el}_{nor} > 0.01$.*

overestimated by 70% (the largest error found is in fact approximately 7500%). Secondly, it is seen that the results tend to converge over the models, i.e. the largest spread is found for the "GR" model and the smallest for the "CB18020" model. This is in line with the theory of the CMS methods, where the error in the global sense decreases by adding more and more modes in the reduction basis.

In figure 7.22b the normalized damage, computed according to Eq. (7.15), with respect to the relative error is given. Here it can be seen that the fatigue damage obtained using the "GR"

model is about 70% underestimated in the four most critical elements, which demonstrates the extreme poor fatigue damage estimates obtained from applying direct expansion to the modal coordinates obtained using a Guyan reduced model. The Craig-Bampton model does a bit better, but still shows substantial underestimates and the Augmented Craig-Bampton models perform a lot better. Nonetheless, the fatigue damage for the four most critical elements is overestimated by about 5% to 10% for the "CB1820" model and about 5% to 18% for the "CB2020" model. Comparing these results with the ones obtained using the original UpWind reference jacket in section 7.5.1, it is clear that the "GR" model results in the same extremely poor fatigue damage estimates and that both the "CB2020" and "CB18020" show a slight deterioration in the fatigue damage estimates obtained.

7.6.3 Improving the direct expansion results using a quasi-static correction

In order to improve the results obtained using a direct expansion (which are shown in figure 7.22), the quasi-static correction is applied. The results are presented in figure 7.23. From

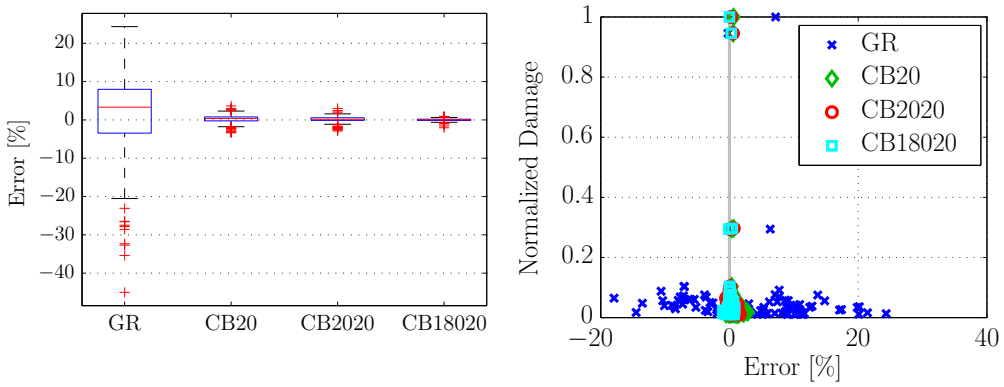

(a) ***(b)***

Figure 7.23: *Relative fatigue damage errors from improving the direct expansion using the quasi-static correction for DLC 1.2 with $v_a = 13$ m/s and $H_s = 3.75$ m.* ***(a)*** *Box-and-whisker plot of all elements.* ***(b)*** *Error versus normalized damage for elements with $D^{el}_{nor} > 0.01$.*

the results it is clear that the quasi-static correction greatly improves the results. Firstly, very accurate results in terms of fatigue damages are obtained using both the both Augmented Craig-Bampton models. In addition, the difference between these results is negligible, even though the "CB18020" model is reduced with far more modes than the "CB2020" model. The quasi-static correction is able to "fix" the limited spatial convergence of the "CB20" model, thereby resulting in fatigue damage estimates that are highly accurate. The improvements for the "GR" model are again immense; from a range of errors of almost -100% - 7500% to a range of -46% to 26% and the error on the critical elements has improved from a 75% underestimation to a 7% overestimation. All these findings are in line with what has been found and discussed in section 7.5.2.

7.6.4 Force and displacement controlled results: Performance of the reduced models

The results for the foundation are also obtained using the force and displacement controlled approaches, presented in section 7.2.2. The box-and-whisker plots showing the distribution

of the results for all elements are given in figure 7.25. The results are given here in a matrix-representation with two rows and two columns of subfigures, where the rows show the effect of a quasi-static (1st row) or dynamic (2nd row) post-processing analysis and the columns represent the force (1st column) and displacement (2nd column) controlled approaches.

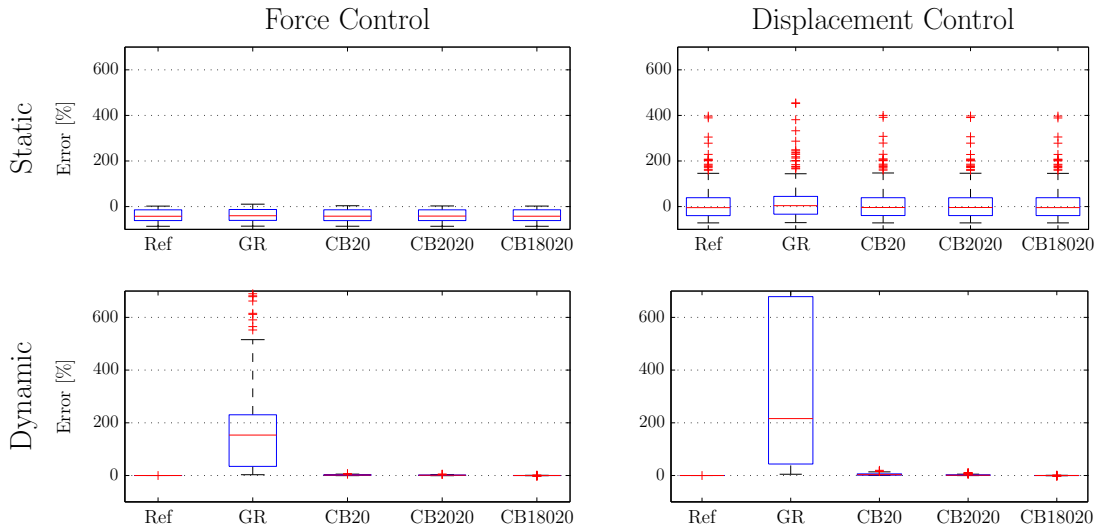

Figure 7.24: *Relative fatigue damage errors from static (1st row) and dynamic (2nd row) force (1st column) and displacement (2nd column) controlled analysis: DLC 1.2 with $v_a = 13$ m/s, $H_s = 3.75$ m.*

It is easily observed that the static force control approach leads to underestimating the fatigue damage for almost all elements using all the different models, thereby indicating that the participation of the jacket in the integrated wind turbine is in fact dynamic and not quasi-static.

A large spread in the results is obtained from a static displacement control analysis, indicating that for about 50% of the elements the fatigue damages are underestimated and are overestimated for the remaining elements. Thereby indicating that also this approach is unsuited for reconstructing the full nodal response of the jacket.

Accurate results are obtained using the dynamic force and displacement controlled methods in combination with either the reference model or the (Augmented) Craig-Bampton models. However, large overestimations are obtained from using the Guyan reduced model. It has already been shown and discussed in section 7.5.3 that the spectral mismatch of the Guyan reduced model leads to overestimating the fatigue damages when using the dynamic force and displacement control approaches. From figure 7.25b it is seen that the dynamic force control approach in combination with the Guyan reduced foundation models, leads to overestimating the fatigue damage for the four most critical elements by approximately 150% to 180%. In addition, the dynamic displacement control approach with the "GR" model gives an 85% to 115% overestimation for the fatigue damages in these elements. Clearly, if one would use the Guyan reduced model for the integrated analysis of this specific offshore wind turbine, one could either end up with a jacket structure that is significantly under- (using direct expansion) or over-designed (using the dynamic FC and DC methods). In the former case this would mean that the structure might not survive its design life and in the latter case one would end up with a jacket design that is too expensive, thereby hindering the economical viability of a particular wind farm.

If one compares these results with the one obtained for the original UpWind reference jacket model in section 7.5, it can easily be concluded that all the effects described are amplified when using a more flexible foundation. Or in other words, the more a component's own dynamics

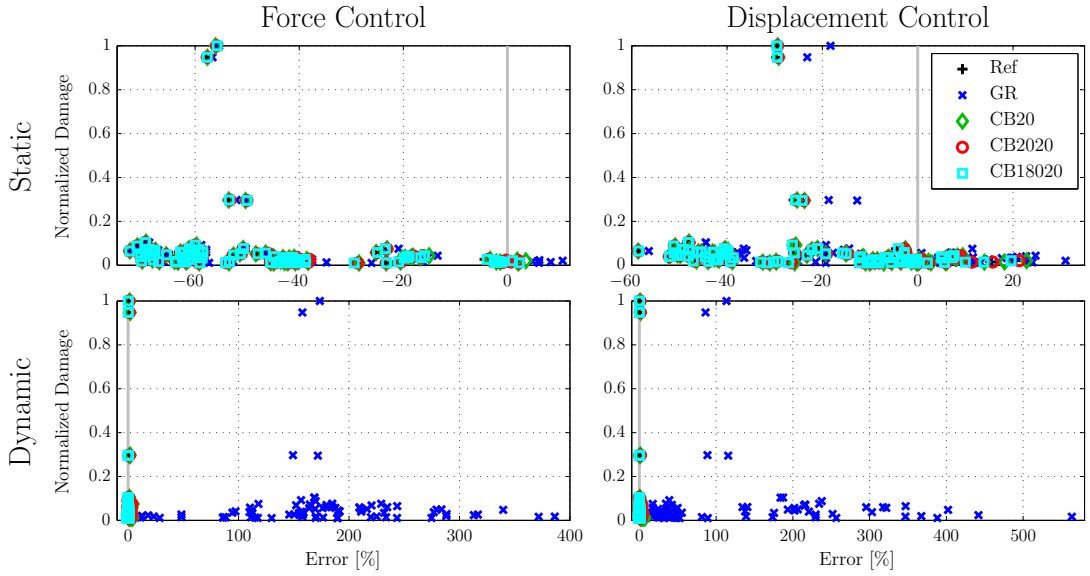

Figure 7.25: *Relative fatigue damage errors from static (1^{st} row) and dynamic (2^{nd} row) force (1^{st} column) and displacement (2^{nd} column) controlled analysis: $v_a = 13$ m/s, $H_s = 3.75$ m for elements with $D^{el}_{nor} > 0.01$.*

move (in frequency) towards the dynamics of the integrated structure and its loading, the more pronounced the effect of the component's local dynamics on the global dynamics of the integrated structure becomes. Therefore, a correct representation of this component in the integrated structure becomes ever more vital.

7.7 Comparison of the computation times

As the process for designing the support structure of an offshore wind turbine requires many thousands of simulations, an important aspect to consider is the computational cost. In figure 7.26 the normalized computation times of the subsequent steps in the calculation process are shown. Note that the computation times are normalized with respect to the computation time of the reference model. The total computation time is build up from the three main steps in the process: starting with the reduction of the jacket model, followed by the aero-elastic simulations using BHawC and finally, the post-processing analysis to obtain the full nodal jacket response.

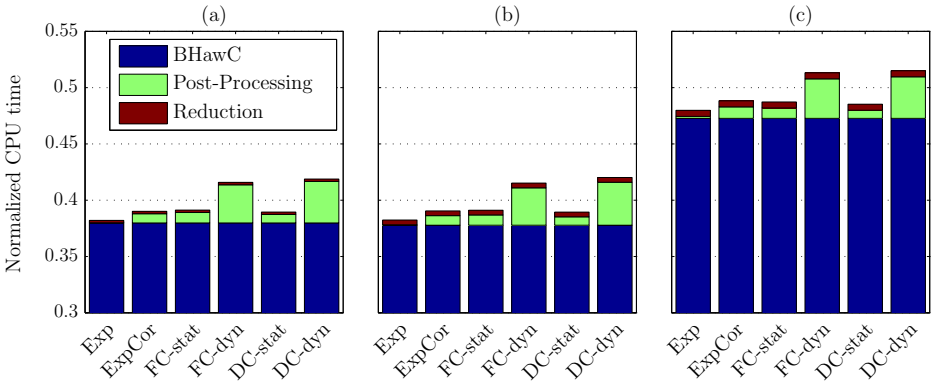

Figure 7.26: *Normalized computation times for the subsequent steps in the computational process using different reduced models;* ***(a)*** *GR;* ***(b)*** *CB2020;* ***(c)*** *CB18020.*

The different subfigures result from the different reduced models and the stacked bars within the subfigures represent the total (normalized) computation times for the entire process, using the different post-processing analysis methods available. Note that, as the times associated to the "CB20" model are indistinguishable from the "GR" and "CB2020" computational times, they are left out of the current comparison.

Firstly, it can be observed that the computational cost of the aero-elastic simulations represent by far the largest part of the total cost for all the different models. Note that one generally only requires one reduced model (or a small number of load case dependent reduced models) for all the thousands of simulations, hence one should divide the cost of the reduction by the number of simulations performed. This will obviously cause the cost of the reduction to be negligible. The cost of the direct expansion, denoted by "Exp", can also be considered as negligible for all the models. As the quasi-static residual corrections ("ExpCor") requires one to factorize the stiffness matrix (in addition to computing the residual), as is also required for the quasi-static FC and DC approaches, the computation costs are similar. The dynamic force and displacement control approaches are the most expensive methods for reconstructing the foundation response. Nonetheless, in combination with the Augmented Craig-Bampton models, the most accurate results are obtained using these dynamic reconstruction approaches.

Even though performing the time simulations for the post-processing analysis also only requires factorizing the time-stepping matrix once (as the system at hand is linear), the implicit time integration scheme still involves a high number of matrix-vector calculations, as one loops over the different time steps. In addition, due to the construction of the damping matrix (see section 7.3.1.2), the stepping matrix that has to be factorized is a full matrix. These costs are saved by using the static post-processing approach and in addition one can solve the entire time series of displacements in a single step using multiple right-hand-sides at once.[4]

Hence, the most optimal approach, from a cost of computations point of view, would be to use a reduced model that (i) can be considered as spectrally converged and (ii) is able to capture at least the wave forces that affect the global response of the system, such as the "CB20" and "CB2020" models that have been used. By correcting the results from the expansion with a quasi-static residual correction step, one is able to accurately reconstruct the global, as well as all the local deformations.

7.8 Summary

Firstly, it has been found that both the static FC and DC underestimate the fatigue damage for all models tested. This thus means that the inertia and damping forces play a crucial role in the response of the jacket structure and cannot be neglected. This is confirmed by the fact that the Guyan reduced model is the only model that does not give accurate results in the dynamic FC and DC methods; a detailed explanation for this observation was given above.

Furthermore it is observed that both the dynamic FC and DC approaches lead to better results than a direct expansion of the (Augmented) Craig-Bampton models. It is also seen that these approaches are able to accurately reconstruct small, local deformations which are not even captured by a highly accurate reduced model such as the "CB18020". The fatigue damages computed from the expanded "CB2020" results slightly overestimate the actual damage for the critical elements, whereas the "CB20" model can result in an underestimation of the fatigue

[4] Obviously, these effects are all dependent on the size of the problems one tries to solve. Another important factor is the implementation of all methods and in which language the programs are written; MatLab, which is used for these calculations, might not be the most efficient choice.

damage for these elements and shows a larger spread in the errors. Nonetheless, applying the residual quasi-static correction to the expanded results significantly improved these. In fact, results as accurate as the dynamic FC and DC approaches were obtained, at a lower (computation) cost. The actual magnitude of the errors will obviously be highly dependent on the actual design of an offshore jacket and therefore one cannot make any general statements on the amount of modes that one requires in a reduction basis.

It should also be noted that the large errors found for the majority of the post-processing approaches when using the Guyan reduced jacket superelement, could not have been predicted by looking only at the wind turbine results (sections 7.4 and 7.6), as these are less sensitive to the reduction applied to the foundation model.

In addition, it has been found in section 7.6 that all the effects described here tend to escalate in case of a more flexible foundation structure, where the local dynamics start to influence the global dynamic behavior of the integrated wind turbine. Hence, uneducated choices for the reduction method and post-processing analysis could result in a pre-mature failure of the integrated wind turbine, or could lead to jacket designs that are too expensive, thereby hurting the future economical viability of offshore wind power.

From the point-of-view of computation times, the best approach would be to use an accurate, but still compact, reduced model (such as the "CB20" or "CB2020") and to apply an expansion with a quasi-static residual correction afterwards, as in this case the reduced model ensures the correct global response of the entire OWT. The local response can then be significantly improved afterwards, by applying the correction step. On the other hand, if one is working with commercial finite element software for the modeling and reduction of the foundation structure, it could be that computing the residual and applying a correction due to this residual could prove the be tedious or practically impossible. In that case the dynamic force and displacement controlled approaches should be the post-processing methods of choice. As it was found that, even though these approaches are more expensive (from a computational point of view) than a direct expansion, they allow for applying more compact (Augmented) Craig-Bampton models in the aero-elastic simulations. As these simulations take up most of the computing time, relatively small saving here can easily outweigh the extra costs in the post-processing analysis.

8

Integrated Offshore Wind Turbine Simulations using Equivalent Interface Loading

"People are very open-minded about new things - as long as they're exactly like the old ones."

– Charles F. Kettering

8.1 Introduction

The accuracy of the response of the foundation's internal DoFs is dependent on both the effect of the spectral and spatial convergence of the superelement in the frequency bandwidth of interest, as was already outlined in chapter 2 and section 7.1.2. In chapter 7 the forces exciting the internal DoFs of the jacket were handled in a more "traditional" manner, as these were reduced using the same reduction basis that was used to reduce the finite element model. Therefore, both the spectral and spatial effects are responsible for the results obtained in sections 7.4 and 7.5. Nonetheless, some general statements about these effects could be distilled from the results.

In this chapter the spatial effect on the results is eliminated by replacing the wave forces on the internal (and thus reduced) DoFs by different types of equivalent excitations that are directly applied on the interface DoFs, which are retained after the reduction. In chapter 6 it has been shown that one is able to determine sets of equivalent interface loads that result in the exact response for the neighboring substructures. One thereby eliminates the effect of the spatially reduced wave forces on the coupled response obtained from the integrated OWT simulations. This approach has a number of advantages with respect to reducing the forces applied to the internal DoFs, as was already introduced in chapter 6:

- Firstly, it can be shown that (in the case of an unreduced "source" substructure) the forcing effect on the "receiver" substructures is exact. Hence, the responses of the "receivers" that are obtained, are not approximated but exact.
- Secondly, only forces on the interface need to be shared between project groups. This will typically involve much less data compared to the process of sharing either the full set of forces or even the set of reduced wave forces.

- Thirdly, one does not require a load case dependent reduction basis per load case. For instance, if waves come from different compass directions one would either have to create a superelement for each compass direction, or build one (probably) very large reduced model that can accurately account for wave loading from all possible directions. As in this case the loading is directly applied to the (retained) interface DoFs, one can employ the "classical" CMS methods to find a single unique superelement that can be used for all load cases.

Nonetheless, the approach also poses a number of disadvantages:

- Firstly, in order to obtain the different types of equivalent loading, a time integration per load case is required using the "source" substructure. Hence, a large number of different load cases requires also a large number of these "pre-processing" time integrations to obtain the equivalent interface excitations. However, as the "source" substructure and its loading is required to be linear, the time integrations are relatively cheap from a computational point of view, when compared to simulating nonlinear systems.
- Secondly, the response found for the "source" substructure in the coupled analysis is erroneous, when directly compared to the reference solution. However, the obtained response can easily be corrected, as is shown in sections 6.3 and 6.4.

In order to demonstrate the approach, a single iteration loop in the design process of an offshore wind turbine support structure, as presented in section 1.5, is mimicked.

8.1.1 Models and load case used for the demonstration

The test case used for demonstrating the equivalent loading approaches is based on the models that are already presented in section 7.3. Hence, the wind turbine is the SWT-3.6-120 modeled in the Siemens in-house aero-elastic code BHawC and the foundation is a finite element model of the (original) UpWind reference jacket, which is introduced in section 7.3.1.2 and also used in the OC4 benchmark study [37, 188].

Jacket model			**Turbine model**	**Total model**	
# $\boldsymbol{\Psi}_C$	# $\boldsymbol{\Phi}_{[i]}$	# DoFs	# DoFs	Total # of DoFs	Name
-	-	1062	406	1062 + 406	Ref
6	-	6	406	6 + 406	GR
6	20	26	406	26 + 406	CB20
6	180	186	406	186 + 406	CB180
-	-	1062	406	1062 + 406	Full

Table 8.1: *Overview of simulation models of offshore turbine.*

However, as the wave forces are applied as equivalent loads on the (retained) interface DoFs, there is no need to use the Augmented Craig-Bampton method that is outlined in section 2.5.[1] Therefore, the Augmented Craig-Bampton models are replaced by "classical" Craig-Bampton models employing either 20 ("CB20") or 180 ("CB180") fixed interface modes. An overview of the simulation models used in the current test case is given in table 8.1. The reference model, that includes both the full FE model of the jacket and the original set of distributed wave forces,

[1] Note that augmentation is not only used for accurately capturing the response due to forces on the non-retained DoFs, but also to improve the truncation of the modes in the reduction basis by adding quasi-static modes of the interface, as is shown in [41, 137].

is indicated by "Ref". The model denoted as "Full" includes the full FE model, but with the equivalent interface excitations applied to it.

In the current test case only one of the two DLC 1.2 load cases, that are presented in section 7.3.2, is considered. It has been chosen to include the load case that corresponds to the wind speed where the turbine is operating around its nominal power (13 m/s). The associated significant wave heights (H_s) were chosen at 3.75 m. Again, six seeds are considered for the wind speed in order to get some statistical averaging.

8.1.2 Chapter outline

This chapter is organized such that firstly, in section 8.2, the different steps for obtaining and applying the equivalent interface excitations are outlined. In addition, the different types of equivalent interface excitations are introduced and discussed. In section 8.3 the results for the wind turbine substructure, that are obtained from applying equivalent excitations on the interface, are presented. Following this, in section 8.4, the effect on the obtained fatigue damages for all foundation elements is presented and discussed. A comparison of the computational costs associated to the different approaches is made in section 8.5. Finally, a summary of the chapter and results obtained is given in section 8.6.

8.2 Use of equivalent interface forces and displacements in the integrated analysis

In order to use the concept of equivalent loading on the interface for the integrated analysis of an offshore wind turbine, a number of steps are required, as is shown in figure 8.1. The first step is to use the full set of external wave forces and the jacket model to determine the equivalent loading on the interface, as is presented in sections 6.3 and 6.4. In these sections it is shown that the forces on the internal DoFs of a linear "source" component, can be taken into account as either a set of equivalent forces on the interface or as a compatibility error when using dual assembly. Hence, in the first case one needs to constrain the substructure at its interface, determine the fixed-interface response due to the forces applied on the internal DoFs and compute the corresponding constraint (or blocked) forces. The latter of the two approaches requires one to perform a time integration taking into account the free interface model and applied external forces. The displacement response of the interface DoFs can be used as a compatibility error in the coupled time integrations, such that the exact forcing effect onto the "receiver" substructures is obtained.

The foundation model is then simultaneously reduced using one of the CMS methods presented in section 2.2. As a next step in the total process, the reduced foundation model and wind turbine model are assembled to form an integrated model of the offshore wind turbine. The integrated model is used, together with the set of equivalent excitations applied to the interface of the foundation and the wind input for the aero-dynamic model, to perform the aero-elastic simulations. The coupled results obtained have to be analyzed further, using one of the post-processing analysis methods presented in section 7.2, in order to determine the fatigue loading in all the elements of the foundation model.

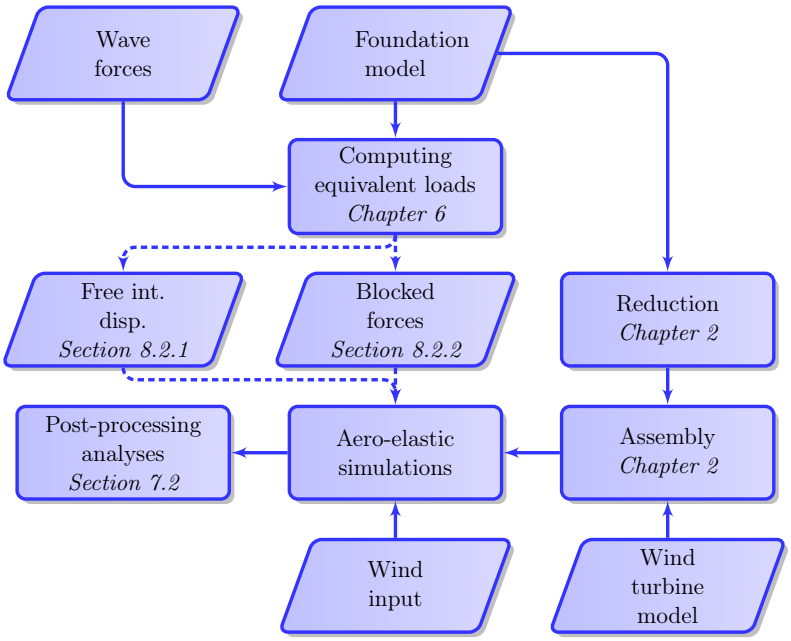

Figure 8.1: *Steps needed when employing equivalent excitations on the interface.*

8.2.1 Equivalent loads using the blocked force approach

In section 6.3 it is shown that one needs to perform a full dynamic analysis *per load case* using the fixed interface jacket that is excited by the set of distributed wave forces in order to obtain the equivalent forces on the interface. In addition, the time integration method and parameters used need to be fully consistent with the time integration used for the integrated aero-elastic wind turbine simulations. Obviously, if one has to deal with a large number of different wave load cases, this pre-processing step can become computationally quite expensive. An approach, introduced at the end of section 6.3.3, that would save some computational cost is to perform these pre-processing analyses statically, such that one assumes that the response of the stand-alone jacket to the wave loads is in the quasi-static regime. In that case, one can neglect all the damping and inertia contributions and one simply has to solve the associated static problem, given in Eq. (6.27). A strong indication of whether a (quasi-) static analysis is allowed is given by comparing the first fixed interface eigenfrequency $\omega_{[i],1}$, obtained from the following eigenvalue problem:

$$\left(\boldsymbol{K}_{[ii]} - \omega^2_{[i],j}\boldsymbol{M}_{[ii]}\right)\boldsymbol{\phi}_{[i],j} = \boldsymbol{0},$$

with the spectrum of the wave loads, given as the magnitude of the Fourier transform of the wave forces obtained from:

$$\begin{cases} \hat{\boldsymbol{F}} = \mathcal{F}(\boldsymbol{f}^{(F)}) \\ |\boldsymbol{f}^{wave}(\omega)| \triangleq \left(\hat{\boldsymbol{F}}^H(\omega)\hat{\boldsymbol{F}}(\omega)\right)^{\frac{1}{2}} \end{cases}, \tag{8.1}$$

where $\hat{\boldsymbol{F}}(\omega)$ is defined as the Fourier transform of the time series of (externally applied) wave forces and $\star^H$ is defined as the Hermitian transpose. The obtained wave load spectrum and the first couple of eigenfrequencies of the fixed-interface stand-alone jacket are shown in figure 8.2. It can clearly be seen that the first eigenfrequency of the jacket is much higher in frequency than the main bandwidth of the wave forces. Therefore, the assumption of a quasi-static response appears to be valid. In addition to this, one can compare the spectra of the sets of *dynamically*

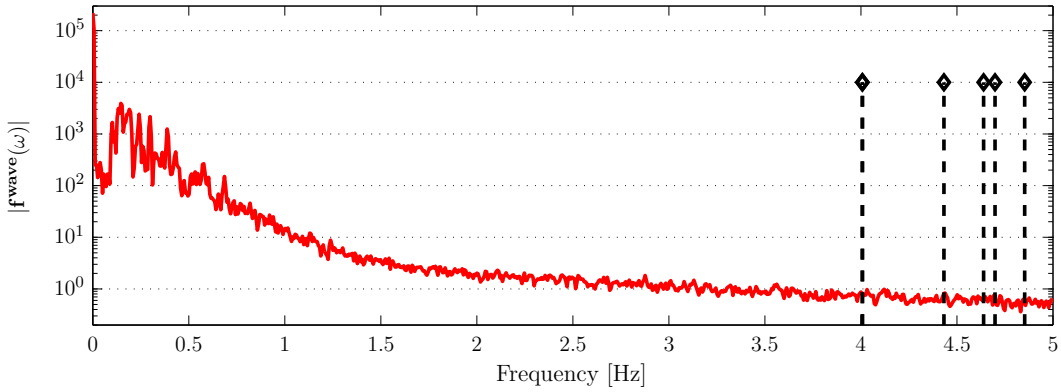

Figure 8.2: *Frequency spectrum of the wave forces versus the fixed interface eigenfrequencies of the UpWind jacket.*

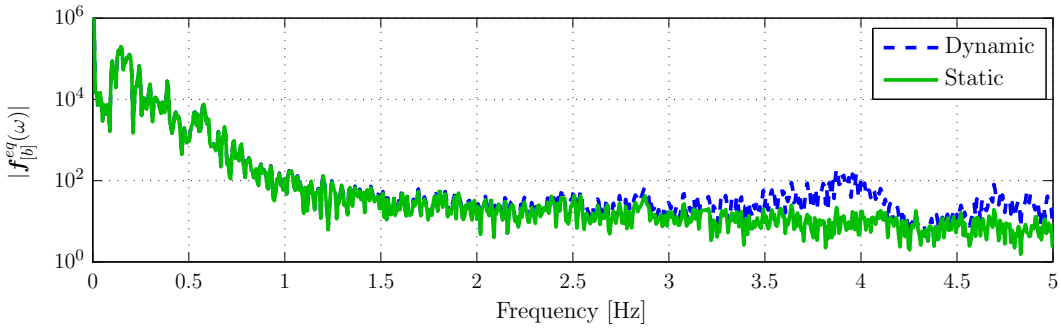

Figure 8.3: *Spectrum of statically and dynamically obtained blocked forces.*

and *statically* obtained blocked forces, which are given in figure 8.3. Here one can clearly see that the spectral content of the blocked forces, computed according to Eq. (8.1), only starts to differ around the fixed interface eigenfrequencies, as was already expected from figure 8.2. However, due to the low amplitude, it is expected that this will have limited effects on the computed coupled response.

Note that even though performing the time simulations for obtaining the dynamic blocked forces also only requires factorizing the time-stepping matrix once (as the system at hand is linear), it still involves solving the implicit time integration scheme per time step. These costs are saved by using the static approach for determining blocked forces and, in addition one can solve for the entire set of static blocked forces in a single step using multiple right-hand-sides.[2]

8.2.2 Equivalent loads using free interface displacements

It is shown in section 6.4 that one can also use free interface displacement as an alternative forcing term on the interface. The forcing effect is obtained by imposing the obtained free interface displacement as a compatibility error between dually assembled systems. Again, in order to obtain the free interface displacements, a time integration using the free interface stand-alone jacket and nodal wave forces *per load case* is required. If one could obtain these interface responses using a static analysis (section 6.4.3) a signification amount of computational time could be saved, as was outlined in section 8.2.1. Therefore, if the inertia and damping contributions can be neglected, one only has to solve the associated static problem, which is given in

[2] As is also discussed in section 7.7.

Eq. (6.49). Note however that one can only neglect the damping and inertia contributions in case the first free interface eigenfrequency (ω_1), which are found from:

$$\left(\boldsymbol{K} - \omega_j^2 \boldsymbol{M}\right) \boldsymbol{\phi}_j = \boldsymbol{0}, \tag{8.2}$$

is much higher that the spectrum of applied forces.

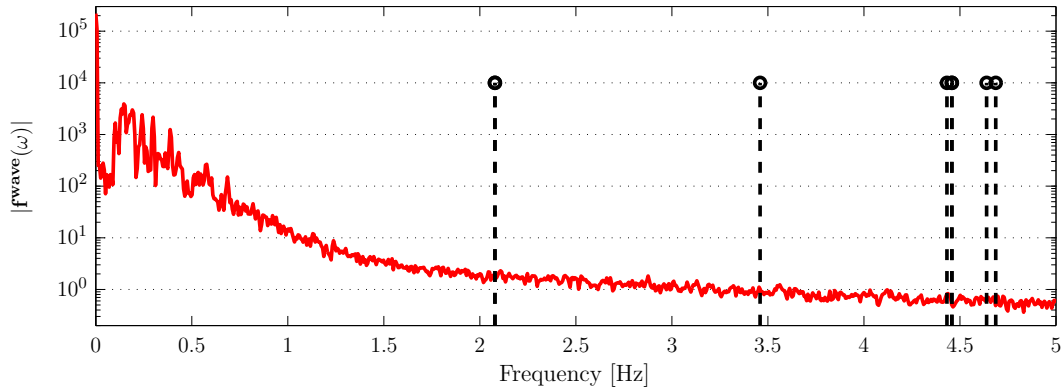

Figure 8.4: *Frequency spectrum of the wave forces versus the free interface eigenfrequencies of the UpWind jacket.*

The result of this analysis is shown in figure 8.4, where it is seen that the eigenfrequencies are still separated from the main bandwidth of loading. Nonetheless, it is clear that the first

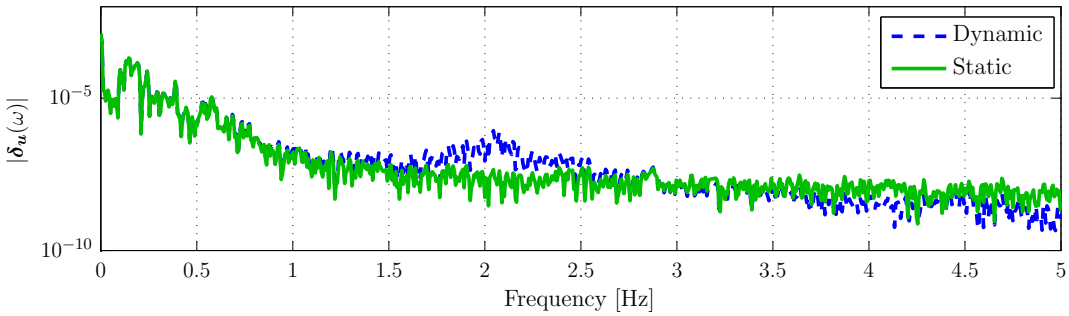

Figure 8.5: *Spectrum of statically and dynamically obtained free interface displacements.*

eigenfrequency is (as expected) significantly lower than that of the fixed jacket model. The effect of this can be seen in figure 8.5, where the difference between the dynamically and statically obtained free interface displacements is shown. Here, the difference between the dynamically and statically obtained interface displacements is already at a lower frequency, when compared to the equivalent blocked forces.

8.3 Effect of using equivalent interface excitations on the wind turbine response

The focuss is again, as in chapter 7, on assessing the results in terms of fatigue damages induced on the jacket's elements. Nonetheless, a brief overview of the results obtained for the wind turbine substructure is given in this section. The results are given in terms of (normalized) resultant bending moments and DELs (see section 7.4) in a selection of elements of the wind turbine, as was also presented in section 7.4.

Firstly, the wind turbine results for the equivalent blocked force approach, which is derived in section 6.3, are presented in section 8.3.1. Additionally, in section 8.3.2 the effect of neglecting the inertia and damping contributions in the pre-processing analysis for obtaining the blocked forces is investigated.

The second variant of the equivalent loading methods, that is presented in section 6.4, employs free interface displacements. The coupled substructures are in this case excited by an error enforced in the compatibility equation. In section 8.2.2 the interface displacements have been determined using a dynamic time stepping analysis, giving the dynamically obtained interface displacements, and from solving the entire time sequence as a series of static load cases, which gives the statically obtained interface displacements. The results from using the former are presented in section 8.3.3 and the results the latter are given in section 8.3.4.

8.3.1 Results using dynamically obtained equivalent blocked forces

The DELs in three different elements; the tower bottom, tower top and the root of blade 1, are shown in figure 8.6. These results are obtained for the different integrated wind turbine

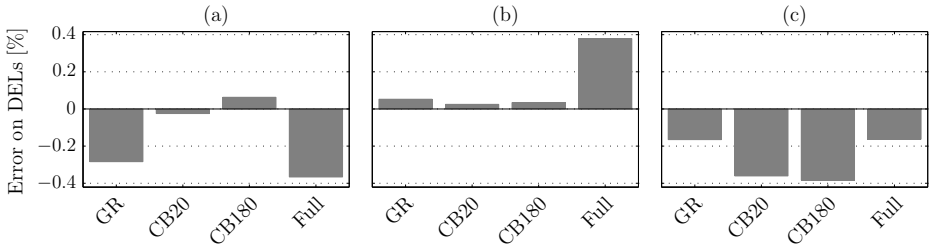

Figure 8.6: *Error on the damage equivalent loads for different elements, obtained from using dynamically computed blocked forces. Result from DLC 1.2 with $v_a = 13$ m/s and $H_s = 3.75$ m.* ***(a)*** *Tower bottom element;* ***(b)*** *Tower top element;* ***(c)*** *Blade 1 root element.*

models, as presented in table 8.1. From this figure, one can again draw the same conclusion as before, namely that for this test case the influence of the reduced jacket on the turbine results is negligible. Also note that the relative error found for the "Full" model is not zero, even though in section 6.3 it was shown that the blocked force approach is analytically exact. Note however that, due to the tolerance setting in the Newton-Raphson (NR) process a "zero-error" can never be achieved. Setting a stricter tolerance for the NR process resulted in a significant increase of the number of iterations and/or non-converging time steps, hence this was deemed impossible. On the other hand, this result does give a good insight in our level of "numerical noise", i.e. an

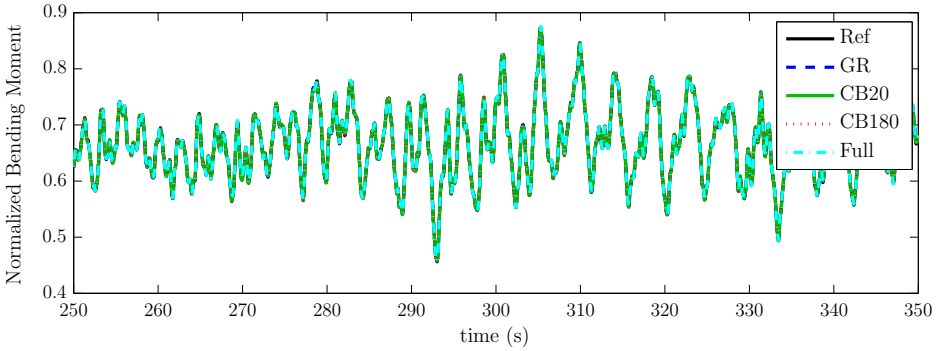

Figure 8.7: *Normalized resultant bending moment for the root of blade 1. Result from DLC 1.2 with $v_a = 13$ m/s and $H_s = 3.75$ m.*

error bandwidth in which we can still define the results as numerically exact. Hence, it can be concluded that the equivalent blocked forces perform excellently. This can also be easily seen from figure 8.7, where the normalized bending moments are shown over time for all the different models used in this test case.

8.3.2 Results using statically obtained equivalent blocked forces

In section 8.2.1 it is shown that that the main bandwidth of the wave loading is much lower than the first fixed eigenfrequency of the jacket and that the difference between the dynamic and static blocked forces is minimal. This can also be seen in figure 8.8, as the errors of the DELs computed for the different turbine elements are in the order of the error associated to the settings in the NR process. Hence, it can be concluded that the turbine results found from using statically obtained blocked forces are accurate enough for any practical purpose.

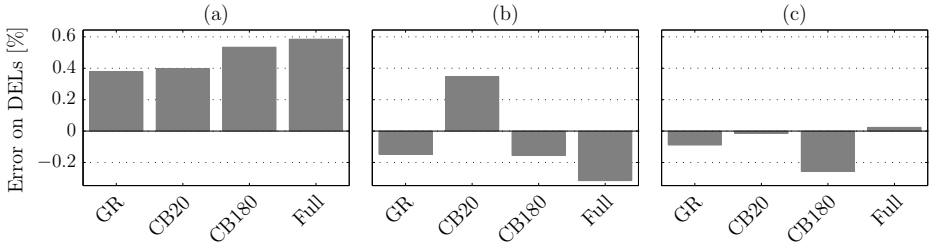

Figure 8.8: *Error on the damage equivalent loads for different elements, obtained from using statically computed blocked forces. Result from DLC 1.2 with $v_a = 13$ m/s and $H_s = 3.75$ m.* ***(a)*** *Tower bottom element;* ***(b)*** *Tower top element;* ***(c)*** *Blade 1 root element.*

8.3.3 Results from using dynamic equivalent interface displacements

In figure 8.9 the results are given again in terms of DELs for the three elements of interest.

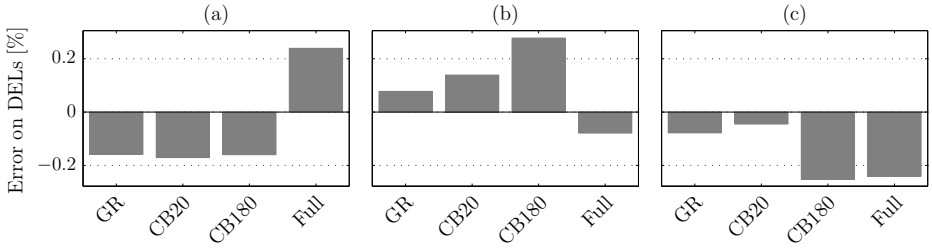

Figure 8.9: *Error on the damage equivalent loads for different elements, obtained from using dynamically computed free interface displacements in the integrated analysis. Result from DLC 1.2 with $v_a = 13$ m/s and $H_s = 3.75$ m.* ***(a)*** *Tower bottom element;* ***(b)*** *Tower top element;* ***(c)*** *Blade 1 root element.*

Again, the small errors seen on the DELs associated to the "Full" model are due to the tolerance setting in the NR process, as the method is proven to be analytically exact in section 6.4. Hence, it can be concluded that accurate results are obtained for all models.

8.3.4 Results from using static equivalent interface displacements

In figure 8.4 it is seen that the first free interface eigenfrequency is closer to the spectrum of wave forces, when compared to the fixed interface eigenfrequencies, given in figure 8.2. Hence,

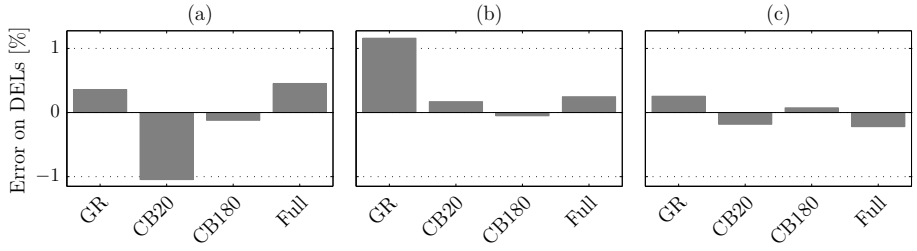

Figure 8.10: *Error on the damage equivalent loads for different elements, obtained from using statically computed free interface displacements in the integrated analysis. Result from DLC 1.2 with v_a = 13 m/s and H_s = 3.75 m.* ***(a)*** *Tower bottom element;* ***(b)*** *Tower top element;* ***(c)*** *Blade 1 root element.*

it is expected that the effect of neglecting the inertia and damping effects in the pre-processing steps to obtain the equivalent free interface displacements, will in general have a greater effect on the coupled responses found, when compared to the coupled responses found using the static equivalent blocked forces. The results for the three different wind turbine elements are shown in figure 8.10. Even though the errors on the DELs are for some models and/or elements slightly larger and are beyond the error-limits associated to the tolerance settings for the NR iterations, the results can still be considered as accurate.

8.4 Time simulation results for the foundation using equivalent loading

As was mentioned in the introduction, the goal of this chapter is to gain insight in the effects of reduced foundation models in combination with the different equivalent loading methods, that are introduced in chapter 6, on the accuracy of the fatigue damages computed in the foundation. In order to obtain the fatigue damage for each beam element, the different steps that are presented in section 7.5 and figure 7.9, need to be performed after the full nodal foundation response is obtained from the post-processing analysis methods available. Note that it was already shown in section 7.5 that both the *static* force controlled and *static* displacement controlled approaches significantly underestimate the fatigue damages induced. Therefore, these methods are not used throughout this chapter to obtain the fatigue damage in the elements of the jacket.

In addition, it is chosen not to apply the quasi-static correction in this chapter. As the external wave forces are not reduced, but transformed using the equivalent loading methodology, the spatial aspect is eliminated. Hence, if one compares the direct expansion results from this chapter, with those obtained in chapter 7, the effects of the spatial and spectral convergence can be deduced. Note however, that one can still apply the residual correction on the results obtained.

The results of the analysis are given again in a pair of plots. Firstly the relative error on the fatigue damage is given for all elements in a box-and-whisker plot, which is introduced in section 7.5.1. Secondly, by plotting the normalized damages for the elements with $D_{nor}^{el} > 0.01$ versus the relative error on the damage obtained, one can determine if large errors are found for the

critical elements. The normalized damage of all elements is therefore determined according to:

$$D^{el}_{i,norm} = \frac{D^{el}_{i}}{D^{el}_{max}}, \text{ for } i = 1 \cdots n_{el},$$

where D^{el}_{nor} is the normalized damage that ranges from zero to one, D^{el}_{max} is the maximum cumulative damage occurring (obtained from the reference solutions) and D^{el}_{i} is the damage in element i.

8.4.1 Fatigue damage estimates obtained using the dynamically computed blocked forces

The relative errors on the fatigue damages incurred by all elements are shown in figure 8.11. The results presented in the left and middle sub-figures are obtained using, respectively, the

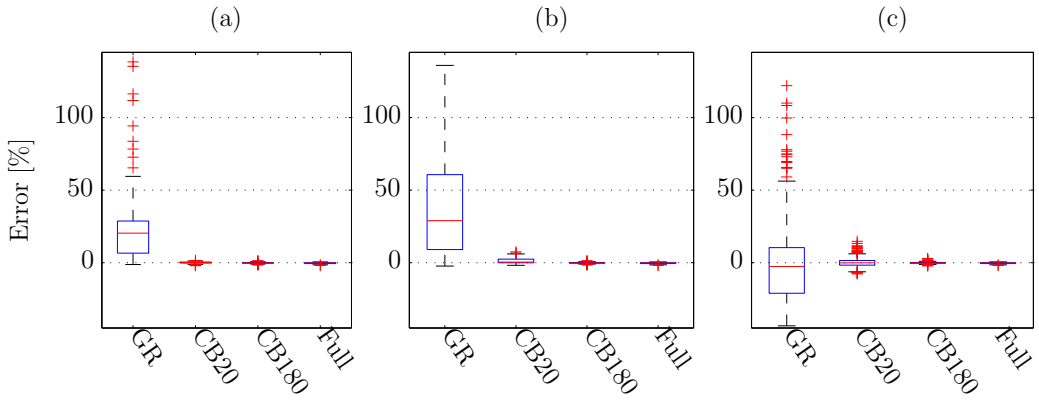

Figure 8.11: *Relative error on the fatigue damage obtained using dynamic blocked forces for all elements from DLC 1.2 with $v_a = 13$ m/s and $H_s = 3.75$ m. Results obtained using;* ***(a)*** *Force control;* ***(b)*** *Displacement control;* ***(c)*** *Expansion.*

(dynamic) force and displacement controlled approaches. The right sub-figure is obtained from a direct expansion of the modal coordinates in combination with the time series of nodal displacements computed in the pre-processing step for obtaining the blocked forces, as is given in Eq. (6.26) and recited here:

$$\boldsymbol{u}_{[i],n} = \boldsymbol{R}_{[i]}\tilde{\boldsymbol{q}}_n + \boldsymbol{u}^{con}_{[i],n}.$$

Firstly, it is seen that the damages obtained using the "Full" model are highly accurate, which is as expected. In addition, the "CB180" also leads to highly accurate results for all the post-processing methods used. Obviously, this result is expected as it was shown in section 6.3 that the blocked force approach is analytically exact. A slightly bigger spread in the results is found for the "CB20" model in the case of displacement control and direct expansion. Use of the Guyan reduced model (GR) results in a large spread in results, like was also found in chapter 7. In addition, the force and displacement controlled approaches tend to overestimate the fatigue damages in almost all the elements for this model. The median of the "GR" results is close to the 0% error in case of a direct expansion, but there is a large scatter in the results, leading both to overestimating and underestimating the actual fatigue damages. Note that not all results for the DC approach are shown, as the largest errors are almost 500%.

By examining figure 8.12, where the relative errors with respect to the normalized damages are given, it is clear that very accurate results are obtained for the most critical elements using the "Full" and "CB180" models and only slight underestimations (1% - 2%) are found from

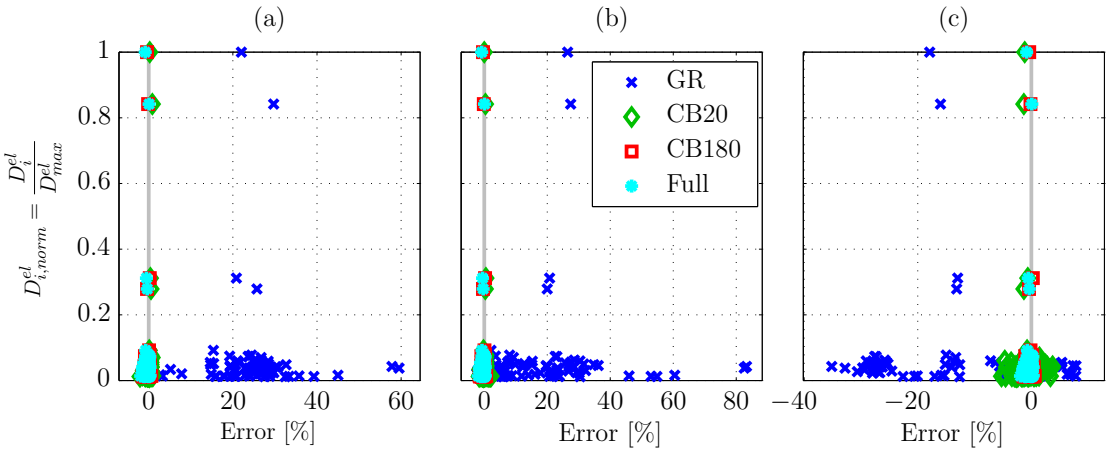

Figure 8.12: *Relative error versus normalized damage for $D_{nor}^{el} > 0.01$ from DLC 1.2 with $v_a = 13$ m/s and $H_s = 3.75$ m. Results obtained from using dynamic blocked forces and different post-processing analyses:* ***(a)*** *Force control;* ***(b)*** *Displacement control;* ***(c)*** *Expansion.*

directly expanding the "CB20" results. The results for the Guyan reduced model are in line with what is found from the results presented in chapter 7. Firstly, due to a spectral mismatch, the fatigue damages for the critical elements are overestimated using both the dynamic force and displacement controlled approaches. Secondly, directly expanding the results leads to an underestimation of the fatigue damages incurred on the critical elements.

By comparing the results presented in figures 7.10 and 8.12 and realizing that by applying the equivalent loads on the interface one has eliminated the spatial effect on the errors found, it is possible to separate the spatial and spectral contributions of the errors obtained from a direct expansion in section 7.5.1.

8.4.2 Fatigue damage estimates obtained using the statically obtained blocked forces

The second set of equivalent loads that are tested in this section are the statically obtained blocked forces. The results obtained are almost equal to those found from using dynamically

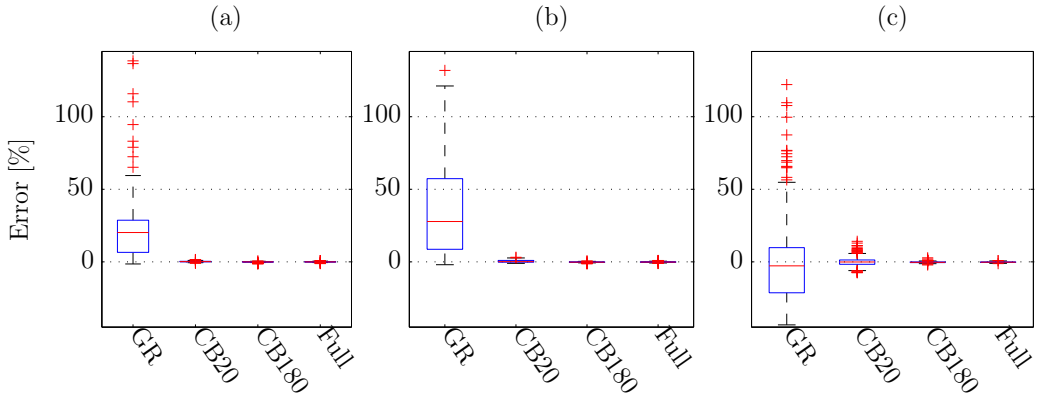

Figure 8.13: *Relative error on the fatigue damage obtained using static blocked forces for all elements from DLC 1.2 with $v_a = 13$ m/s and $H_s = 3.75$ m. Results obtained using;* ***(a)*** *Force control;* ***(b)*** *Displacement control;* ***(c)*** *Expansion.*

obtained equivalent blocked forces, as is shown in figure 8.11. By focussing on the results for the critical elements, which are shown in figure 8.14, and comparing these with the results from

figure 8.12, almost no differences can be identified. Hence, for the marine foundation used in this model, the OC4 UpWind reference jacket, one can apply the static blocked forces without any loss of accuracy in the obtained fatigue damages.

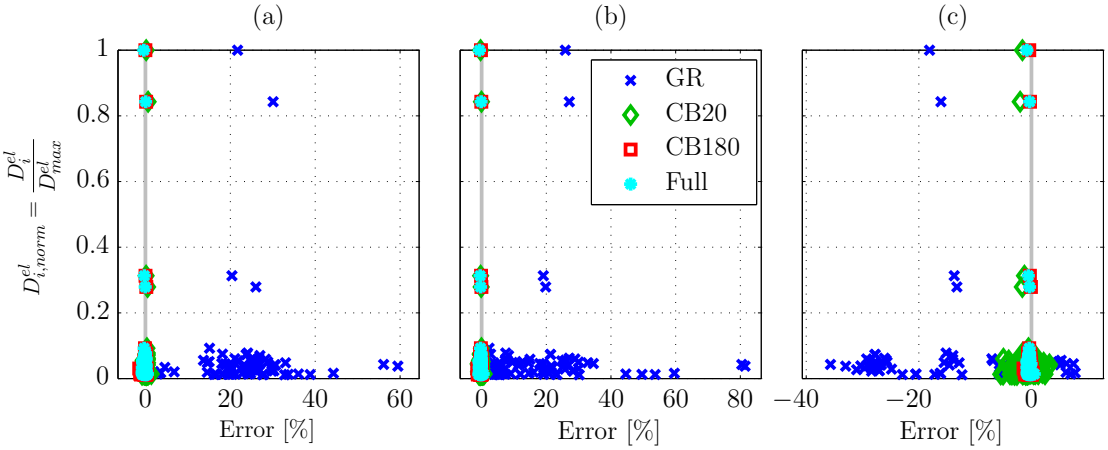

Figure 8.14: *Relative error versus normalized damage for $D^{el}_{nor} > 0.01$ from DLC 1.2 with $v_a = 13$ m/s and $H_s = 3.75$ m. Results obtained from using static blocked forces and different post-processing analyses:* ***(a)*** *Force control;* ***(b)*** *Displacement control;* ***(c)*** *Expansion.*

8.4.3 Results obtained by using the dynamically computed interface displacements

The second approach that allows for applying equivalent excitations at the interface is by means of enforcing a compatibility error, as is discussed in section 8.3. The results for the foundation

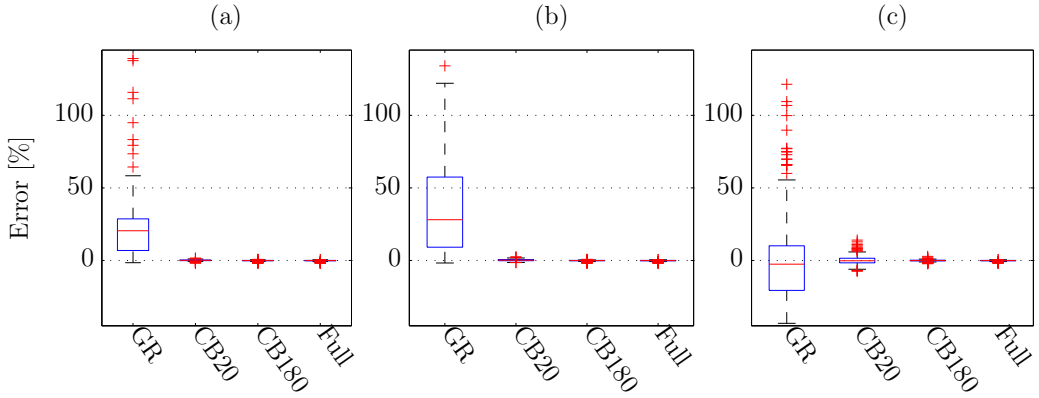

Figure 8.15: *Relative error on the fatigue damage obtained using dynamic interface displacements for all elements from DLC 1.2 with $v_a = 13$ m/s and $H_s = 3.75$ m. Results obtained using;* ***(a)*** *Force control;* ***(b)*** *Displacement control;* ***(c)*** *Expansion.*

substructure are presented in figures 8.15 and 8.16. The right sub-figures are obtained from a direct expansion of the modal coordinates in combination with the nodal displacements computed in the pre-processing step for obtaining the free interface displacements, as is given in Eq. (6.48) and recited here:

$$\boldsymbol{u}_n = \boldsymbol{R}\tilde{\boldsymbol{q}}_n + \boldsymbol{u}_n^{free}.$$

The results found are fully in line with the results found in section 8.4.1. This is expected, as it was shown in section 6.4 that this method, which employs free interface displacements to

enforce a compatibility error in the coupled analysis, is analytically exact with respect to the reference solution.

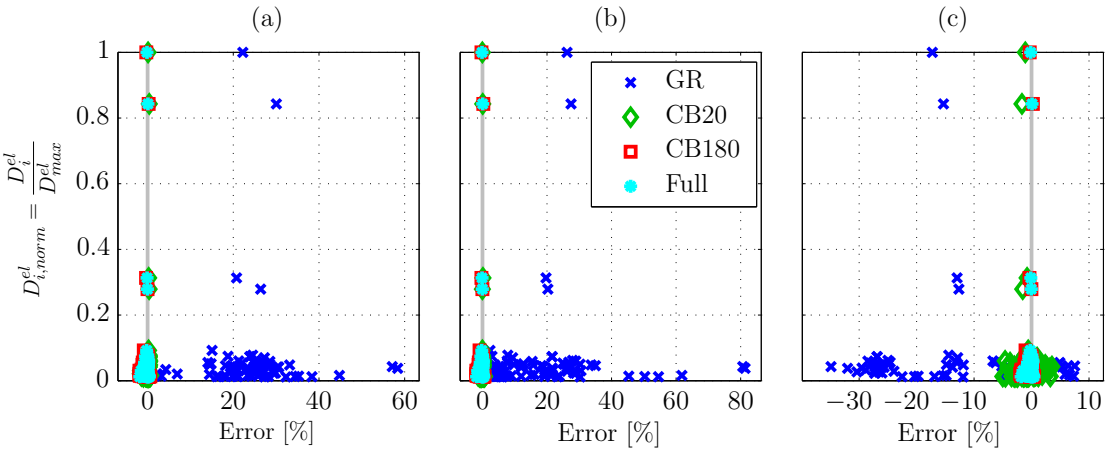

Figure 8.16: *Relative error versus normalized damage for $D^{el}_{nor} > 0.01$ from DLC 1.2 with $v_a = 13$ m/s and $H_s = 3.75$ m. Results obtained from using dynamic interface displacements and different post-processing analyses:* ***(a)*** *Force control;* ***(b)*** *Displacement control;* ***(c)*** *Expansion.*

8.4.4 Applying static interface displacements as equivalent loading

Finally, the results obtained from using static free interface displacements are shown in figures 8.17 and 8.18. As was already discussed in section 8.2.2 (and shown in figure 8.5), the differences between the dynamically and statically obtained interface displacements occur at a lower frequency, when compared to the statically and dynamically obtained blocked forces, given in figure 8.3. The effect of this can be seen in the results, presented in figures 8.17 and 8.18.

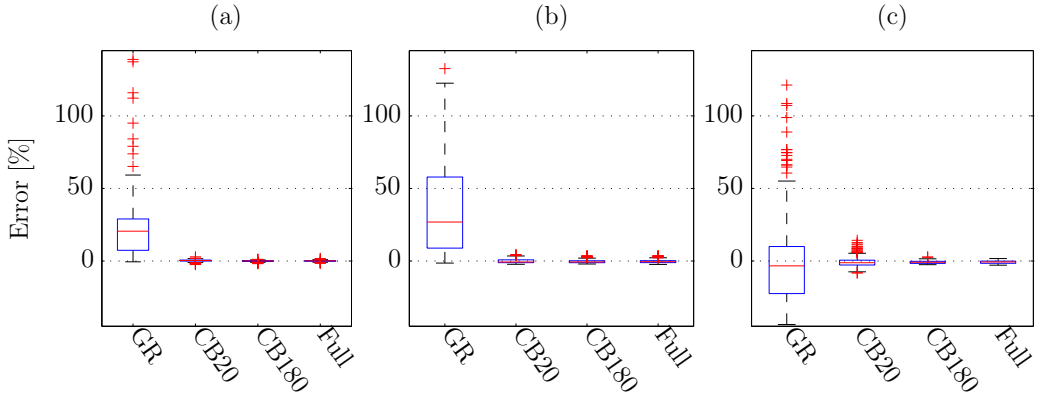

Figure 8.17: *Relative error on the fatigue damage obtained using static interface displacements for all elements from DLC 1.2 with $v_a = 13$ m/s and $H_s = 3.75$ m. Results obtained using;* ***(a)*** *Force control;* ***(b)*** *Displacement control;* ***(c)*** *Expansion.*

Firstly, it is obvious that the Guyan reduced model under-performs, thereby leading to erroneous fatigue damage estimates for all the post-processing approaches. Secondly, the force controlled approach leads to accurate estimates for all the the other models. However, the damages obtained for the critical elements using displacement control are underestimated by 1%-2%, for all models except the "GR" model. The direct expansion of the modal coordinates leads to

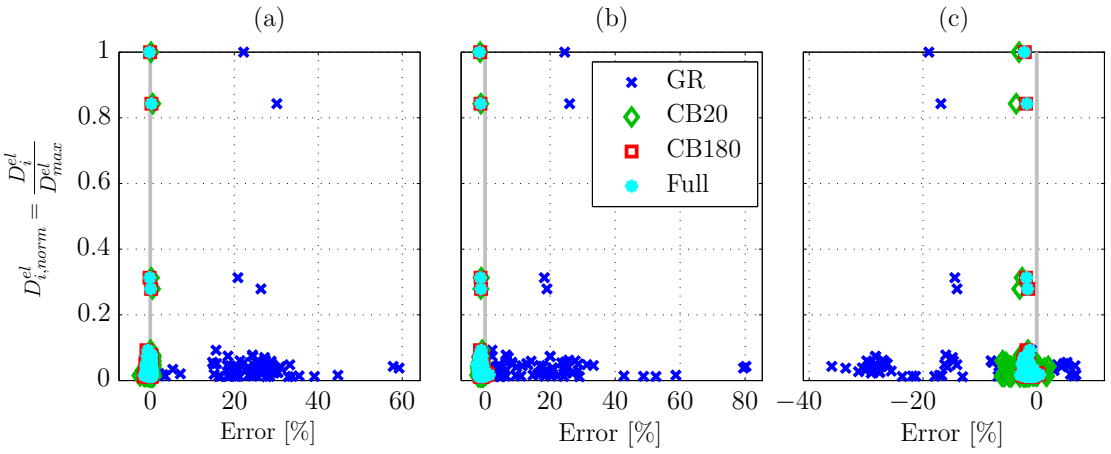

Figure 8.18: *Relative error versus normalized damage for $D^{el}_{nor} > 0.01$ from DLC 1.2 with $v_a = 13$ m/s and $H_s = 3.75$ m. Results obtained from using dynamic interface displacements and different post-processing analyses:* ***(a)*** *Force control;* ***(b)*** *Displacement control;* ***(c)*** *Expansion.*

underestimations between 2% to 4% for the "CB20" model and of about 2% for the "Full" and "CB180" models.

The underestimations found from the latter two models, are directly related to using the static interface displacements as equivalent loading on the interface. Even though the differences might not be critical in the current example, one can imagine that these underestimations will become more pronounced for foundation models that are more dynamically active in the low frequency spectrum of the wave forces. Hence, before neglecting the inertia and damping effects in the pre-processing analysis for obtaining the interface displacements, it is essential that one has verified a priori that this will not (significantly) affect the fatigue damages found.

8.5 Comparison of the computation times

As computational cost are an important aspect in a real life engineering setup, a comparison in terms of normalized computation times is given in this section. Note that in the current chapter, the simulations have been performed for four different models, using four different types of equivalent loading on the interface and the nodal response of the jacket are determined using three different post-processing strategies. This culminates in a total of 48 possibilities for obtaining the fatigue damages in the foundation and wind turbine structures. As the focus of this chapter is on demonstrating the different equivalent loading types, the computation times are presented accordingly.

Hence, in section 8.5.1 the normalized times are given for the simulations using the dynamic and static blocked forces. The normalized times for the simulations using the dynamic and static equivalent interface displacements are given in section 8.5.2.

8.5.1 Computational cost when using blocked forces

The normalized computation times for the simulations using dynamically obtained equivalent blocked forces are shown in figure 8.19. Note that time is normalized with respect to (the mean of) the computation time for the reference simulations. In addition, as one would not apply the "Full" model in practice, its computational times are not shown here. Again, it is easily

observed that the majority of the computational effort results from the aero-elastic simulations in BHawC. The cost associated to the reduction step are again negligible. One performs a full

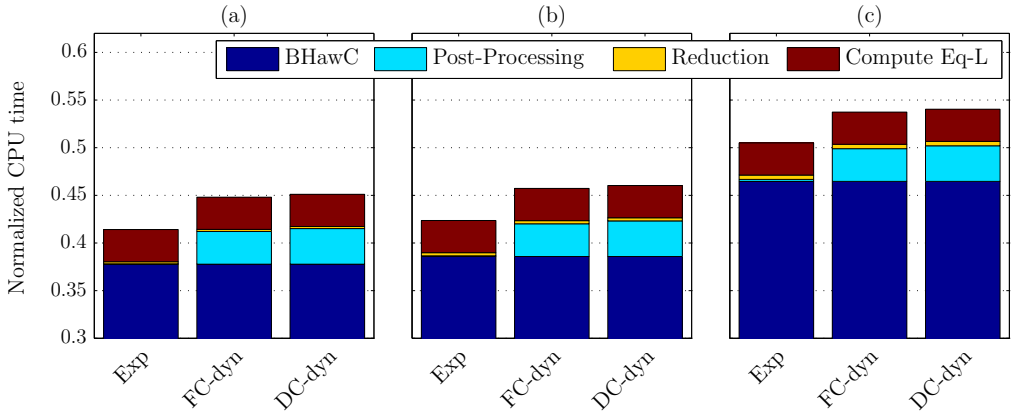

Figure 8.19: *Normalized computation times for the subsequent steps in the computational process using dynamic equivalent blocked forces and different reduced models;* ***(a)*** *GR;* ***(b)*** *CB20;* ***(c)*** *CB180.*

time integration on the stand-alone jacket to obtain the (dynamic) blocked forces, but a full time integration is also performed to reconstruct the full foundation response afterwards (using the FC and DC approaches). Hence, the computation times associated to these steps, denoted respectively by "Compute Eq-L" and "Post-Processing", are approximately equal.

In figure 8.20 the computational cost are shown for the test case with the statically obtained

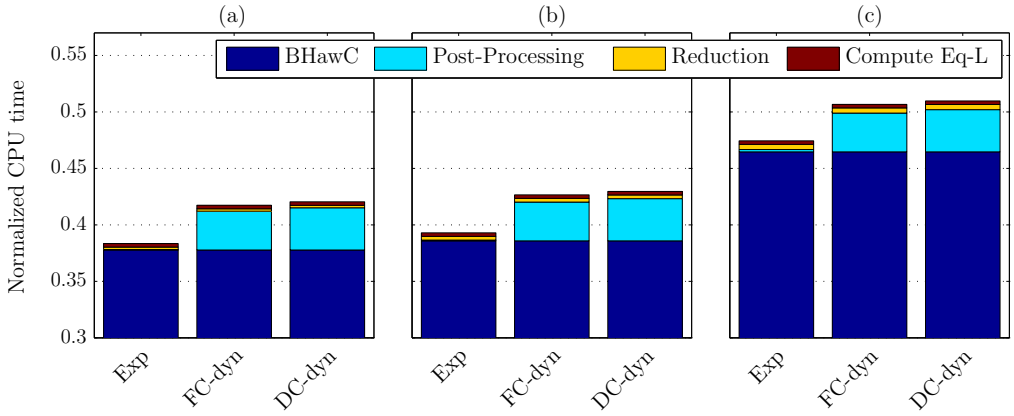

Figure 8.20: *Normalized computation times for the subsequent steps in the computational process using static equivalent blocked forces and different reduced models;* ***(a)*** *GR;* ***(b)*** *CB20;* ***(c)*** *CB180.*

blocked forces. It can easily be seen here, that the major difference with respect to the times shown in figure 8.19, is in computing the equivalent blocked forces. Here one only needs to solve a series of (linear) static problems to obtain the blocked forces, which is cheaper than performing a full time integration, as is discussed in section 7.7. Therefore, for the test case used, using static equivalent blocked forces provides a computational cheaper alternative that results, in combination with the correct reduced models, in highly accurate fatigue damage estimates.[3]

[3]See sections 7.7 and 8.2.1 for a more detailed discussion on computation times.

8.5.2 Computational cost when using free interface displacements

Similar results are found in case one uses free interface displacement as the equivalent loading to excite the compatibility condition in the coupled simulations. Again, by comparing the

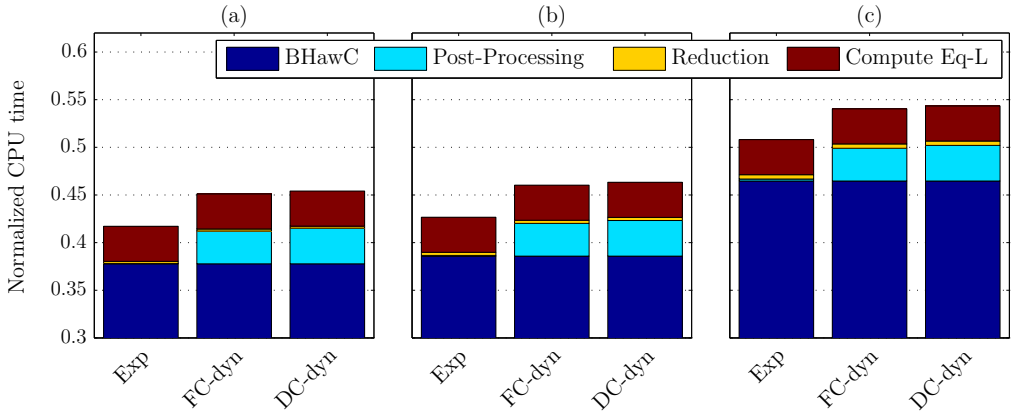

Figure 8.21: *Normalized computation times for the subsequent steps in the computational process using dynamic equivalent interface displacements and different reduced models;* ***(a)*** *GR;* ***(b)*** *CB20;* ***(c)*** *CB180.*

computational cost associated with the dynamically obtained free interface displacement in

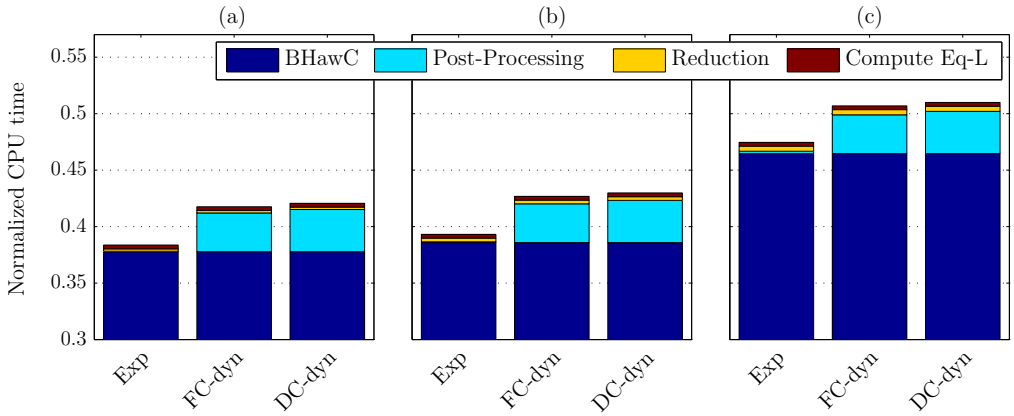

Figure 8.22: *Normalized computation times for the subsequent steps in the computational process using static equivalent interface displacements and different reduced models;* ***(a)*** *GR;* ***(b)*** *CB20;* ***(c)*** *CB180.*

figure 8.21 with the static ones in figure 8.22, it is clear that the latter require less computational effort.[3] Although the static approach is also cheaper here, the results from a direct expansion showed minor underestimations in the fatigue damage. This indicates that one must always be aware of potential errors due to neglecting the inertia and damping contributions in the equivalent interface displacements.

8.6 Summary

Using equivalent loading on the interface of reduced components, has a number of advantages over reducing the external forces that are applied to the internal DoFs, as is outlined in section 8.1. The only benefit recited here is the fact that one does not require a load case dependent reduction basis, such that one can apply the “classical” CMS methods.

Applying an equivalent type of loading on the interface requires some extra steps in the process of obtaining fatigue damages or damage equivalent loads in all the elements of the integrated wind turbine structure, as is outlined section 8.2. In addition, it has been shown that one can approximate both types of equivalent loading by neglecting the inertia and damping contributions in the pre-processing step, thereby finding the static equivalent loading. It is shown that differences between the dynamic and static equivalent blocked forces occur from the first eigenfrequency of the associated fixed interface dynamic problem and onwards. In the case of equivalent interface displacements this difference occurs already at a lower frequency. This is due to the fact that the first eigenfrequency of the associated free interface substructure, used for determining the free interface displacements, is always lower then the first eigenfrequency of the fixed interface component.

The different types of equivalent loading have been demonstrated using the same test case as in chapter 7. However, as one does not require any MTAs in the reduction basis, the reduced models are created using Guyan's reduction and the classical Craig-Bampton method. Thereby resulting in four different reduced and unreduced models, one from employing Guyan's reduction, two from employing the Craig-Bampton method and one full FE model of the jacket foundation in order to demonstrate the accuracy of the equivalent loading approaches.

In section 8.3 it has been shown that the approaches using either equivalent blocked forces or equivalent interface displacements lead to accurate estimates for the DELs in the tower bottom, tower top and blade root elements for all the models considered. The static equivalent blocked forces and free interface displacements result in a negligible error on the DELs in the three wind turbine elements, thereby showing that these can be applied without any loss of accuracy (on the turbine response) for the UpWind reference jacket.

The results for the foundation, in terms of the relative error on the fatigue damage induced on the elements, have been given in section 8.4. These have been obtained from applying a direct expansion of the modal coordinates and from using the dynamic force and displacement controlled approaches. All the different types of dynamic and static equivalent loading have shown to result in excellent fatigue damage estimates for all the elements of the jacket foundation in the case of the Craig-Bampton and full FE models. Using the Guyan reduced jacket in the integrated wind turbine model again results in errors on the fatigue damages obtained from the direct expansion, as well as the force and displacement controlled approaches. Since the wave loads have not been reduced, the errors obtained here are solely due to the spectral mismatch of the Guyan reduced jacket.

The equivalent loading approaches can be used to facilitate the data exchange between different project groups. As one only needs to provide each one another with classically reduced models and the associated equivalent loads on the interfaces in order to allow for the integrated analysis of composed structures. Note that, when considering the entire computational process as one would apply it in practice, there are different choices for each step:

- The applied type of equivalent load; one can compute and apply either the blocked forces or equivalent interface displacements (chapter 6).
- The entire range of reduction methods, as was briefly outlined in section 2.2.
- Different approaches that can be taken in the assembly of the subsystems, as is outlined in section 2.6.
- How to reconstruct the full foundation response; force control, displacement control or an expansion of the modal coordinates (section 7.2).

Nonetheless, one can still define several combinations of methods that are more "natural" than

others.

A "natural" combination would be, for instance, to use blocked forces, a Craig-Bampton reduced model, primal assembly and the displacement control approach. Firstly, obtaining the blocked forces and performing the (dynamic) displacement control approach requires factorizing the same time-stepping matrix. In addition, if one initializes the time integration from a quasi-static equilibrium, a factorization of the internal part of stiffness matrix ($\boldsymbol{K}_{[ii]}$) is also required in these steps. Also, solving the fixed interface modes, that are used in the reduction basis for the Craig-Bampton method, using a for instance a Lanczos procedure, also requires factorizing the internal part of stiffness matrix. Finally, as was discussed in chapter 2, primal assembly is straightforward for assembling superelements. Hence, this combination of methods can be considered as "natural". Using similar reasoning, one can define more of these combinations.

9

Offshore Wind Turbine Simulations using Impulse Based Substructuring

"Nothing is particularly hard if you divide it into small jobs."

– Henry Ford

9.1 Introduction

An alternative approach for coupling linear foundation models and nonlinear aero-elastic wind turbine models is by means of Impulse Based Substructuring, which is introduced in chapter 5. It has been outlined a number of times in this thesis that the design process of a wind turbine support structure generally involves a foundation designer and a wind turbine manufacturer. The former is responsible for the detailed foundation design and the latter for the integrated analysis of the entire wind turbine using aero-elastic simulations.

One approach suited for exchanging reduced models of the foundation is by applying Component Mode Synthesis methods, as is evaluated in chapter 7. An alternative approach to exchange a "reduced" foundation model is by means of IRFs, which can serve as a sort of "superelement in time".[1] Similar to exchanging classically reduced models, exchanging IRFs exhibits a number of advantages. Firstly, one is only required to exchange data on the interface, which generally limits the amount of data exchange considerably. Secondly, all the substructure dynamics are implicitly included in the IRFs, without exposing any of the underlying modeling details. Finally, the IBS method has the potential to significantly speed up the calculations [172].

In order to demonstrate the potential use of the IBS method in the design process of an offshore wind turbine support structures, a single computational loop in the entire design process is mimicked again. In order to facilitate a comparison to the CMS methods, the test case used in the current chapter is similar to those used in chapters 7 and 8. Therefore, the different

[1] Note that the IBS method is not a reduction technique in the usual sense: the solution is not approximated, but just computed in a different way, by concentrating the full information of a substructure on its interface in the form of a precomputed IRF.

steps required for obtaining the fatigue damages and damage equivalent loads in the different component models, as shown in figure 9.1, are evaluated in this chapter.

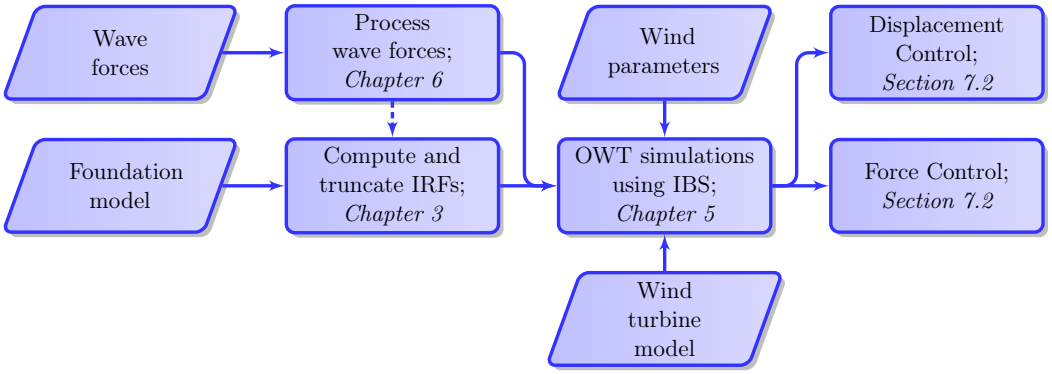

Figure 9.1: *Steps required for applying the Impulse Based Substructuring methodology in the integrated analysis of offshore wind turbines.*

Firstly, one needs to process the full time series of wave forces to generate either a reduced set of wave loads, as is discussed in section 6.2, or compute either the blocked forces or free interface displacement that can serve as equivalent interface loading, as is described in sections 6.3 and 6.4 and evaluated in chapter 8. Secondly, one needs to compute and truncate the IRFs related to the interface DoF of the foundation model. If one chooses to use a reduced set of wave forces, the IRFs due to the set of spatial reduction vectors have to be computed as well, as is outlined in section 3.4.4. The set of foundation IRFs, processed wave forces, the wind turbine model and the input parameters for the aerodynamic model are then combined using the IBS method to compute the response of the integrated OWT for the different load cases. Finally, the force and/or displacement control methods are used to reconstruct the full foundation response. Using the time series of nodal displacements, one can determine the fatigue damage in all the foundation elements, as is outlined in figure 7.9.

The outline of this chapter is such that firstly, in section 9.2, the substructure models and load case are given. The models and load case are used in the integrated analysis of the entire offshore wind turbine. The results for the wind turbine substructure are briefly presented in section 9.3. Following this section, the results for the foundation are given in section 9.4. In section 9.5 the effect of truncating and windowing the impulse response functions is investigated. An evaluation of the total computational effort required is given in section 9.6. Finally, in section 9.7 a summary of, and discussion on, the obtained results is given.

9.2 Component models and applied load case

To demonstrate the IBS method using a realistic industrial test case, it is chosen to use the exact same test case that is employed in chapters 7 and 8. Hence, the integrated OWT model is composed of the Siemens SWT-3.6-120 wind turbine and the UpWind reference jacket, which are both described in section 7.3.1. The wind turbine is modeled and simulated in the in-house aero-servo-elastic code BHawC, thereby giving a full nonlinear finite element model that is coupled to the integrated aerodynamic and controller models. The jacket is given as impulse response functions that are coupled to the wind turbine model using the Impulse Based Substructuring methodology, that is presented in section 5.3.

Note that the IBS method has not been integrated in BHawC, therefore use is made of the ability to connect BHawC simulations directly to MatLab based simulations, using the Sequen-

tial Multi-Domain Time Integration approach that is presented in section 4.2 and verified in appendix A. This allows for solving the convolution based time integration of the jacket substructure in MatLab, while computing the coupled response of the wind turbine directly in BHawC, which employs the generalized-α scheme.

The IBS approach is able to deal with distributed external forces using the same collection of methods that is available for the CMS methods. These methods, described in chapter 6, are all tested in the current test case, thereby leading to the different models that are given in table 9.1. The first model is again the full model which gives the reference solution and serves as the benchmark for all the other models. All other models are given as the IRFs related to the coupling DoF ($\boldsymbol{u}_{[b]}$). The IRFs are truncated and windowed using the combination window, which is outlined in section 3.6.3. The windowing parameters ϵ_w and ϵ_k are chosen respectively as 1×10^{-3} and 1×10^{-4}. Note that the effect of windowing and truncating the IRFs is investigated in section 9.5.

Jacket model			**Turbine model**	**Total model**	
# $\boldsymbol{u}_{[b]}$	# POMs	Model size	# DoF	Total # of DoF	Name
-	-	1062×1062	406	1062 + 406	Ref
6	20	$6 \times 26 \times 1327$	406	6 + 406	IBS 20POM
6	-	$6 \times 6 \times 1327$	406	6 + 406	IBS EqIntF
6	-	$6 \times 6 \times 1327$	406	6 + 406	IBS EqIntUb

Table 9.1: *Overview of the IBS demonstration models of an offshore turbine.*

For the second model, "IBS 20POM", a spatial reduction is applied to the time series of external wave forces, thereby adding the IRFs that are associated to the first 20 POMs (see sections 3.4.4 and 6.2). Note that the same 20 POMs are used in the reduction bases of the Augmented Craig-Bampton models used in the test case presented in chapter 7. The other models, "IBS EqIntF" and "IBS EqIntUb" are respectively excited by the (dynamic) equivalent blocked forces and equivalent interface displacements that have been obtained in chapter 8.

In the Impulse Based Substructuring test case only one of the two DLC 1.2 load cases, given in section 7.3.2, is considered. It has been chosen to include the load case that corresponds to the wind speed where the turbine is operating around its nominal power (13 m/s). The associated significant wave heights (H_s) were chosen at 3.75 m. Again, six seeds are considered for the wind speed in order to get some statistical averaging.

9.3 Evaluation of the results obtained for the wind turbines

The results of this chapter are presented in the same manner as is done in chapters 7 and 8. In figure 9.2 the error on the damage equivalent loads, which are introduced in section 7.4, are given for: (a) the tower bottom element, (b) the tower top element and (c) the blade root element of blade 1.

It can again be seen that one finds a small underestimation (<0.6%) of the DEL obtained at the tower bottom element using the reduced wave forces ("IBS 20POM"). As a part of the wave forces, that are applied to the jacket, are "reduced away", the small underestimations in the three focus elements are as expected. For all the other methods and elements smaller errors are found. It is seen that highly accurate results are obtained if one applies the different types of equivalent interface loading. The small errors found are a combined result of truncating

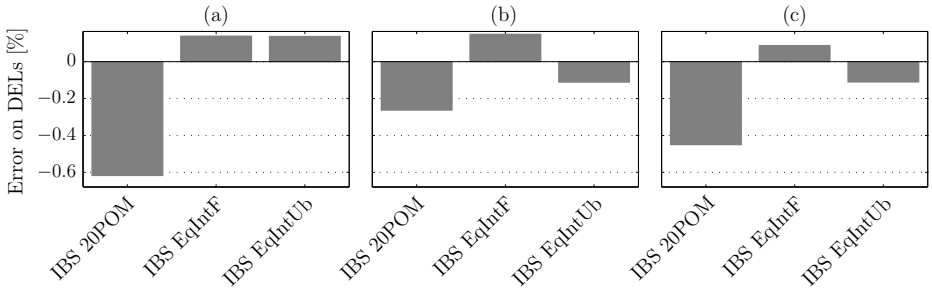

Figure 9.2: *Error on the damage equivalent loads for different elements, obtained using IBS. Result from DLC 1.2 with $v_a = 13$ m/s and $H_s = 3.75$ m.* ***(a)*** *Tower bottom element;* ***(b)*** *Tower top element;* ***(c)*** *Blade 1 root element.*

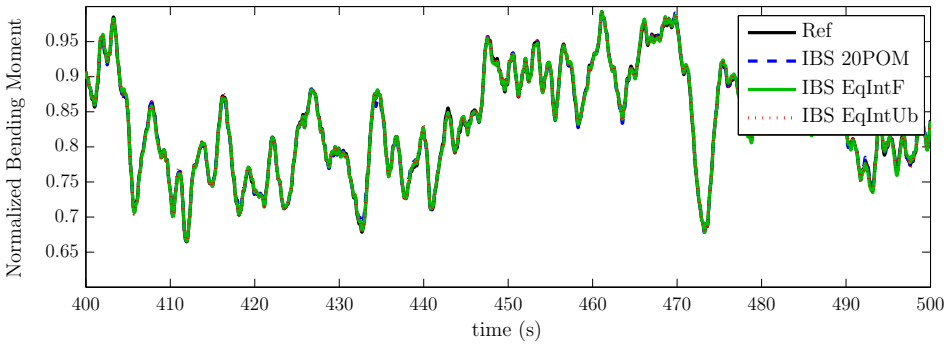

Figure 9.3: *Normalized resultant bending moment in the tower bottom element. Result from DLC 1.2 with $v_a = 13$ m/s and $H_s = 3.75$ m.*

the IRFs and the tolerance settings in the Newton-Raphson process, the latter of these is also discussed in section 8.3.1, and can thus be considered as numerical noise.

The normalized resultant bending moment obtained from one of the 6 simulations is shown for a period of 100 s in figure 9.3. Here, no differences between the obtained resultant bending moments using IBS and the reference solution can be visually distinguished. Hence, one can easily conclude that all the different IBS approaches lead to accurate results for the wind turbine.

9.4 Foundation results using Impulse Based Substructuring

In order to obtain the fatigue damage for each beam element, the steps that are presented in section 7.5 and figure 7.9 need to be performed after the full foundation response is obtained. Note that only the force and displacement control methods are applied to reconstruct the nodal responses of the jacket. In theory one could use the full set of IRFs of the jacket to expand the results of the IBS analysis using the convolution product, but as this offers no practical benefits, it is not discussed and used here. In addition it was already shown in section 7.5 that both the *static* force controlled and *static* displacement controlled approaches significantly underestimate the fatigue damages induced. Therefore, these methods are not used to obtain the fatigue damage in the elements of the jacket throughout this chapter.

The results of the analysis are given again in a pair of plots. Firstly the relative error on the fatigue damage is given for all elements in a box-and-whisker plot, which is introduced in section 7.5.1. Secondly, by plotting the normalized damages for the elements with $D_{nor}^{el} > 0.01$ versus the relative error on the damage obtained, one is able to get an insight into the

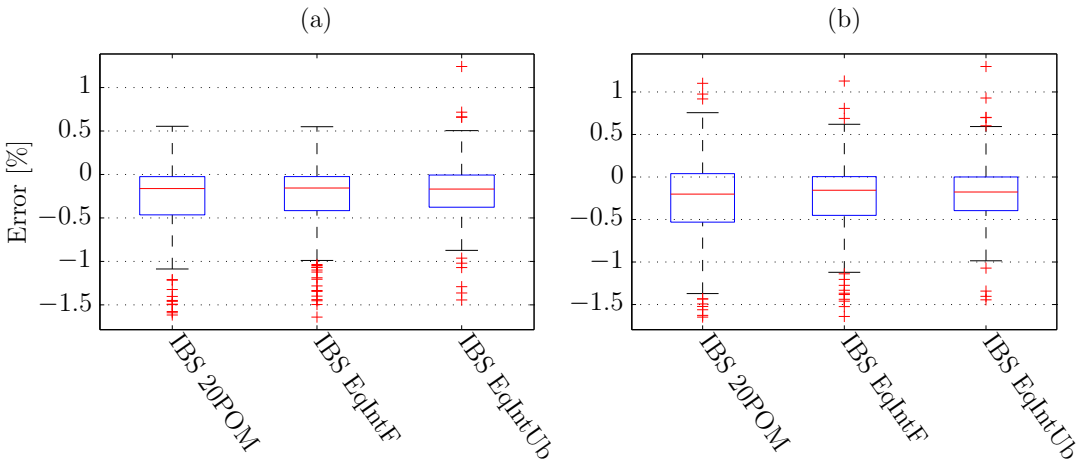

Figure 9.4: *Relative error on the fatigue damage obtained using dynamic blocked forces for all elements from DLC 1.2 with v_a = 13 m/s and H_s = 3.75 m. Results obtained from using the IBS method and different types of post-processing analyses:* ***(a)*** *Force control;* ***(b)*** *Displacement control.*

errors obtained for the critical elements. The normalized damage of all elements is therefore determined according to:

$$D^{el}_{i,norm} = \frac{D^{el}_{i}}{D^{el}_{max}}, \text{ for } i = 1 \cdots n_{el},$$

where D^{el}_{nor} is the normalized damage that ranges from zero to one, D^{el}_{max} is the maximum cumulative damage occurring (obtained from the reference solutions) and D^{el}_{i} is the damage in element i.

The relative error on the fatigue damages obtained for all elements from the IBS simulations are shown in figure 9.4, where the left and right subfigures respectively depict the results obtained using force and displacement control. From the y-scale of both subfigures one can already see that all methods provide very accurate results; i.e. all outliers are within a 2% error. Nonetheless, as it has been proven that the IBS method applied is analytically exact in section 5.3, one would expect the errors to be zero. However, a number of sources of errors in the computational process can be identified here. Firstly, the IRFs are truncated and windowed, thereby generating small errors in the coupled simulations (as is discussed further in section 9.5). Secondly, there is the effect of the tolerance settings in the Newton-Raphson process used in the time integration process, as is discussed in more detail in section 8.3.1. Thirdly, the wave forces have been spatially reduced for obtaining the results from the "IBS 20POM" model, as is discussed in section 9.4. However, as the results from both the reduced wave loading and equivalent wave loading show the same range of errors, this indicates that the spatial (force) reduction basis employing 20 POMs is adequate to capture the part of the wave forces that is important for the global integrated OWT response.

Figure 9.5 allows one to examine the results in some more detail. The relative error for the most critical elements is within 0.55% for all models and associated loading types and can thus be considered as negligible. This clearly demonstrates that the IBS method offers an attractive alternative the the CMS methods evaluated in chapters 7 and 8.

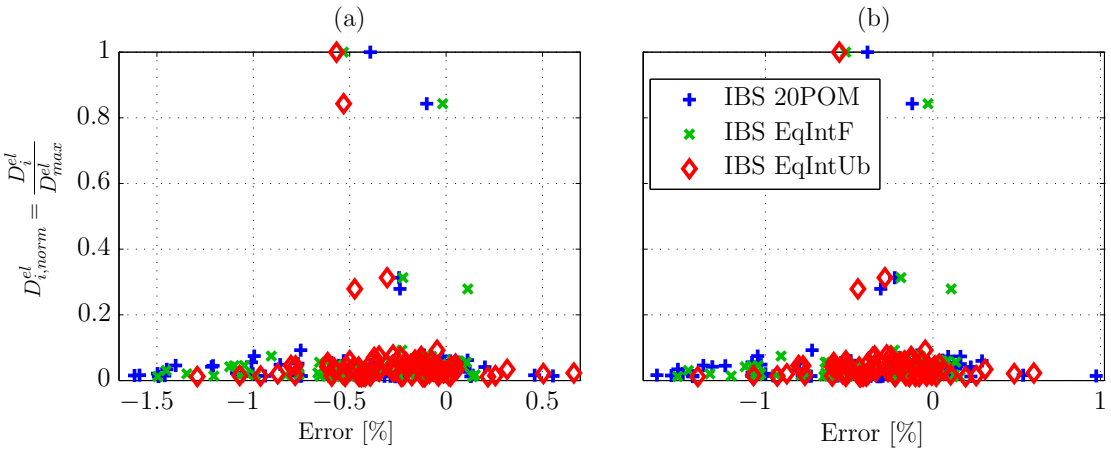

Figure 9.5: *Relative error versus normalized damage for $D^{el}_{nor} > 0.01$ from DLC 1.2 with $v_a = 13$ m/s and $H_s = 3.75$ m. Results obtained from using the IBS method and different types of post-processing analyses:* ***(a)*** *Force control;* ***(b)*** *Displacement control.*

9.5 Effect of truncating the foundation's impulse response functions

As is mentioned in section 9.2, the IRFs are truncated and windowed using the combination of a rectangular and cosine window, as is outlined in section 3.6.3. These windows smoothly force the IRFs to be zero over the length of the window, which can physically be interpreted as adding a type of nonphysical damping to the system (as is briefly discussed in section 3.6.3).

9.5.1 Models and load case used

To investigate the effect of this truncation and windowing action, a number of different IRFs have been generated from varying the windowing parameters, as is given in table 9.2. It can be seen that the first set of IRFs ("IRF_{01}") gets forced to zero at the point in time where the set of original IRFs would still have amplitudes of motion of around 10% of its peak values. Therefore, as the influence of windowing is the largest for this model, it is expected that the results obtained from this model will show the largest error.

Jacket model				Total model	
# $\boldsymbol{u}_{[b]}$	ϵ_w	ϵ_k	Model size	Total # of DoF	Name
-	-	-	1062×1062	1062 + 406	Ref
6	1×10^{0}	1×10^{-1}	$6 \times 6 \times 239$	6 + 406	IRF_{01}
6	1×10^{-2}	1×10^{-3}	$6 \times 6 \times 952$	6 + 406	IRF_{23}
6	1×10^{-4}	1×10^{-5}	$6 \times 6 \times 1702$	6 + 406	IRF_{45}

Table 9.2: *Overview of models used for investigating the effect of truncating and windowing IRFs.*

For investigating the effect of truncation, the same load case as in section 9.2 is used: the wind turbine is operating at the mean wind speed of 13 m/s with significant wave heights of 3.75 m. In order to avoid errors induced by reducing the wave forces, it has been chosen to apply the equivalent (dynamic) blocked forces at the interface of the jacket model.

9.5.2 Results obtained for the wind turbine substructure

The results for the wind turbine structure are presented again as DELs for the three different focuss elements: the tower bottom element, tower top element and root element of blade 1, and are given in figure 9.6. From these results it is seen that the biggest effect of the truncation

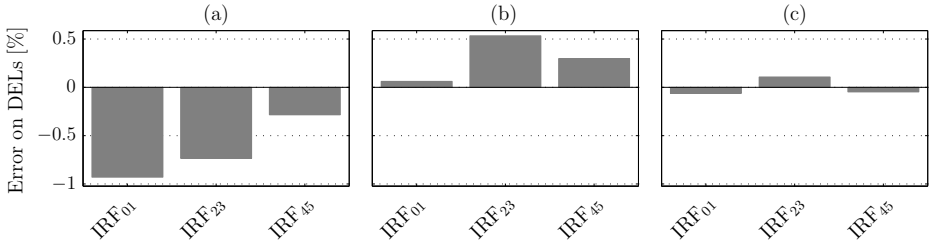

Figure 9.6: *Error on the damage equivalent loads for different elements, obtained using IBS. Result from DLC 1.2 with $v_a = 13$ m/s and $H_s = 3.75$ m.* ***(a)*** *Tower bottom element;* ***(b)*** *Tower top element;* ***(c)*** *Blade 1 root element.*

can be observed for the tower bottom element (figure 9.6a). As this element is closest to the interface, where the "error" due to the truncation is introduced, this is as expected. It is interesting to note that the tower bottom DEL show the largest underestimation for the "IRF_{01}" model, which is in line with the fact that in this model the largest amount of "extra" damping is introduced by the windowing action. Nonetheless, all models remain within 1% error, thereby showing that even highly windowed IRFs still lead to accurate fatigue load estimates for the wind turbine component.

In general it is expected that the truncation mainly affects the response of coupled substructures that have very little damping. Due to the fact that the main damping contribution for complete offshore wind turbine comes from the aero-dynamics, the effect of "extra" damping introduced by the truncation appears to be of no importance. Note however that the aero-dynamic damping is significantly less in idling load cases, such that the effect of truncating the IRFs could become important for these load cases.

9.5.3 Results obtained for the jacket substructure

The results for the jacket structure are again given as relative errors on the fatigue damage induced by all the elements, which is shown in figure 9.7. Here it can be observed that the errors for the fatigue damage are all within the range of -2.2% to 1.5%, but also that the fatigue damage is underestimated in approximately 75% of the elements and overestimated in approximately 25% of the elements. In addition, the median, but also the spread, of the errors slowly converges towards zero for increasing IRF lengths. In figure 9.8, where the relative error with respect to the normalized damage is given, the same convergence over the models is observed for the critical elements in case of a displacement control approach. However, in the results obtained using force control it is seen in figure 9.8 that the error obtained using the "IRF_{23}" model is larger for the fatigue driving element than the one obtained using the "IRF_{01}" model.

Nonetheless is can be concluded that in the current test case the effect of truncating and windowing the IRFs is negligible, even for the "IRF_{01}" model.

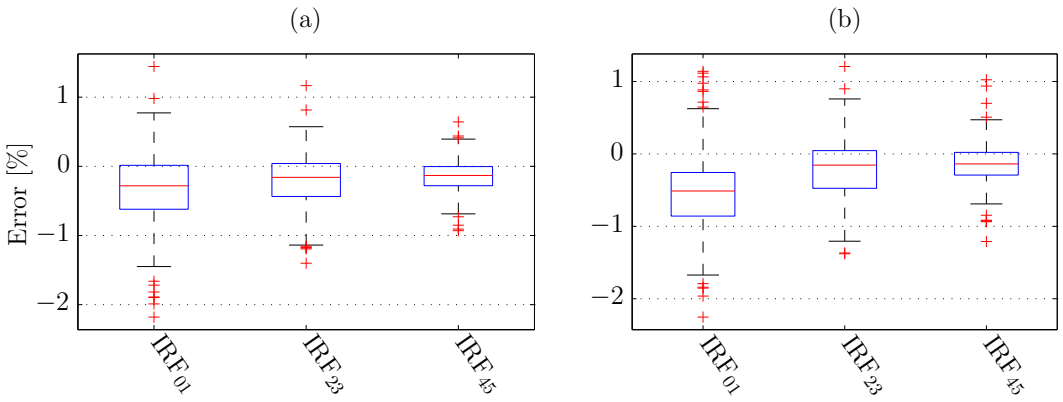

Figure 9.7: *Relative error on the fatigue damage obtained using dynamic blocked forces for all elements from DLC 1.2 with $v_a = 13$ m/s and $H_s = 3.75$ m. Results obtained from using the IBS method and different types of post-processing analyses:* ***(a)*** *Force control;* ***(b)*** *Displacement control.*

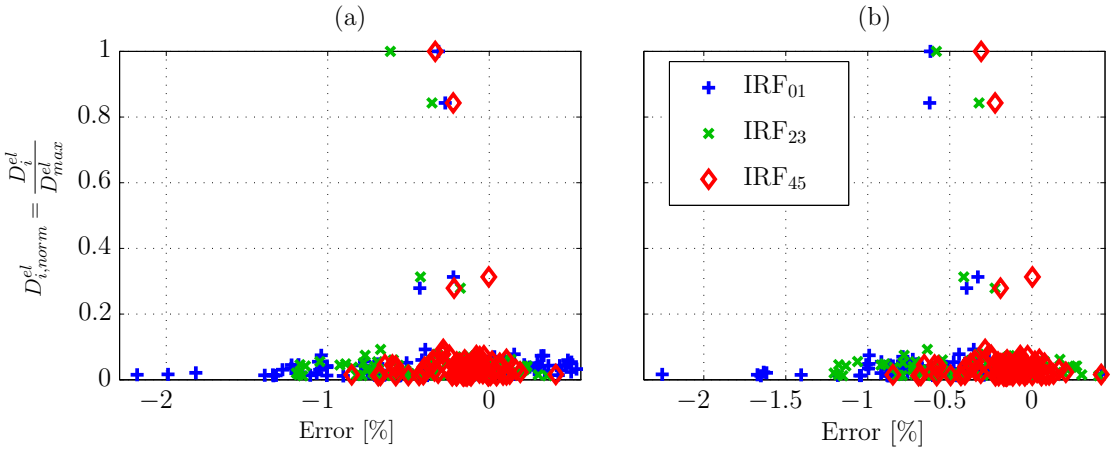

Figure 9.8: *Relative error versus normalized damage for $D^{el}_{nor} > 0.01$ from DLC 1.2 with $v_a = 13$ m/s and $H_s = 3.75$ m. Results obtained from using the IBS method and different types of post-processing analyses:* ***(a)*** *Force control;* ***(b)*** *Displacement control.*

9.6 Comparison of the computational costs

Again, computational cost are an important aspect to consider, therefore a comparison in terms of normalized computation times is given in this section. Note that time is normalized with respect to (the mean of) the computation time for the reference simulations.

Firstly, in figure 9.9 the normalized computation times associated to the test case presented in section 9.2 are shown. Like in the previous chapters, the BHawC simulation represent the largest part of the computational effort. In addition it is observed that in the case of applying equivalent loading on the interface, the aero-elastic simulations require less time. As the IRFs needed in these approaches have less input DoFs, as is seen in table 9.1, the convolution product requires less computational effort to solve. Also note that for multiple load cases, the approach using equivalent loading could become more expensive. As one only requires one set of IRFs (or a limited number of different sets) when using reduced wave loads, the equivalent loading has to be computed for each load case, therefore a break-even point might be found when simulating multiple load cases.

The computation times from evaluating the effect of truncating and windowing the IRFs are

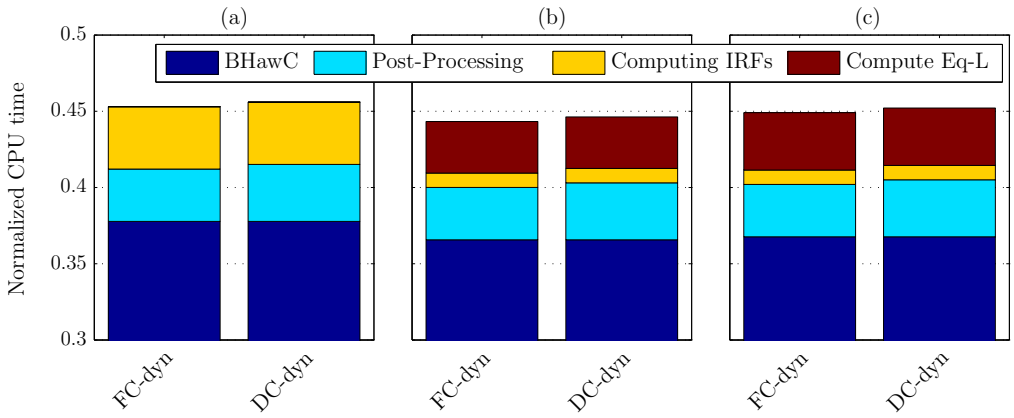

Figure 9.9: *Normalized computation times for the subsequent steps in the computational process;* ***(a)*** *IRF 20POM;* ***(b)*** *IRF EqIntF;* ***(c)*** *IRF EqIntUb.*

given in figure 9.10. Firstly, from table 9.2 it is clear that the lower the windowing parameters are set, the longer the IRFs are. This effect is also observed in figure 9.10, as the computation times for determining the IRFs increase accordingly. The computation times required for the BHawC simulations, are however hardly affected. This shows that solving the convolution product requires a negligible computational effort, with respect to the computations required for solving the full nonlinear and aero-elastic wind turbine part.

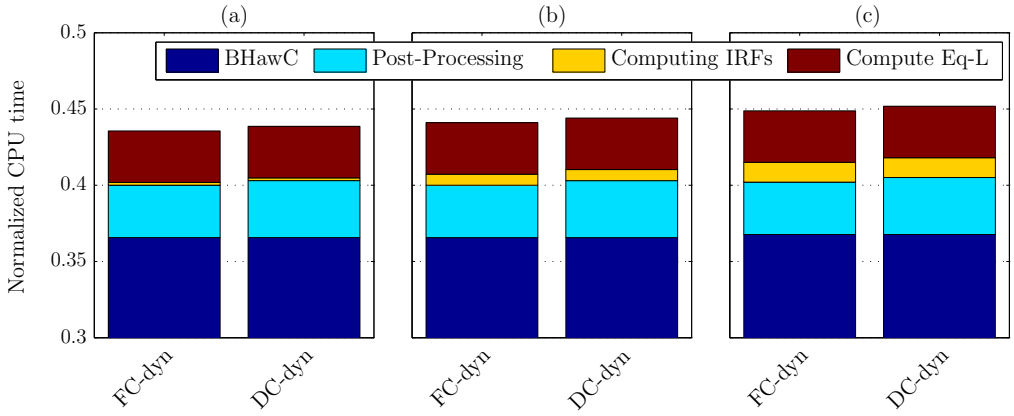

Figure 9.10: *Normalized computation times for the subsequent steps in the computational process;* ***(a)*** IRF_{01}*;* ***(b)*** IRF_{23}*;* ***(c)*** IRF_{45}*.*

Finally it is noted that the computational efforts of the IBS approach are comparable to those required for applying the CMS methods, as can be seen in sections 7.7 and 8.5.

9.7 Summary of results

In the current chapter it has been demonstrated that the Impulse Based Substructuring methodology can serve as an excellent replacement for the CMS methods often applied in the analysis of integrated offshore wind turbines.

To allow for a cross-comparison, the load case and models used for the IBS case study, given in section 9.2, are equal to those used in chapters 7 and 8. The three different methods for handling distributed forces on component models that have been introduced in chapter 6 are

used in combination with the IBS technique. This gives three different models that are used in the test case: the first model uses reduced wave forces, the second model uses equivalent blocked forces and the last model employs free interface displacements. Note that in all these different models, the jacket foundation is included as a set of IRFs.

The results for the wind turbine component are given as DELs for the tower bottom, tower top and blade root elements in section 9.3. Here it has been shown that excellent results are obtained for the wind turbine substructure using all the different models. The fatigue damage estimates for the elements of the jacket are also highly accurate for all models. Thereby verifying that the IBS method is an effective alternative for the CMS methods.

In order to investigate the effect of truncating and windowing the IRFs on the DELs and fatigue damages found, three differently windowed IRFs have been created. From the results it has been found that even in case one truncates (and windows) the IRFs at 10% of the peak amplitudes, accurate results are obtained for both the wind turbine and foundation parts. This demonstrates that the integrated wind turbine response (of the operating turbine) is quite insensitive to the added (nonphysical) damping introduced in the IRFs of the jacket.

In addition, it has been shown that the computational effort of applying the IBS method in the aero-elastic simulations, is comparable to the computational effort required when applying the CMS methods for including reduced foundation responses.

In the IBS approach applied here, one has a choice on how to deal with the forces acting on the non-retained DoFs of the full model. In addition, as using a non-truncated set of IRFs is (for long simulations) highly unpractical and computationally expensive, one also has to decide on truncating and windowing the IRFs. From a computational point-of-view it might be cheaper to use the approach using the reduced wave loads. However, when multiple parties are involved in the design process, this could involve a lot of data transfer. In that case, it would also be simpler to only exchange information on the interface: equivalent forces/displacements, IRFs associated to the coupling DoFs and returning interface responses in terms of forces or displacements.

Concerning the truncation of the IRFs it is good to consider the tolerance settings used in the Newton-Raphson process, as this is the limiting factor for the obtained accuracy in the aero-elastic simulations of an operational offshore wind turbine. Note however that the costs associated to solving a larger convolution product are almost negligible in the coupled simulations performed. In addition, only a significant increase in computation costs is seen in the step of obtaining the IRFs. Hence, by choosing higher ϵ_w and ϵ_k one mainly limits the amount of pre-processing work and data that needs exchanged between different parties.

Part III

Conclusions and Recommendations

10

Conclusions and Recommendations

Life is the art of drawing sufficient conclusions from insufficient premises

– Samuel Butler

10.1 Conclusions

In the current strive to use economies-of-scale to lower the cost of offshore wind energy, ever larger wind turbines, in terms of rated power and sheer size, are being developed. Supporting these large turbines requires also similar developments for the foundations. Therefore, multi-membered foundation solutions are starting to become more and more popular. In addition, the pressure on lowering the LCOE of offshore wind energy requires to optimize the support structure as much as possible. This generally leads to more flexible structures, where correct modeling of the dynamic behavior becomes vital in the design process, that requires thousands of simulations and involves multiple parties. Hence, this resulted in the following research objective:

"Development of simulation procedures, based on the dynamic substructuring methodology, for the integrated analysis of offshore wind turbines with multi-membered support structures."

In this thesis it has been proven that the dynamic substructuring methodology can be used for formulating accurate simulation procedures for analyzing wind turbines installed on multi-membered foundation structures. In addition it was shown that these methods are well suited to be used in a multi-party design process and are able to substantially reduce the overall computation costs involved.

10.1.1 Conclusions on Component Mode Synthesis approaches

The first option for including complex foundation models in aero-elastic simulations is by means of reduced foundation models. The outlined methods, which are classified in the Component Mode Synthesis family, allow spatially reducing and assembling linear foundation models. From the theory of model reduction it was found that in order to arrive at an accurate superelement,

one has to consider both spectral and spatial convergence. The former means that the reduced model should be accurate in the spectral bandwidth of the loading while the latter implies that the reduced basis should be able to accurately capture the effects of the external loading. The spatial aspect is handled by either applying types of equivalent interface loading at the boundary DoFs or by augmenting the reduction basis with force-dependent MTA vectors. The spectral performance is improved by adding vibration modes to the reduction basis.

In the different test cases it was shown that accurate results are obtained if one designs a reduction basis where both the spectral and spatial aspects are taking into account. Hence, the (Augmented) Craig-Bampton models are able to result in relative errors of less than 0.5% in terms of damage equivalent loads in the wind turbine and fatigue damage in critical jacket elements. However, the Guyan reduced model led to errors up to 11.5% for the DELs in the wind turbine elements. In addition, underestimations of approximately 80% up to overestimation of approximately 180% were found for the fatigue damage estimates in the most critical jacket elements. These could however be reduced to approximately 2% to 6% using a correction step, as is discussed further in section 10.1.4. However, it is clearly demonstrated that the Guyan reduced jacket is not spectrally and spatially converged and will therefore always result in errors. Note that all the overall computation costs were lowered with respect to the reference solution using any combination of reduction and post-processing methods.

10.1.2 Conclusions on Impulse Based Substructuring

Secondly, a framework for the Impulse Based Substructuring method has been derived that allows one to obtain the coupled responses of multiple substructures, that can either be given as impulse response functions or finite element models. For deriving the approach, it has been assumed that the IRFs are obtained from numerical models, but the method also holds for experimentally obtained IRFs. Although working with measurements is altogether challenging, the technique should enable time integrations which include measured components. The proposed method can handle arbitrary initial conditions and is compatible with all time integration methods within the generalized-α and Newmark family. It has been proven that in those cases the IBS approach is fully equivalent to the associated generalized-α or Newmark method and the same properties in terms of accuracy and stability are obtained.

Highly accurate results were obtained from combining the IBS method with any of the three methods for handling distributed forces on component models. Errors on the damage equivalent loads in the wind turbine were found to be less than 1% and the relative errors on the fatigue damage in *all* the jacket elements where within 2%. In addition it was found that the errors smaller than 0.55% were found for the most critical elements in the jacket. Finally note that the overall computation costs were substantially reduced, with respect to those associated to the reference solution, using the IBS method.

10.1.3 Conclusions on monolithic multi-domain time integration

Finally, two monolithic multi-domain time integration methods have been introduced. Even though these are not substructuring methods in the classical sense, they are still derived from some of the basic substructuring ideas. The first approach is a sequential scheme, which is similar to applying the idea of a frontal solver for monolithically solving the coupled dynamic problems. Therefore, the response obtained is analytically exact with respect to solving the total structure in a single domain using the associated generalized-α or Newmark method. Even though the sequential nature of the method is a downside from a computational point-of-view,

it does guarantee that the method can be unconditionally stable. This method was applied for coupling the wind turbine simulations performed in BHawC with the jacket simulations in Matlab. By taking advantage of the fact that the jacket model is linear, a speedup of approximately 70 was achieved for obtaining the reference solution.

The second method introduced is a parallel monolithic multi-domain time integration method and can be considered as a further development of a FETI solver. Its main benefits are the parallel nature and easy implementation. However, no extensive analysis on the accuracy and stability of the method has been performed. Nonetheless, accurate and stable results were obtained in a simple test study.

10.1.4 Conclusions on reconstruction approaches for foundation response

Three methods were identified for reconstructing the full foundation response, namely: i) direct expansion of the reduced DoFs using the reduction basis, ii) a displacement controlled (DC) reconstruction using the interface displacements and iii) a force controlled (FC) reconstruction using the interface force.

The accuracy of an expansion is directly related to the quality of the reduced model. The Guyan reduced model underestimated the fatigue damages for the critical elements by approximately 80% in case the applied forces were reduced and one would apply a direct expansion. Also in the case of applying equivalent interface loading, an underestimation was found of up to 18% for the critical elements. From this result one can directly conclude that 62% of the underestimation in the former case is due to a lack of spatial convergence and 18% is due to a lack of spectral convergence. The (Augmented) Craig-Bampton models performed much better as both the spectral and spatial aspects were accounted for in the reduction basis. Typically the errors for the critical elements, when using reduced wave forces, were within 4%. However, in one case an overestimation of 16%-20% was found for the CB2020 model. In the case of using equivalent forces, these errors were typically smaller than 2%. Note that the quasi-static residual correction was able to reduce the errors found using the Guyan reduced model to approximately 2% to 6% for the critical elements. By using the same approach, the Augmented Craig-Bampton models resulted in errors smaller than 1% for *all* jacket elements and even within 0.1% for the most critical elements.

The FC and DC approaches can be performed statically and dynamically; it was proven that in case of unreduced models, the dynamic FC and DC methods yield the exact same results as the reference analysis. The static variants of both methods are only accurate if the inertia and damping forces in the foundation can be neglected, i.e. when the spectral bandwidth of the loading is (much) lower than the first eigenfrequencies of the associated dynamic problems. It was found that regardless of the (reduced) models used, the static FC and DC methods led to underestimations of the fatigue damages in the most critical jacket elements of 5% to 60% depending on the load case, method and jacket model used. This clearly indicates that one cannot neglect the (internal) inertia and damping forces of jacket foundations. Hence, these static reconstruction methods should not be used for designing multi-membered foundation structures such as jackets.

The dynamic force control and displacement control methods gave very good results for all reduced models, with fatigue damage errors within 1% for *all* elements, except for the Guyan model. In the case of a Guyan reduced model errors in the interface response led to overestimations of the fatigue damages in the most critical elements of approximately 5% to 30% for the original UpWind jacket and up to 180% for the tuned UpWind jacket. Indeed, the spectral mismatch of the Guyan reduced models leads to underestimations in a direct expansion and

overestimations in case of the dynamic post-processing methods, thereby rendering it effectively useless.

10.2 Recommendations

In this thesis the use of the dynamic substructuring paradigm for load calculation procedures has been investigated for all the different steps in the computational process for designing offshore wind turbine support structures. From the knowledge obtained in this thesis, several recommendations for load calculation procedures of multi-membered wind turbine foundations have been distilled and are given in section 10.2.1. Nonetheless, as in science questions answered generally also generate new questions, there will always remain points for further research. Therefore, in section 10.2.2, recommendations are given for future research efforts into both the theoretical and practical aspects of the computational design procedures.

10.2.1 Recommendations for the design process of support structures

Taking into account the current level of maturity of the different substructuring methods and their availability in existing commercial finite element packages, the approach using blocked forces, a Craig-Bampton reduced model and a dynamic force/displacement controlled reconstruction is likely to be the easiest to adopt in practice. Even though from a computational point-of-view using an Augmented Craig-Bampton model in the coupled simulations, and reconstructing the foundation response using an expansion with residual correction would likely be more efficient. The Impulse Based Substructuring methodology proposed in this thesis can serve as an efficient and accurate alternative in case one is not able to create Craig-Bampton (or similar) reduced models, as one only needs to perform a series of time integrations in order to obtain the impulse response functions.

However, due to the iterative nature of the current computational setup, it will always involve exchanging large data sets. Therefore, reducing this significantly will require fundamental changes in the current load calculation process. For instance, if one would assume that the WTM would be responsible for the entire load calculation process (including the foundation), then the FD would only require the ultimate (ULS) and fatigue loads (FLS) in order to update its foundation design. This would obviously reduce the amount of data that needs to be exchanged.

Ultimately, a setup can be imagined were a single party would be responsible for the design of the entire support structure (tower and foundation). This would open a range of possibilities for performing integrated design optimization, as the current slow converging iterative process with multiple design parties would be eliminated. In fact integrated support structure optimization has the potential of lowering the capital expenditure, and thus the cost of energy, for both monopile based support structures, as is shown in [68], and their jacket counterparts [95].

10.2.2 Open points for research

Despite the work presented in the thesis, a number of interesting research topics still remain unaddressed. In addition, new developments in the field of offshore wind energy, such as floating turbines, have also created new interesting research topics.

Although the focus of this thesis has been on multi-membered foundation structures, it could also prove to be useful for the next generation of monopiles that is currently under development;

the XL-monopiles. In [47] the approach was tested on a 6 meter diameter monopile. Here it was found that the wave forces distributed over the monopile can cause local deformations of the cross section. It is not hard to imagine that this effect will be more pronounced on XL-monopiles with even larger diameters (up to 10 m) and would therefore need to be included in the load analysis of XL-monopile based support structures.

Also some (multi-) physical effects have been neglected in demonstrating the proposed methodologies, such as:

- The effect of the soil where the wind turbine foundation is installed in. Firstly, accurately modeling the dynamic behavior of the soil itself is all but trivial and an active field of research in its own. The second challenge would then be to create engineering models that are both accurate and computationally efficient, such that one can integrate these effects in the load calculation process for offshore wind turbines. As the current industry practice of using a Winkler foundation model in combination with P-Y curves [1], has only been validated for static load cases and slender piles [106, 130], further research is required.

  Note that the technology developed in this thesis can readily be extended to include the effects of soil dynamics. In case the resulting soil model can be considered linear, one can apply one of the reduction methods or the IBS approach. Otherwise, if the soil-structure interaction results in a nonlinear substructure for the soil, the coupled time integration methodologies presented in chapter 4 are applicable.

- In addition, there is the effect of the hydrodynamics. In this thesis, it was assumed that the influence of the structure on the hydrodynamic forces is negligible, thereby resulting in linear equations for obtaining wave forces from wave kinematics. Although this is reasonable for relatively stiff fixed offshore structures (like the UpWind reference jacket), one can easily imagine that this effect can become important in the load calculation process for more compliant foundation structures. Hence, it is essential to study the limits of the current assumption and if necessary, extend the current methodology to be able to include this nonlinear coupling.

Also, as nations with steep coastlines wish to develop large scale offshore wind energy, it is only a matter of time before the first commercial floating wind farms will arise. This brings entirely new challenges, as the hydro-elastic effects and nonlinear mooring dynamics cannot be neglected. Thereby resulting in full nonlinear descriptions of the structure itself and the CMS and IBS methods outlined in this thesis might not be applicable for floating turbines.

As the topics described above all involve nonlinearities that need to be taken into account during the aero-elastic simulations and post-processing analyses, nonlinear model reduction schemes will need to be developed in order to extend the current approach. These nonlinear superelements must thus be able to handle localized nonlinearities due to the soil-structure and/or hydro-elastic interactions.

One of the topics that has not been the focus of this thesis but is nonetheless one of the most important research topics for the near future, is the use of experimental data for validation of the simulation models and the inputs used. Uncertainties on the input parameters and the models themselves require one to take into account a number of safety factors in order to ensure that the design is conservative. By validating the inputs and models, more reliable results are obtained and less additional safety would be required. An example is for instance the use of structural damping ratios in the wind turbine simulations for design. As it is known that the amplitude and the persistency of the vibrations are inversely related to modal damping ratios, these structural parameters play an essential role in lifetime predictions for an offshore wind

turbines. Hence, if one can prove that the actual damping ratios are higher than those currently allowed for design, design fatigue loads will lower, thereby resulting in more slender and less costly supporting structures for wind turbines.

Following the use of experimental data for the validation of simulation models, as well as their inputs and individual components, an interesting idea would be to directly include measurements as experimental substructures in the analysis. Even though the IBS method should, in theory, enable directly including measured IRFs in the analysis, it is in practice all but trivial [161, 162].

Bibliography

[1] DNV-OS-J101 - Design of Offshore Wind Turbine Structures.

[2] F. Adam, T. Myland, F. Dahlhaus, and J. Grossmann. Scale tests of the GICON-TLP for wind turbines. In *Proceedings of the ASME 2014 33rd International Conference on Ocean, Offshore and Arctic Engineering, OMEA 2014, June 8-13, San Francisco, California, USA*, 2014.

[3] R. J. Allemang. The Modal Assurance Criterion - Twenty Years of Use and Abuse. In *Proceedings of the Twenty First International Modal Analysis Conference, Kissimmee, FL*, 2003.

[4] K. F. Alvin, A. N. Robertson, G. W. Reich, and K. C. Park. Structural system identification: from reality to models. *Computers & structures*, 81(12):1149–1176, 2003.

[5] A. C. Antoulas, D. C. Sorensen, and S. Gugercin. A survey of model reduction methods for large-scale systems. *Contemporary mathematics*, 280:193–220, 2001.

[6] A. Arapogianni, A.-B. Genachte, et al. Deep Water - The next step for offshore wind energy. Technical report, EWEA, 2013.

[7] M. Arnold and O. Brüls. Convergence of the generalized-α scheme for constrained mechanical systems. *Multibody System Dynamics*, 18(2):185–202, 2007.

[8] R. M. Bamford. A Modal Combination Program for Dynamic Analysis of Structures. Technical report, Jet Propulsion Laboratory, Pasadena, CA, 1967.

[9] B. Barahona, L. C. Henriksen, A. D. Hansen, N. A. Cutululis, and P. Sørensen. Coupling of HAWC2 and Matlab: Towards an integrated simulation platform. In *European Wind Energy Conference*, pages 1–5, 2010.

[10] R. E. D. Bishop and D. C. Johnson. *The Mechanics of Vibration*. Cambridge University Press, 1960.

[11] S. Bittanti and M. Lovera. Bootstrap-based estimates of uncertainty in subspace identification methods. *Automatica*, 36(11):1605 – 1615, 2000.

[12] C. Böker. *Load simulations and local dynamics of support structures for offshore wind turbines*. PhD thesis, Gottfried Wilhelm Leibniz Universität Hannover, 2010.

[13] A. Brandt. *Noise and vibration analysis: signal analysis and experimental procedures*. John Wiley & Sons, 2011.

[14] M. L. Buhl and A. Manjock. A Comparison of Wind Turbine Aeroelastic Codes Used for Certification. In *44th AIAA Aerospace Sciences Meeting and Exhibit, 9-12 January 2006, Reno, NV, AIAA Meeting Papers on Disc.*, 2006.

[15] O. Bursi, L. He, A. Bonelli, and P. Pegon. Novel generalized-alpha methods for interfield parallel integration of heterogeneous structural dynamic systems. *Journal of Computational and Applied Mathematics*, 234:2250–2258, 2010.

[16] O. Bursi, Z. Wang, C. Jia, and B. Wu. Monolithic and partitioned time integration methods for real-time heterogeneous simulations. *Computational Mechanics*, 52(1):99–119, 2013.

[17] B. Byrne, G. Houlsby, C. Martin, and P. Fish. Suction caisson foundations for offshore wind turbines. *Wind Engineering*, 26(3):145–155, 2002.

[18] T. G. Carne and A. R. Nord. Modal testing of a rotating wind turbine. In *Proc Sixth Biennial Wind Energy Conf and Workshop*, pages 825–34, 1983.

[19] A. Chatterjee. An introduction to the proper orthogonal decomposition. *Current Science*, 78(7):808–817, April 2000.

[20] J. Chung and G. M. Hulbert. A Time Integration Algorithm for Structural Dynamics With Improved Numerical Dissipation: The Generalized-alpha Method. *Journal of Applied Mechanics*, 60(2):371–375, 1993.

[21] A. Combescure, A. Gravouil, and B. Herry. An algorithm to solve transient structural non-linear problems for non-matching time-space domains. *Computers & structures*, 81(12):1211–1222, 2003.

[22] R. Courant. Variational Methods for the Solutions of Problems of Equilibrium and Vibrations. *Bulletin of the American mathematical Society*, 49, 1943.

[23] R. Craig. Coupling of Substructures for Dynamic Analyses – An Overview. In *Proceedings of AIAA/ASME/ASCE/AHS/ASC Structures, Structural Dynamics, and Materials Conference and Exhibit*, pages 1573–1584, April 2000.

[24] R. Craig and M. Bampton. Coupling of Substructures for Dynamic Analysis. *AIAA Journal*, 6(7):1313–1319, 1968.

[25] R. Craig and A. Kurdila. *Fundamentals of Structural Dynamics*. John Wiley and Sons, Ltd., New York, London, Sydney, second edition edition, 2006.

[26] R. Crawford. Life cycle energy and greenhouse emissions analysis of wind turbines and the effect of size on energy yield. *Renewable and Sustainable Energy Reviews*, 13(9):2653–2660, 2009.

[27] P. Cresta, O. Allix, C. Rey, and S. Guinard. Nonlinear localization strategies for domain decomposition methods: Application to post-buckling analyses . *Computer Methods in Applied Mechanics and Engineering*, 196(8):1436 – 1446, 2007.

[28] J. Crowley, A. Klosterman, G. Rocklin, and H. Vold. Direct Structural Modification using Frequency Response Functions. In *Proceedings of the Second International Modal Analysis Conference, Orlando, FL*, pages 58–65, Bethel, CT, February 1984. Society for Experimental Mechanics.

[29] K. Cuppens, P. Sas, and L. Hermans. Evaluation of the FRF Based Substructuring and Modal Synthesis Technique Applied to Vehicle FE Data. In *PROCEEDINGS OF THE INTERNATIONAL SEMINAR ON MODAL ANALYSIS, Leuven. Belgium*, pages 1143–1150, 2000.

[30] M. Damgaard, L. B. Ibsen, L. V. Andersen, and J. K. F. Andersen. Cross-wind modal properties of offshore wind turbines identified by full scale testing. *Journal of Wind Engineering and Industrial Aerodynamics*, 116:94–108, 2013.

[31] D. de Klerk. *Dynamic Response Characterization of Complex Systems through Operational Identification and Dynamic Substructuring*. PhD thesis, Delft University of Technology, Delft, the Netherlands, October 2008.

[32] D. de Klerk, D. Rixen, and C. Valentin. An experimental Gear Noise Propagation Method for a Gearbox on a Test Bench. In *Proceedings of the Twenty Fifth International Modal Analysis Conference, Orlando, FL*, Bethel, CT, 2007. Society for Experimental Mechanics.

[33] D. de Klerk and D. J. Rixen. Component transfer path analysis method with compensation for test bench dynamics. *Mechanical Systems and Signal Processing*, 24:1693 – 1710, 2010.

[34] D. de Klerk, D. J. Rixen, and J. de Jong. The Frequency Based Substructuring (FBS) Method Reformulated According to the Dual Domain Decomposition Method. In *Proceedings of the Twenty Fourth International Modal Analysis Conference, St. Louis, MO*, Bethel, CT, February 2006. Society for Experimental Mechanics.

[35] D. de Klerk, D. J. Rixen, and S. N. Voormeeren. General Framework for Dynamic Substructuring: History, Review and Classification of Techniques. *AIAA Journal*, 46(5):1169–1181, May 2008.

[36] P. C. de Valk. Accuracy of Calculation Procedure for Offshore Wind Turbine Support Structures. Master's thesis, Delft University of Technology, 2013.

[37] W. de Vries, N. K. Vemula, P. Passon, T. Fischer, D. Kaufer, D. Matha, B. Schmidt, and F. Vorpahl. Final report WP 4.2 - Support Structure Concepts for Deep Water Sites. Technical report, Project UpWind, 2011.

[38] C. Devriendt, P. J. Jordaens, G. De Sitter, and P. Guillaume. Damping estimation of an offshore wind turbine on a monopile foundation. *IET Renewable Power Generation*, 7(4):401–412, 2013.

[39] C. Devriendt, F. Magalhães, M. E. Kafafy, G. D. Sitter, Álvaro Cunha, and P. Guillaume. Long-Term Dynamic Monitoring of an Offshore Wind Turbine. In *Topics in Dynamics of Civil Structures*, volume 4 of *Conference Proceedings of the Society for Experimental Mechanics Series 2013*, pages 253–267, 2013.

[40] J. M. Dickens, J. M. Nakagawa, and M. J. Wittbrodt. A critique of mode acceleration and modal truncation augmentation methods for modal response analysis. *Computers & Structures*, 62(6):985 – 998, 1997.

[41] J. M. Dickens and A. Stroeve. Modal Truncation Vectors for Reduced Dynamic Substructure Models. In *Structures, Structural Dynamics and Material Conference*, Atlanta, April 3-6 2000. 41st AIAA/ASME/ASCE/AHS/ASC Structures, Structural Dynamics, and Materials Conference and Exhibit. AIAA-2000-1578.

[42] E. Dowell. Free Vibrations of a Linear Structure with Arbitrary Support Conditions. *J. App. Mech., ASME*, 38:595–600, 1971.

[43] E. Dowell. Free Vibrations of an Arbitrary Structure in Terms of Component Modes. *J. App. Mech., ASME*, 39:727–732, 1972.

[44] E. H. Dowell. Component Mode Analysis of a Simple Non-Linear, Non-Conservative System. *Jnl. Sound and Vibration*, 80(2):233–246, 1982.

[45] S. D. Downing. Simple rainflow counting algorithms. *International Journal of Fatigue*, 4(1):31–40, 1982.

[46] J. Dubois, M. Muskulus, and P. Schaumann. Advanced Representation of Tubular Joints in Jacket Models for Offshore Wind Turbine Simulation. *Energy Procedia*, 35(0):234 – 243, 2013. DeepWind'2013 - Selected papers from 10th Deep Sea Offshore Wind R&D Conference, Trondheim, Norway, 24 - 25 January 2013.

[47] R. Engels. Superelement Modeling of Offshore Wind Turbine Support Structures - Application to Monopile Based Structures. Master's thesis, University of Twente, 2013.

[48] Ernst & Young. Analysis of the value creation potential of wind energy policies, 2012.

[49] L. Euler. *Institutionum calculi integralis Volumen Primum.* Opera Omnia Series Prima, 1768.

[50] European Wind Energy Association. The European offshore wind industry - key trends and statistics 2013. Technical report, EWEA, 2013.

[51] C. Farhat, L. Crivelli, and M. Géradin. Implicit time integration of a class of constrained hybrid formulations - part i: Spectral stability theory. *Computer Methods in Applied Mechanics and Engineering*, 125:71 – 107, 1995.

[52] C. Farhat and D. Rixen. *Encyclopedia of Vibration*, chapter Linear Algebra, pages 710–720. Academic Press, 2002. isbn 0-12-227085-1.

[53] C. Farhat and F.-X. Roux. A Method of Finite Element Tearing and Interconnecting and its Parallel Solution Algorithm. *International Journal of Numerical Methods in Engineering*, 32(6):1205–1227, 1991.

[54] V. Faucher and A. Combescure. A time and space mortar method for coupling linear modal subdomains and non-linear subdomains in explicit structural dynamics. *Computer methods in applied mechanics and engineering*, 192(5):509–533, 2003.

[55] C. Felippa and K. Park. Staggered transient analysis procedures for coupled mechanical systems: formulation. *Computer Methods in Applied Mechanics and Engineering*, 24(1):61–111, 1980.

[56] C. A. Felippa, K. Park, and C. Farhat. Partitioned analysis of coupled mechanical systems. *Computer Methods in Applied Mechanics and Engineering*, 190(24):3247–3270, 2001.

[57] D. Findeisen. *System Dynamics and Mechanical Vibrations: An Introduction.* Engineering online library. Springer, 2000.

[58] T. Fischer, W. de Vries, P. Rainey, B. Schmidt, K. Argyriadis, and M. KÃijhn. Offshore support structure optimization by means of integrated design and controls. *Wind Energy*, 15(1):99–117, 2012.

[59] S. H. J. A. Fransen. An overview and comparison of OTM formulations on the basis of the mode displacement method and the mode acceleration method. In *Worldwide Aerospace Conference & Technology Showcase, Toulouse, France*, pages 8–10, 2002.

[60] S. H. J. A. Fransen. Data Recovery Methodologies for Reduced Dynamic Substructure Models with Internal Loads. *AIAA journal*, 42(10):2130–2142, 2004.

[61] P. Gardonio and M. Brennan. On the origins and development of mobility and impedance methods in structural dynamics. *Journal of Sound and Vibration*, 249(3):557 – 573, 2002.

[62] M. Géradin and D. Rixen. *Mechanical Vibrations – Theory and Application to Structural Dynamics*. John Wiley & Sons, Chichester, England, December 1997.

[63] G. Gladwell. Branch Mode Analysis of Vibrating Systems. *Journal of Sound and Vibration*, 1:41–59, 1964.

[64] J. H. Gordis. Integral equation formulation for transient structural synthesis. *AIAA Journal*, 33(2):320–324, 1995.

[65] J. H. Gordis and J. Radwick. Efficient transient analysis for large locally nonlinear structures. *Shock and Vibration*, 6(1):1–9, 1999.

[66] T. D. Griffith, T. G. Carne, and J. A. Paquette. Modal testing for validation of blade models. *Wind Engineering*, 32(2):91–102, 2008.

[67] R. Guyan. Reduction of Stiffness and Mass Matrices. *AIAA Journal*, 3(2):380, February 1965.

[68] R. Haghi, T. Ashuri, P. L. C. van der Valk, and D. P. Molenaar. Integrated Multidisciplinary Constrained Optimization of Offshore Support Structures. In *Proceedings of the Science of Making Torque from Wind (TORQUE) 2012. Oldenburg, Germany*, 2012.

[69] T. Hald and M. Høgedal. Implementation of a finite element foundation module in Flex5 using Craig-Bampton substructuring. *Proceedings of Copenhagen offshore wind*, 2005.

[70] Z. Hameed, Y. Hong, Y. Cho, S. Ahn, and C. Song. Condition monitoring and fault detection of wind turbines and related algorithms: A review. *Renewable and Sustainable Energy Reviews*, 13(1):1 – 39, 2009.

[71] E. Hau. *Wind Turbines*. Springer-Verlag Berlin Heidelberg, 2006.

[72] H. M. Hilber, T. J. R. Hughes, and R. L. Taylor. Improved numerical dissipation for time integration algorithms in structural dynamics. *Earthquake Engineering & Structural Dynamics*, 5:283–292, 1977.

[73] J. Hobohm, L. Krampe, F. Peter, A. Gerken, P. Heinrich, and M. Richter. Cost Reduction Potentials of Offshore Wind Power in Germany. Technical report, Prognos AG and The Fichtner Group, 2013.

[74] C. Hoff and P. J. Pahl. Development of and Implicit Method with Numerical Dissipation from a Generalized Single-Step Algorithm for Structural Dynamics. *Computer Methods in Applied Mechanics and Engineering*, 67:367–385, 1988.

[75] H. Holl and H. Irschik. A substructure method for the transient analysis of non-linear rotordynamic systems using modal analysis. In SEM, editor, *IMAC-XII: International Modal Analysis Conference, Honolulu, HI*, number 1638-1643, pages 1638–1643, 1994.

[76] A. Hrennikoff. Solution of problems of elasticity by the frame-work method. *ASME Journal of Applied Mechanics*, 8:619–715, 1941.

[77] T. J. R. Hughes. *The Finite Element Method - Linear Static and Dynamic Finite Element Analysis*. Prentice Hall Inc., New Jersey, 1987.

[78] G. M. Hulbert and T. Hughes. An Error Analysis of Truncated Starting Conditions in Step-by-Step Time Integration: Consequences for Structural Dynamics. *Earthquake Engineering & Structural Dynamics*, 15:901–910, 1987.

[79] W. Hurty. Dynamic Analysis of Structural Systems using Component Modes. *AIAA Journal*, 3(4):678–685, 1965.

[80] W. C. Hurty. Vibrations of Structural Systems by Component Mode Synthesis. *Journal of Engineering Mechanics, Division American Society of Civil Engineers*, 86(4):51–69, 1960.

[81] S. R. Idelsohn and A. Cardona. A reduction method for nonlinear structural dynamic analysis. *Computer Methods in Applied Mechanics and Engineering*, 49(3):253 – 279, 1985.

[82] International Electrotechnical Commission. IEC 61400-3. *Wind Turbines-Part 3: Design Requirements for Offshore Wind Turbines*, 2009.

[83] B. Irons. Structural eigenvalue problems: elimination of unwanted variables. *AIAA Journal*, 3(5):961–962, 1965.

[84] B. Irons. A Frontal Solution Program for Finite Element Analysis. *International Journal of Numerical Methods in Engineering*, 2:5–32, 1970.

[85] H. Jakobsson, F. Bengzon, and M. G. Larson. Adaptive Component Mode Synthesis in Linear Elasticity. *International Journal for Numerical Methods in Engineering*, 86(7):829–844, 2011.

[86] H. Jakobsson and M. G. Larson. A posteriori error analysis of component mode synthesis for the elliptic eigenvalue problem. *Computer Methods in Applied Mechanics and Engineering*, (200):2840–2847, 2011.

[87] G. H. James, T. G. Carne, and J. P. Lauffer. The Natural Excitation Technique (NExT) for Modal Parameter Extraction From Operating Wind Turbines. Technical report, Sandia National Laboratories, Albuquerque, New Mexico, 1993.

[88] B. Jetmundsen, R. Bielawa, and W. Flannelly. Generalized Frequency Domain Substructure Synthesis. *Journal of the American Helicopter Society*, 33:55–65, January 1988.

[89] J. Jonkman, S. Butterfield, W. Musial, and G. Scott. Definition of a 5-MW Reference Wind Turbine for Offshore System Development. Technical report, National Renewables Energy Laboratory, 2009.

[90] J. Jonkman and D. Matha. Dynamics of offshore floating wind turbines–analysis of three concepts. *Wind Energy*, 14(4):557–569, 2011.

[91] J. M. Jonkman. Dynamics of offshore floating wind turbines–model development and verification. *Wind Energy*, 12(5):459–492, 2009.

[92] D. Kaufer, N. Cosack, C. Böker, M. Seidel, and M. Kühn. Integrated analysis of the dynamics of offshore wind turbines with arbitrary support structures. In *European Wind Energy Conference, Marseille, France*, 2009.

[93] G. Kerschen and J. Golinval. Physical Interpretation of the Proper Orthogonal Modes using the Singular Value Decomposition. *Journal of Sound and Vibration*, 249(5):849–865, 2002.

[94] G. Kerschen, J.-C. Golinval, A. F. Vakakis, and L. A. Bergman. The Method of Proper Orthogonal Decomposition for Dynamical Characterization and Order Reduction of Mechanical Systems: An Overview. *Nonlinear Dynamics*, 41:147–169, 2005.

[95] J. King, A. Cordle, G. McCann, et al. Cost Reductions in Offshore Wind Turbine Jacket Design using Integrated Analysis Methods and Advanced Control. In *The Twenty-third*

International Offshore and Polar Engineering Conference. International Society of Offshore and Polar Engineers, 2013.

[96] L. Klein. Transverse Vibrations of Non-uniform Beams. *Journal of Sound and Vibration*, 37(4):491–505, 1974.

[97] C. Kost, T. Schlegel, J. Thomson, S. Nold, and J. Mayer. Levelized Cost of Electricity; Renewable Energies. Technical report, Fraunhofer-Institut für Solare Energiesysteme ISE, 2012.

[98] S. Krohn, P.-E. Morthorst, and S. Awerbuch. The Economics of Wind Energy. Technical report, European Wind Energy Association, 2009.

[99] R. J. Kuether and M. S. Allen. Craig-Bampton Substructuring for Geometrically Nonlinear Subcomponents. In *Proceedings of the SEM IMAC XXXII Conference, 2014, Orlando, FL*, 2014.

[100] P. la Cour. *Forsøgsmøllen*. Det Nordiskke Forlag, Copenhagen, 1900.

[101] T. Larsen, H. Aagaard Madsen, A. Hansen, and K. Thomsen. *Investigation of stability effects of an offshore wind turbine using the new aeroelastic code HAWC2*. Copenhagen Offshore Wind, 2005.

[102] Y.-T. Leung. An Accurate Method of Dynamic Condensation in Structural Analysis. *International Journal of Numerical Methods in Engineering*, 12:1705–1715, 1978.

[103] R. MacNeal. A Hybrid Method of Component Mode Synthesis. *Computers & Structures*, 1(4):581–601, 1971.

[104] N. Mahjoubi, A. Gravouil, and A. Combescure. Coupling subdomains with heterogeneous time integrators and incompatible time steps. *Computational Mechanics*, 44(6):825–843, 2009.

[105] N. Mahjoubi, A. Gravouil, A. Combescure, and N. Greffet. A monolithic energy conserving method to couple heterogeneous time integrators with incompatible time steps in structural dynamics. *Computer Methods in Applied Mechanics and Engineering*, 200(9):1069–1086, 2011.

[106] H. Matlock. Correlations for design of laterally loaded piles in soft clay. *Offshore Technology in Civil Engineering's Hall of Fame Papers from the Early Years*, pages 77–94, 1970.

[107] C. Michler, S. Hulshoff, E. van Brummelen, and R. de Borst. A monolithic approach to fluid-structure interaction. *Computers & Fluids*, 33(5):839 – 848, 2004. Applied Mathematics for Industrial Flow Problems.

[108] M. P. Mignolet, A. Przekop, S. A. Rizzi, and S. M. Spottswood. A review of indirect/non-intrusive reduced order modeling of nonlinear geometric structures. *Journal of Sound and Vibration*, 332(10):2437 – 2460, 2013.

[109] M. A. Miner. Cumulative Damage in Fatigue. *Journal of Applied Mechanics*, 12:159–164, 1945.

[110] D.-P. Molenaar. Experimental modal analysis of a 750 kW wind turbine for structural model validation. In *ASME 2003 Wind Energy Symposium*, pages 332–339. American Society of Mechanical Engineers, 2003.

[111] J. R. Morison, M. P. O'Brien, J. W. Johnson, and S. A. Schaaf. The force exerted by surface waves on piles. *Petroleum Transactions (American Institute of Mining Engineers)*, 189:149–154, 1950.

[112] N. Newmark. A Method of Computation For Structural Dynamics. *Proceedings of the American Society of Civil Engineers, Journal of the Engineering Mechanics Division*, 85(EM3):67–94, 1959.

[113] M. G. L. Ogno. Identifying structural parameters of an offshore wind turbine using operational modal analysis. Master's thesis, Delft University of Technology, 2013.

[114] M. Özbek. *Optical monitoring and operational modal analysis of large wind turbines*. PhD thesis, Delft University of Technology, 2013.

[115] M. Özbek and D. J. Rixen. Optical measurements and operational modal analysis on a large wind turbine: lessons learned. In *Rotating Machinery, Structural Health Monitoring, Shock and Vibration*, volume 5, pages 257–276. Springer, New York, 2011.

[116] T. Pahn, M. Kohlmeier, and R. Rolfes. System identification of a jacket support structure for a 5 MW offshore wind turbine due to artificial and ambient excitation. In *TORQUE 2010: The Science of Making Torque from Wind, June 28-30, Crete, Greece*, 2010.

[117] K. C. Park, M. Justino, and C. Felippa. An Algebraically Partitioned FETI Method for Parallel Structural Analysis: Algorithm Description. *International Journal for Numerical Methods in Engineering*, 40(15):2717–2737, 1997.

[118] P. Passon. Design of Offshore Wind Turbine Foundations in Deeper Water. In *TORQUE 2010: The Science of Making Torque from Wind, June 28-30, Crete, Greece*, 2010.

[119] P. Passon, M. Kühn, S. Butterfield, J. Jonkman, T. Camp, and T. Larsen. OC3-Benchmark Exercise of Aero-elastic Offshore Wind Turbine Codes. *Journal of Physics: Conference Series*, 75:1–12, 2007.

[120] J. Pebrel, C. Rey, and P. Gosselet. A Nonlinear Dual-Domain Decomposition Method: Application to Structural Problems with Damage. *International Journal for Multiscale Computational Engineering*, 6(3):251–262, 2008.

[121] J. T. Petersen. *Kinematically Nonlinear Finite Element Model of a Horizontal Axis Wind Turbine*. PhD thesis, Technical University of Denmark, 1990.

[122] K. B. Petersen and M. S. Pedersen. The matrix cookbook, February 2008.

[123] S. Piperno, C. Farhat, and B. Larrouturou. Partitioned procedures for the transient solution of coupled aroelastic problems Part I: Model problem, theory and two-dimensional application. *Computer Methods in Applied Mechanics and Engineering*, 124(1):79–112, 1995.

[124] W. Popko, F. Vorpahl, A. Zuga, M. Kohlmeier, J. Jonkman, A. Robertson, T. J. Larsen, A. Yde, K. Sætertrø, K. M. Okstad, et al. Offshore Code Comparison Collaboration Continuation (OC4), Phase I–Results of Coupled Simulations of an Offshore Wind Turbine with Jacket Support Structure. In *22nd International Society of Offshore and Polar Engineers Conference. Rhodes, Greece*, 2012.

[125] W. H. Press, B. P. Flannery, S. A. Teukolsky, and W. T. Vetterling. *Numerical Recipes in C: The Art of Scientific Computing*. Cambridge University Press, New York, NY, USA, 1988.

[126] T. J. Price. James Blyth - Britain's first modern wind power pioneer. *Wind Engineering*, 29:191–200, 2005.

[127] Z.-Q. Qu. *Model Order Reduction Techniques – With Applications in Finite Element Analysis*. Springer-Verlag, London, 2004.

[128] D. Quarton et al. An International Design Standard For Offshore Wind Turbines. *Garrad Hassan*, 13, 2005.

[129] J. W. S. Rayleigh. *The Theory of Sound*. Dover Publications, 1896.

[130] L. C. Reese, W. R. Cox, F. D. Koop, et al. Field Testing and Analysis of Laterally Loaded Piles om Stiff Clay. In *Offshore Technology Conference*. Offshore Technology Conference, 1975.

[131] R. W. Righter. *Wind Energy in America: A History*. University of Oklahoma Press, 1996.

[132] W. Ritz. Uber eine neue Methode zur Lösung gewisser Variations Probleme der Mathematishen Physik. *Journal für die Reine und Angewandte Mathematik*, 135:1–61, 1909.

[133] D. J. Rixen. Generalized Mode Acceleration Methods and Modal Truncation Augmentation. In *Structures, Structural Dynamics and Material Conference and Exhibit*, Seattle, WA, USA, April 2001. 42st AIAA/ASME/ASCE/AHS/ASC. AIAA, 2001-1300.

[134] D. J. Rixen. Extended preconditioners for the FETI method applied to constrained problems. *International Journal for Numerical Methods in Engineering*, 54:1–26, 2002.

[135] D. J. Rixen. High Order Static Correction Modes for Component Mode Synthesis. In *Fifth World Congress on Computational Mechanics*, Vienna, Austria, July 2002. http.//wccm.tuwien.ac.at, isbn 3-9501554-0-6.

[136] D. J. Rixen. A dual Craig-Bampton method for dynamic substructuring. *Journal of Computational and Applied Mathematics*, 168:383–391, 2004.

[137] D. J. Rixen. Dual Craig-Bampton with enrichment to avoid spurious modes. In *Proceedings of the Twenty Seventh International Modal Analysis Conference, Orlando, FL*, 2009.

[138] D. J. Rixen. A Substructuring Technique Based on Measured and Computed Impulse Response Functions of Components. In *Proceedings of the International Conference on Noise and Vibration Engineering (ISMA 2010), Leuven, Belgium, 20-22 September 2010*, 2010.

[139] D. J. Rixen. Substructuring using Impulse Response Functions for Impact Analysis. In *Proceedings of the IMAC - XXVIII, Jacksonville, Florida USA*, 2010.

[140] D. J. Rixen and N. Haghighat. Truncating the Impulse Responses of Substructures to Speed Up the Impulse-Based Substructuring. In *Proceedings of the SEM IMAC XXX Conference Jan. 30 - Feb. 2, 2012, Jacksonville, FL USA*, 2012.

[141] D. J. Rixen and P. L. C. van der Valk. An Impulse Based Substructuring approach for impact analysis and load case simulations. *Journal of Sound and Vibration* , 332(26):7174–7190, 2013.

[142] D. Roddier, C. Cermelli, A. Aubault, and A. Weinstein. WindFloat: A floating foundation for offshore wind turbines. *Journal of Renewable and Sustainable Energy*, 2(3):033104, 2010.

[143] R. Rubak and J. r. T. Petersen. Monopile as part of aeroelastic wind turbine simulation code. In *Proceedings of Copenhagen Offshore Wind*, 2005.

[144] S. Rubin. Improved Component-Mode Representation for Structural Dynamic Analysis. *AIAA Journal*, 13:995–1006, 1975.

[145] C. Runge. Ueber die numerische Auflösung von Differentialgleichungen. *Mathematische Annalen*, 46(2):167–178, 1895.

[146] A. J. C. B. Saint-Venant. Memoire sur la Torsion des Prismes. *Mem. Divers Savants*, 14:233–560, 1855.

[147] W. H. Schilders, H. A. Van der Vorst, and J. Rommes. *Model order reduction: theory, research aspects and applications*, volume 13. Springer, 2008.

[148] P. Schubel, R. Crossley, E. Boateng, and J. Hutchinson. Review of structural health and cure monitoring techniques for large wind turbine blades. *Renewable Energy*, 51(0):113 – 123, 2013.

[149] H. A. Schwarz. *Gesammelte Mathematische Abhandlungen*, volume 2, pages 133–143. J. Springer, Berlin, 1890. First published in Vierteljahrsschrift der Naturforschenden Gesellschaft in Zürich, volume 15, 1870, 272-286.

[150] B. Schweizer and D. Lu. Predictor/corrector co-simulation approaches for solver coupling with algebraic constraints. *ZAMM-Journal of Applied Mathematics and Mechanics/Zeitschrift für Angewandte Mathematik und Mechanik*, 2014.

[151] M. Seidel, F. Ostermann, A. Curvers, M. Kühn, D. Kaufer, and C. Böker. Validation of Offshore load simulations using measurement data from the DOWNVInD project. In *Proceedings of European Offshore Wind Conference 2009, Stockholm, Sweden*, 2009.

[152] M. Seidel, M. von Mutius, P. Rix, and D. Steudel. Integrated analysis of wind and wave loading for complex support structures of Offshore Wind Turbines. In *Conference Proceedings Offshore Wind 2005, Copenhagen*, 2005.

[153] W. Siemens. Ueber die Umwandlung von Arbeitskraft in elektrischen Strom ohne Anwendung permanenter Magnete. *Annalen der Physik*, 206(2):332–335, 1867.

[154] J. C. Simo, P. Wriggers, and R. L. Taylor. A Perturbed Lagrangian Formulation for the Finite Element Solution of Contact Problems. *Computer Methods in Applied Mechanics and Engineering*, 50(2):163–180, 1985.

[155] P. Sjövall. *Identification and Synthesis of Components for Vibration Transfer Path Analysis*. PhD thesis, Chalmers University of Technology, Göteborg, Sweden, October 2007.

[156] Sociaal-Economische Raad. Energy Agreement for Sustainable Growth. Technical report, SER, 2013.

[157] H. Stiesdal. Hywind: The world's first floating MW-scale wind turbine. *Wind Directions*, pages 52–53, December 2009.

[158] D. Tcherniak, S. Chauhan, and M. H. Hansen. Applicability limits of operational modal analysis to operational wind turbines. In *Proceedings of the IMAC-XXVIII, February 1-4, 2010, Jacksonville, Florida, USA*, 2010.

[159] The MathWorks. *Introducing MATLAB Engine*, 2014.

[160] P. Tiso and D. J. Rixen. Discrete Empirical interpolation method for finite element structural dynamics. *Nonlinear Dynamics: an international journal of nonlinear dynamics and chaos in engineering systems*, 35(1):203–212, 2013.

[161] D. D. van den Bosch. Impulse Based Substructuring Unravelled: Simulation and Coupling of Structural Dynamics in the time domain. Master's thesis, Delft University of Technology, 2014.

[162] T. van der Horst. Experimental dynamic substructuring using direct time-domain deconvolved impulse response functions. Master's thesis, Delft Univerisity of Technology, 2014.

[163] M. V. van der Seijs and D. J. Rixen. Efficient impulse based substructuring using truncated impulse response functions and mode superposition. In *International Conference on Noise and Vibration Engineering, ISMA, 17-19 September 2012, KU Leuven, Belgium*, 2012.

[164] M. V. van der Seijs, P. L. C. van der Valk, T. van der Horst, and D. J. Rixen. Towards Dynamic Substructuring Using Measured Impulse Response Functions. In M. Allen, R. Mayes, and D. Rixen, editors, *Dynamics of Coupled Structures, Volume 1*, Conference Proceedings of the Society for Experimental Mechanics Series, pages 73–82. Springer International Publishing, 2014.

[165] J. van der Tempel. *Design of Support Structures for Offshore Wind Turbines*. PhD thesis, Delft University of Technology, 2006.

[166] P. L. C. van der Valk. Model Reduction & Interface Modeling in Dynamic Substructuring; Application to a Multi-Megawatt Wind Turbine. Master's thesis, Delft University of Technology, 2010.

[167] P. L. C. van der Valk and M. G. L. Ogno. Identifying Structural Parameters of an Idling Offshore Wind Turbine Using Operational Modal Analysis. In F. N. Catbas, editor, *Dynamics of Civil Structures, Volume 4*, Conference Proceedings of the Society for Experimental Mechanics Series, pages 271–281. Springer International Publishing, 2014.

[168] P. L. C. van der Valk and D. J. Rixen. An Effective Method for Assembling Impulse Response Functions to Linear and Non-Linear Finite Element Models. In *Proceedings of the SEM IMAC XXX Conference Jan. 30 - Feb. 2, 2012, Jacksonville, FL USA*, 2012.

[169] P. L. C. van der Valk and D. J. Rixen. Impulse Based Substructuring for Coupling Offshore Structures and Wind Turbines in Aero-Elastic Simulations. In *Proceedings of 53rd AIAA/ASME/ASCE/AHS/ASC Structures, Structural Dynamics and Materials Conference, 23 - 26 April 2012, Honolulu, Hawaii*, 2012.

[170] P. L. C. van der Valk and D. J. Rixen. A Co-Simulation Method for Coupling Complex Foundation Models and Wind Turbine Models in Aero-Elastic Simulations. In Z. Dimitrovovťa, J. R. de Almeida, and R. Gonçalves, editors, *Proceedings of the 11th International Conference on Vibration Problems, Lisbon, Portugal, 9-12 September 2013*, 2013.

[171] P. L. C. van der Valk and D. J. Rixen. Substituting Internal Forces for Blocked Forces or Free Interface Displacements in Substructured Simulations. In *Topics in Experimental Dynamic Substructuring, Volume 2: Proceedings of the 31st IMAC, A Conference on Structural Dynamics, 2013*, 2013.

[172] P. L. C. van der Valk and D. J. Rixen. An Impulse Based Substructuring Method for Coupling Impulse Response Functions and Finite Element Models. *Computer Methods in Applied Mechanics and Engineering*, 275:113–137, 2014.

[173] P. L. C. van der Valk and D. J. Rixen. Towards a Parallel Time Integration Method for Nonlinear Systems. In *Dynamics of Coupled Structures, Volume 1: Proceedings of the 32nd IMAC, A Conference and Exposition on Structural Dynamics, 2014*, 2014.

[174] P. L. C. van der Valk and S. N. Voormeeren. An overview of modeling approaches for complex offshore wind turbine support structures. In *Proceedings of ISMA2012-USD2012*, 2012.

[175] P. L. C. van der Valk, S. N. Voormeeren, P. C. de Valk, and D. J. Rixen. Dynamic Models for Load Calculation Procedures of Offshore Wind Turbine Support Structures: Overview, Assessment and Outlook. *Journal of Computational and Nonlinear Dynamics*, Accepted for publication:1–24, 2014.

[176] P. L. C. van der Valk, J. B. Wuijckhuijse, and D. Klerk. A Benchmark Test Structure for Experimental Dynamic Substructuring. In T. Proulx, editor, *Structural Dynamics, Volume 3*, Conference Proceedings of the Society for Experimental Mechanics Series, pages 1113–1122. Springer New York, 2011.

[177] G. van Schothorst, M. A. Boogaard, G. W. van der Poel, and D. J. Rixen. Analysis of ground vibration transmission in high precision equipment by Frequency Based Substructuring. In *Proceedings of ISMA, Leuven, Belgium*, 2012.

[178] M. Verhaegen and V. Verdult. *Filtering and system identification: a least squares approach*. Cambridge University Press, 2007.

[179] M. Verhaegen, V. Verdult, and N. Bergboer. *Filtering and System Identification: An Introduction to using Matlab Software*. Delft University of Technology, 2007.

[180] W. G. Versteijlen, A. Metrikine, J. S. Hoving, E. H. Smidt, and W. D. Vries. Estimation of the vibration decrement of an offshore wind turbine support structure caused by its interaction with soil. In *Proceedings of the EWEA Offshore 2011 Conference, Amsterdam, The Netherlands*, 2011.

[181] S. N. Voormeeren. *Dynamic Substructuring Methodologies for Integrated Dynamic Analysis of Wind Turbines*. PhD thesis, Delft University of Technology, Delft, the Netherlands, October 2012.

[182] S. N. Voormeeren, B. P. Nortier, and D. J. Rixen. Error Estimation and Adaptive Model Reduction Applied to Offshore Wind Turbine Modeling. In *IMAC-XXXI: International Modal Analysis Conference, February 11-14, 2013, Garden Grove, CA*, number 354, 2013.

[183] S. N. Voormeeren, P. L. C. van der Valk, B. P. Nortier, D.-P. Molenaar, and D. J. Rixen. Accurate and Efficient Modeling of Complex Offshore Wind Turbine Support Structures using Augmented Superelements. *Wind Energy*, 17:1035–1054, 2014.

[184] S. N. Voormeeren, P. L. C. van der Valk, and D. J. Rixen. A General Mixed Boundary Model Reduction Method for Component Mode Synthesis. In *Proceedings of the WCCM/APCOM 2010*, 2010.

[185] S. N. Voormeeren, P. L. C. van der Valk, and D. J. Rixen. A Truly Hybrid Approach to Substructuring Problems Using Mixed Assembly and Implicit Solving Strategies. In T. Proulx, editor, *Linking Models and Experiments, Volume 2*, Conference Proceedings of the Society for Experimental Mechanics Series, pages 329–347. Springer New York, 2011.

[186] S. N. Voormeeren, P. L. C. van der Valk, and D. J. Rixen. Generalized Methodology for Assembly and Reduction of Component Models for Dynamic Substructuring. *AIAA Journal*, 49(5):1010–1020, May 2011.

[187] S. N. Voormeeren, P. L. C. van der Valk, and D. J. Rixen. Practical aspects of dynamic substructuring in wind turbine engineering. In *Structural Dynamics and Renewable Energy, Volume 1*, pages 163–185. Springer, 2011.

[188] F. Vorpahl, W. Popko, and D. Kaufer. Description of a basic model of the "UpWind reference jacket" for code comparison in the OC4 project under IEA Wind Annex XXX. Technical report, Fraunhofer Institute for Wind Energy and Energy System Technology (IWES), 2011.

[189] F. Vorpahl and A. Reuter. Fully-coupled wind turbine simulation including substructuring of support structure components: Influence of newly developed modeling approach on fatigue loads for an offshore wind turbine on a tripod support structure. In *Proceedings of the Twenty-first International Offshore and Polar Engineering Conference. Maui, HI: International Society of Offshore and Polar Engineers*, pages 284–290, 2011.

[190] F. Vorpahl, M. Strobel, J. M. Jonkman, T. J. Larsen, P. Passon, and J. Nichols. Verification of aero-elastic offshore wind turbine design codes under IEA Wind Task XXIII. *Wind Energy*, 17:519–547, 2013.

[191] T. M. Wasfy and A. K. Noor. Computational strategies for flexible multibody systems. *Applied Mechanics Reviews*, 56(6):553–614, 2003.

[192] F. Wenneker and P. Tiso. Nonlinear component mode synthesis using modal derivatives. In *Proceedings of the 11th Intenational conference RASD 2013*, 2013.

[193] F. Wenneker and P. Tiso. A substructuring method for geometrically nonlinear structures. In *Dynamics of Coupled Structures, Volume 1*, pages 157–165. Springer, 2014.

[194] D. Williams. Dynamic loads in aeroplanes under given impulsive loads with particular reference to landing and gust loads on a large flying boat. Technical Report 3309 and 3316, Royal Aircraft Establishment, SME, U.K., 1945.

[195] C. Willow and B. Valphy. Offshore wind, forecasts of future costs and benefits. Technical report, BVG Associates, 2011.

[196] E. L. Wilson. A Computer Program for the Dynamic Stress Analysis of Underground Structures. SESM Report 68-1, Division of Structural Engineering and Structural Mechanics, University of California, Berkeley, CA, 1968.

[197] R. Wiser, M. Bolinger, and et al. 2012 Wind Technologies Market Report. Technical report, Department of Energy, 2013.

[198] J. Wolf. *Soil-structure-interaction analysis in time domain.* Prentice-Hall international series in civil engineering and engineering mechanics. Prentice Hall, 1988.

[199] W. L. Wood, M. Bossak, and O. C. Zienkiewicz. An Alpha Modification of Newmark's Method. *International Journal for Numerical Methods in Engineering*, 15:1562–1566, 1981.

[200] S. Yang and M. S. Allen. Output-only Modal Analysis using Continuous-Scan Laser Doppler Vibrometry and application to a 20kW wind turbine. *Mechanical Systems and Signal Processing*, 31(0):228 – 245, 2012.

[201] L. Zhang, R. Brincker, and P. Andersen. An overview of operational modal analysis: major development and issues. In *Proceedings of the 1st IOMAC Conference, Copenhagen, Denmark*, 2005.

Part IV

Appendices

A

Coupling BHawC and MatLab Simulations: A Verification Study

A.1 Introduction

The monolithic sequential multi-domain time integration scheme, presented in section 4.2, is employed to couple the time integrations of BHawC and foundations modeled and simulated in MatLab. In order to verify both the multi-domain time integration scheme and the implementation in the software, a verification study has been performed. In this appendix, the test case for the verification and its results are presented.

A.2 Verification test case: Model and load case

In the current verification study, the model of a SWT-3.6-120 wind turbine with a 87.5 meter tower is installed on the simplest possible foundation model; a single Euler beam element with a length of 20 m, a diameter of 6 m and a wall thickness of 50mm. Two identical models are created, as is shown in figure A.1. The first model, given in figure A.1a, is fully modeled and simulated in BHawC and serves as the reference model. For the second model, given in figure A.1b, the wind turbine part is time integrated in BHawC, the foundation element is modeled and integrated in Matlab and both time integrations are coupled through the Matlab COM Engine [159], using the monolithic sequential multi-domain time integration scheme presented in section 4.2.

A single time simulation is performed without any aerodynamics. In this test case, an imperfect impulse is applied at $t = 30s$, with an impact time of approximately $0.9s$ in the direction parallel to the main shaft, at the interface to excite the coupled structure. The simulation is started from a quasi-static equilibrium, as explained in section 4.3, followed by a 10 second dynamic initialization, which is performed to damp out any transients due to the initialization. Note that, due to the fact that the rotor-brake is not applied in the simulations, the rotor slowly rotates under the influence of gravity, thereby given already a small response of the turbine before the impulse is applied. After initialization, the simulations are performed for 150 seconds real time, with a step size of 0.02 seconds and the high frequency spectral radius $\rho_\infty = 0.85$.

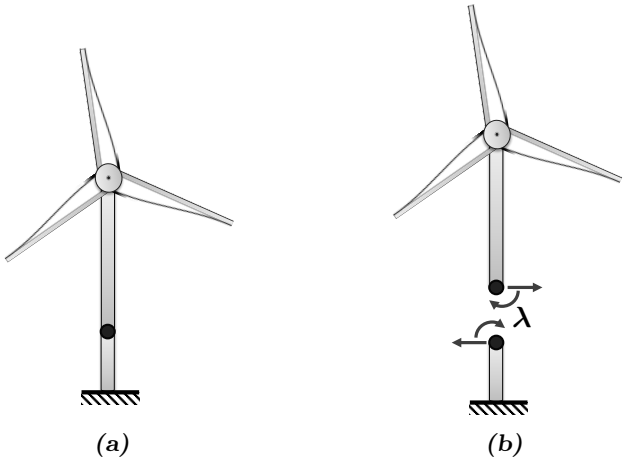

Figure A.1: *Models used in the verification study;* ***(a)*** *Full model of the wind turbine is modeled in BHawC.* ***(b)*** *"Foundation" beam element is modeled and simulated in MatLab, whereas the rest of the wind turbine is simulated in BHawC.*

A.3 Results of the verification study

In order to compare the results from both models, the relative differences of the translations between the reference ($\boldsymbol{u}_n^{ref}$) and test solutions ($\boldsymbol{u}_n^{test}$), computed according to:

$$\epsilon_n = \frac{|\boldsymbol{u}_n^{ref} - \boldsymbol{u}_n^{test}|}{|\boldsymbol{u}_n^{ref}|},$$

obtained at the interface and tower top node have been computed.

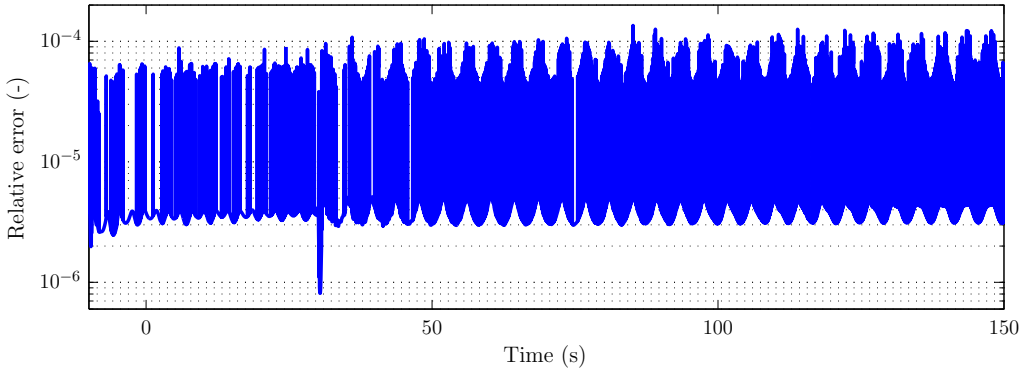

Figure A.2: *Relative difference (ϵ) between the reference and test solutions at the interface.*

In figure A.2 the relative difference at the interface node is shown and in figure A.3 the relative difference at the tower top node can be seen. It can be seen that accurate results are obtained using the coupled BHawC-MatLab simulations, where only a small difference between the models is seen. However, as this is dictated by the numerical tolerance settings for the Newton-Raphson process, the differences can be considered as negligible. Similar results are obtained for all the other nodes, although these are not shown here.

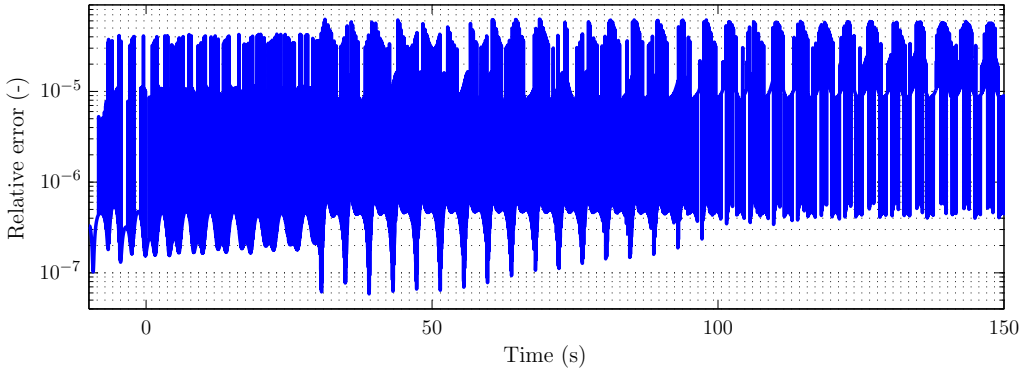

Figure A.3: *Relative difference (ϵ) between the reference and test solutions at the tower top node.*

A.4 Summary

A simple test case has been devised in order to verify the monolithic sequential multi-domain time integration method, as well as its implementation to couple time simulations in BHawC and MatLab. The study uses two identical models, that are solved in different ways. Firstly, a reference model is created and simulated in BHawC only. In the second model, the simulations are split between the foundation and the wind turbine. The foundation is simulated in MatLab and the wind turbine is simulated in BHawC and both simulations are coupled at the interface using the proposed method.

Numerically exact results are found from the test case, thereby verifying the proposed method and its implementation in BHawC and MatLab.

B

Demonstrating the Monolithic Parallel Multi-Domain Time Integration Technique

B.1 Introduction to the simple academic case

In order to demonstrate the monolithic parallel multi-domain time integration technique, proposed in section 4.4, a simple test problem has been created.[1] All the test cases are based on the same model (figure B.1), where the generic topology for the system is given. Subsystem A is

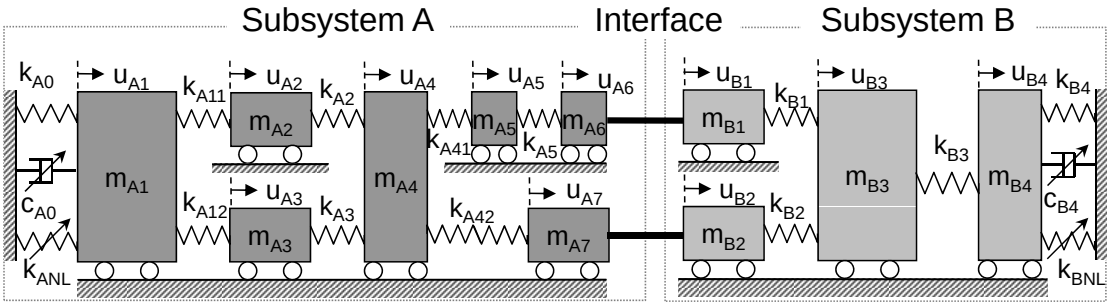

Figure B.1: *Simple academic system used for case study.*

a 7 DoFs mass-spring system and subsystem B is a 4 DoFs system that is also is modeled using spring and mass elements. In both models damping is modeled using Rayleigh damping. The total system consists of 9 DoFs, as u_{A6} is rigidly connected to u_{B1} and u_{A7} is rigidly connected to u_{B2}. A number of nonlinear elements are added to both subsystems; a nonlinear spring (with spring constant k_{A0}) and damper (with damping constant c_{A0}) in subsystem A and a nonlinear spring and damper in subsystem B (with spring constant k_{B42} and damping constant c_{B4}). As all nonlinearities are taken as being cubic, the nonlinear forces working on the systems are obtained from:

$$\begin{aligned} f_{nl}^{(A)} &= k_{A0}u_{A1}^3 + c_{A0}\dot{u}_{A1}^3 \\ f_{nl}^{(B)} &= k_{B42}u_{B4}^3 + c_{B4}\dot{u}_{B4}^3. \end{aligned} \tag{B.1}$$

In order to demonstrate the method, the system is excited by a random force on m_{B3} from $t = 0$ onwards and a second random force is applied at m_{A1} from $t = 2s$ onwards. The responses

[1] Note that this appendix is based on work presented in [173].

obtained using the monolithic parallel multi-domain time integration technique introduced in section 4.4 are compared to a reference solution, which is obtained by performing a Newmark time integration on the total (primal assembled) system.

B.2 Results from starting the simulation from an initial static equilibrium

For the first test case, it is chosen to demonstrate the method if one chooses to start the simulations from a quasi-static equilibrium, as is outlined in section 4.5.2. The model parameters are given in table B.1. It can be seen that, due to the fact that $k_{BNL} = k_{B4} = 0$, substructure B has a rigid body mode. This will lead to a singular stiffness matrix and one needs to apply some extra steps, as is outlined in section 4.5.2, in order to solve the initial static problem.

System parameters of the model in figure B.1				
	Subsystem A		Subsystem B	
	Mass [kg]	Stiffness [N/m]	Mass [kg]	Stiffness [N/m]
general	$m_{A1} = 10$ $m_{A2} = 3$ $m_{A3} = 3$ $m_{A4} = 6$ $m_{A5} = 2$ $m_{A6} = 2$ $m_{A7} = 4$	$k_{A0} = 1 \cdot 10^3$ $k_{A11} = 2 \cdot 10^3$ $k_{A12} = 2 \cdot 10^3$ $k_{A2} = 1 \cdot 10^3$ $k_{A3} = 1 \cdot 10^3$ $k_{A41} = 0.5 \cdot 10^3$ $k_{A42} = 1 \cdot 10^3$ $k_{A5} = 1 \cdot 10^3$	$m_{B1} = 4$ $m_{B2} = 7$ $m_{A3} = 8$ $m_{B4} = 5$	$k_{B1} = 1 \cdot 10^3$ $k_{B2} = 1 \cdot 10^3$ $k_{B3} = 2 \cdot 10^3$ $k_{B4} = 0$
non-linear parts		$k_{ANL} = 3 \cdot 10^7$ $c_{A0} = 1 \cdot 10^7$	$k_{BNL} = 0$ $c_{B4} = 5 \cdot 10^7$	

Table B.1: *Parameters of mass-spring system used in the section.*

The time integration is performed with the parameters that constitute the constant average acceleration Newmark method ($\beta = \frac{1}{4}, \gamma = \frac{1}{2}$) and a time step of $h = 0.005$ s. The simulation results, in terms of displacements, are given in figures B.2 and B.3. These response are obtained with the same global tolerance settings (GloTol) in both simulations (10^{-8}), the local tolerance (LoTol) for the decomposed time integration has been set to (10^{-4}) in this example. The tolerances are used such that the norm of the residual has to be smaller than the tolerance multiplied by a force norm,

$$|\boldsymbol{r}_n| < tol \times |\boldsymbol{p}_n + \boldsymbol{B}^T \boldsymbol{\lambda}_n - \boldsymbol{f}_n|, \tag{B.2}$$

where *tol* denotes the tolerance setting.

Visually, no difference between the responses can be seen, but in order to show that the responses of both simulations are exactly identical, a global error measure has been determined,

$$\epsilon_n = \frac{|\boldsymbol{u}_n^{(ref)} - \boldsymbol{u}_n^{(sub)}|}{|\boldsymbol{u}_n^{(ref)}|}, \tag{B.3}$$

which is shown in figure B.4. Here, one can clearly see that the decomposed time integration yields the exact same response. An overview of the computational effort, in terms of total numbers of iterations, is given in table B.2. Note that that the nonlinear damper is the only source of the nonlinearity in substructure B, the initial static problem is a linear problem. This

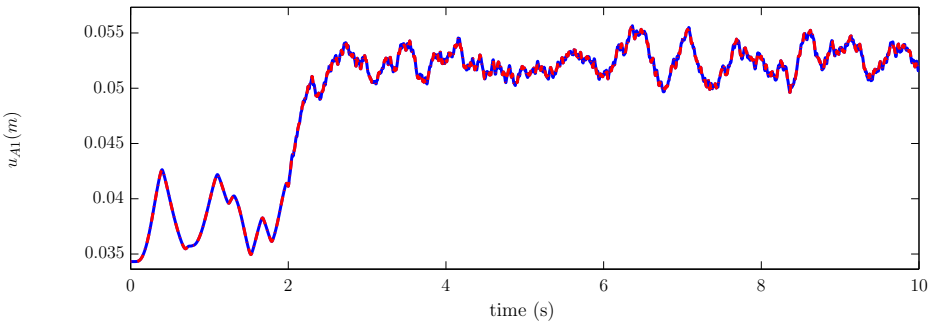

Figure B.2: *Response of mass m_{A1}; showing the reference solution (—); and the one obtained with the monolithic parallel time integration approach (- -).*

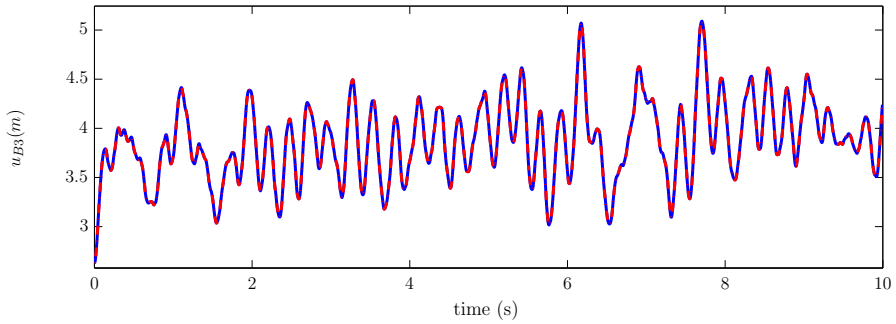

Figure B.3: *Response of mass m_{B3}; showing the reference solution (—); and the one obtained with the monolithic parallel time integration approach (- -).*

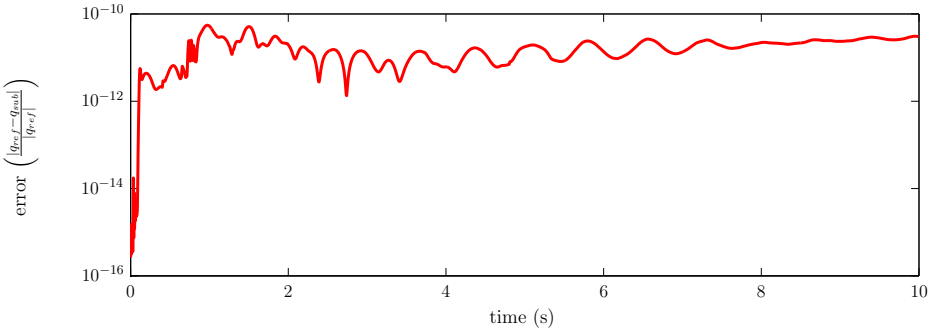

Figure B.4: *Global error of the decomposed time integration, as given in Eq.* (B.3).

Total # of iterations				
	Reference	Subsystem A	Subsystem B	Global
1st time step	16	16	1	1
Other time steps	12558	12865	4052	4044

Table B.2: *Total number of iterations.*

is also observed from the results in table B.2, as it only requires one iteration to solve. Hence, almost all of the computational effort is in solving the static equilibrium for substructure A, which requires the same amount of iterations as the reference problem. A similar result holds for the iterations required to solve the other steps: The "grunt" of the nonlinearities is in substructure A and hence, this substructure requires the most iterations.

From the results it can clearly be concluded that having inadequately constrained substructures

in the analysis poses no problems for the proposed parallel monolithic time integration approach.

B.3 Results from starting the simulation using initial accelerations

The simulations can also be initialized using initial accelerations at t_0, as is shown in section 4.5.1. The results are again obtained with the same time integration settings as were used in section B.2. The parameters of the model are different however and are given in table B.3. Again, the responses of the force loaded DoFs are shown in figures B.5 and B.6 and the relative

System parameters of the model in figure B.1				
	Subsystem A		Subsystem B	
	Mass [kg]	Stiffness [N/m]	Mass [kg]	Stiffness [N/m]
general	$m_{A1} = 10$ $m_{A2} = 3$ $m_{A3} = 3$ $m_{A4} = 6$ $m_{A5} = 2$ $m_{A6} = 2$ $m_{A7} = 4$	$k_{A0} = 0$ $k_{A11} = 2 \cdot 10^3$ $k_{A12} = 2 \cdot 10^3$ $k_{A2} = 1 \cdot 10^3$ $k_{A3} = 1 \cdot 10^3$ $k_{A41} = 0.5 \cdot 10^3$ $k_{A42} = 1 \cdot 10^3$ $k_{A5} = 1 \cdot 10^3$	$m_{B1} = 4$ $m_{B2} = 7$ $m_{A3} = 8$ $m_{B4} = 5$	$k_{B1} = 1 \cdot 10^3$ $k_{B2} = 1 \cdot 10^3$ $k_{B3} = 2 \cdot 10^3$ $k_{B4} = 2 \cdot 10^2$
non-linear parts		$k_{ANL} = 2 \cdot 10^7$ $c_{A0} = 1 \cdot 10^7$	$k_{BNL} = 1 \cdot 10^7$ $c_{B4} = 5 \cdot 10^7$	

Table B.3: *Parameters of mass-spring system used in this section.*

error is shown in figure B.7.

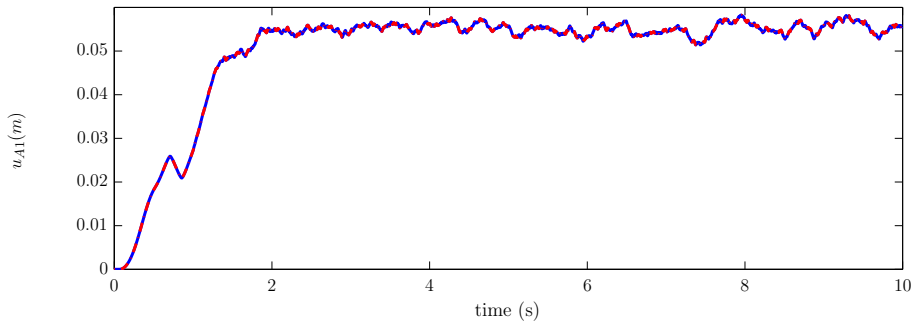

Figure B.5: *Response of mass m_{A1}; showing the reference solution (—); and the one obtained with the monolithic parallel time integration approach (- -).*

From the figures it is clear that the proposed approach leads to the exact same response as the reference structure. Thereby verifying that the parallel monolithic multi-domain time integration approach can also be initiated with initial accelerations.

B.4 Small study on the computational aspects

Two aspects of the procedure are independently investigated in some more detail. Firstly, a brief study to the effect of setting the local and global tolerances is given in section B.4.1.

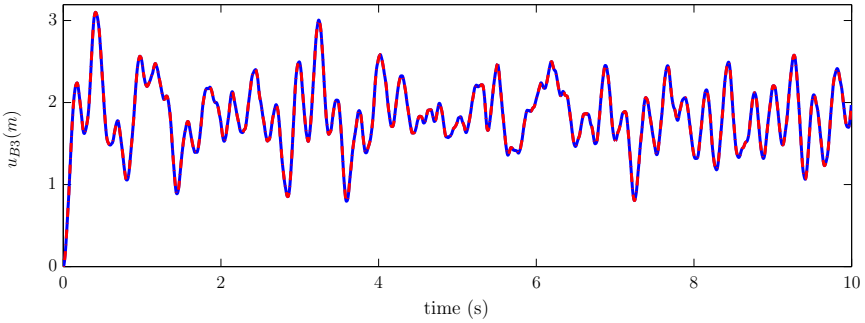

Figure B.6: *Response of mass m_{B3}; showing the reference solution (—); and the one obtained with the monolithic parallel time integration approach (- —).*

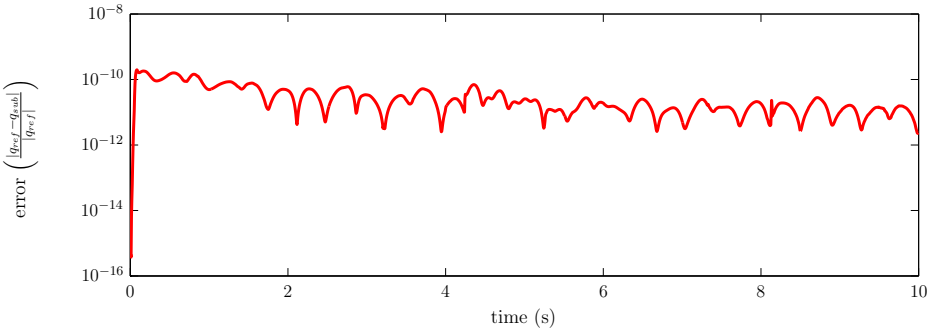

Figure B.7: *Global error of the decomposed time integration, as given in Eq.* (B.3).

Secondly, the effect of the level of nonlinearity in the subsystems onto the number of iterations required is investigated in section B.4.2.

B.4.1 Effect of setting the local and global tolerances

In order to show the effect of the global and local tolerance settings on the number of iterations and computational time, we've defined a ratio between the two,

$$ratio = \frac{LoTol}{GloTol}. \tag{B.4}$$

By fixing the global tolerance to (10^{-8}) and varying the ratio given in Eq. (B.4) between 1 and 10^{10}, one could get an idea of the optimal ratio between the local and global tolerances. The result of this analysis is shown in figure B.8. Note that one cannot draw any conclusions for the general case about this, as this setting could very well be problem dependent as well. Nonetheless, some interesting effects are shown here.

Firstly, for low ratios the problem is dominated by the local iterations, as a too small ratio will require more local iterations then strictly required. Also note that the number of global iterations are at its minimum here. One can also clearly identify the subsystem with the strongest nonlinearities, as subsystem A requires about 3 times the number of iterations that subsystem B requires. By increasing the ratio between the tolerances, the number of local iterations decrease for both substructures, while keeping the global iterations at a constant level. At a certain moment, the iterations of subsystem B and the global iterations start to "couple", meaning that subsystem B only requires (approximately) one iteration per global iteration. In addition to this, it appears that Subsystem A also starts to converge towards

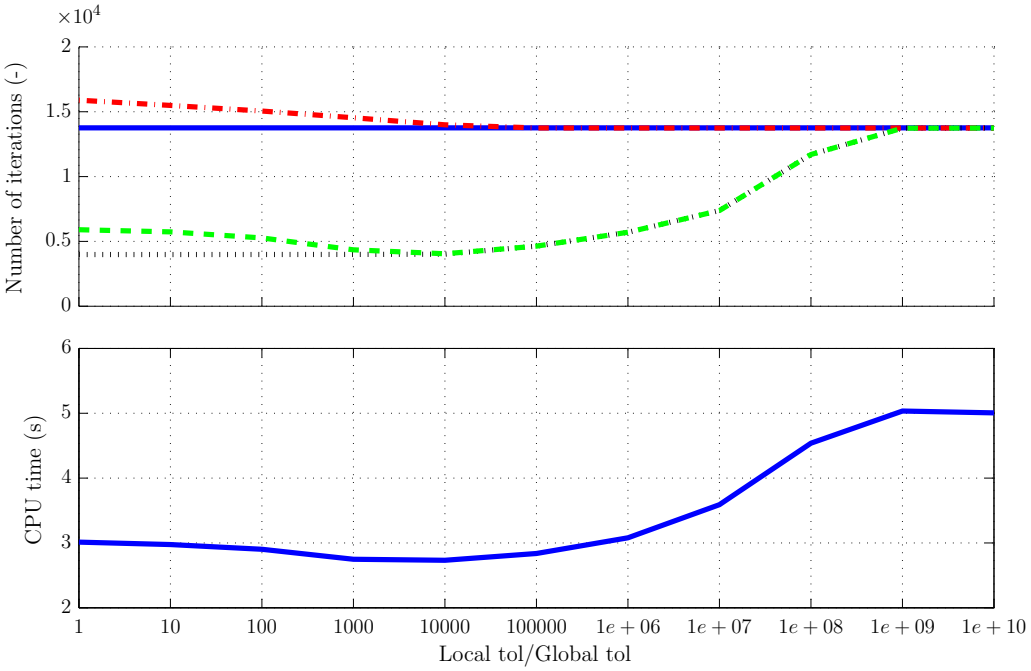

Figure B.8: *Number of iterations (upper graph) and computational time (lower graph) as a function of the ratio between the local and global tolerances. In the upper graph, the different lines denote the different iterations; reference solution iterations (——); Subsystem A iterations (-·—); Subsystem B iterations (– –); Global iterations (····).*

its "iteration asymptote". As can be seen from the lower graph, this point also denotes the minimum in terms of CPU time.

By further increasing the ratio, the number of global iterations (and hence of subsystem B) start to increase, without any substantial decrease in the number of iterations for subsystem A, thereby also increasing the CPU time required. Finally, at extremely large ratios the method will degrade into a standard FETI method and will require the same amount of iterations for subsystem A, B and the global interface problem, which are also equal to the number of iterations required for the reference solution.

B.4.2 Effect of the level of nonlinearity in the subsystems

The last effect that is briefly investigated is the impact of the nonlinearities on the performance of the method. In subsystem B, there is only a relatively mild cubic spring that links m_{B4} to the fixed wall. In this section it will be investigated what the effects on the amount of iterations are if we would increase the nonlinearity currently present in subsystem B ($k_{B42} = 1 \cdot 10^7$, $c_{B4} = 5 \cdot 10^7$), or if one would remove the nonlinearity from subsystem B ($k_{B42} = 0$, $c_{B4} = 0$). For this analysis it was chosen to use the "optimal" ratio between the local and global tolerances the was found from figure B.8, therefore GloTol is taken as 10^{-8} and LoTol is set to 10^{-4}. The results of the investigation are shown in figure B.9, here the colors of the bars indicate the different models as is indicated in the caption. The bars denoted by *Ref* are the number of iterations performed for the reference solution, the bars denoted *A* and *B* denote the number of iterations on the local level and the bar denoted *Global* is the associated number of global iterations performed. Firstly it can be seen that a higher level of nonlinearity in the system leads to more iterations in general. What is important to notice here is that the number

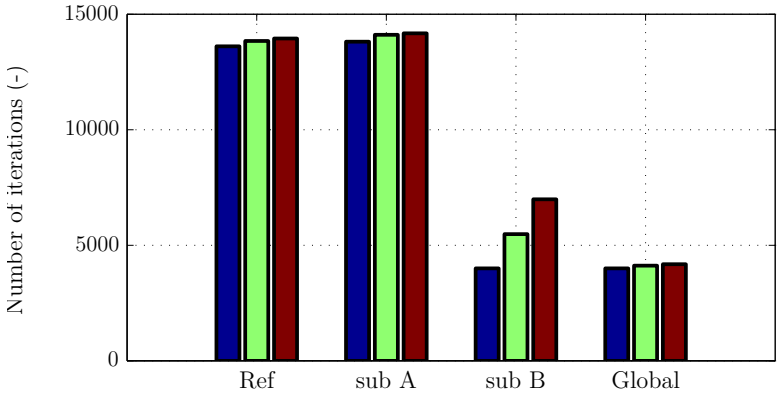

Figure B.9: *Number of iterations required for different levels of nonlinearity in subsystem B; Subsystem B linear (■); Subsystem B mildly nonlinear (■); Subsystem B strongly nonlinear (■).*

of iterations for substructure A and the global problem only slightly increase, whereas the iterations for substructure B significantly increase. This was already expected in section 4.4, where we stated that the decomposed method puts its computational effort there where it is needed. By increasing the nonlinearities in subsystem B, the iterations for this substructure will be mostly affected, whereas the change in the number of iterations for the other substructures and on the global level is only slightly affected. Also, what should be noted here is that in the limit case of a linear substructure B, the number of local iterations on B are equal to the number of global iterations, as was also expected.

B.5 Summary

In this appendix a simple demonstration of the parallel monolithic multi-domain time integration approach was performed in which several aspects of the method were investigated and from which the following can be summarized.

- The method yields the same accuracy as the associated standard Newmark time integration approach.
- The ratio between the global and the local tolerance settings determine for a large part the efficiency of the method.
- The number of local and global iterations are, for this example, at the lower range of this ratio ($1 \leq ratio \leq 10000$) inversely related to each other; A minimum of global iteration, results in a maximum of local iterations.
- By splitting the local and global (interface) level of the total structure, one is able to put the grunt of the computations there were it is needed, while reducing this work for the other substructures with milder nonlinearities.

Finally it should be noted that the method is highly suited to be efficiently implemented in a parallel computing environment.

C

Identifying structural parameters of an idling Offshore Wind Turbine using Operational Modal Analysis

The following appendix has been published as:

P. L. C. van der Valk and M. G. L. Ogno. Identifying Structural Parameters of an Idling Offshore Wind Turbine Using Operational Modal Analysis. In F. N. Catbas, editor, *Dynamics of Civil Structures, Volume 4*, Conference Proceedings of the Society for Experimental Mechanics Series, pages 271–281. Springer International Publishing, 2014[1]

Abstract

The design of modern day offshore wind turbines (OWTs) relies on numerical models, which are used for simulating the dynamic behavior in different operational and environmental conditions. From these results one can estimate ultimate and fatigue loads, which are needed for determining the design life of the turbines. The dynamic behavior, and thus the lifetime, of the turbines are influenced for a large part by its structural properties, such as the natural frequencies and damping ratios. Hence, it is important to obtain accurate estimates of these modal properties. For this purpose Operational Modal Analysis (OMA) techniques are used to estimate the modal domain of the OWT. As, for instance, the loads in the structure and the damping ratios are inversely related, higher damping values will results in lower loads, and hence in more optimized and less costly support structures. In this paper the data-driven Stochastic Subspace Identification (SSI) method is used to evaluate the modal domain of the OWT by using output-only measurements obtained from an installed 3.6 Megawatt offshore wind turbine. In order to better satisfy the OMA assumptions of having a Linear Time-Invariant (LTI) system and white noise uncorrelated input, the analyses are performed in case of idling turbines, thereby avoiding the effect of rotational harmonic components, changing system properties due to yawing and pitching actions, as well as strong aerodynamic nonlinearities. In this paper we focuss on the first four global eigenfrequencies that were found and the associated damping ratios. Even though

a sensor mix of several strain gauges and a single bi-directional accelerometer are available, the best results were obtained by only using the accelerometer on the nacelle.

C.1 Introduction

In order to achieve the goal of 20% renewable energy in 2020, as set by the European Union, large scale developments of different types of renewable energy are in full progress throughout Europe. One of the more promising ways of generating renewable electricity on a large scale is provided by wind energy. However, as many of the favorable onshore locations are usually also densely populated and therefore not suited for large wind farms, much of these farms will have to be built offshore. Unfortunately this technology is still more expensive than the conventional power generation methods, therefore continuous design optimization and technical innovations are required to lower the Levelised Cost of Electricity (LCOE).

Currently the design of modern wind turbines relies on aero-servo-elastic simulation tools that are used for simulating the dynamic behavior of the OWT in different operational and environmental conditions. In these models the structure is typically modeled as a flexible (nonlinear) multi-body model, that is coupled with a steady-state aerodynamic model and a controller model. The design of the support structure of a wind turbine can be frequency driven, fatigue load or ultimate load driven, depending on the windfarm location. However, as loads generated by the waves, which are mainly low frequent, are able to significantly excite the firsts global resonances modes, most of the support structure designs are fatigue driven. As it is known that the amplitude and the persistency of the vibrations are inversely related to modal damping ratios, these structural parameters play an essential role in lifetime prediction for an offshore wind turbine.

The global damping ratio for an OWT is a summation of aerodynamic damping, due to the rotor interaction with the air, hydrodynamic damping, resulting from a combination of radiation damping and flow separation, soil damping, caused by inner soil friction and radiation, the damping of the steel structure itself, the damping coming for the many joints in the assembled structure and its components and potential extra damping contributions from passive dampers installed in the turbine. As many of these damping contributions are dependent on the environmental conditions in which the turbine is operating and on the operational mode itself, these damping values need to be determined in situ. By comparing these with the damping values used in the associated load simulations for design, one can verify wether these are under- (or over-) estimated.

Obtaining these structural parameters from measurements is quite a challenge, as exciting large and environmentally loaded structures, such as wind turbines, with measurable input forces is an almost impossible endeavor. Hence, already over twenty years ago, the first modal identifications based on output-only measurements were performed on wind turbines [87]. These operational modal analysis methods, and also the wind turbines they are applied on, have developed ever since and more experience is gained at each step [115]. In the last couple of years, an interest has been developed into obtaining estimates for the structural parameters of offshore wind turbines using large sets of measurement data obtained from actual installed OWTs [30, 39, 180].

In this paper, which is based on findings from [113], Stochastic Subspace Identification is used to estimate the modal damping ratios and resonance frequencies of an installed, idling, offshore wind turbine. The paper is organized such that in section C.2 a brief introduction of the SSI method used is given. Section C.3 introduces the turbine from which the measurements where taken, also the obtained data itself will be discussed. After which, in section C.4, the normalized

frequencies and the modal damping ratios obtained using the modal identification are presented. Finally, in section C.5, some conclusions and recommendations are given.

C.2 Operational Modal Analysis and the Stochastic Subspace Identification method

Contrary to the classical Experimental Modal Analysis (EMA) techniques, where the modal parameters are estimated from the transfer of a measured input to a measured output, Operational Modal Analysis methods are able to identify the modal model using output-only measurements. In general, when the modal properties have to be identified from large structures in operation, the possibilities to control and measure the input excitations are limited or even impossible. This is common for big structures such as buildings, bridges and wind turbines.

An overview of the different techniques available for OMA can be found in [201]. Generally they can be divided in frequency domain (FD) methods and time domain (TD) methods. In this research the data-driven Stochastic Subspace Identification, which operates in the time domain, is used. In section C.2.1 the output-only variant of the SSI Past Outputs Multivariable Output-Error StatesPace (PO-MOESP) method is briefly presented. Afterwards, in section C.2.2, some of the challenges encountered when applying OMA methods for identifying the structural parameters of an OWT are discussed.

C.2.1 Stochastic subspace identification

The SSI method is an evolution of the basic Subspace Identification (SI) developed in system and control engineering, which offers numerically reliable and effective state-space model for complex dynamic system directly from measured data. In particular, since the identification has to be performed in presence of measurement and system noise, the so called SSI Past Outputs Multivariable Output-Error StatesPace (PO-MOESP) method is employed. In this section it is only shown how the method is applied in case of output-only measurements, for a detailed introduction the reader is referred to [178].

For OMA purposes it is assumed that no deterministic inputs $\mathbf{u}(k)$ are acting on the system and that the structure is, instead, excited by system noise $\mathbf{w}(k)$. Consequently the discrete-time state-space representation of a linear-time-invariant (LTI) system can be expressed in the following form:

$$\begin{aligned} \mathbf{x}(k+1) &= \mathbf{A}\mathbf{x}(k) + \mathbf{w}(k) \\ \mathbf{y}(k) &= \mathbf{C}\mathbf{x}(k) + \mathbf{v}(k) \end{aligned} \tag{C.1}$$

where the $\mathbf{u}(k) \in \mathbb{R}^m$ and $\mathbf{y}(k) \in \mathbb{R}^\ell$, are the input and output vectors at discrete time instant k, of respectively m inputs and ℓ outputs of the process. The vector $\mathbf{x}(k) \in \mathbb{R}^n$ is the state vector, where n denotes the order of the system. The measurement noise $\mathbf{v}(k)$ is acting directly on the outputs $\mathbf{y}(k)$, without directly affecting the states of the system. The system noise $\mathbf{w}(k)$ instead has a direct effect on the states $\mathbf{x}(k+1)$. It is assumed that the process noise $\mathbf{w}(k)$ and the measurement noise $\mathbf{v}(k)$ is zero-mean Gaussian white-noise sequences. The matrix $\mathbf{A} \in \mathbb{R}^{n \times n}$ is called the (dynamic) system matrix. It describes the dynamics of the system, from which the eigenvalues, modal frequencies and modal damping ratios can be estimated. $\mathbf{C} \in \mathbb{R}^{\ell \times n}$ is the output matrix, which describes how the internal state is transferred to the outside world in the observations $\mathbf{y}(k)$, thus enabling the evaluation of the modeshapes. Therefore, by first

obtaining system matrices **A** and **C** matrices, the modal domain can be extracted as shown in details in [4].

This representation can be written in its innovation formulation:

$$\begin{aligned} \mathbf{x}(k+1) &= \mathbf{A}\mathbf{x}(k) + \mathbf{K}\mathbf{e}(k) \\ \mathbf{y}(k) &= \mathbf{C}\mathbf{x}(k) + \mathbf{e}(k). \end{aligned} \tag{C.2}$$

where $\mathbf{e}(k)$ is called the innovation and is a zero-mean Gaussian white-noise process and $\mathbf{K}$ is the Kalman gain. As a consequence, measurement and system noise are both modeled with $\mathbf{e}(k)$, which represents their mutual effects over the outputs. Using this innovation state-space representation, the input-output data equation can be written in a compact form with the help of the block Hankel matrices as:

$$Y_{i,s,N} = \mathcal{O}_s X_{i,N} + \mathcal{S}_s E_{i,s,N} \tag{C.3}$$

where $Y_{i,s,N}$ and $E_{i,s,N}$ are the block Hankel matrices constructed respectively from the sequences $\mathbf{y}(k)$ and $\mathbf{e}(k)$, and $\mathcal{S}_s$ is its weighting matrix between the noise sequences and the outputs. N indicates the number of discrete time samples recorded. $X_{i,N}$ contains the different sequences of the states for different time instants. And,

$$\mathcal{O}_s = \begin{bmatrix} \mathbf{C} \\ \mathbf{CA} \\ \vdots \\ \mathbf{CA}^{s-1} \end{bmatrix} \tag{C.4}$$

is called extended observability matrix, and since it contains the **A** and **C** matrices, it must be estimated in order to identify the modal domain of the system.

In this specific case, making use of the instrumental variable $Z_N = Y_{0,s,N}$ which satisfy the following properties:

$$\lim_{N\to\infty} \frac{1}{N} E_{i,s,N} Z_N^T = 0 \tag{C.5}$$

$$rank\left(\lim_{N\to\infty} \frac{1}{N} X_{i,N} Z_N^T\right) = n \tag{C.6}$$

Therefore, by post-multiplying $Y_{i,s,N}$ with Z_N^T, the term $\mathcal{S}_s E_{i,s,N}$ drops out of the equation (C.3):

$$\lim_{N\to\infty} \frac{1}{N} Y_{i,s,N} Z_N^T = \lim_{N\to\infty} \frac{1}{N} \mathcal{O}_s X_{i,N} Z_N^T \tag{C.7}$$

At this point the second property (C.6) of the instrumental variable matrix Z_N ensures that the previous multiplication does not change the rank of the right-hand side of the last equation. Following the reasoning given in [178], it is possible to determine an asymptotically unbiased estimate of the column space of $\mathcal{O}_s$ from the SVD of the matrix $Y_{i,s,N} Z_N^T$ for an infinite number of output samples N, as is shown in Eq. (C.8).

$$range\left(\lim_{N\to\infty} \frac{1}{N} Y_{i,s,N} Z_N^T\right) = range(\mathcal{O}_s) \tag{C.8}$$

From this last statement it can be concluded that the modal domain of the system can be evaluated by looking at output-only data records. The method described in this section is available in the *LTI System Identification Toolbox* [179] developed at the *Delft Center for Systems and Control*, which was used in this research.

C.2.2 Challenges of operational modal analysis

Even though the SSI methods only require that the structure of interest fulfills three conditions; namely that

- it is linear,
- it is time invariant,
- it is excited by zero-mean Gaussian white-noise processes,

as could be read in section C.2.1, an operating offshore wind turbine fulfills none of these [158].

Firstly, the linearity condition is violated by a number of effects. The largest contribution to the nonlinearities are most likely the aero-elastic effects, due to the large relative velocities of the rotor blades with respect to the surrounding flow field of the air. Additionally considering that the rotor blades are over $50m$ in size and that their tip velocity can reach $300km/h$, geometrical nonlinearities due to large deformations are expected. Hydrodynamic effects and soil interaction can also introduce nonlinearities. However this contribution is considered of minor relevance with respect to the aerodynamic effects during electricity production.

Secondly, the system is not time invariant. Due to the rotating rotor, the configuration of the structure is constantly changing. In addition to this, the structure is actively controlled, thereby constantly adapting the pitch of the blades, yaw of the nacelle and power output of the generator, in order to maximize the energy production, while trying to minimize the loads on the structure.

Finally, the environmental loads exciting an offshore wind turbine are not the zero-mean Gaussian white-noise excitations that would be required according to the theory. For instance, wave loading is mainly low frequent, as the largest part of the energy is contained in the spectrum below $0.2Hz$. Another issue arising here are the harmonic loads caused by the rotating rotor, which puts a lot of energy in small bands in the spectrum The nature of these excitations are such that they do not equally distribute the energy over all the frequencies (white spectrum), but both disturbances create a colored input spectrum due to periodic excitations. The majority of these disturbances are caused by the non-homogeneous wind field that passes through the spinning rotor such as rotor unbalance (1P), tower shadow (3P), wind shear, yaw misalignment and half wakes. Moreover these input excitations are correlated. In fact, the cross-correlation of two closely spaced points on the blades and on the foundation respectively due to wind and wave excitation, is expected to be relevant.

With these effects in mind, it was decided to analyse the structural behavior of the turbine during idling condition. There are a number of advantages when using measurement data obtained from an idling turbine rather using the measurement data taken during electricity production. During idling there are less aerodynamic effects since the rotor is only slowly rotating, hence the system can be considered time invariant. This is valid in case wind direction and speed are not changing continuously. Consequently also the periodic disturbances are negligible. The blades, only subjected to the wind excitation, are pitched, reducing the loads and hence their deformations (and possible non-linearities). Therefore, if the output data used for the identification is chosen such that the yaw angle, the pitch angle and the wind speed are close to being constant, then in idling conditions almost all the assumptions for the OMA methods are met to a large extend.

C.3 Measurement data used for the identification

Firstly, the turbine from which the measurement data is obtained is introduced. In addition to this, a brief introduction to the different measurement channels that were available is given.

C.3.1 Burbo Banks wind turbine number 16

In this paper the data coming from the idling Burbo Bank turbine number 16 (BB16) are used. Burbo Bank (BB) windfarm, owned by DONG Energy, is a fully operational farm offshore of the west coast of England, close to Liverpool in the Irish sea. It consists of 25 Siemens SWT-3.6-107 turbines, which have a rated power of 3.6 MW and are equipped with a rotor that has a diameter of 107m. The wind farm was officially inaugurated on 18 Oktober 2007 and has, since then, been providing electricity for about 80 thousand households. The site location is shown in figure C.1. Turbine number 16 in the wind farm is equipped with additional instrumentation for monitoring and analysis purposes. Considering the position of the windfarm it is reasonable

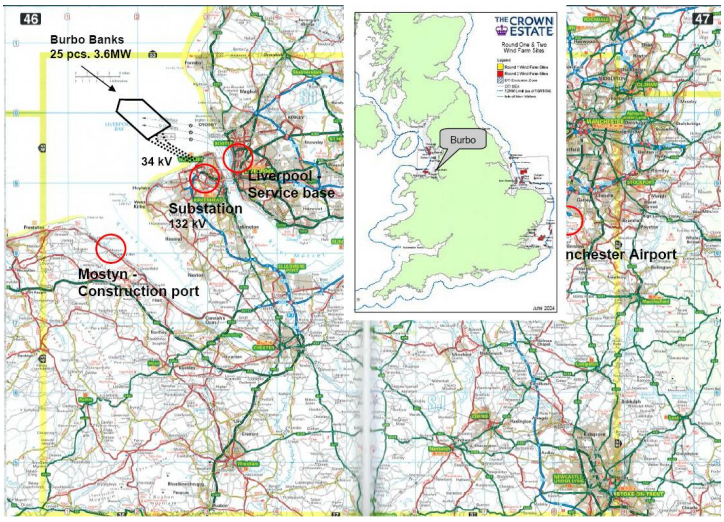

Figure C.1: *Location of the Burbo Banks offshore wind farm, where the measurement data was obtained from turbine 16.*

to expect that the wind and the wave excitations are mainly from the west side, which is the oceanic side of the wind farm. The available information for the sea conditions indicate a typical wave period of $T_w = 7 - 10[s]$ with an averaged significant wave height of $H_w = 5[m]$. Maximum waves height of $H_{max} = 10[m]$ are registered in extreme conditions. As a consequence the highest wave excitations are expected in the frequency range of $f_w = 0.1 - 0.15[Hz]$.

C.3.2 Selection of measurement data

Several sensors were available on the offshore wind turbine. Firstly, a bi-directional accelerometer was installed in the back-end of the nacelle. In addition a number of strain gauges at the tower top, which measured the bending moments and the torsional moment, and strain gauges at the tower bottom, that measured the bending moments, were available.

The measurement data from these sensors is sampled at $25Hz$ and stored in a central database. As this wind farm has already been operating for a couple of years, large amounts of data are available for analysis. Using the synchronized measurements of the generator speed, several

blocks where found where the turbine is idling. The turbines can be in idling mode if the wind speeds are too low, or due to planned maintenance and/or system malfunctions, therefore measurement data in different environmental conditions could be extracted from the database. For this analysis, five different blocks of measurement data were obtained at average wind speeds of $1.7m/s$, $3.7m/s$, $6.3m/s$, $8.0m/s$ and $10m/s$. As it was required that the conditions remained stationary, the blocks of measurement data have varying time lengths, ranging from 20 minutes to over one hour. Some of the data used is shown in figure C.2. In the figures one

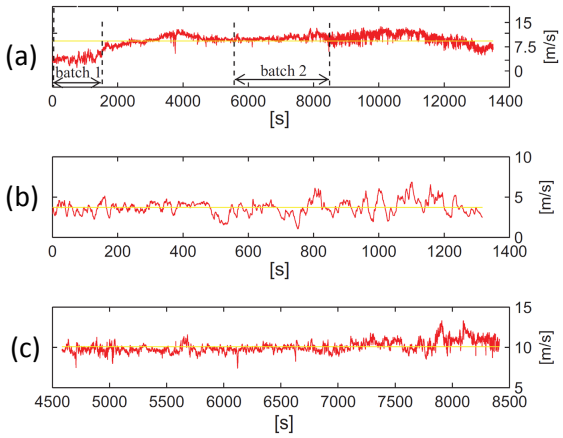

Figure C.2: *Wind speeds measured while idling;* ***(a)*** *The original set of over 2 hours of data;* ***(b)*** *the first batch selected;* ***(c)*** *the second batch selected. All figures showing the mean wind speeds (—) and the actual measured wind speeds (—) on top of the nacelle.*

can identify the lines for the actual measured wind speeds and the mean of the wind speed over the measurement block, who have their y-axis on the right side of the figure. These data blocks came, among others, with synchronized measurement data from the different strain gauges and the bi-directional accelerometer.

C.4 Modal identification of the idling wind turbine

In order to obtain the modal domain of the idling wind turbine, a number of steps were required. In this section, this process will be discussed and some intermediate results are shown, finally resulting in the the eigenfrequencies and modal damping ratios of the first four global modes. Even though a sensor mix of accelerometers and strain gauges was available, the results shown in the section are obtained from using only the measured accelerations. It was found that the quality of the measurement data obtained from the strain gauges was less than that from the accelerometers. Hence, including the measured strains in the identification process gave more noisy and less stable and clear stability diagrams (section C.4.2). Nonetheless, the measurements of the strain gauges were still used to be able to distinguish between the different modes, as will be described in section C.4.3. All the intermediate steps in these subsections are illustrated using the measurements taken while idling in 1.7 m/s wind speeds. Finally, in section C.4.4, a global overview of the (normalized) eigenfrequencies and damping ratios estimated at different environmental conditions is given and discussed.

C.4.1 Preparations for the identification

All five measurement blocks are pre-processed in the same way, hence all signals are de-trended, scaled to unitary variance, low-pass filtered using a zero-phase low-pass 8th order Butterworth filter with a cut-off frequency of $12Hz$. The zero-phase filtered signal is obtained by performing both a forward and backward filtering operation, thereby preventing phase shifts.

The SSI tools used, allow for concatenating different measurement batches under approximately the same operating conditions. Therefore it also allows to divide single large blocks of measurement data in several smaller batches of data, which is advantageous for the computations required, as the memory consumption can be kept within limits. Hence, each of the five measurements is cut in sequences of 5 minutes and fed to the SSI algorithm which processes them as 12 consecutive batches (in case of a single measurement block of an hour). This approach also gives better results as, within each batch, smaller variations of the environmental conditions are more probable. For all identifications performed, the same maximum subspace dimension

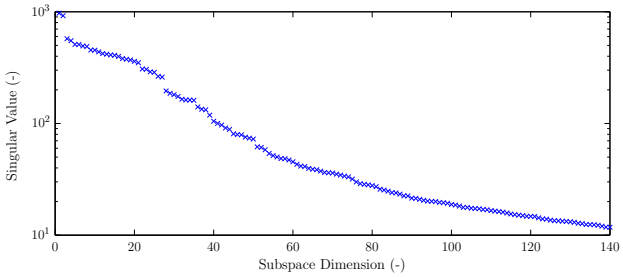

Figure C.3: *Estimating the order of the system using the Singular Values, computed from the measurement data obtained at 1.7 m/s wind speeds.*

$s = 140$ is used. This value was iteratively determined as the upper limit of the model order, in accordance with [179] that suggests using a maximum subspace dimension a factor 2-3 larger than the expected physical model order n. In fact, this physical order was assessed before and it is estimated for this value to be between $36 < n < 44$ at best. Nonetheless, from figure C.3 one cannot get a good estimate of the system order from the singular values. Even though one can identify a number of drops in singular values (n), at for instance $n = 3$ and $n = 28$, these drops are relatively small and give no clear indication where the division between "modal" domain and the "noise" domain is. Hence, we are forced to estimate the system order from the stability diagrams. Nonetheless, the initial estimate for the order of the system to be in the range of $36 < n < 44$, appears to be an underestimation of the actual system order.

C.4.2 Stability diagram and the poles of the system

As it was found in section C.4.1 that we cannot a priori estimate the system order, we will use the stability diagram to get an estimate of the system order or at least an indication of the range of the order of the system. Therefore, the system identification is performed for all the different orders between $4 \leq n \leq 100$. By plotting all the eigenfrequencies and associated damping values as dots in a figure for the entire range of system orders, the stability diagram is obtained in figure C.4. Visually, it can already be seen that the eigenfrequencies do not vary much over the different model orders. The damping values, on the other hand, can vary over the different model orders. In order to get an idea of this variation, the poles corresponding to a single mode are clustered. As the first two modes in figure C.4 are closely spaced, the MAC criterion [3] is used to distinguish between the different modes. As we know that the

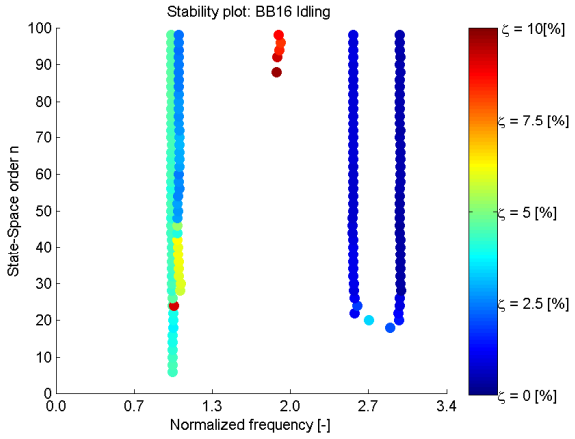

Figure C.4: *Stability diagram obtained from the measurement data acquired at an average wind speed of 1.7 m/s.*

first two modes of the wind turbine are the fore-aft mode and side-side mode, they can easily be separated from each other, regardless of the fact that we only have measurements from one bi-directional accelerometer. This can be seen in figure C.5(a), where 2 blocks of modes can be distinguished. Using the results from the modal clustering, the eigenfrequencies and associated

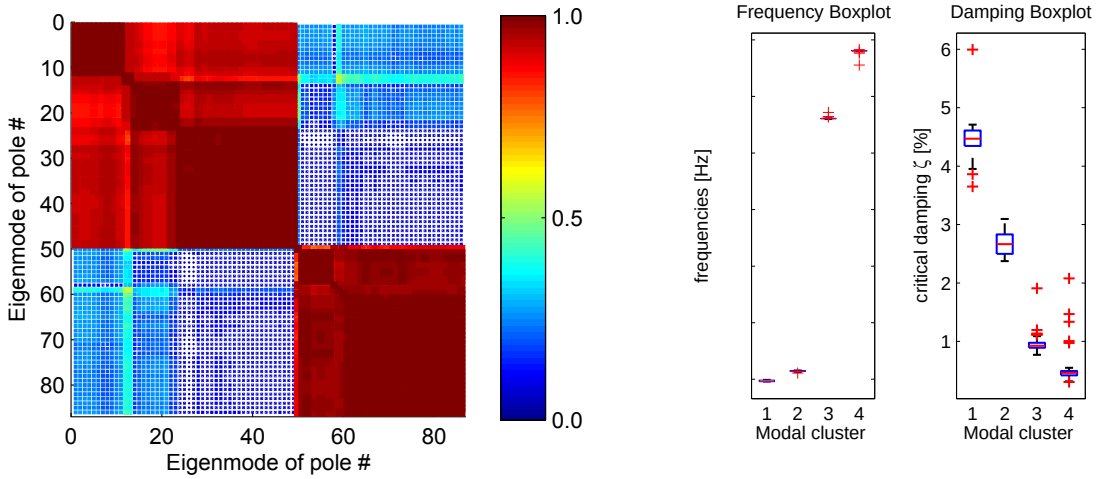

(a) MAC plot showing the modal clusters of the first two poles found in figure C.4.

(b) Boxplots showing the variation in the eigenfrequencies and modal damping ratios.

Figure C.5

modal damping ratios can be reorganized in a box-plot as is shown in figure C.5(b). Due to the high variations found in the modal damping ratios at low model order, the low order model results are discarded before creating figure C.5(b). Here one can identify the median of the modal parameters (red line within the blue box), the interquartile range (IQR) as the blue box, and the whiskers denoting the 1.5 times IQR range with respect to the IQR and finally the outliers as red crosses. Hence it is clear that the identification leads to very stable results for the first four eigenfrequencies, but that there is a big spread in the damping values found for the different model orders. It should be noted, that the statistics obtained in figure C.5(b) are not appropriate for determining the confidence interval of the damping ratios. In order to obtain the confidence intervals, we would have to apply for instance bootstrapping techniques [11]. Nonetheless, by comparing figure C.5(b) and figure C.4, it can be seen that the damping values

tend to converge for the higher order models.

C.4.3 Identified modes of the wind turbine

As is clear from the stabilization diagram, four different modes could be identified. The first two modes could easily be identified as the global fore-aft (1st tower bending longitudinal - 1 T LO) and side-side (1st tower bending lateral - 1 T LA) modes, which are shown in figure C.6. One could also deduce this result from figure C.5(b), as the first mode has a significantly higher damping than the second. As the frequencies of these modes are design considerations, they are thus known beforehand. The third and fourth mode found however, are not so straight

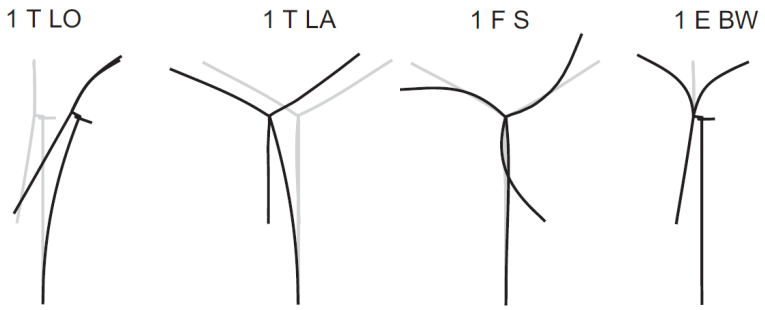

Figure C.6: *Modes of the offshore wind turbine that were identified [113].*

forward to link to the global modes of the wind turbine. As only a limited number of sensors were available, of which non of them was located on the blades, one cannot distinguish directly between all the rotor modes. Hence, by comparing the result from the identification with results from the numerical model and simple reasoning, we were able to classify the modes. Therefore, the third mode identified is considered to be the first flapwise symmetric (blade) mode (1 F S). This because its identified frequency is close to the numerical one and the identified modeshape contained a contribution (at the bi-directional accelerometer) parallel to the main shaft. In addition to this its relative modal damping is higher than the modal damping associated to the fourth mode identified and it is assumed that the modal damping is higher for flapwise motions in idling conditions. The fourth mode identified is estimated to be the first edgewise backward whirling (blade) mode (1 E BW). This mode excited a strong torsional moment in the tower, that could be identified by including the torsional tower top strain gauge in the identification.

C.4.4 Overview of all the results

After performing the steps listed in sections C.4.1 and C.4.2 for all the different measurement blocks, a global overview of the results was created, which is shown in figure C.7. These plots show the relation between the identified natural frequencies and modal damping ratios as a function of wind speed and thus give a global picture of the identified modal domain for different wind speeds. It is clear that the frequency estimation is much more stable than the estimated damping ratios. In addition to the very low standard deviation on the eigenfrequencies found from assessing the different model orders, the frequencies themselves do not change very much with respect to the wind speed. The damping values on the other hand, result in a large standard deviation over the different model orders and can also vary significantly over the different wind speeds. As one can see from figure C.2, the wind speed is varying (within margins) as well over the duration of the measurement, hence it is expected that the aerodynamic damping

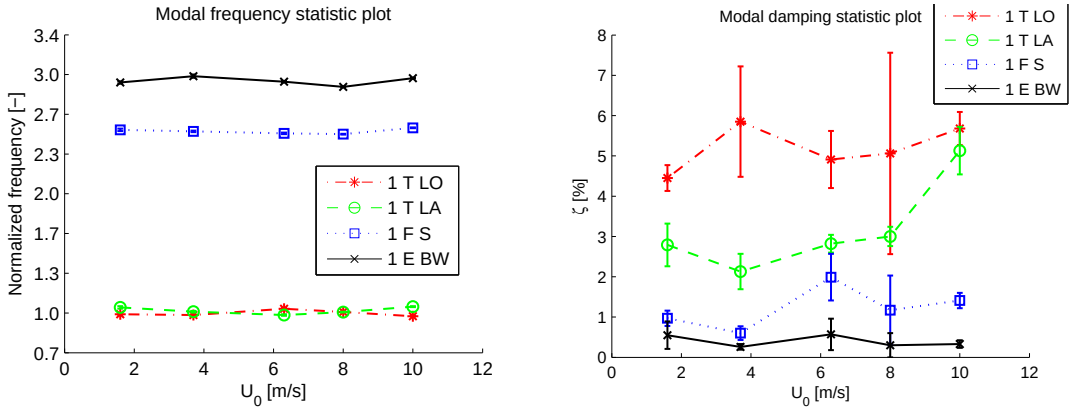

(a) Eigenfrequencies ***(b)*** Modal damping ratios

Figure C.7: *Mean and standard deviation of the poles, obtained from the different model orders, as function of the wind speed.*

contribution will vary as well. Therefore, it is expected that the large deviation of the damping ratios over the different model order is related to these non-stationary aerodynamic damping contributions. In addition, there could be two other possible reasons for this relatively poor damping estimation. Firstly, as mentioned in section C.2.1 the SSI method is only to guarantee asymptotically unbiased estimates if one has an infinite number of measurement points, which is clearly not the case here. Secondly, due to the fact that the rotor of an idling turbine is still rotating at very low speeds, system in constantly changing. Some of this time varying could translate in high damping variation, as the identification tries to fit a LTI system and tunes the damping to get a good fit. Additionally for the blade modes, where this deviation is smaller, an increase in modal damping ratio with increasing wind can be detected for the flapwise motion 1 F S, whereas the 1 E BW mode instead shows more constant damping values.

It should be noted here that the wind speeds recorded are estimated from the anemometer that is installed on top of the nacelle and therefore do not directly measure the undisturbed wind field. In addition to this there is an other important unknown; the wave loading on the offshore turbine, as no data regarding wave heights and periods are available. Therefore, due to only limited data available about the environmental conditions, no conclusive statements can be made about the results.

C.5 Conclusions and future work

From the results obtained a number of conclusions and findings can be formulated. As was already mentioned throughout the paper; due to the number of unknowns, no conclusive statements can be given yet about a number of effects encountered. Nonetheless a number of conclusions can still be drawn:

- Four modes were identified in the low frequency range. The first two modes were easily and with a high certainty identified to be the two tower bending modes (1 T LO and 1 T LA). The third and fourth mode could not be classified directly from the obtained modeshapes, as only one bi-directional accelerometer was used in the identification. By using the numerical model of the turbine and the data from an of auxiliary tower torsion strain gauge, we estimated that the third mode is the first flapwise symmetric (blade) mode (1 F S) and the that fourth mode is probably the first edgewise backward whirling

(blade) mode (1 E BW).

- Accurate estimates of the eigenfrequencies were found for all wind speeds, but a big spread was found in the associated damping ratios. In fact the results show large deviations from the mean values, emphasizing the difficulty of accurately quantifying the damping contribution, especially as it the contribution itself is expected to vary over time as well.
- The comparison between the identified modal parameters of the idling BB16 under different wind speeds shows certain specific, mode dependent, trends in frequencies and damping variations. Since no information about the waves is available, it is impossible to determine which part of the estimated global modal damping value is due to the hydrodynamic contribution and which due to aerodynamic damping. However, the trend of increasing modal damping as a function of increasing wind speeds, indicates that there the aerodynamic damping is most likely one of the most important damping mechanism of an offshore wind turbine.

Future work on the subject will be needed to come to a better understanding of the relation between the environmental conditions and the damping ratios identified. A number of steps that we would like to take are:

- Obtain proper statistics with respect to the identified modal damping ratios. If we can get reliable estimates of the damping ratios identified, we'll at least know in which range the actual damping ratios are. By choosing the lowest values of this range, we can ensure that the load simulation will be conservative, without being overly conservative. One method for obtaining these statistic would for instance to use bootstrapping methods, as was discussed in section C.4.2.
- Try to separate the different damping contributions in the global damping ratios that are identified from an OMA procedure. This will allow for fine tuning the aero-elastic models used in the design phase, such that not only the stiffness and mass distributions are accurate, but also the distribution of damping will more accurately represent reality.

Finally it should be noted that from the authors point of view, input and model validation of aero-elastic models will be one of the key aspects in bringing down the cost of (offshore) wind generated electricity in the coming years. Over the last years the modeling and simulation capabilities have been enhanced, by ever increasing computational power and a growing availability of state-of-the-art simulation tools. Hence an important step that needs to be taken is to feed these advanced models with validated inputs and to validate the models themselves, thereby reducing the uncertainty of the models and their output. This in turn would reduce the need for applying extra safety factors for covering the potential modeling errors and thus lead to more optimized and less costly designs.

D

List of personal publications

Journal publications

P. L. C. van der Valk, S. N. Voormeeren, P. C. de Valk, and D. J. Rixen. Dynamic Models for Load Calculation Procedures of Offshore Wind Turbine Support Structures: Overview, Assessment and Outlook. *Journal of Computational and Nonlinear Dynamics*, Accepted for publication:1–24, 2014

P. L. C. van der Valk and D. J. Rixen. An Impulse Based Substructuring Method for Coupling Impulse Response Functions and Finite Element Models. *Computer Methods in Applied Mechanics and Engineering*, 275:113–137, 2014

D. J. Rixen and P. L. C. van der Valk. An Impulse Based Substructuring approach for impact analysis and load case simulations. *Journal of Sound and Vibration* , 332(26):7174–7190, 2013

S. N. Voormeeren, P. L. C. van der Valk, B. P. Nortier, D.-P. Molenaar, and D. J. Rixen. Accurate and Efficient Modeling of Complex Offshore Wind Turbine Support Structures using Augmented Superelements. *Wind Energy*, 17:1035–1054, 2014

S. N. Voormeeren, P. L. C. van der Valk, and D. J. Rixen. Generalized Methodology for Assembly and Reduction of Component Models for Dynamic Substructuring. *AIAA Journal*, 49(5):1010–1020, May 2011

Conference publications

P. L. C. van der Valk and M. G. L. Ogno. Identifying Structural Parameters of an Idling Offshore Wind Turbine Using Operational Modal Analysis. In F. N. Catbas, editor, *Dynamics of Civil Structures, Volume 4*, Conference Proceedings of the Society for Experimental Mechanics Series, pages 271–281. Springer International Publishing, 2014

P. L. C. van der Valk and D. J. Rixen. Towards a Parallel Time Integration Method for Nonlinear Systems. In *Dynamics of Coupled Structures, Volume 1: Proceedings of the 32nd IMAC, A Conference and Exposition on Structural Dynamics, 2014*, 2014

M. V. van der Seijs, P. L. C. van der Valk, T. van der Horst, and D. J. Rixen. Towards Dynamic Substructuring Using Measured Impulse Response Functions. In M. Allen, R. Mayes, and D. Rixen, editors, *Dynamics of Coupled Structures, Volume 1*, Conference Proceedings of the Society for Experimental Mechanics Series, pages 73–82. Springer International Publishing, 2014

P. L. C. van der Valk and D. J. Rixen. A Co-Simulation Method for Coupling Complex Foundation Models and Wind Turbine Models in Aero-Elastic Simulations. In Z. Dimitrovovťa, J. R. de Almeida, and R. Gonçalves, editors, *Proceedings of the 11th International Conference on Vibration Problems, Lisbon, Portugal, 9-12 September 2013*, 2013

P. L. C. van der Valk and D. J. Rixen. Substituting Internal Forces for Blocked Forces or Free Interface Displacements in Substructured Simulations. In *Topics in Experimental Dynamic Substructuring, Volume 2: Proceedings of the 31st IMAC, A Conference on Structural Dynamics, 2013*, 2013

R. Haghi, T. Ashuri, P. L. C. van der Valk, and D. P. Molenaar. Integrated Multidisciplinary Constrained Optimization of Offshore Support Structures. In *Proceedings of the Science of Making Torque from Wind (TORQUE) 2012. Oldenburg, Germany*, 2012

P. L. C. van der Valk and S. N. Voormeeren. An overview of modeling approaches for complex offshore wind turbine support structures. In *Proceedings of ISMA2012-USD2012*, 2012

P. L. C. van der Valk and D. J. Rixen. Impulse Based Substructuring for Coupling Offshore Structures and Wind Turbines in Aero-Elastic Simulations. In *Proceedings of 53rd AIAA/ASME/ASCE/AHS/ASC Structures, Structural Dynamics and Materials Conference, 23 - 26 April 2012, Honolulu, Hawaii*, 2012

P. L. C. van der Valk and D. J. Rixen. An Effective Method for Assembling Impulse Response Functions to Linear and Non-Linear Finite Element Models. In *Proceedings of the SEM IMAC XXX Conference Jan. 30 - Feb. 2, 2012, Jacksonville, FL USA*, 2012

S. N. Voormeeren, P. L. C. van der Valk, and D. J. Rixen. A Truly Hybrid Approach to Substructuring Problems Using Mixed Assembly and Implicit Solving Strategies. In T. Proulx, editor, *Linking Models and Experiments, Volume 2*, Conference Proceedings of the Society for Experimental Mechanics Series, pages 329–347. Springer New York, 2011

P. L. C. van der Valk, J. B. Wuijckhuijse, and D. Klerk. A Benchmark Test Structure for Experimental Dynamic Substructuring. In T. Proulx, editor, *Structural Dynamics, Volume 3*, Conference Proceedings of the Society for Experimental Mechanics Series, pages 1113–1122. Springer New York, 2011

S. N. Voormeeren, P. L. C. van der Valk, and D. J. Rixen. Practical aspects of dynamic substructuring in wind turbine engineering. In *Structural Dynamics and Renewable Energy, Volume 1*, pages 163–185. Springer, 2011

S. N. Voormeeren, P. L. C. van der Valk, and D. J. Rixen. A General Mixed Boundary Model Reduction Method for Component Mode Synthesis. In *Proceedings of the WCCM/APCOM 2010*, 2010

Curriculum Vitae

Paul van der Valk was born in Naalwijk, the Netherlands, on the 30$^{\text{th}}$ of March 1985. After completing the pre-university education at the *Interconfessionele Scholengroep Westland* in Naaldwijk, he started studying Mechanical Engineering at Delft University of Technology (DUT) in September 2003. In September 2007 he obtained his BSc. degree, after which he enrolled in the MSc. specialization of Engineering Dynamics. As part of his Master he conducted an internship and graduation project at Siemens Wind Power (SWP) under the guidance of dr. Sven Voormeeren. After completing his MSc. thesis, entitled "Model Reduction & Interface Modeling in Dynamic Substructuring; Application to a Multi-Megawatt Wind Turbine", Paul graduated *Cum Laude* in January 2010.

Since May 2010 he has been working as a PhD. candidate in the Engineering Dynamics research group at DUT, under the supervision of prof. Daniel Rixen, on a collaborative research project between SWP and DUT. During the course of this project he supervised a number of BSc. and MSc. students, published several papers and also helped to implement some of the tools and methods developed in the engineering practise at SWP.

Index